NATIONAL TECHNICAL UNIVERSITY OF ATHENS
SCHOOL OF NAVAL ARCHITECTURE AND MARINE ENGINEERING
DIVISION OF SHIP AND MARINE HYDRODYNAMICS

# A boundary element method for the hydrodynamic analysis of flapping-foil thrusters operating beneath the free surface and in waves

Diploma Thesis

**February 2013**

Author : Evangelos S. Filippas

Supervisor : Konstantinos A. Belibassakis, Associate Professor, NTUA

Commitee : Gerasimos K. Politis, Associate Professor, NTUA

Georgios S. Triantafyllou, Professor, NTUA

***Dedicated to my Grandparents***

**Acknowledgements**

The present Diploma Thesis is completing a five-year period of studies at the School of Naval Architecture and Marine Engineering of National Technical University of Athens. Thus, I grab the chance to express my sincere gratitude to a number of people whose contribution where valuable for the accomplishment of this work and of my studies.

First of all, I would like to thank my supervisor and mentor Associate Professor K. Belibassakis for his guidance and support during the preparation of this thesis. His deep and wide knowledge in the field of marine hydrodynamics provided me with the required background to overcome the difficulties encountered during this study. Furthermore, he gave me inspiration and encouragement during that educational as well as preceptive journey.

Another special thank would be to Associate Professor G. Politis for supporting me and introducing me to application of BEM's on the problem of unsteady hydrofoils in infinite domain (Chapter 2).

Moreover, of utmost importance was the inspiration of the aforementioned Professors as well as Professors G. Athanassoulis, G. Triantafyllou and G. Tzabiras, during my studies.

Also, I am very grateful to researcher Giannis Georgiou and PhD Candidates Aris Kapelonis, Ivi Tsantili and Vasilis Tsarsitalidis for the support and their very useful advice and my fellow student Orestis Vlachos for the help with the figures.

Last but not least, I would like to thank my family, Evie and my friends as without their help, support and understanding it would be very difficult to finish my studies.

## Contents

## Abstract

The analysis of an oscillating wing located beneath the ship's hull is investigated at NTUA as an unsteady thruster, augmenting the overall propulsion of the ship and offering dynamic stabilization. The unsteady thruster undergoes a combined oscillatory motion in the presence of waves. One mode of operation of the above system is with the wings in horizontal arrangement, where the vertical heaving motion is induced by the motion of the ship in waves, essentially ship heave and pitch, while the rotational pitching motion of the flapping propulsor about its pivot axis is set by an active control mechanism. For the detailed investigation of the effects of the free surface in the present thesis a potential-based panel method has been developed for the hydrodynamic analysis of 2D hydrofoil operating beneath the free surface, undergoing heaving (vertical) and pitching oscillations while moving with constant forward speed. The instantaneous angle of attack is influenced by the foil oscillatory motion and by the incident waves. At a first stage of development we consider moderate submergence and relatively low speeds permitting us to approximately assume low free-surface amplitudes and neglect nonlinear effects due to breaking waves and cavitation.

We begin with a historic review concerning biomimetic wing systems, and then the motivation for the present study and research is described. We also present a brief historical review in panel methods, focused on their application, from the first simple version, until modern Boundary Element Methods applied to complex problems of mechanics, hydrodynamics, etc.

Subsequently, a direct potential-based low order boundary element method developed to treat the unsteady flapping hydrofoil problem in infinite domain is presented. Numerical results concerning convergence, stability and efficiency are shown and discussed. Furthermore, present predictions are compared against analytical unsteady thin hydrofoil theory, presented in Appendix C, and experimental results by Schouveiler et al (2005) for validation of the method.

For simplicity in the description of the present method and especially as concerns the treatment of the free surface conditions (including the conditions at infinity), in the third chapter we present the boundary integral formulation in the case of non-lifting flow around a body of smooth but arbitrary geometry, undergoing general motion. This simplified problem is associated with the wave generation by the body and the treatment of memory effects, and includes two subproblems of special interest, the wave resistance problem and the enforced radiation problem due to body oscillations (heaving and pitching).

In the last chapter we extend our scheme in order to treat the complex problem of unsteady lifting bodies beneath the free surface and in the presence of incoming waves. The latter includes as special subproblems the resistance due to the waves generated by the foil, the added resistance due to the incident waves and the corresponding enforced radiation and diffraction problems. Numerical results are presented concerning the numerical performance of the developed BEM. Also results concerning the thrust coefficient and the efficiency of the system in flapping mode are presented over a range of motion parameters, including reduced frequency, Strouhal number, feathering parameter and Froude number and compared against other methods. Our analysis indicates that significant thrust can be generated under optimal operating conditions. Also, it is demonstrated that the effects of the free surface are important and cannot be neglected. Thus, the present method can serve as a useful tool for assessment and the preliminary design and control of such systems extracting energy from sea waves for marine propulsion.

# 1 Introduction

In the present introductory chapter, we begin with a brief historic review, concerning research on biomimetic systems, such as flapping wings propulsors, inspired by swimming and flying creatures. These systems, as we will demonstrate, have been are ideally suited for converting directly environmental (sea wave) energy to useful thrust for ships and other marine vehicles. In the second part of this chapter we will present the basic effort that have been done in this direction, as well as, the recent ideas and finally the contribution of the present thesis in that topic.

## 1.1 Propulsion using biomimetic flapping foil thrusters

We will present a brief historic review concerning the research and development of biomimetic systems, such as flapping wings, for propulsion and maneuvering purposes in ships and in general. We begin with a reference to the premature research in fish-motion and propulsion, until the first half of 20th century. In the next section we present a brief review in the experimental investigation over the years. We continue with the major theoretical contributions and finally we dedicate a section to the more recent numerical study of biomimetic flapping-foil systems.

First of all, we mention the basic historic reviews we have consulted, where someone can find a more detailed bibliographic study. A detailed reference in the development of sea creatures' mechanics published by Alexander in 1983. Also, a review can be found in Sparenberg (2002) concerning fundamental theoretical developments by Lighthill (1969) and Wu (1971) with additional reference to Gray's paradox (1936) (see also Section 4.6.1.). Also, research and development of flapping wing propulsors and results concerning application to marine vehicles equipped with such systems is reviewed and discussed in Rozhdestvensky & Ryzhov (2003). A detailed presentation of experimental state of the art can be found in Triantafyllou et al (2004). Furthermore, a survey of experimental hydrodynamic data on undulatory locomotion in fishes, providing as background a general description of the major theoretical propulsion models, has also been presented by Lauder & Tyttel (2006). Finally state-of-the-art in experimental research on the physics of swimming and flying organisms is presented by Taylor et al (2010).

*Premature research*

We will now give a brief survey on the research of fish locomotion during the early stages of history. The first reference to the study of the anatomy and locomotion of hydrobionts rests in the ancient years by Greek philosopher Aristotle, according to Alexander (1983). Also in 1490, Leonardo da Vinci in his drawings presented a attempt to the understanding of the basic principle of thrust generation by a flapping wing (Rozhdestvensky & Ryzhov, 2003). After this, however, it took a long time before significant progress to be noticed.

During the latter years of 17th century, the development of mercury barometer by Torricelli and air pump by von Guericke were the threshold of a rapid increase in research activities. For instance, the mechanism called swim bladder was used extensively to study fish locomotion. As Sparenberg (2002) explains: *"By decreasing the pressure on the surface of the water in a vessel in which a fish was present, the bladder of the fish expanded, by which the fish rose to the surface*

*and could not swim downwards. When the original pressure was restored, the fish sank to the bottom of the vessel since, as turned out by dissection, too little air was left in the bladder"*. In the period between 1700 and 1800 some progress had been made due to the invention of photography and film, by which fish locomotion were recorded. Sparenberg (2002) mentions the names of A. Moreau, regarding measurements at the bladder and E.J. Marey, for the recording of fish movements.

In the first half of 20th century collaborated research by zoologists and engineers, using wooden models or weighted dead fish for experimental measurements of hydrodynamic characteristics, was the begging of a very productive era in experimental research of fish mechanics.

*Understanding of fish locomotion for the design of efficient biomimetic systems through experimental research*

The superior swimming and maneuvering capabilities of aquatic animals have been motivated research on fish-like propulsion for many years. Most fish generate thrust by a wave-type deformation of their full body. In 1926, Breder in "The locomotion of fishes" named plenty of swimming forms. When the amplitude is large along the whole body, the swimming is of undulatory type and is called anguilliform; if the undulations are confined in the posterior part of the body the swimming is said to be carangiform. Ultimately, when the amplitude is significant only at the tail, the swimming is oscillatory. In the last case which is the most popular to cetaceans, thrust generation occurs by the horizontal flapping motion of the tail in the case of whales or dolphins, or by the oscillations of the vertical fin, in the case of sharks and tunas. This last family of hydrobionts is called thunniform, they are equipped with a rigid body and an oscillating moon-shaped tail that attaches to the body with a stem, in a way that minimizes recoil (Lighthill, 1969). As Lighthill mentioned in 1970, "*the thunniform swimming mode is known as the most efficient for fast swimming*". An extensive review on the fish swimming modes can be found in Sfakiotakis et al (1999). Also, many reviews addressing various aspects of fish propulsion have been presented by Webb (1975), Lindsey (1978), Blake (1983), Webb & Weihs (1983), Videler (1993).

In 1969, Lighthill was the first one that suggested a biomimetic flapping foil device as an alternative to the conventional screw propellers, for thrust production purposes. The basic thrust production mechanism on flapping-foil systems is based on the jet reaction principle. Under appropriate kinematical conditions, a jet-like flow is created downstream the foil and thus, for conservation of momentum, a thrust force acts on the body. In this case in foil's wake alternate vortices appears, similar to the well-known von Karman vortex street behind blunt shaped bodies, except that the vorticity is reversed. Extensive work on flow visualizations pertaining to foils may be found in Scherer (1968), Ohashi & Ishikawa (1972), Oshima and Oshima (1980), Oshima and Natsume (1980), Freymuth (1988), Koochesfahani (1989), and Anderson et al(1998).

Plenty researches shown that biomimetic systems inspired by hydrobionts not only could produce high thrust but also in a high degree of efficiency. For instance, Bose and Lien (1989) estimated that the maximum hydromechanical efficiency of a whale is about 85%. Furthermore, Triantafyllou, Triantafyllou & Gopalkrishnan (1991) and Triantafyllou, Triantafyllou & Grosenbaugh (1993) shown that optimal propulsive efficiency occurs at non-dimensional frequencies corresponding to the maximum growth of the jet flow behind the foil.

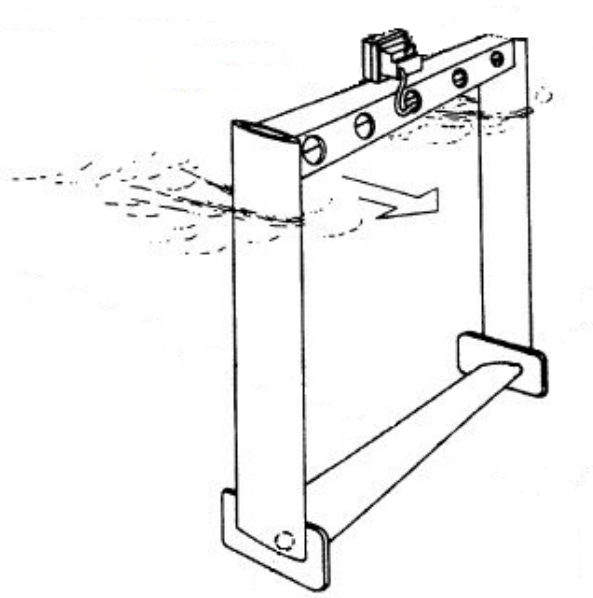

Figure 1: Apparatus used for conducting force measurements experiments by Anderson et al (1998).

In 80's, study of flapping motion under large angle's of attack revealed that high values of lift coefficient were associated with the formation of a leading-edge vortex, also referred to as a dynamic-stall vortex, McCroskey (1982), Reynolds & Carr (1985). Concerning leading edge separation, Ellington (1984) notes the significant delay in stall caused by unsteady effects, as found earlier, for example, by Maresca, Favier & Rebout (1979) for a foil at large angles of attack in steady flow undergoing axial oscillations. Furthermore, Freymuth (1988) studied the effect of angle of attack and frequency in thrust generation using a NACA0015 hydrofoil, performing flapping motion, in a wind tunnel at Reynolds numbers between 5200 and 12000 and noticed that a reverse Karman vortex street is formed by a weak leading edge separation merged with the trailing edge vortex. He mentioned also that in larger angles of attack strong leading edge separation weakens the thrust producing qualities of the vortex wake. Furthermore, while reducing the frequency of oscillation, the reverse Karman vortex wake is becoming more and more sluggish and finally the usual von Karman street which is associated to viscous pressure drag is becoming evident. In 1988, Koochesfahani and Dimotakis concentrated to the pitching mode of oscillation. They noticed that at pitch angles larger than 41°, leading-edge vortices occurs, and the tendency to thrust production decreases as the oscillation amplitude increases. Latter in 90s, Anderson (1996) performed digital particle image velocimetry (DPIV) on a foil in flapping motion. After numerous experiments he created a vortex pattern map for wake forms, where someone can notice cases that large heave amplitude oscillations leads to the creation of leading edge vortexes as well as trailing edge ones, that coalesce to indicate an optimal thrust-generation condition. In addition, many researchers stated that an oscillating foil can be further used for manipulation of incoming vorticity, and recapturation of vortical energy, see Koochesfahani and Dimotakis (1988), Cortelezzi et al (1997), Streitlien et al (1996); Gopalkrishnan et al (1994).

More detailed experimental study on the motions of flapping wing system, with additional evidence for the efficiency came in 1989 and 1990 by Hoppe (1989), Koochesfahani (1989) for a foil in pitching motion, and also by Freymuth(1990) for a foil in a flapping motion. In the same period, Ohmi et al (1990), (1991) studied the vortex formation in the flow around a translating and harmonically pitching foil at Reynolds numbers between 1500 and 10000, with mean incidence angle of 15° or 30°. At large angles they found that the patterns in the vortex wake depend on whether the translational or rotational motion dominates the flow. In the case of the flow dominated by the rotational motion, the governing parameter is the product of the reduced frequency and the pitch amplitude, which is closely related to the Strouhal number, see also Triantafyllou et al (1991, 1993). Ohmi et al in 1990 found that the Reynolds number effect was secondary importance. Also, MacCroskey (1982), who studied extensively the effects of unsteady flow mechanisms on foils, including dynamic-stall vortex formation, tends to agree with that statement. Gursul and Ho (1992) through experiments on stationary hydrofoils in a background sinusoidal field demonstrated that some dramatic effects occurs due to the unsteadiness of the flow.

In the last decades of 20th century and the first of 21th, extensive experimental work have been done by many other researchers like Lai, Bose & McGregor (1993), and a serious amount of work have been made by Triantafyllou and co-workers in MIT laboratories (1991, 1993, 2000, 2002, 2004), see also Barrett et al (1999), Schouveiler et al (2005), Anderson et al (1998). Until 1998, linear inviscid theory had predicted that an oscillating foil can reach, for certain parametric combinations, very high propulsive efficiency. Older experimental results, however, have often provided lower efficiencies that potential theory. Scherer (1968), for example, stated that the maximum efficiency of a flapping-foil system is typically less than 70%. In 1998, Anderson et al (1998) show that under optimal conditions, efficiency higher than 85% can be stably achieved. These findings were supplemented by Lai and Platzer (1999), Zhu et al (2002), Read et al (2003), Hover at al (2004) and Schouveiler at al (2005). Read et al (2003), found that the introduction of higher harmonics in the heave motion, so as to ensure a sinusoidal variation in the angle of attack, produced much higher thrust coefficient at high Strouhal numbers. In 2004, Hover et al studied the effect of angle's of attack time history and reported that the most efficient situation is achieved with a cosine profile, while highest thrusts are found with a sawtooth profile. Later Scouveiler et al (2005) identified a parameter range where efficiency and high thrust conditions are achieved together, as required for use of flapping foils, as a propulsion system.

High efficiency is not the only advantage of a flapping-foil biomimetic system. As Gursul and Ho (1992) mentioned, unsteady vortex control creates very high lift coefficients for maneuvering. Additional work on underwater vehicle propulsion and maneuvering has been performed by Bandyopadhyay et al(1997) and Kato (1998). Experimental evidence by Read et al (2003) and Scouveiler et al (2005) also, demonstrates that when flapping foils perform undergoing nonsymmetrical flapping, extraordinary maneuvering capacity occurs.

Finally, the three dimensionality of flapping wings and fins has also been studied experimentally by Hart et al (1992), Dickinson et al(1999), and Drucker & Lauder (1999).

*A note in the history of fish-propulsion theory*

As we have already mentioned experimental research was very fruitful; in addition, as Sparenberg (2002) notices, a third group entered the scene around 1950. That group developed theories, for quantitative analysis of swimming propulsion, as a continuation of the previously and concurrently developing qualitative methods. In 1952, G.I. Taylor in his article "Analysis of the swimming of long and narrow animals", presented resistive theory. According to that theory when a bending wave travels with constant speed along the body of the animal the forces per unit of length of each element of the swimming body are assumed to be the same as the resistance experienced per unit of length by a long cylinder with the same surface structure, moving through the fluid with a steady velocity that equals the mean value of the unsteady velocity field, at the same inclination to the direction of the relative flow. This theory is suitable for the swimming of snakes, leeches and certain marine worms.

Later, theories were developed in a different direction. For instance, the reactive theory that considers the flow of the fluid outside the thin boundary layer on the fish's body. Thus inertial effects are dominant and an inviscid fluid assumption is precise. Also, significant theoretical developments are attributed to the works of Lighthill (1960), (1969), (1975), Wu (1961), (1971) and Longvinovich (1971). In 1970, Lighthill applied the linear 2-D theory of oscillating hydrofoils, developed by Karman and Sears in 1938, in order to study thunniform swimming. That theory were enhanced, in order to be suitable for large amplitude flapping, and extended in 3-D by Chopra (1974), (1976). Three dimensional effects such as wingtip vortices were also studied by Cheng and Murillo (1984). After that, the presumed optimal propulsive performance of oscillating foils, studied extensively using analytical and semi-analytical techniques, see e.g. Karpouzian, Spedding & Cheng (1990), McCune & Tavares (1993).

*Recent advances in numerical study of unsteady hydrofoils and wings*

On the other hand during the last period, direct simulations of the fully 3D fish propulsion problems have been presented, based either on Boundary Element Method formulations or Navier Stokes solvers. Starting from the pioneering work by Hess & Smith (1962), where the 3D panel method based on source-sink distribution is presented, for analyzing the flow around arbitrary non-lifting bodies, this approach has been further extended by Hess (1972) for lifting flows. Boundary element methods (BEM) in aero/hydrodynamics are established as main tools for the solution of flow problems around isolated or systems of bodies, with or without lift, see e.g. Katz & Plotkin (1991), Paris & Canas (1997), Dragos (2003).

In the case of 3D flapping propulsors, an unsteady vortex lattice technique was developed by Belibassakis et al (1997) and applied to the analysis of a pair of vertical oscillating wing tails, in order to investigate quantitatively their propulsive performance. A free-wake analysis is incorporated in order to account for the effects of non-linearity, especially at increased amplitudes of oscillatory motion. Wing thickness effects are taken into account approximately and the effects of viscosity considered by means of a frictional drag coefficient applied to the solid surface. The previous model is extended by Politis & Belibassakis (1999) to model 3D unsteady leading-edge separated flow and dynamic-stall effects, which become quite significant at large oscillatory motions, leading to temporary angle of attack well exceeding the static stall angle of wing sections, see also von Ellenrieder et al (2008).

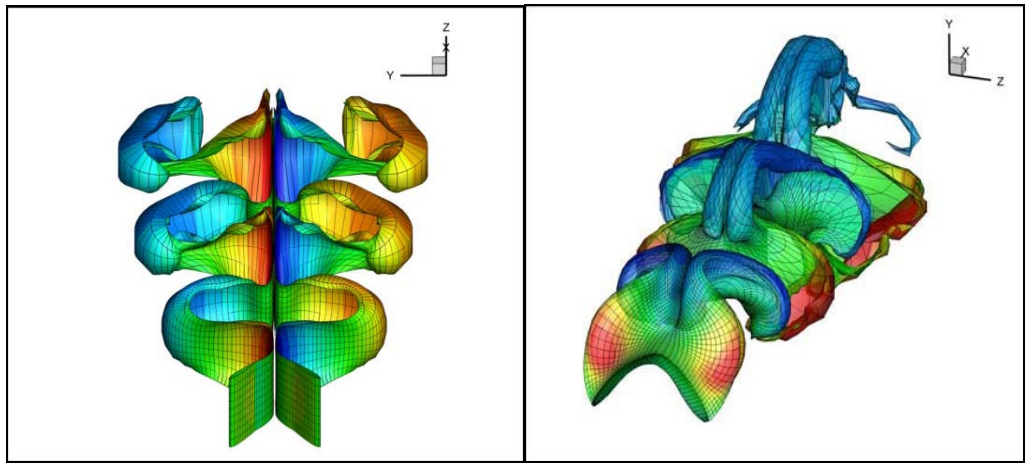

Figure 2: Vortex pattern visualization of two flapping wings (left) and of bird flight (right) using Boundary Element Method by Politis and Tsarsitalidis (2009),(2010).

Furthermore, Liu and Bose (1999) combine a 3D panel code with a boundary layer model and applied their method to estimate the effect of shape of wing planform, to the propulsive performance. Zhu et al (2002) has employed a 3D panel code together with experimental data to establish the features of the flow around fish-like bodies and He et al (2006) used such method to treat tandem oscillating foils.

Moreover, Liu & Bose (1997) presented a 3D BEM method to study the effect of wing flexibility in the efficiency of a whale's fin by adapting the commercial code VSAERO to treat unsteadiness of the flow. Also, a 3D BEM code for the calculation of flow around systems of independently moving bodies including free wake analysis and its application to prediction of complex unsteady propulsion hydrodynamic phenomena is developed by Politis (2009) and (2011). Furthermore, the problem of flow around, one or more, rigid or flexible wings, performing unsteady motions (heaving and pitching or flapping and twisting), while travelling with a given velocity, in an infinitely extended fluid, is formulated and solved using the latter potential based 3D BEM by Politis & Tsarsitalidis (2009). The same method is explored to model and study biomimetic propulsion systems based on flapping wings, as in birds flight and oscillating/pulsating flexible duct, Politis & Tsarsitalidis (2010), (2011). Previous analyses concerning the power required to propel an actively swimming fishlike body, e.g. Barrett et al (1999) show that inviscid 3D methods are capable of providing very useful results concerning both the vortical wake pattern and prediction of the integrated quantities that compare very favorably with experimental data. Moreover, free vorticity methods could be combined with BEM for the prediction dynamic stall effects and also of wave resistance and nonlinear responses of ship and floating bodies e.g., Lewis (1991), Riziotis and Voutsinas (2007) and Belibassakis (2010), (2011).

Finally, in the context of viscous flow solvers, Borazjani and Sotiropoulos (2008) present calculations of swimming forces and efficiency of a carangiform swimmer, finding that swimming power is decreased for higher Reynolds numbers. They also present interesting visualizations regarding the vortical structures and 3D wake pattern formation of carangiform swimmers.

## 1.2 Augmenting ship propulsion in rough sea by biomimetic flapping-foil system

Biomimetic propulsors is the subject of extensive investigation, since they are ideally suited for converting directly environmental (sea wave) energy to useful thrust. In addition, in the last period, requirements and inter-governmental regulations related to vehicle technology for reduced pollution and environmental impact (e.g. Kyoto treaty and enactment of Energy Efficiency Design Index, EEDI, Energy Efficiency Operational Indicator, EEOI and North American Emission Control Area Regulations, ECA, for ships) have become strict, and response to the demand of greening of transport has been recognized to be an important factor concerning global warming and climate change. The contribution of cargo ships in world pollution has been recognized as one of the most important factors (e.g. Colvile 2001, Flannery 2005), taking also into account the bad fuel quality of seagoing vessels in relation to other modes of transport. Indeed, images and data available from satellites (MARINTEK et al 2000) reveal that large areas around the main sea-ocean shipping lines are almost permanently covered by clouds with large concentrations of pollutants from ships' engines. In this direction, current studies examine - among other issues - the optimization of propulsive efficiency of ships operating in realistic sea states, taking into account added resistance effects (Belibassakis 2009). We note that in moderate and severe sea conditions, due to waves, wind and other reasons, ship propulsion energy demand is usually increased well above the corresponding value in calm water for the same speed, especially for bow/quartering seas.

On the other hand, evolution of air and sea creatures, through million years of natural selection/optimization, arrived to the flapping wing as their single propulsion system. The main difference between a biomimetic (flapping wing) propulsor and a conventional propeller is that the former absorbs energy by two independent motions, the heaving and the pitching motion, while for the propeller there is only rotational power feeding.

Early research regarding utilization of biomimetic systems as ship propulsors, concentrated on qualitative and quantitative investigation of proper non-dimensional physical parameters (and their range), where optimum wake formation is produced corresponding to high propulsive efficiency. In those investigations energy feeding of both of flapping wing motion modes (i.e. heaving and pitching) is considered (see Section 1.1). Also most studies concentrate on situations where effects of free-surface and incident waves are not taken into account.

In real sea conditions, the ship undergoes moderate or higher-amplitude oscillatory motions, due to waves. In this case the ship motions, especially the vertical to the free surface plane, could be exploited for providing one of the modes of combined/complex oscillatory motion of a biomimetic propulsion system, free of cost. This idea has already been exploited by other scientists; More specifically, the initial attempts focused on using passively flapping wings underneath the ship hull, to transform energy stored in ship motions to useful propulsive thrust with simultaneous reduction of ship motions. In such cases pitching motion is induced by a spring loaded by the unsteady wing pressure distribution. In the following we will present a brief history, while Rozhdestvensky & Ryzhov (2003) could be a good reference for a more detailed review.

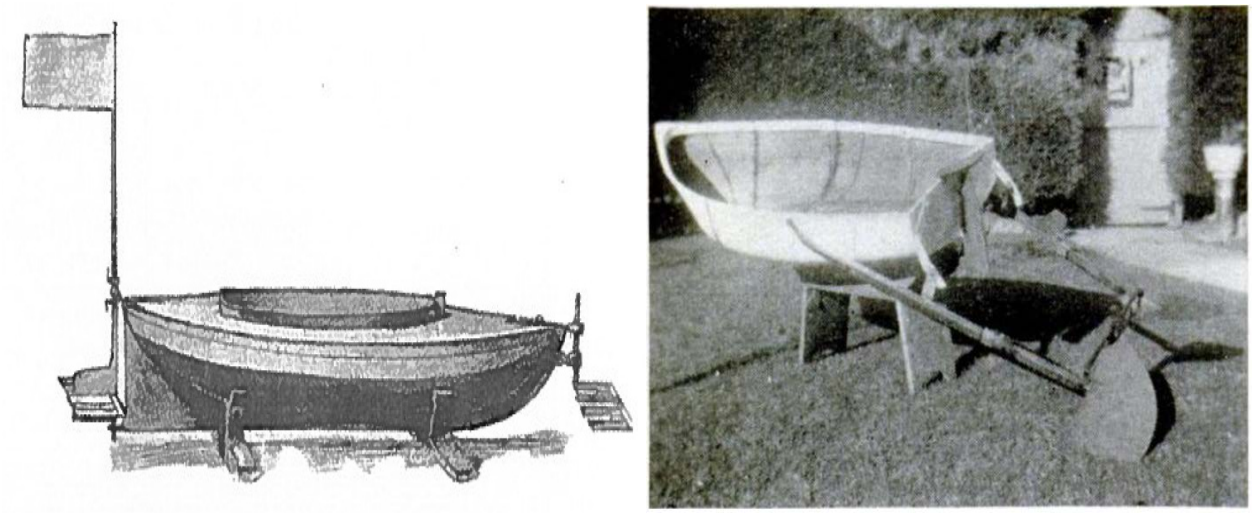

Figure 3: At left, first wave power boat by Linden (1895), from Burnett's work (1979), at right, John S. McCubbin's boat (1950) published in Popular Science (1950).

The first published attempt was in 1895 by Herman Linden who filed a British patent for a wave powered boat (Burnett,1979). Linden's 13 ft long boat named Autonaut, moved against the waves with a speed of three to four miles per hour, powered purely by wave-energy. The boat was equipped with two underwater steel plates, one at the bow and one at the stern (Fig.3 left). Other similar attempts have been done by John S. McCubbin of Victoria (Fig.3 right), Australia (Popular Science, 1950), and Robert Gause (1969).

Latter, Einar Jakobsen (1981) performed experiments in Norwegian Hydrodynamics Laboratories (today MARINTEK) in Trondheim, Norway with model boat of length 1.02 m, at a speed of 1.15 m/s in harmonic head sea waves of waveheight 0.13 m and wave period 1.2 s. Froude-scaled to full scale, this is equivalent of a 40 m long ship propelling itself forward solely by wave power in head sea waves of height 5.2 m at a speed of 14 kn. The speed in following waves was about 15% lower. The model had spring-regulated wings, one above the bow, and another beneath the stern. Furthermore, Jakobsen and his Wave Control Company used combinations of two and four foils. A maximum speed of six knots was recorded on one occasion. He also, latter, by gaining a funding from Norwegian Government, equipped the fishing research vessel Kystfangst, owned by the Institute of Fishery Technology Research, with two horizontal foils on the bow (Anon., 1983), see Fig. 4. Fuel savings of about 15-20 % were obtained in a wave height of 3 m by using the foils at speeds of 4-8 knots (Berg, 1985). However, the project was terminated due to structural problems.

Similar problem concerning wave energy extracting systems has been studied by Isshiki (1982). In the latter work, a 2D model, treating the problem of an oscillating hydrofoil in water waves was developed, extending Wu (1972) theory by introducing a free surface effect, and applied to the investigation of the possibility of wave devouring propulsion. Another Japanese, Yukata Terao (1982) was also worked on the same direction. Isshiki's work has been further extended

Figure 4: Jakobsen equipped fishing research vessel Kystfangst, owned by the Institute of Fishery Technology Research, with a bulbous bow and two foils on each side of the bow (Dybdahl, 1988).

both theoretically and experimentally by Isshiki and Murakami (1984) where the basic concept of passive type wave devouring capability of an oscillating hydrofoil was studied. Furthermore, Grue et al (1988) developed a theory for a two-dimensional flat plate near the free surface using frequency-domain integral equation approach, where unsteady foil motions and wave devouring capabilities were illustrated. Predictions from the above theoretical model were found to be in good agreement with the experimental measurements by Isshiki and Murakami (1984) for both head and following waves. However, at lower wave numbers there were systematic discrepancies between theory and experimental results attributed to nonlinear and free surface effects which were not fully modelled. In 1991, Isshiki and Terao performed full scale tests on with a 15.7 m long fishing vessel. The projected hydrofoil area was 7.4% of the ship's waterline area. Using the bow foil not only managed to reduce pitching motion and bow slamming, but also a speed increase was achieved in waves. In 2008, the longest known voyage by a wave-powered boat took place. A wave-propulsion mechanism, designed by Terao, was equipped to Suntory Mermaid II catamaran (Figure 5). In this way, Japanese sailor and environmentalist Kenichi Horie, sailed the from Honolulu, Hawaii, to the Kii Channel, Japan (Geoghegan, 2008) in 110 days with pure wave energy, which was longer than planned, due to unusually good weather and calm seas.

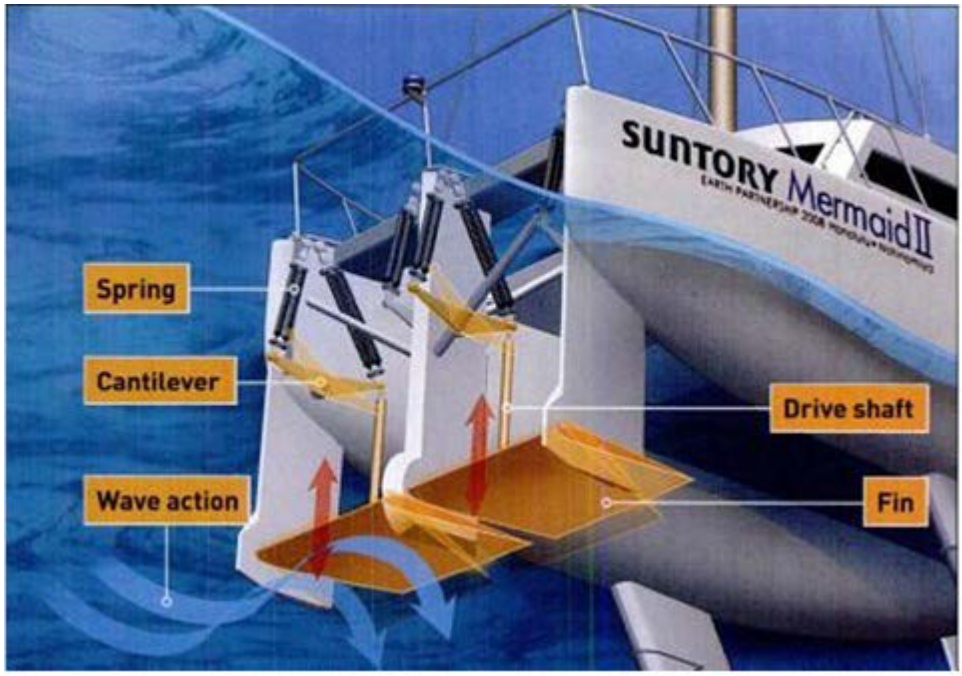


Figure 5: The Suntory Mermaid II which sailed from Hawaii to Japan in 2008 (Popular Science, 2008)

More recently, De Silva & Yamaguchi (2012) examined in detail the possibility of extracting energy from gravity waves for marine propulsion, by numerically studying a two-dimensional oscillating hydrofoil using commercially available CFD software. The overall results suggest that actively oscillating-foil systems in waves, under suitable conditions, have the possibility to recover the wave energy rendering these systems applicable to marine unsteady thrusters.

Working in the above direction, the research team of the laboratory of Ship and Marine Hydrodynamics of the School of Naval Architecture and Marine Engineering (SNAME) of National Technical University of Athens (NTUA) proceed some steps further. as follows:

(a) Substituting the passive pitching setup by an active pitching control, using a proper control mechanism and a pitch setup algorithm, on the basis of the (known) random motion history of the wing, Politis & Politis (2012).

(b) Developing theoretical/numerical tools capable of analysing/designing ships equipped with such biomimetic wing propulsors, Belibassakis & Politis (2012a,b), Filippas & Belibassakis (2013).

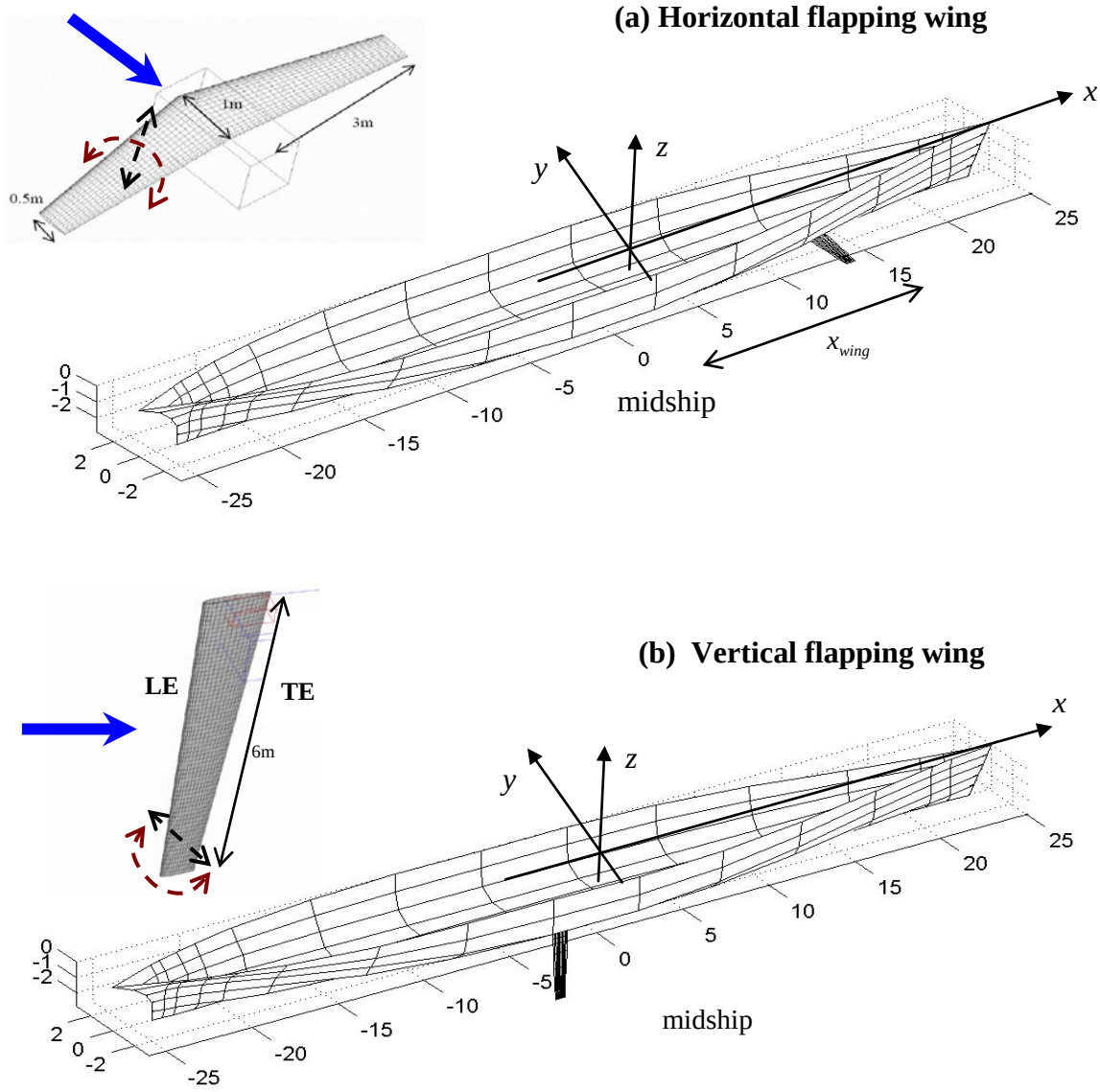


Figure 6. (a) Ship hull equipped with a flapping wing located below the keel, at a forward station. (b) Same hull with a vertical flapping wing located below the keel, at the midship section. Geometrical details of the flapping wings are included in the upper subplots. The main flow direction relative to the flapping wings is indicated using a blue arrow. Black arrows indicate linear oscillatory motion and red ones the actively controlled (pitching) motion of the wing about its pivot axis, for which only a quite small amount of energy is provided.

More specifically, ongoing research work is focused on the hydrodynamic analysis of flapping wings located beneath the ship's hull, operating in random motion; see Fig.6. The wing(s) undergo a combined transverse and rotational oscillatory motion, while the ship is steadily advancing in the presence of waves, modeled by directional spectrum. The present system is investigated as an unsteady thrust production mechanism, augmenting the overall propulsion system of the ship. In the first arrangement (Fig6a), the horizontal wing undergoes a combined vertical and angular (pitching) oscillatory motion, while travelling at constant forward speed. The

vertical motion is induced by the random motion of the ship in waves, essentially due to ship heave and pitch, at the station where the flapping wing is located. Wing pitching motion is controlled as a proper function of wing vertical motion and it is imposed by an external mechanism. A second arrangement of a vertical oscillating wing-keel located beneath the ship's hull is also considered (Fig6b). The transverse motion is induced by ship rolling and swaying motion in waves, respectively. The angular motion of the wing about its pivot axis, is again properly controlled on the basis of the ship rolling motion in order to produce thrust, with simultaneous generation of significant antirolling moment for ship stabilization.

Belibassakis & Politis (2012a,b) developed a method based on coupling the seakeeping operators, associated with the longitudinal and transverse ship motions, with the hydrodynamic forces and moments produced by the flapping lifting surfaces, using unsteady lifting line theory and non-linear 3D panel methods (Politis 2011). First numerical results indicate that high levels of efficiency are obtained in sea conditions of moderate and higher severity, under optimal control settings.

In the present work, whose results will be published in the proceedings of 32nd International Conference on Ocean, Offshore Mechanics and Arctic Engineering (OMAE 2013) in Nantes, France (Filippas & Belibassakis, 2013), we will present a two dimensional BEM (which can be directly extended in three dimensions) for the detailed investigation of the free surface effects on hydrodynamics of general shaped bodies in unsteady motion. To be more specific, a potential-based panel method has been developed and applied to the hydrodynamic analysis of 2-D lifting bodies of general geometry, operating beneath the free surface, undergoing general motion in waves. The instantaneous angle of attack is influenced by the body's motion and by the incident waves. At a first stage of development we consider moderate submergence and relatively low speeds permitting us to approximately neglect effects due to breaking waves and cavitation. However, the motions and the geometry of the body are not considered as small and thus no linearization has applied. The mathematical formulation is based on potential theory and the problem is treated in the framework of Boundary Integral Equations (BIE), supporting the development of fast and robust Boundary Element Method (BEM) for the numerical estimation of hydrodynamic quantities of interest, as well as the examination of the effects of basic geometrical and physical parameters.

Numerical results are presented concerning the thrust coefficient and the efficiency of a flapping hydrofoil biomimetic system over a range of motion parameters, including reduced frequency, Strouhal number, feathering parameter, maximum angle of attack and compared against ones in infinite fluid or deep submergence. Also, comparisons against other methods are presented and discussed. Our results indicate that good performance can be obtained under optimal operating conditions. Also it is demonstrated that the effects of the free surface are important and cannot be neglected. Finally we conclude that the present method, after enhancements and extensions, can serve as a useful tool for assessment and the preliminary design and control of such systems extracting energy from sea waves for marine propulsion.

# 2 Mathematical formulation of unsteady hydrofoils in infinite domain

## 2.1 Summary

In the present section, we study the problem of an unsteady hydrofoil in unbounded domain or in infinite submergence. The effects of a non-uniform background field (gust) is also examined. That problem have been also studied in the past, using perturbation techniques by many scientists like Theodorsen and Sears, these linear theories are presented in Appendix C, see also the textbook "Marine Hydrodynamics" by Newman (1977). Before proceeding to the formulation of the problem we will present a brief bibliographic review to BEM's. Mathematical formulation is based on the theory of incompressible, inviscid, 2D flow. In order to solve the problem we use knowledge from potential theory and the boundary integral equations (BIE). The motions and the geometry of the body are not considered small - thus no linearization have been applied - the body contour is modeled as a curve of discontinuity of the potential. That lifting problem has unsteady character and thus a vortex sheet is generated from the trailing edge of the hydrofoil, modeled as a curve of potential discontinuity too. We begin with the definition of the problem in unbounded domain and the application of Green's formula in the representation of the potential from its boundary values which can be evaluated solving a singular Boundary Integral Equation (BIE). Derivation of representation theorem and BIE and also the treatment of the singular integrals that appear in them are discussed in appendixes A and B, respectively. In the next, we describe the way we can obtain numerical solution, using a low order BEM (panel method) through discretisation of the boundaries, that satisfies an approximate form of the boundary condition on body's contour through collocation. Also, an approximate Bernoulli's equation, for the calculation of pressure is derived integrating Euler's equations for incompressible flows. Numerical performance of the scheme is tested through plenty simulations over a variety of unsteady motion parameters. Finally, the very interesting problem of efficient thrust production using biomimetic flapping-foil systems is investigated. We begin with steady hydrofoils in forward motion and then we add first heaving and then rotational oscillatory motions, to obtain finally the more complex flapping motion that is used for thrust production purposes by hydrobionts. Additionally, the effect of a sinusoidal gust as a background field is investigated. That last problem has interesting applications, e.g. the motion of a hydrofoil-ship in waves, an airplane in turbulence or the motion of the propeller blades in a spatially non uniform ship's wake. Also, energy extraction from non-uniform internal wavy flows using biomimetc flapping-foil systems, could be another possibility. The present method is applied to obtain numerical estimations of basic hydrodynamic quantities such as lift and thrust coefficient, over a range of motion parameters, including reduced frequency, Strouhal number, maximum angle of attack, while accuracy and limitations of the method are demonstrated by comparison with unsteady thin hydrofoil theory (Appendix C) and experimental measurements.

## 2.2 Boundary Element Methods - A brief bibliographic review

Boundary element methods were developed through the effort to deal with problems of aerodynamics. To be more specific, research concerning flows with circulation disturbed by hydrofoils is the topic where the first steps were made. It is worth to mention the thin hydrofoil theory developed first by Munk (1923) and evolved by Glauert (1926), see also Abbott & Doenhoff (1949) and its unsteady version by Theodorsen and Sears (Appendix C and Newman 1977), that reach to analytic solution under some strict assumptions. That assumptions are small perturbation speeds, thickness gust velocity and oscillatory motions of the foil. The linearized solutions concerning the lift coefficient at the steady problem are satisfying and have used for many years for the design of lifting surfaces as rudders, wings and propellers. However that theory is not used anymore due to the significant drawbacks that the latter assumptions introduce:

- The solution ignores the effect of thickness distribution of the hydrofoil, that is significant for the pressure distribution.

- Thin hydrofoil theory is unable to deal with complex shapes of hydrofoils which may include more than one components of interaction between many bodies. That type of wing sections are very popular in high-speed ships' stabilization fins and in combat aircrafts, that operates in a width range of speeds and have strong demands of maneuverability.

- The results concerning pressure coefficient are satisfying only far from the stagnation points at the leading and trailing edges where the assumptions of linearization are realistic. Although, in real flows the boundary pressure distribution is very important for the flow into the boundary layer that controls both friction and separation resistance and the maximum lift force because of the limitation due to dynamic stall phenomenon. Furthermore, cavitation takes place in the vicinity of the minimum pressure point near the leading edge. Thus, the study of cavitating foils, which is very important for the design of the lifting surface is depended from the prediction of pressure in that vicinity.

From the above discussion it is evident that for the deeper understanding of the flow around hydrofoils some steps ahead had to be done. The first one came in the decade of 1930. Theodorsen (1933) developed an semi-analytic method based on the theory of complex functions and conformal mapping for the solution of the non-linear problem. Later at 1960, a variation of that method is applied by Brockett (1965) for the study of cavitating hydrofoils. During the same decade, in laboratories of Douglas aircraft company Hess & Smith (1962), (1966) and Hess (1972) developed the first panel method for the treatment of steady lifting flow around arbitrary bodies. Hess's & Smith's method was only the beginning, rapid evolution of computers and information technology in 1970 leads to the development of Finite Element Methods (FEM) and Boundary Element Methods (BEM). A synoptic description and comparison of the most popular methods for the numerical solution of Boundary Value Problems (BVP) follows.

Almost every physical phenomenon can be described using differential equations and proper boundary conditions. A BVP, only in very simple and not so interesting cases, can be solved analytically, i.e. solutions is possible to be found, that satisfy both the governing equation and the boundary conditions. Thus, two different philosophies begun from the same threshold, the

approximate solution of BVPs. The Finite Element Method is based on the theory of Ritz (1909) and the basic idea was that the solution should satisfy exactly the boundary conditions and the effort is concentrated to the best, approximate, satisfaction of the differential equation. On the other hand, Boundary Element Method have been developed in the foundations of Trefftz's (1926) theory. In the latter case, differential equation is satisfied exactly and the boundary conditions are approximated with the minimum error.

In FEM the domain is divided into elementary subdomains where the equation is satisfied. In that way the solution is not enforced to satisfy exactly both the differential equation and the boundary conditions. The unknown parameters of the solution, consist to its values at the intersection points (nodes) of the elementary subdomains, are evaluated under the demand of minimization of the error due the approximation of the differential equation. The achievement of that method is that the solution has the minimum divergence from the exact solution which satisfies the governing equation globally at the domain, however there are points in the domain where the equation is violated.

On the contrary, BEM does not require a subdivision of the domain and an approximation of the solution of the differential equation. Solution is composed of fundamental solutions/singularities also known as Green functions, each of them satisfies the equation and through the appropriate representation theorem (based on Greens theorem, see e.g. Kress 1989) the total does too. The singularities are distributed on the boundaries where the boundary conditions should be valid. The demand of boundary conditions' satisfaction with maximum accuracy leads to the solution of a Boundary Integral Equation (BIE). The boundary is divided in boundary elements where we can approximate the boundary conditions using e.g. a collocation scheme.

Comparing the two numerical methods we can see that BEM seems to be superior at many points:

- In BEM only a surface (or linear for 2D) and not space (or surface for 2D) integration is involved and thus the dimension of the problem is of one order lower in comparison with FEM and finally the number of unknowns is significantly smaller in the first case.

- Another advantage is that the solutions in BEM satisfies a priory the differential equation (or almost everywhere, because we have to except the singularity points) and thus the method is able to encounter problems with infinite domain, which is practically impossible for FEM for obvious reasons.

- Furthermore in BEM, spatial subdivision is not required, which is in many cases a difficult problem of numerical analysis (see Beer et all 2008 and Kress 1991)

- Finally, as a result of the first advantage and the fact that usually in low order BEMs (panel methods) the required integral calculations can be evaluated analytically, the computational cost and the time of computation are significantly lower. This last advantage of BEMs indicate that they are ideal for 3D and strongly unsteady problems

However, BEM is not panacea and has some drawbacks. The requirement of simple fundamental solution is the most serious one. If the fundamental solution is not simple, the computational cost rises. Furthermore, the evaluation of singular integrals that appears in BEMs presents difficulties. However, extended study has been done concerning the singularities of fundamental functions which consists of integral kernels form boundary integral equations e.g. we mention Muskhelishvili (1953), Mikhlin (1965), Polyanin & Manzhirov (2008).

Finally, we mention that the state of the art in computational methods is concentrating in the development of higher order BEM (see e.g. Cottrel et al, 2009, Lee and Kerwin, 2003, Belibassakis et al, 2013) as well as sophisticated hybrid BEM-FEM models. These models applies every method in the region that it works more efficient (e.g. concerning Computational Fluid Dynamics, CFD, in the thin boundary layer region FEM is applied for the solution of Direct Navier Stokes, DNS, and outside of the boundary layer, or when the unsteadiness is strong, BEM is applied, due to the great amount of calculations) in this way the advantages of both methods are exploited see e.g. Beer et al (2008). A more detailed reference list in the advances of numerical methods, concentrated in the research of biomimetic systems such as flapping hydrofoil propulsors has presented at the end of Section 1.1.

### 2.3 Definition of the unsteady lifting problem and construction of the BIE

Let's now consider a lifting body performing unsteady motion on a non-uniform background field and in infinite submergence. The domain of definition of the problem (Fig.7) is an open semi-bounded domain $D \subseteq \mathbb{R}^2$ with boundary $\partial D$ which is supposed to be smooth everywhere except the trailing edge. The total velocity field $\mathbf{V}_T(x,y;t)$ consists of the gust velocity $\mathbf{V}_g(x,y;t)$, which is assumed to be known and the perturbation velocity $\mathbf{V}(x,y;t)$. We assume that the perturbation flow is irrotational and thus a potential for the velocity $\Phi(x,y;t)$ can be defined as a twice differentiable function in $D$. Also the trace of potential, denoted by $\Phi^*(x,y;t)$, is defined on the boundary. Defining the boundary values by traces, each $\Phi$ is made by definition to be continuous in the closure of $D$, even if it is discontinuous through the boundary, like in the case of the trailing vortex sheet, where $\Phi^*$ has different values as we approach the boundary from the upper or the lower side.

To proceed, let $\partial D$ denote the boundary and A a point on it. Let also $s$ denote curvilinear coordinate on $\partial D$. Then, in the case of moving boundary, we can describe the curve which represents $\partial D$ as

$$\boldsymbol{r}_A = \boldsymbol{r}_A(s;t) = \{x_A(s;t), y_A(s;t)\}. \tag{2.1}$$

The trace of $\Phi$ on $\partial D$ is denoted by the function $\Phi^*$, defined by:

$$\Phi^*(s;t) \doteq \lim_{\delta \to 0} \Phi\{\boldsymbol{r}_A(s;t) + \boldsymbol{n}_A \delta; t\}. \tag{2.2}$$

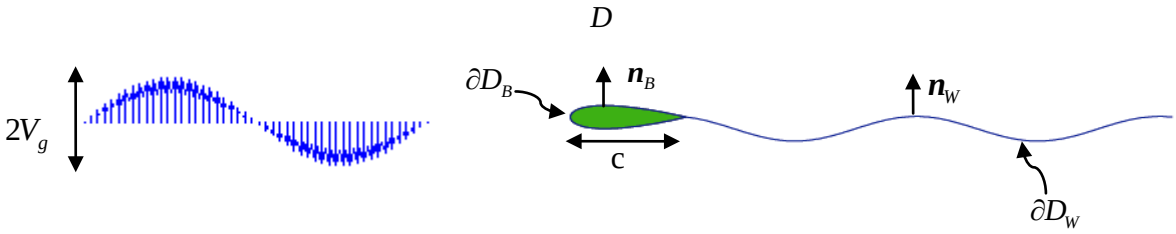


Figure 7: Definition of the studied problem in the case of hydrofoil (of chord c) in unbounded domain and on a non-uniform background field, e.g. sinusoidal gust with velocity amplitude $V_g$.

where δ is a small parameter and $\boldsymbol{n}_A$ a unit vector which is not tangent to $\partial D$ at A. Thus the trace function $\Phi^*$ has as domain of definition the curve $\partial D$ and equals the limiting value of $\Phi(x,y;t)$ as $(x,y)\to A\in\partial D$. In the most general case, as we have mentioned, the function $\Phi(x,y;t)$ can be discontinuous through the boundary.

The problem is time dependent and the unsteady foil is represented by a moving boundary $\partial D_B(t)$, whose motion is prescribed. Another boundary $\partial D_W(t)$, that represents the trailing vortex sheet, is generated from the trailing edge. The reference frame we use is earth-fixed. In order to evaluate the total velocity field we need to solve the problem for the unknown disturbance potential field $\Phi(x,y;t)$, thus in the following we will present the mathematical formulation for the disturbance field.

The governing equation is the Laplace equation

$$\Delta\Phi(x,y;t)=0\ ,\ (x,y)\in D, \tag{2.3}$$

which represents the conservation of mass for incompressible and irrotational fluid.

Also, the boundary condition on the body

$$\frac{\partial\Phi_B(x,y;t)}{\partial n_B}=\left[\boldsymbol{V}_B(x,y;t)-\boldsymbol{V}_g(x,y;t)\right]\cdot\boldsymbol{n}_B(x,y;t)\doteq b(x,y;t)\ ,\ (x,y)\in\partial D_B, \tag{2.4}$$

is the Neumann type, no entrance condition, which ensures that the fluid particles follows the body surface and not penetrate into it. The second term in Eq. (2.4) is the gust velocity on the body contour.

We treat the above as an initial value problem and we assume that the potential and its derivatives vanish at large distance from the body

$$\lim_{r\to\infty}\Phi \text{ and } \nabla\Phi = 0, \qquad r = \sqrt{\left(x - x_B\right)^2 + \left(y - y_B\right)^2}. \tag{2.5}$$

In the above equations $\boldsymbol{V}$ denotes the velocity at $\left(x_B, y_B\right) \in \partial D_B$, $\boldsymbol{n}$ is the unit vector normal to the boundary pointing into $D$.

Furthermore, dynamic and kinematic boundary conditions should be satisfied on the wake $\partial D_W$. The dynamic boundary condition

$$p_W^u(x,y;t) = p_W^l(x,y;t) \ , \ (x,y) \in \partial D_W, \tag{2.6}$$

necessitates that a free shear layer cannot carry loading and thus the pressure at the both sides of it should be the same.

The kinematic boundary condition

$$\frac{\partial \Phi_W^u(x,y;t)}{\partial n_w} = \frac{\partial \Phi_W^l(x,y;t)}{\partial n_w} \ , \ (x,y) \in \partial D_W, \tag{2.7}$$

demands that the upper and the lower side of the shear layer cannot be separated to two distinct curves during the flow, thus the normal to the surface velocity is continuous through $\partial D_W$. The indices $\{B,W\}$ are used to denote values of the potential field and its derivative and the body surface and the wake of the hydrofoil, respectively.

We note that in the case of lifting flow around bodies with sharp edges like a hydrofoil, the problem is supplemented by the Kutta condition, a physical assumption necessitating finite velocity at the trailing edge. The classic pressure-type Kutta condition demands that the pressure should be continuous through the boundary at the trailing edge. This condition, using an approximate Bernoulli's theorem, for small rotation of gust velocity (see section 2.7)

$$\frac{\partial \Phi}{\partial t} + \frac{1}{2}\left(\nabla\Phi\right)^2 + \mathbf{V}_g \nabla\Phi + \frac{p}{\rho} = 0, \ (x,y) \in D, \tag{2.8}$$

leads to a quadratic (nonlinear) relation between the potential and its derivative on the both sides of the trailing edge. In the present work we use a Morino-type version of the Kutta condition

$$\lim_{(x,y)\to(x_{TE},y_{TE})}\left(\Phi_B^u - \Phi_B^l\right) = \mu_W\left(x_{TE}, y_{TE}\right) \ , \ (x,y) \in \partial D_B, \tag{2.9}$$

where $\mu_W = \Phi_W^u - \Phi_W^l$ denotes the potential jump (the dipole intensity) on the free wake.

That relation can be derived from pressure-type Kutta, under the assumption of linearized quasi-steady flow. Morino condition is also compatible with Kutta-Joukowski hypothesis that no vortex filament exists at the trailing edge, see Mohammadi-Amin et al (2012) and Morino et al (1992). That condition has introduced by Morino & Kuo (1974) for steady state problems, see also Suzuki (1980) or Moran (1984) and has been implemented by Politis (2011), Mohammadi-Amin et al (2012) and others, for unsteady lifting flows, see also Katz & Plotkin (1991). It is also worth to mention that, as stated by La Mantia and Dabnichki (2009), pressure-type Kutta condition is not panacea. Poling and Telionis (1986) examined a number of unsteady flow-fields and their experimental results indicate that the classical pressure-type Kutta condition, is not valid in certain conditions, i.e. it is a function of the parameters of the motion. Other experimental studies, Satyanarayana & Davis (1978), Ho & Chen (1981), reached similar conclusions by analyzing the flow in the proximity of the trailing edge of an oscillating wing. Katz and Weihs (1981) studied numerically the wake rollup for hydrofoils oscillating at high frequency and stated that the classical steady Kutta condition can be applied for engineering force and moment prediction in unsteady small-amplitude non-separated flows. McCroskey (1982), in a wide ranging review of unsteady aerodynamics, expressed the opinion that finite pressure loading and abrupt streamline curvature can exist in the trailing-edge region of an oscillating wing in some situations. The numerical results of Young and Lai (2004) show that flow separation occurs at the trailing edge of heaving foils, creating an effective blunt-edge body. More precisely, the flow streamlines form a time-dependant trailing-edge vortex rather than smoothly departing from the trailing edge on both sides. The edge flow mechanism was independently analyzed by Liebe (2007), who proposed to replace the classical Kutta condition with a more general condition based on the formation and periodic shedding of trailing-edge vortices. This led to the development of a novel approach (finite vortex model) for computing the forces acting on fixed and moving wings. There is no experimental evidence supporting the notion that the pressure difference at the trailing edge for unsteady motion of high frequency and large amplitude ought to be equal to zero. Contrary to this, the works of Poling and Telionis (1986), Satyanarayana and Davis (1978) and Ho and Chen (1981) suggest that the pressure difference could be finite rather than zero. In essence a logical first step in the formulation of a comprehensive unsteady Kutta condition could be the relaxation of the postulated zero pressure difference at the trailing edge. This would allow considering the variation in direction and magnitude of velocities across the trailing edge (that is, to consider the formation and shedding of trailing-edge vortices) by a more general pressure condition that also aims to account for viscosity effects in the numerical model. A modified trailing-edge condition for unsteady flows was implemented in a potential panel method to study the motion of two-dimensional rigid foils La Mantia et al (2006). It was already used for a preliminary analysis of the dynamic loads and strength requirements for oscillating wing Dabnichki et al (2006). Finally La Mantia et al (2009) investigate the effect of finite pressure difference at the trailing edge and found that good agreement with experiments could be obtained when finite pressure difference occurs.

Using Eqs. (2.6), (2.7) and (2.8), we obtain (see also Politis 2011)

$$\frac{D\mu_w(x,y;t)}{Dt} = 0 \ , \ (x,y) \in \partial D_W . \tag{2.10}$$

In the above equation $\frac{D}{Dt}=\frac{\partial}{\partial t}+\boldsymbol{V}_{T,m}\cdot\nabla$ is a material derivative based on the mean total velocity of the trailing vortex sheet $\boldsymbol{V}_{T,m}=\frac{\nabla\Phi^{u}_{T,W}+\nabla\Phi^{l}_{T,W}}{2}$. Eq.(2.10) states that $\partial D_W$ evolves in time, moving with the mean fluid velocity.

Continuous generation of the free wake is associated with trailing edge's motion. A simplified "frozen wake" model is derived by assuming that the trailing vortex sheet has the shape of the trail of hydrofoil's trailing edge, see e.g. Politis (2011). This model gives satisfying predictions in the case of low and moderate unsteadiness. According to "frozen wake" model, using Kutta condition (2.9), Eq. (2.10) and linearization, we reach to the following expression concerning the potential jump on the trailing vortex sheet:

$$\mu_W(\mathbf{x};t)=\mu_W(\mathbf{x}+\mathbf{V}_{TE}\cdot\Delta t;t-\Delta t),\ \ \mathbf{x}=(x,y)\in\partial D_W, \tag{2.11}$$

where $\mathbf{V}_{TE}$ denotes an appropriate velocity determined from the motion derivative of the foil's trailing edge.

Finally, we would like to notice that some simplifications have been used, concerning the treatment of the vortex wake. In fact, those simplifications permit the calculation of vorticity transport on the free trailing vortex sheet, which is geometrically modeled by the motion of hydrofoil. Future extensions of the present work will include a fully non-linear free wake model, in conjunction with enhanced pressure-type Kutta condition, requiring that the pressure difference at the trailing edge must be zero; see e.g. Bose (1992) and Politis (2011).

Applying Green's theorem for the case of our problem, with the assumptions (2.5) for the treatment of infinite domain, as described in Appendix A, we can express the potential at every point of $D$ as a function of boundary values of $\Phi$ and $\frac{\partial\Phi}{\partial n}$ as follows

for $(x_0,y_0)\in D$:

$$\begin{aligned}\Phi(x_0,y_0;t)=&\int_{\partial D_B(t)}\frac{\partial\Phi_B(x,y;t)}{\partial n}G(x_0,y_0\,|\,x,y)-\Phi_B(x,y;t)\frac{\partial G(x_0,y_0\,|\,x,y)}{\partial n}ds(x,y)\\&+\int_{\partial D^{u}_W(t)}\frac{\partial\Phi^{u}_W(x,y;t)}{\partial n}G(x_0,y_0\,|\,x,y)-\Phi^{u}_W(x,y;t)\frac{\partial G(x_0,y_0\,|\,x,y)}{\partial n}ds(x,y)\\&+\int_{\partial D^{l}_W(t)}\frac{\partial\Phi^{l}_W(x,y;t)}{\partial n}G(x_0,y_0\,|\,x,y)-\Phi^{l}_W(x,y;t)\frac{\partial G(x_0,y_0\,|\,x,y)}{\partial n}ds(x,y),\end{aligned} \tag{2.12}$$

where $\partial D^{u}_W$ and $\partial D^{l}_W$ are the upper and the lower sides of the shear layer, defined using a branch cut.

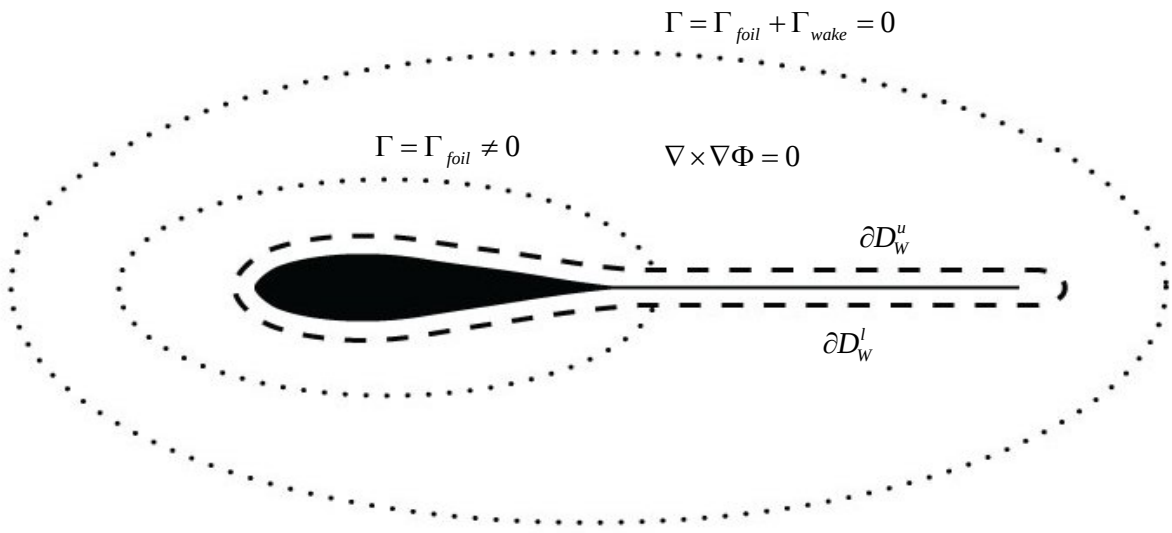


Figure 8: Introduction of a branch cut that permits the existence of circulation around lifting bodies without breaking irrotationality of the flow.

Introduction of the wake surface of potential discontinuity and the use of branch cut, permit the existence finite circulation around the lifting body (Figure 8), that is required for lift generation according Kutta-Joukowski theorem, see e.g. Moran (1984), Batchelor (1987) or Kundu (2004).

The following Green's function and its derivative, appeared in the representation theorem:

$$G(x_0, y_0 \mid x, y) = \frac{1}{2\pi} \ln r(x_0, y_0 \mid x, y) \ , \ (x, y) \in \mathbb{R}^2, (x_0, y_0) \in \mathbb{R}^2, \tag{2.13}$$

$$\frac{\partial G(x_0, y_0 \mid x, y)}{\partial n} = -\frac{1}{2\pi} \frac{\boldsymbol{n} \cdot \boldsymbol{r}(x_0, y_0 \mid x, y)}{\left[ r(x_0, y_0 \mid x, y) \right]^2} \ , \ (x, y) \in \mathbb{R}^2, (x_0, y_0) \in \mathbb{R}^2, \tag{2.14}$$

with

$$\mathbf{r}(x_0, y_0 \mid x, y) = \{(x_0 - x), (y_0 - y)\}. \ r = |\mathbf{r}|. \tag{2.15}$$

The above functions represent source and dipole singularities respectively. The last form of representation theorem eq. (2.12) is suitable for a physical interpretation. The first order in the integral is the potential induced at $(x_0, y_0)$ from a distribution of sources (singularities) with intensity $\frac{\partial \Phi(x, y)}{\partial n}$ located on the boundary, while the second one is the potential from a distribution of dipoles (singularities), with intensity $\Phi(x, y)$. In this way all the information for the potential in $D$ is stored on $\partial D$ whose dimension is one order lower, i.e. if we know the boundary values of the potential (boundary derivative is already known from Neumann condition Eq.2.4) on the boundary, using Green's formula (2.12) we can evaluate potential everywhere in $D$.

Green's formula can also be applied on the boundary $\partial D_B$ (Appendix A)

for $(x_0, y_0) \in \partial D$:

$$\frac{1}{2}\Phi_B(x_0,y_0;t) = \int_{\partial D_B(t)} \frac{\partial \Phi_B(x,y;t)}{\partial n} G(x_0,y_0 \mid x,y) - \Phi_B(x,y;t)\frac{\partial G(x_0,y_0 \mid x,y)}{\partial n} ds(x,y)$$
$$+ \int_{\partial D_W^u(t)} \frac{\partial \Phi_W^u(x,y;t)}{\partial n} G(x_0,y_0 \mid x,y) - \Phi_W^u(x,y;t)\frac{\partial G(x_0,y_0 \mid x,y)}{\partial n} ds(x,y)$$
$$+ \int_{\partial D_W^l(t)} \frac{\partial \Phi_W^l(x,y;t)}{\partial n} G(x_0,y_0 \mid x,y) - \Phi_W^l(x,y;t)\frac{\partial G(x_0,y_0 \mid x,y)}{\partial n} ds(x,y). \quad (2.16)$$

Using now boundary conditions (2.4), (2.7) we conclude the following Fredholm 2nd kind weak singular integral equation:

for $(x_0, y_0) \in \partial D$:

$$\frac{1}{2}\Phi_B(x_0,y_0;t) + \int_{\partial D_B(t)} \Phi_B(x,y;t)\frac{\partial G(x_0,y_0 \mid x,y)}{\partial n} ds(x,y) =$$
$$= \int_{\partial D_B(t)} \underbrace{\left(\boldsymbol{V}_B - \boldsymbol{V}_g\right)\cdot \boldsymbol{n}_B}_{b(x,y;t)} G(x_0,y_0 \mid x,y) ds(x,y) - \int_{\partial D_W(t)} [\![\Phi_W]\!](x,y;t)\frac{\partial G_s(x_0,y_0 \mid x,y)}{\partial n} ds(x,y), \quad (2.17)$$

where $[\![\Phi_W]\!] = \Phi_W^u - \Phi_W^l = \mu_W$ is the potential jump or the dipole intensity on the wake. The potential jump at the trailing edge is equal to the instantaneous value of circulation around the hydrofoil as we can see from the definition of circulation:

$$\Gamma(t) = \oint_{\partial D_B(t)} \nabla\Phi(x,y;t) ds(x,y) = [\![\Phi_{TE}]\!](t). \quad (2.18)$$

From Morino condition (2.9), we know the value of the potential jump at the intersection of the wake and the body, as a function of the potential jump at the trailing edge. In problems of unsteady motion $[\![\Phi]\!]$ varies along the trailing vortex sheet and $\Gamma$ changes in time too. According to Kelvin's theorem this change is associated with the change at dipole intensity at the wake. Taking into account vorticity continuity and considering the fact that $\partial D_W$ has to be a material curve that travels with the flow with mean velocity of the upper and lower surface of the shear layer in the sense of Eq.(2.10), we conclude that $[\![\Phi_W]\!]$ or $\mu_W$ is not constant along $\partial D_W$, contrary to the steady case, Moran (1984), but it changes and represents the history of circulation. Thus, information concerning the flow motion is stored in values of $\mu_W$ on $\partial D_W$ in the sense of

(2.17). Therefore free wake has a memory effect which is represented by the last integral at relation (2.17).

Before we continue, it is important to take a closer look to the integrals appeared in (2.17). Since $(x_0, y_0) \in \partial D$ there is a point at the domain of integration where $(x_0, y_0) \equiv (x, y) \Rightarrow r = 0$. At this point the r.h.s. integrals become infinite and has no meaning in the usual Riemann sense. These integrals are called singular and can be determined as the limit of a well defined regular integral. The integrals appeared in (2.17) are weakly singular i.e. the rate of blow up equals the rate that $ds$ tends to zero. The definition of weakly or Cauchy principal value (that appears in the representation theorem of the velocity which is necessary for the extension to a fully non-linear method) as the limit of a well defined integral is presented in Appendix B.

Relation (2.17) is a boundary integral equation, together with Morino condition (2.9), consist a system of equation for the unknowns $\Phi(x, y)$ on the boundary. The above system of equations can be solved numerically after the appropriate discretisation, as we will see in the following section, with the method of collocation, i.e. demanding from the solution to satisfy them in a finite set of control points.

## 2.4 Discretisation of the boundary integral equation

Following a low-order panel method, the body contour is replaced by a closed polygonal line with $N_B$ denoting the number of panels. The trailing vortex sheet is also approximated by an open polygonal line composed of $N_W(t)$ panels, which increases in time. The potential and its normal derivative, at each time step, are approximated by piecewise constant distributions, as follows:

$$\Phi_B(x, y; t) = \Phi_{Bi}, \text{ at panel i, i=1,...,N}_B, \tag{2.19}$$

$$[\![\Phi_W]\!](x, y; t) = [\![\Phi_W]\!]_i = \mu_{Wi}, \text{ at panel i, i=1,...N}_{W,} \tag{2.20}$$

$$\frac{\partial \Phi_B(x, y; t)}{\partial n} = \frac{\partial \Phi_{Bi}}{\partial n} = \left[ \left( \boldsymbol{V}_B - \boldsymbol{V}_g \right) \cdot \boldsymbol{n}_B \right]_i = \mathbf{b}_i, \text{ at panel i, i=1,...,N}_B. \tag{2.21}$$

By applying a collocation scheme, we require (2.17) to be satisfied in a finite number of collocation points and in order to avoid singularities we choose the midpoints of the panels. Also we imply Morino condition (2.9) at the neighboring to the trailing edge elements. In this way, the discretisation of equations (2.17) and (2.9) leads to:

$\text{for}\,(x_i, y_i)$ , $i = 1, ..., N_B$ :

$$\sum_{j=1}^{N_B} \left( \frac{\delta_{ij}}{2} + B_{ij} \right) \Phi_{Bj} = \sum_{j=1}^{N_B} \left( A_{ij} \right) \underbrace{\left[ \left( \boldsymbol{V}_B - \boldsymbol{V}_g \right) \cdot \boldsymbol{n}_B \right]_j}_{b_j} + \sum_{j=1}^{N_F} \left( -B_{ij} \right) \mu_{Wj}, \tag{2.22}$$

and

$$\mu_{W1} = \Phi_{\mathrm{BN_B}} - \Phi_{\mathrm{B1}}, \tag{2.23}$$

approximates the jump of the potential on trailing edge. In Eq. (2.22), $\delta_{ij}$ is Kronecker's delta and the quantities $A_{ij}$ and $B_{ij}$ are induced factors and represent the potential at collocation point $i$ due to a unit source and dipole distribution, respectively, at panel j, defined as follows

$$A_{ij} = \int_{panel\ j} G_s(x_i, y_i \mid x_j, y_j) ds(x_j, y_j), \tag{2.24}$$

$$B_{ij} = \int_{panel\ j} \frac{\partial G_s(x_i, y_i \mid x_j, y_j)}{\partial n} ds(x_j, y_j). \tag{2.25}$$

In general, the above integrals are evaluated numerically. In the case of low order boundary element methods, i.e. constant distributions on straight elements, analytical calculation is possible. The calculation of those integrals is presented in the next section.

The unknown $\mu_{W1}$ can be eliminated form Eq. (2.22), using Morino condition (2.23) leading to

$\text{for}\,(x_i, y_i)$ , $i = 1, ..., N_B$ :

$$\sum_{j=1}^{N_B} \left( \frac{\delta_{ij}}{2} + \delta_{N_B j} B_{N_B j} - \delta_{1j} B_{1j} + B_{ij} \right) \Phi_{Bj} = \sum_{j=1}^{N_B} \left( A_{ij} \right) b_j + \sum_{j=2}^{N_F} \left( -B_{ij} \right) \mu_{Wj}. \tag{2.26}$$

Now all the quantities in the r.h.s. are known from the prescribed kinematics of the foil and the history of circulation of the foil, $\mu_{W1}(t) = \Gamma(t)$, Eq. (2.18), that has been evaluated at previous time steps. The above equations consists a set of $N_B$ equations which can be solved at every time step for the unknown values of $\Phi_{Bi}$ which is needed for the evaluation of $\Phi$ in $D$ at every time step through a discretised form of (2.12):

$\text{for}\,(x_i, y_i) \in D$ :

$$\Phi_i = \sum_{j=1}^{N_B} \left( A_{ij} \right) b_j + \sum_{j=1}^{N_B} \left( -B_{ij} \right) \Phi_{Bj} + \sum_{j=1}^{N_F} \left( -B_{ij} \right) \mu_{Wj}. \tag{2.27}$$

## 2.5 Calculation of potential induced from constant-strength singularity elements

In order to solve the linear system (2.26) and calculate the boundary values of the potential we have to evaluate the following integrals:

$$A_{ij} = \frac{1}{2\pi} \int_{panel\ j} \ln r(x_i, y_i \mid x_j, y_j) ds(x_j, y_j), \tag{2.28}$$

$$B_{ij} = -\frac{1}{2\pi} \int_{panel\ j} \frac{\boldsymbol{n} \cdot \boldsymbol{r}(x_i, y_i \mid x_j, y_j)}{\left[ r(x_i, y_i \mid x_j, y_j) \right]^2} ds(x_j, y_j). \tag{2.29}$$

These integrals represent the potential at a point $(x_i, y_i)$ due to a unit source or dipole distribution at panel j. As we have discussed, the above integrals are weakly singular. It is easier to evaluate this integrals using a coordinate system with origin at the first point $(x_{j,1}, y_{j,1})$ of the panel j, with axis $x^*$ parallel to the panel j and axis $y^*$ vertical to it, see Figure 9.

First of all we have to calculate the coordinates of the point $(x_i, y_i)$ in the $(x^*, y^*)$ coordinate system:

$$x_i^* = \left(x^* - x_{j,1}\right)\cos(\theta_0) + \left(y^* - y_{j,1}\right)\sin(\theta_0), \tag{2.30}$$

$$y_i^* = -\left(x^* - x_{j,1}\right)\sin(\theta_0) + \left(y^* - y_{j,1}\right)\cos(\theta_0). \tag{2.31}$$

The first integral (2.28) in the O $x^*$ $y^*$ coordinate system becomes:

$$A_{ij} = \frac{1}{2\pi} \int_0^{l_j} \ln \sqrt{\left(x_i^* - t\right)^2 - y_i^{*2}}\, dt, \tag{2.32}$$

where $l_j = \sqrt{\left(x_{j,2} - x_{j,1}\right)^2 + \left(y_{j,2} - y_{j,1}\right)^2}$ is the length of panel j.

Integral (2.32) can be evaluated analytically:

$$A_{ij} = \frac{1}{4\pi}\left\{ x_i^* \cdot \ln\left[\left(x_i^*\right)^2 + \left(y_i^*\right)^2\right] - \left(x_i^* - l_j\right) \cdot \ln\left[\left(x_i^* - l_j\right)^2 + \left(y_i^*\right)^2\right] + 2 \cdot y_i^* \cdot \left[ \tan^{-1}\left(\frac{y_i^*}{x_i^* - l_j}\right) - \tan^{-1}\left(\frac{y_i^*}{x_i^*}\right)\right]\right\}, \tag{2.33}$$

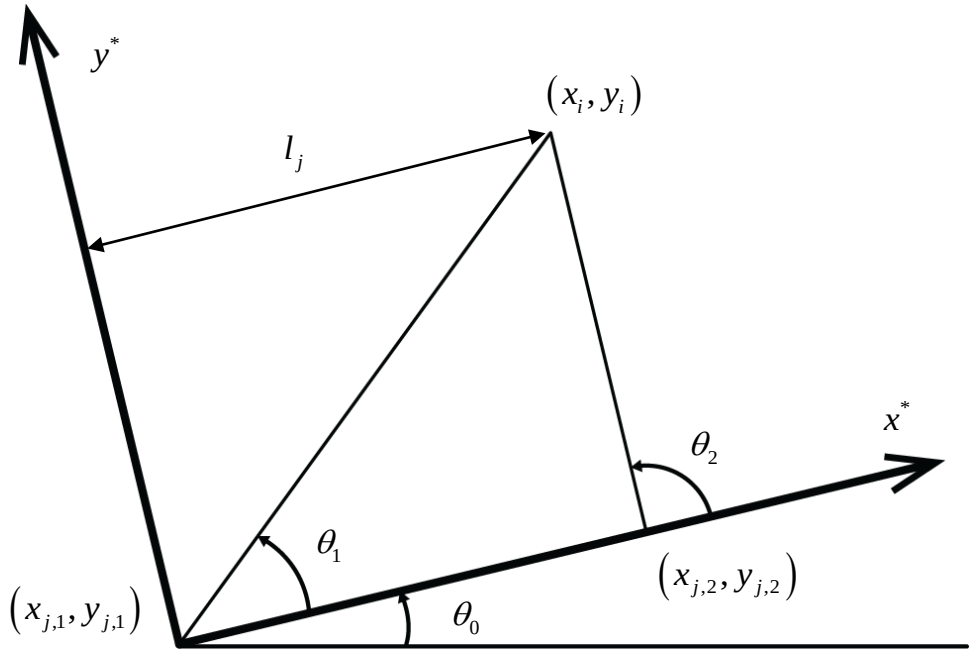


Figure 9: Local system used for evaluation of the potential field induced by constant strength source and dipole panels.

or with the notation of Figure 9:

$$A_{ij} = \frac{1}{4\pi}\left[ x_i^* \cdot \ln r_1^2 - \left(x_i^* - l_j\right) \cdot \ln r_2^2 + 2 \cdot y_i^* \cdot \left(\theta_2 - \theta_1\right)\right], \tag{2.34}$$

when the control point $(x_i, y_i)$ is at the center of the panel j, (2.34) becomes:

$$A_{ij} = \frac{l_j}{2\pi} \cdot \left[ \ln\left(l_j\right) - \ln\left(2\right)\right]. \tag{2.35}$$

Thus, the potential has the same value as we approach the surface element from each side of the boundary. From the above relation we can see that the potential generated by a distribution of sources is continuous through the boundary, as it ought.

The second integral (2.29), expressed in the O $x^*$ $y^*$ coordinate system becomes:

$$B_{ij} = -\frac{1}{2\pi}\int_0^{l_j} \frac{y_i^*}{\left(x_i^* - t\right)^2 - y_i^{*2}}\, dt. \tag{2.36}$$

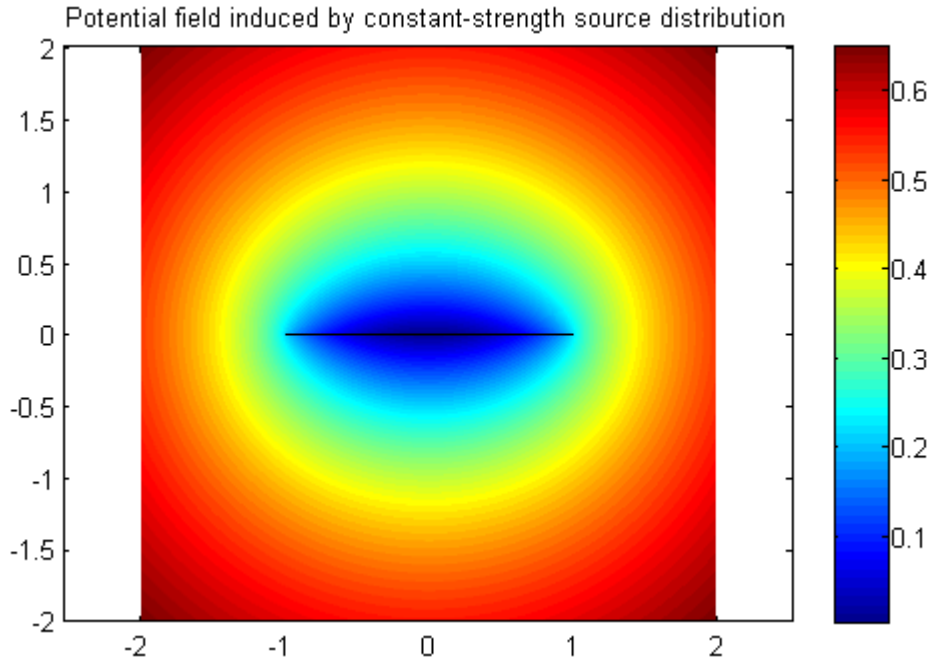


Figure 10: Potential field induced by constant-strength source distribution.

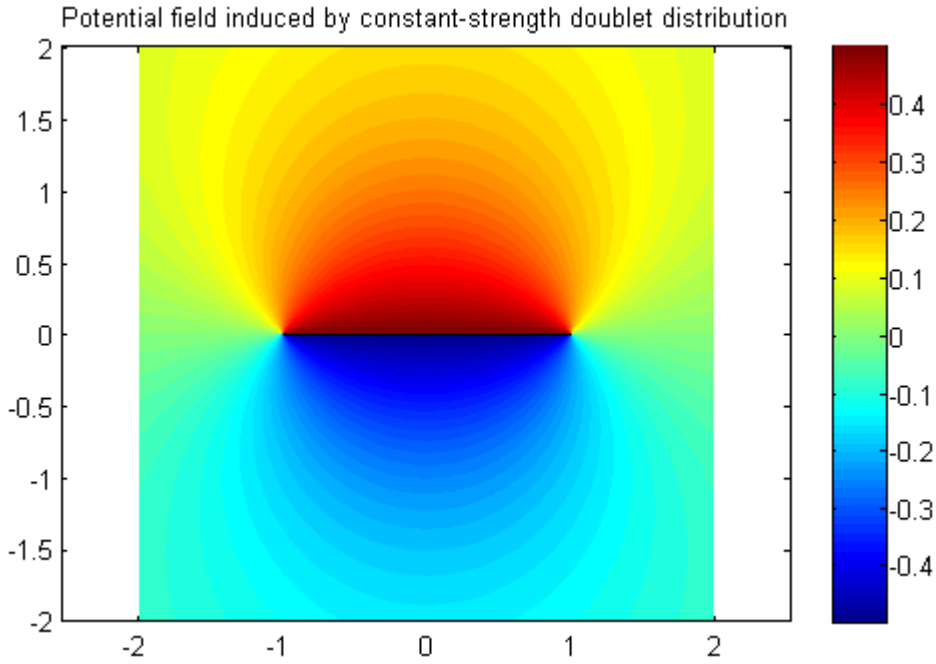


Figure 11: Potential field induced by constant-strength doublet distribution.

The above integral can be evaluated analytically:

$$B_{ij} = -\frac{1}{2\pi}\left[\tan^{-1}\left(\frac{y_i^*}{x_i^* - l_j}\right) - \tan^{-1}\left(\frac{y_i^*}{x_i^*}\right)\right], \tag{2.37}$$

or with the notation of Figure 9:

$$B_{ij} = -\frac{1}{2\pi}\left(\theta_2 - \theta_1\right), \tag{2.38}$$

when the control point $\left(x_i, y_i\right)$ is at the center of the panel j, (2.38) becomes:

$$B_{ij} = \mp\frac{1}{2}, \tag{2.39}$$

where "-" is used when we approach the panel, in the perpendicular to it direction, from the positive of axis $y^*$ and "+" is used when we approach the panel from the negative of axis $y^*$. That discontinuity of the potential, generated by a distribution of dipoles is an example of the discontinuity through the boundary is characteristic of the class of functions involved in present BEM.

In Figures 10 and 11 we present the potential field induced by a unit constant-strength source and dipole distribution around panel j located in $-1 < x < 1$. As we can see the source potential is continuous through the boundary and the doublet potential presents the expected discontinuity.

### 2.6 Evaluation of velocity on the boundary

Having obtained the value of the potential at a control point $\Phi_i$ at the center of each panel $\left(x_i, y_i\right)$ and we want to calculate the velocity $u_i$ along the curvilinear direction surrounding the foil, at the same points. For this aim we apply the following finite difference scheme which requires the knowledge of the potential at the two neighboring control points, i.e. $\Phi_{i-1}, \Phi_{i+1}$.

At the first step we can approximate the velocity at the nodes of the panel:

$$u_{i,1} = \frac{\Phi_i - \Phi_{i-1}}{\sqrt{\left(x_{i,1} - x_{i-1}\right)^2 + \left(y_{i,1} - y_{i-1}\right)^2} + \sqrt{\left(x_i - x_{i,1}\right)^2 + \left(y_i - y_{i,1}\right)^2}}, \tag{2.40}$$

$$u_{i,2} = \frac{\Phi_{i+1} - \Phi_i}{\sqrt{\left(x_{i,2} - x_i\right)^2 + \left(y_{i,2} - y_i\right)^2} + \sqrt{\left(x_{i+1} - x_{i,2}\right)^2 + \left(y_{i+1} - y_{i,2}\right)^2}}, \tag{2.41}$$

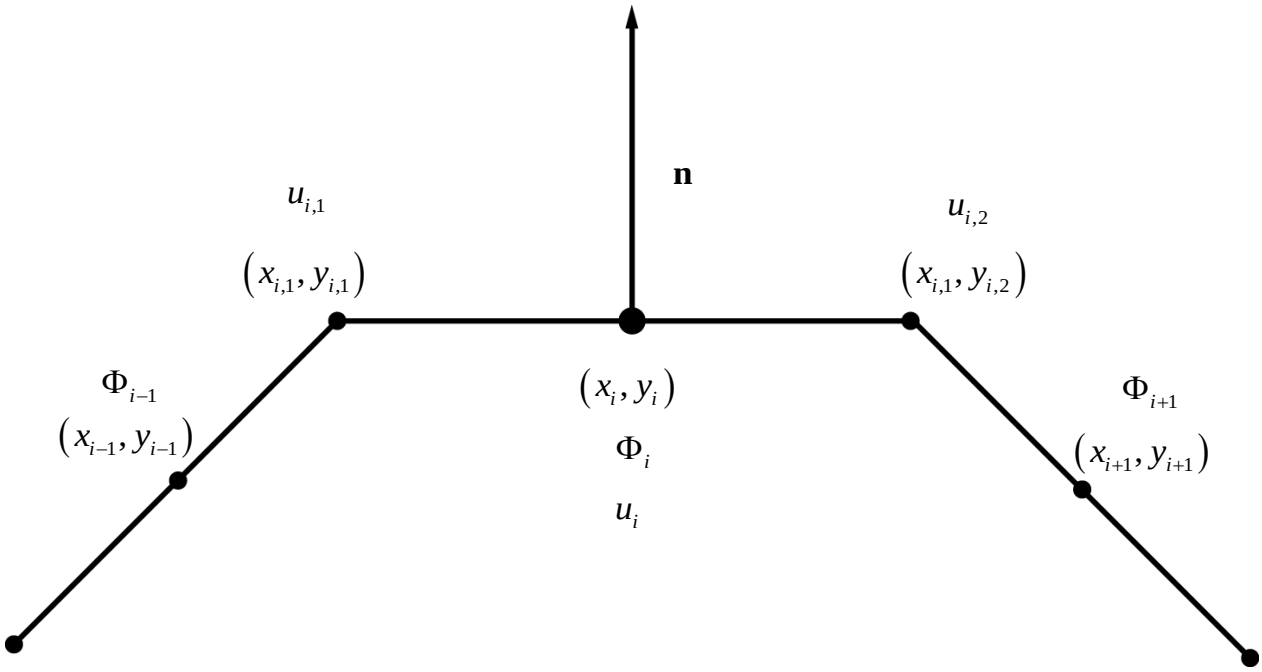


Figure 12: Nomenclature for calculation of velocity on the boundary using finite differences,

where $x_{i,1}\ x_{i,2}\ y_{i,1}\ y_{i,2}\ u_{i,1}\ u_{i,2}$ are the x,y coordinates and the velocities at the first and at the second node of panel i (Figure 12).

Finally the velocity at the midpoint of panel i can be approximated by the mean value:

$$u_i = \frac{u_{i,1} + u_{i,2}}{2}. \tag{2.42}$$

At the fist panel located at the lower side of the sharp trailing edge and at the last one at the upper side forward and backward versions of the above scheme are applied, as follows:

$$u_1 = \frac{\Phi_2 - \Phi_1}{\sqrt{\left(x_{1,2} - x_1\right)^2 + \left(y_{1,2} - y_1\right)^2} + \sqrt{\left(x_2 - x_{1,2}\right)^2 + \left(y_2 - y_{1,2}\right)^2}}, \tag{2.43}$$

and

$$u_2 = \frac{\Phi_{N_b} - \Phi_{N_b-1}}{\sqrt{\left(x_{N_b} - x_{N_b,1}\right)^2 + \left(y_{N_b} - y_{N_b,1}\right)^2} + \sqrt{\left(x_{N_b,1} - x_{N_b-1}\right)^2 + \left(y_{N_b,1} - y_{N_b-1}\right)^2}}. \tag{2.44}$$

## 2.7 Calculation of pressure using an approximate Bernoulli's theorem

Calculation of the force acting on the foil requires the evaluation of pressure on the boundary. This for irrotational flow can be done using Bernoulli's theorem. However in the case of sinusoidal-gust problem the total flow consists of an irrotational part that corresponds to the disturbance field and a weakly rotational sinusoidal background field. In that case we will write Euler's equations, that expresses Newton's second law for every fluid particle, for the total velocity field $\mathbf{V}_T = \nabla\Phi + \mathbf{V}_g$

$$\frac{\partial \mathbf{V}_T}{\partial t} + \frac{1}{2}\nabla\left(\mathbf{V}_T\right)^2 - \mathbf{V}_T \times \left(\nabla \times \mathbf{V}_T\right) + \frac{\nabla p_T}{\rho} = 0 \tag{2.45}$$

$$\Rightarrow \frac{\partial\left(\nabla\Phi + \mathbf{V}_g\right)}{\partial t} + \frac{1}{2}\nabla\left(\nabla\Phi + \mathbf{V}_g\right)^2 - \left(\nabla\Phi + \mathbf{V}_g\right) \times \left[\nabla \times \left(\nabla\Phi + \mathbf{V}_g\right)\right] + \frac{\nabla\left(p + p_g\right)}{\rho} = 0, \tag{2.46}$$

$p_T(x, y)$ is the pressure at (x,y) point of the field, ρ is the density of the fluid and $\frac{\partial \mathbf{V}_T}{\partial t}$ denotes time rate of total velocity field according to a fixed observer with regard to an inertia reference frame.

Disturbance velocity is assumed irrotational, thus

$$\frac{\partial\left(\nabla\Phi + \mathbf{V}_g\right)}{\partial t} + \frac{1}{2}\nabla\left(\nabla\Phi^2\right) + \nabla\left(\nabla\Phi\mathbf{V}_g\right) + \frac{1}{2}\nabla\left(\mathbf{V}_g^2\right) - \nabla\Phi \times \left(\nabla \times \mathbf{V}_g\right) - \mathbf{V}_g \times \left(\nabla \times \mathbf{V}_g\right) + \frac{\nabla\left(p + p_g\right)}{\rho} = 0. \tag{2.47}$$

Appling now Euler equations for the background field we obtain

$$\frac{\partial \mathbf{V}_g}{\partial t} + \frac{1}{2}\nabla\left(\mathbf{V}_g^2\right) - \mathbf{V}_g \times \left(\nabla \times \mathbf{V}_g\right) + \frac{\nabla p_g}{\rho} = 0. \tag{2.48}$$

Subtracting now (2.48) from (2.47), it follows

$$\frac{\partial \nabla\Phi}{\partial t} + \frac{1}{2}\nabla\left(\nabla\Phi^2\right) + \nabla\left(\nabla\Phi\mathbf{V}_g\right) - \nabla\Phi \times \left(\nabla \times \mathbf{V}_g\right) + \frac{\nabla p}{\rho} = 0. \tag{2.49}$$

Furthermore we assume that the rotational term $\nabla\Phi \times \left[\nabla \times \mathbf{V}_g\right]$, is of second order, and can be approximately neglected, and thus

$$\nabla\left[\frac{\partial\Phi}{\partial t} + \frac{1}{2}\left(\nabla\Phi\right)^2 + \nabla\Phi\mathbf{V}_g + \frac{p}{\rho}\right] = 0. \tag{2.50}$$

Finally, integrating the above equation along a curve in $D$ we obtain

$$\frac{\partial\Phi}{\partial t}+\frac{1}{2}\left(\nabla\Phi\right)^2+\nabla\Phi\mathbf{V}_g+\frac{p}{\rho}=C\left(t\right), \tag{2.51}$$

where the x-integration constant $C\left(t\right)$ is time dependent. However $C\left(t\right)$ can be set to zero with redefinition of the potential, i.e. $\Phi\left(x,y;t\right)=\Phi_1\left(x,y;t\right)+\int^t C\left(t\right)d\tau$. Thus relation (2.51) becomes

$$\frac{\partial\Phi_1}{\partial t}+\frac{1}{2}\left(\nabla\Phi_1\right)^2+\nabla\Phi_1\mathbf{V}_g+\frac{p}{\rho}=0. \tag{2.52}$$

In this way we have obtained a formula for the calculation of disturbance pressure

$$\frac{p}{\rho}=-\frac{\partial\Phi}{\partial t}-\frac{1}{2}\left(\nabla\Phi\right)^2-\nabla\Phi\cdot\mathbf{V}_g, \tag{2.53}$$

where $p(x,y)$ is the disturbance pressure, ρ is the density of the fluid and $\frac{\partial\Phi}{\partial t}$ denotes time rate of potential according to a fixed observer with regard to an inertia reference frame.

As we have seen in Sections 2.3-2.5, using BEM we can evaluate the trace $\Phi^*$ on the boundary and differentiating we can calculate corresponding rate of change in a body-fixed reference frame, denoted by $\frac{d\Phi^*}{dt}$. In the following we obtain a relation between the quantities calculated by BEM and the others appeared in Eq. (2.53), see also Politis (2011).

The total differential of the trace $\Phi^*$ with respect to the curvilinear coordinate $s$ along $\partial D$ as a function of $\Phi$ is given by:

$$\begin{aligned} d\Phi^* &= \frac{\partial\Phi}{\partial x}\left(\frac{\partial x}{\partial s}ds+\frac{\partial x}{\partial t}dt\right)+\frac{\partial\Phi}{\partial y}\left(\frac{\partial y}{\partial s}ds+\frac{\partial y}{\partial t}dt\right)+\frac{\partial\Phi}{\partial t}dt \\ &= \nabla\Phi\left(\frac{\partial\boldsymbol{r}}{\partial s}ds+\frac{\partial\boldsymbol{r}}{\partial t}dt\right)+\frac{\partial\Phi}{\partial t}dt, \end{aligned} \tag{2.54}$$

where $\partial D$ is represented by the curve $\boldsymbol{r}=\boldsymbol{r}(s,t)=\left\{x(s,t),y(s,t)\right\}$.

For a specific point B on the boundary, i.e. $s = const$ (2.54) becomes:

$$d\Phi^* = \nabla\Phi \frac{\partial \boldsymbol{r}_B}{\partial t} dt + \frac{\partial \Phi}{\partial t} dt, \tag{2.55}$$

but $\frac{\partial \boldsymbol{r}_B}{\partial t} = \mathbf{V}_B$, the velocity of the body contour and thus we have:

$$\frac{d\Phi^*}{dt} = \nabla\Phi \cdot \boldsymbol{V}_B + \frac{\partial \Phi}{\partial t}, \tag{2.56}$$

Finally we have obtained a relation which connects the inertia rate of change of the potential $\partial\Phi / \partial t$ which is required in Eq. (2.53) with the body-fixed rate of change of the potential's trace $d\Phi^* / dt$ which is calculated using BEMs. Using (2.56), (2.53) becomes:

$$\frac{p}{\rho} = -\frac{d\Phi^*}{dt} + \nabla\Phi \cdot \left(\boldsymbol{V}_B - \mathbf{V}_g\right) - \frac{1}{2}\left(\nabla\Phi\right)^2. \tag{2.57}$$

In relation (2.57), the term $\nabla\Phi$ is the space gradient of $\Phi$. But with BEM as we have seen in sections 2.3-2.6 we calculate the surface gradient $\nabla\Phi^*$ of the trace $\Phi^*$ and thus we have to find a relation between them.

Relation (2.54) for $t = const$ can be written in the form:

$$d\Phi^* = \nabla\Phi \cdot d\boldsymbol{s}, \tag{2.58}$$

where $d\Phi^*$ is a surface gradient of the trace of the potential, $\nabla\Phi$ is a space gradient of potential in D and $d\boldsymbol{s}$ is a surface vector tangent to $\partial D$.

From the definition of differential it holds that:

$$d\Phi^* = \nabla\Phi^* \cdot d\boldsymbol{s}. \tag{2.59}$$

Combining (2.58) and (2.59) we get:

$$\left(\nabla\Phi - \nabla\Phi^*\right) \cdot d\boldsymbol{s} = 0, \tag{2.60}$$

which means that the vector which is the difference between $\nabla\Phi$ and $\nabla\Phi^*$ is normal to $d\boldsymbol{s}$ and thus normal to the boundary $\partial D$.

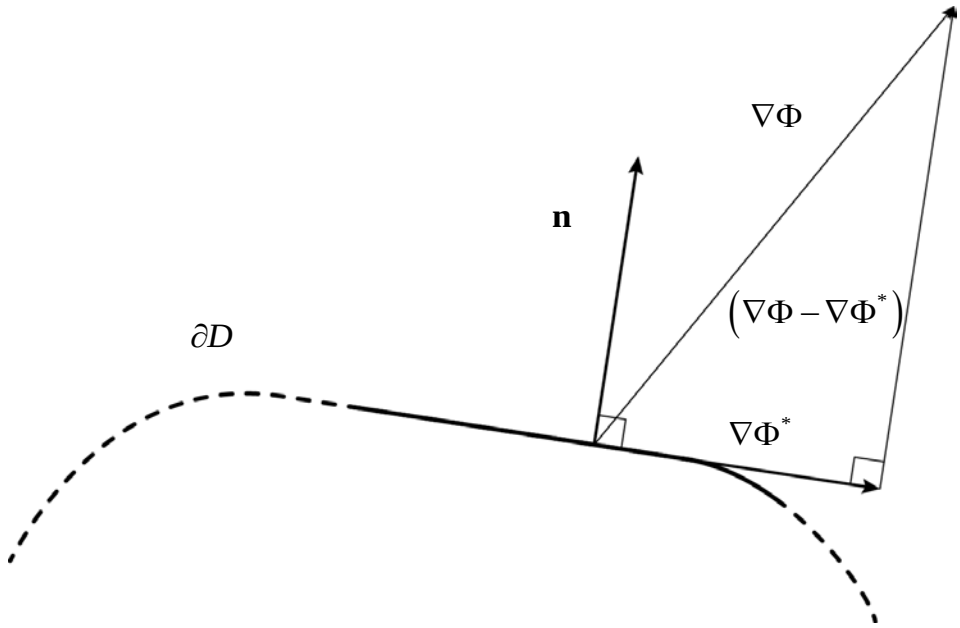


Figure 13: Relation between space gradient $\nabla\Phi$ and surface gradient $\nabla\Phi^*$.

According to Figure 13 we have:

$$\nabla\Phi = \nabla\Phi^* + \left(\boldsymbol{n}\cdot\nabla\Phi\right)\boldsymbol{n}. \tag{2.61}$$

The above relation connects the space gradient of the potential with the surface gradient of the trace of the potential on the boundary.

We want to evaluate pressure on the boundary $\partial D_B$ where no entrance boundary condition (2.4) holds, in that case (2.61) becomes:

$$\nabla\Phi_B = \nabla\Phi_B^* + \underbrace{\left[\left(\boldsymbol{V}_B - \boldsymbol{V}_g\right)\boldsymbol{n}_B\right]}_{b}\cdot\boldsymbol{n}_B. \tag{2.62}$$

Substituting relation (2.62) to (2.57) we get the final form of approximate Bernoulli's theorem which is required for the calculation of pressure distribution on the boundary:

$$\frac{p_B}{\rho} = -\frac{d\Phi_B^*}{dt} + \nabla\Phi_B^*\cdot\left(\boldsymbol{V}_B - \boldsymbol{V}_g\right) - \frac{1}{2}\left(\nabla\Phi_B^*\right)^2 + \frac{1}{2}\underbrace{\left[\boldsymbol{n}_B\cdot\left(\boldsymbol{V}_B - \boldsymbol{V}_g\right)\right]}_{b}^2. \tag{2.63}$$

Or using the definition of the non-dimensional pressure coefficient $C_p = p/0.5\rho U^2$, where $U$ is a characteristic velocity of the motion of the body e.g. the forward velocity of the flapping foil thruster, we get:

$$C_P = \frac{1}{2}U^2\left\{-\frac{d\Phi_B^*}{dt} + \nabla\Phi_B^* \cdot \left(\boldsymbol{V}_B - \boldsymbol{V}_g\right) - \frac{1}{2}\left(\nabla\Phi_B^*\right)^2 + \frac{1}{2}b^2\right\}. \tag{2.64}$$

or in discretised form:

$$C_{Pi} = \frac{1}{2}U^2\left\{-\frac{d\Phi_{Bi}^*}{dt} + \nabla\Phi_{Bi}^* \cdot \left(\boldsymbol{V}_{Bi} - \boldsymbol{V}_{gi}\right) - \frac{1}{2}\left(\nabla\Phi_{Bi}^*\right)^2 + \frac{1}{2}b_i^2\right\},\ (x_i, y_i) \in \bar{D}. \tag{2.65}$$

## 2.8 Calculation of force and moment

If we assume that the pressure is constant along every panel can evaluate the non dimensional coefficients of forces and moments as follows

$$C_{Fx}(t) = \sum_{j=1}^{N} C_P(x_i, y_i; t)\Delta y_i, \tag{2.66}$$

$$C_{Fy}(t) = -\sum_{j=1}^{N} C_P(x_i, y_i; t)\Delta x_i, \tag{2.67}$$

$$C_M(t) = \sum_{j=1}^{N} C_P(x_i, y_i; t)\left[\Delta x_i\left(x_i - x_{ref}\right) + \Delta y_i\left(y_i - y_{ref}\right)\right], \tag{2.68}$$

where $\Delta x_i = x_{i,2} - x_{i,1}$, $\Delta y_i = y_{i,2} - y_{i,1}$, are the projections of the panel i at x and y axis of the foil's body-fixed coordinate system. The dimensionless coefficients of the loadings are defined

$$C_F(t) \equiv \frac{F(t)}{\frac{1}{2}\rho U^2 c},\ C_M(t) \equiv \frac{M(t)}{\frac{1}{2}\rho U^2 c^2}, \tag{2.69}$$

where $F$ is the force acting on the center of pressure of the hydrofoil, $M$ is moment with respect to a reference point $\left(x_{ref}, y_{ref}\right)$ of the foil and c is its chord.

## 2.9 Efficient propulsion using hydrofoils in flapping motion

As we have mentioned in Sec. 1.1, extended research has demonstrated that biomimetic flapping-foil systems can used for efficient propulsion and maneuvering of ships and marine vehicles. In this section the present method is applied to the case of a flapping-foil propulsor illustrating the applicability of such systems. A variety of numerical results are presented in Subsection 2.9.1 in order to examine the rate of convergence, stability and efficiency of the numerical scheme. In Subsection 2.9.2 we present results related with the motion of a hydrofoil with constant angle of attack in comparison with steady panel methods and with experimental results. Moreover, more complex unsteady motions are studied, starting with simple forward and heaving motion (Subsec. 2.9.3) or forward and pitching motion (Subsec. 2.9.4) and finally flapping motion (Subsec. 2.9.5). The latter consists of forward, heaving and pitching motion. Numerical results are presented, for a range of parameters such as Strouhal Number, reduced frequency, heave and pitch amplitude and the maximum angle of attack, and compared with analytical asymptotic and experimental results from the literature enabling as to explore the range and the limitations of applicability of the present method.

The flapping motion of the foil is described by three degrees of freedom, forward motion, heaving and pitching oscillations. The present method can be applied in general motion but for simplicity the oscillations are assumed to be harmonic:

$$s(t) = -U \cdot t \cdot F(t), \tag{2.70}$$

$$h(t) = h_0 \cos(\omega t) \cdot F(t) = \mathrm{Re}\left\{ \dot{h}_o e^{i\omega t} \right\} \cdot F(t), \tag{2.71}$$

$$\theta(t) = \theta_0 \cos(\omega t + \psi) = \mathrm{Re}\left\{ \dot{\theta}_o e^{i\omega t - \psi} \right\} \cdot F(t), \tag{2.72}$$

where $h_0$ and $\dot{h}_o$ are the amplitude and the complex amplitude of heaving motion, $\theta_0$ and $\dot{\theta}_o$ are the amplitude and the complex amplitude of the pitching rotation which is positive counterclockwise, pitching is considered around hydrofoil's pivot axis which is located on the chord and at distance $X_R$ from the leading edge, $\psi$ is the phase difference between the heave and pitch, $\omega$ is the radial frequency which is the same for the two oscillatory motions and $i$ is the imaginary unit. In addition, $F(t) = 1 - \exp\left[ -f_0 (t/T)^2 \right]$ is a filter function permitting smooth transition from rest to the harmonic oscillatory motion.

Thus every point B of the hydrofoil with initial position according to an earth-fixed coordinate system $\left( x_{B0}, y_{B0} \right)$ is moving along the curve:

$$x_B(t) = x_{B0} \cos\theta(t) - y_{B0} \sin\theta(t) - s(t), \tag{2.73}$$

$$y_B(t) = x_{B0} \sin\theta(t) + y_{B0} \cos\theta(t) + h(t), \tag{2.74}$$

where, in order to simplify kinematic equations, the earth-fixed coordinate system is located on the initial location of hydrofoil's pivot axis.

The background velocity field is considered, with respect to the earth-fixed reference frame, to be (after fully transition from rest) a steady sinusoidal disturbance

$$V_G\left(x;t\right)=V_G\cos\left(k_g x\right)\cdot F(t), \tag{2.75}$$

where $V_g$ is the amplitude of the sinusoidal gust velocity and $k_g$ is gust's wave number. With respect to a reference frame moving with hydrofoils mean velocity, the gust is an incident wave disturbance that travels with the forward speed of the foil $U$, thus the radial frequency of the wave is $\omega_g = U\cdot k_g$.

The unsteadiness of the motion is measured by the non-dimensional reduced frequency $k_r = \omega c/2U$, where $c$ is the chord length of the hydrofoil, which can be used both in the cases where heaving motion exists or not. Also, gust's reduced frequency can be defined $k_{r,G} = \omega_G c/2U$. In the case of heaving or flapping motion we can use Strouhal number $St = \omega h/\pi U = \left(2h/\pi c\right)k_r$, which is proportional to the maximum slope of the path and can be considered as a measure of the degree of non-linearity of the motion. It is also connected with the wake of vortices created downstream of the foil. Another motion parameter that is very important is the maximum angle of attack $a_{\max}$ which is connected with the initiation of leading edge separation and the dynamic stall effects. The instantaneous angle of attack in infinite stationary fluid can be evaluated:

$$a(t)=\tan^{-1}\left(\frac{dh/dt}{ds/dt}\right)-\theta. \tag{2.76}$$

In the general case the above formula is extended to include also the gust velocity as well as the induced velocity from the unsteady wake.

Finally, the parameters that control the space and time discretization are, $N_B$ the number of panels on the body contour and Time Sampling Ratio $\left(TSR\right)$ defined as the percentage of the period that equals to the time step

$$TSR=\frac{dt}{T}\cdot 100. \tag{2.77}$$

A wake model is used to linearize free wake dynamics and the corresponding time-dependent discretization parameter $N_W\left(t\right)$ is a function of $N_B$ and $TSR$.

### 2.9.1 Numerical study

Numerical stability, convergence and efficiency of the scheme are tested using as an example a symmetric NACA0012 hydrofoil with rotation axis at $X_R / c = 0.3$ and $\psi = -90°$, over a range of flapping motion's parameters, i.e. Strouhal number $(St = 0.1 \div 0.4)$ reduced frequency $(k_r = 0.1 \div 3.8)$, heaving $(h_0 / c = 0.25 \div 1)$ and pitching $(\theta_0 = 10° \div 40°)$ amplitudes.

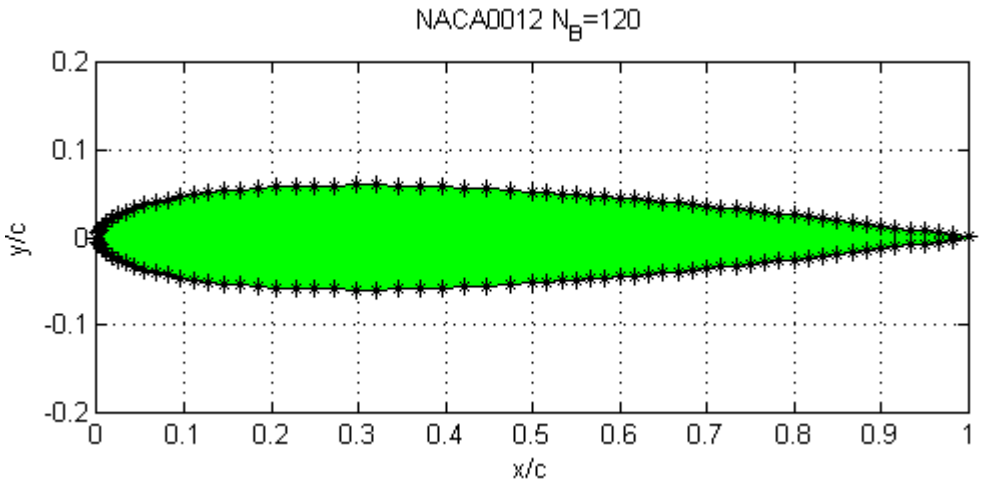


Figure 14: Geometry of a NACA0012 hydrofoil and discretization with non-uniform iso-cosine grid denser at the leading edge.

Presented results concern hydrodynamic quantities, both integrated like non-dimensional Lift $(C_L = F_Y / 0.5\rho U^2 c)$ and Thrust $(C_T = -F_X / 0.5\rho U^2 c)$ coefficients and distributed such as pressure coefficient $(C_P = p / 0.5\rho U^2)$. Transition from rest to harmonic state condition has been accomplished after the third period of oscillation and the integrated quantities have been averaged over the fifth period, i.e. $C_{F,av} = 1/T \int_{4T}^{5T} C_F(t) dt$. The amplitude of force coefficients is considered to be the half of the difference between the maximum and the minimum value in the fifth period, i.e. $C_{F,amp} = 0.5\left[ \max\left\{C_F(t),\ t \in (4T, 5T)\right\} - \min\left\{C_F(t),\ t \in (4T, 5T)\right\}\right]$.

A non-uniform discretisation has been applied on the hydrofoil's boundary in the sense of Fig.14. The grid is denser at the leading edge where the profile changes abruptly and becomes uniform to the trailing edge, so as the panels in the vicinity of the trailing edge to have comparable length with the wake's panels.

In the following figures the mean value of Trust coefficient and the amplitude of Lift coefficient are presented for a range of flapping-motion parameters.

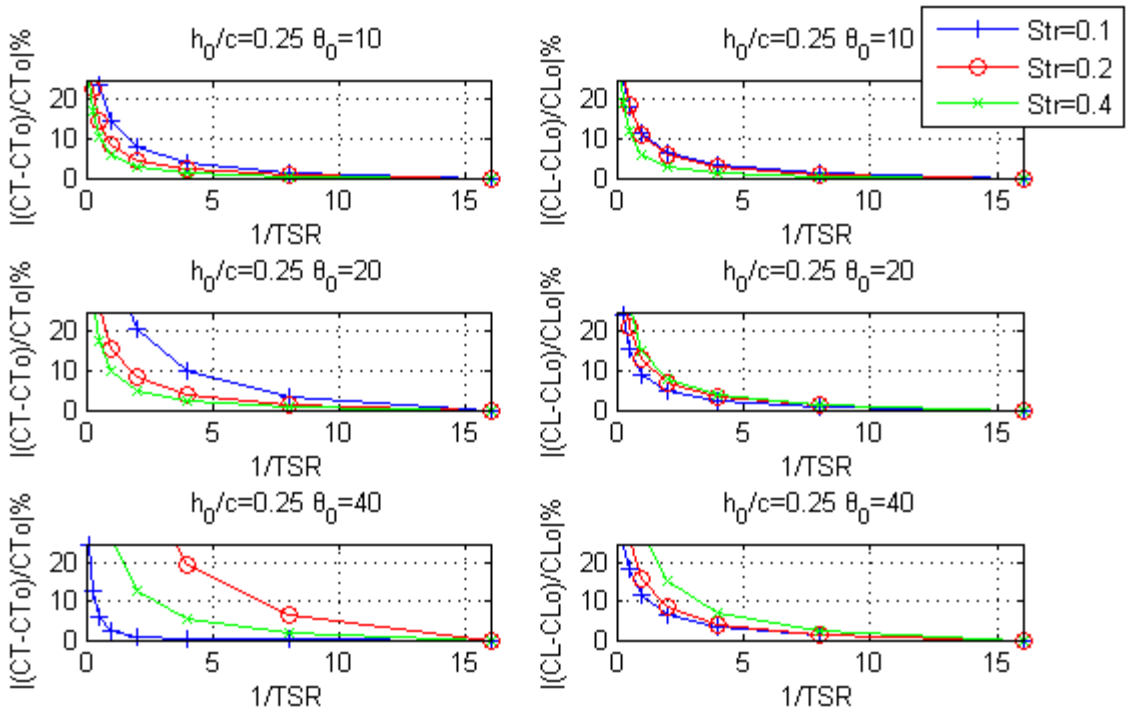


Figure 15: Convergence of Thrust and Lift Coefficients with respect to $1/TSR$, for a NACA0012 hydrofoil in flapping motion with $X_R/c=0.3$, $N_B=120$, $h_0/c=0.25$, $\theta_0=10°,20°,40°$ and $Str=0.1,0.2,0.4$.

In Figs. 15, 16 and 17 convergence characteristics of the numerical scheme concerning integrated force coefficients against time step, expressed by $1/TSR$, for a range of flapping-motion parameters, are demonstrated. We can see that the relevant error $100\left|(C_F-C_{F0})/C_{F0}\right|$ converges practically to zero (less than 3%) for $TSR\le 0.125\%$, which corresponds to more than 800 time steps per period of oscillation while errors less than 10% occurs for $TSR\le 0.25\%$, i.e. for more than 400 time steps per period. The relevant error is measured with respect to the value of the coefficient $C_{F0}$ for $TSR=0.0625\%$.

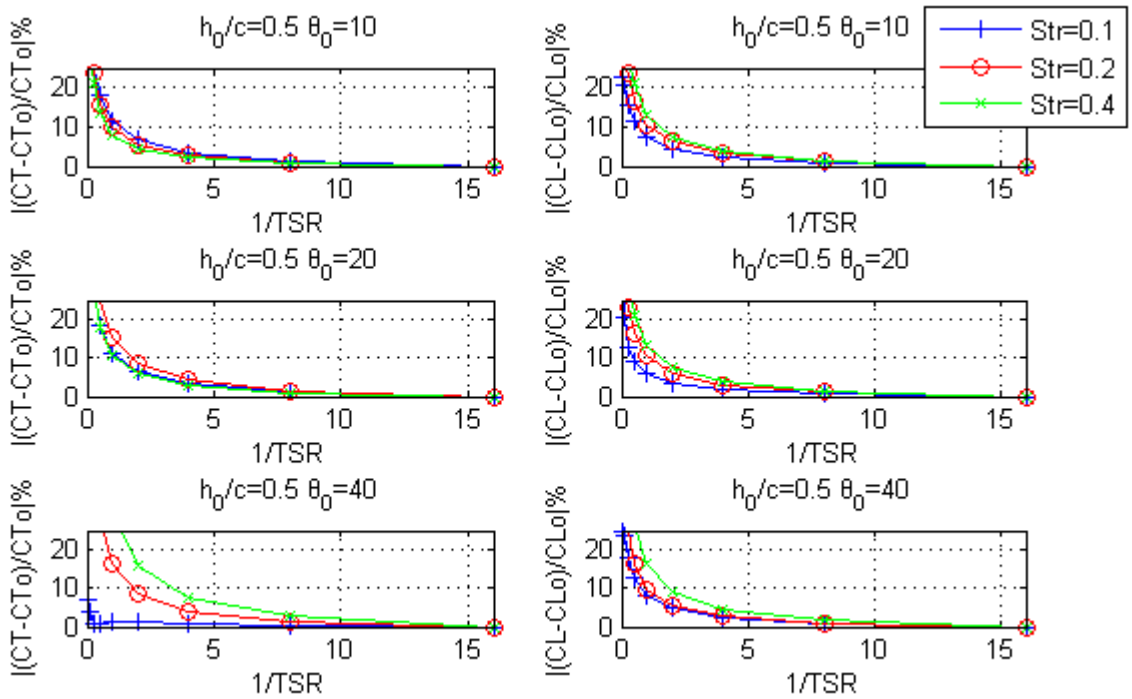


Figure 16: Convergence of Thrust and Lift Coefficients with respect to $1/TSR$, for NACA0012 in flapping motion, $X_R/c=0.3$, $N_B=120$, $h_0/c=0.5$, $\theta_0=10°,20°,40°$ and $Str=0.1,0.2,0.4$.

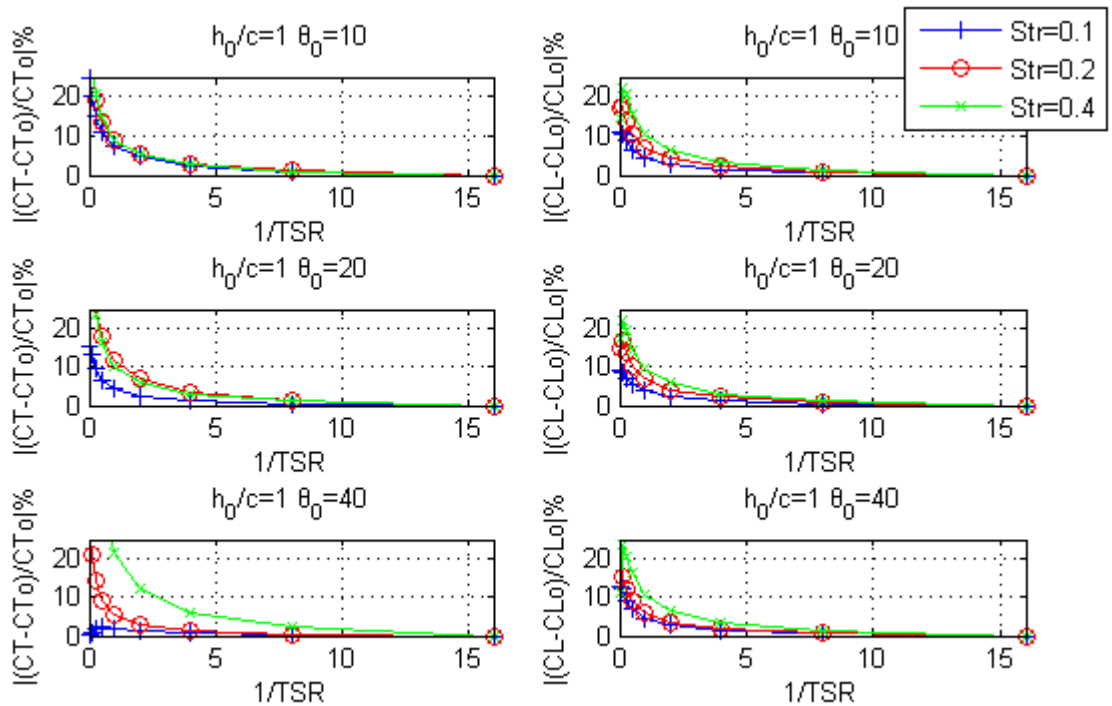


Figure 17: Convergence of Thrust and Lift Coefficients with respect to $1/TSR$, for NACA0012 in flapping motion, $X_R/c=0.3$, $N_B=120$, $h_0/c=1$, $\theta_0=10°,20°,40°$, and $Str=0.1,0.2,0.4$.

Also in Figs. 18, 19 and 20 convergence of the numerical scheme with respect to panel number on the hydrofoil $N_B$ is tested, for a range of kinematic parameters. We can see that the relevant error $100\left|\left(C_F - C_{F0}\right)/C_{F0}\right|$, concerning integrated force coefficients, converges practically to zero (less than 2%) for $N_B \geq 120$, while errors less than 10% occurs for $N_B \geq 60$. The relevant error is measured again with respect to the value of the coefficient $C_{F0}$ for the maximum panel number tested, $N_B = 240$.

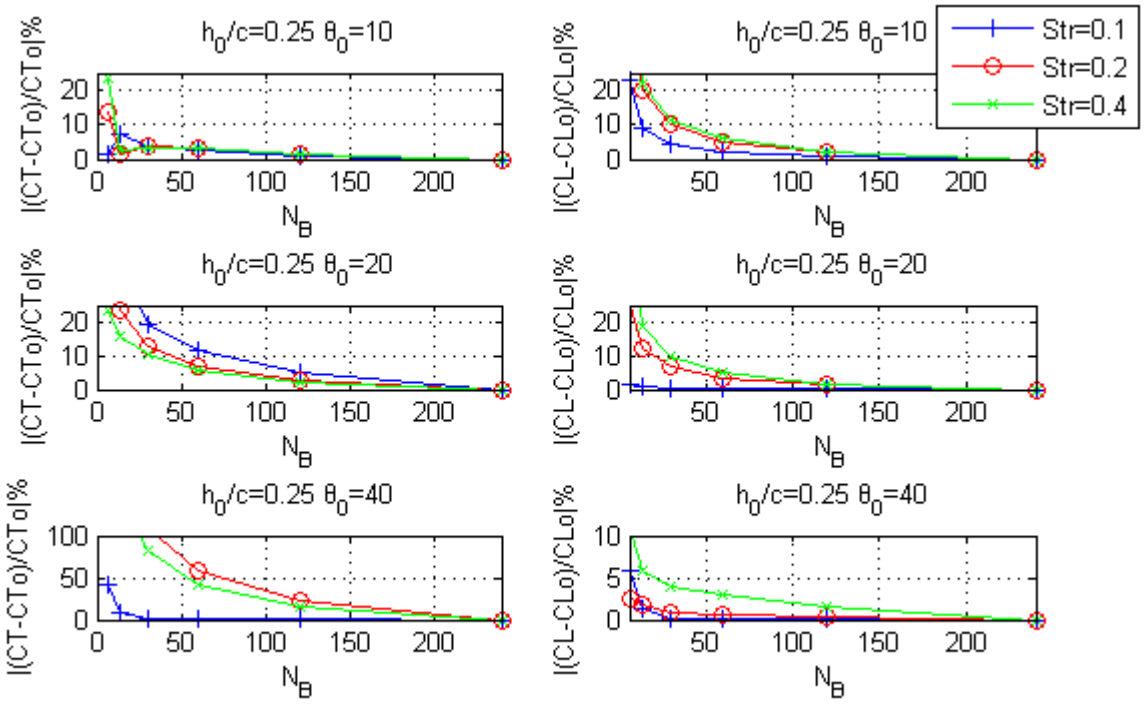


Figure 18: Convergence of Thrust and Lift Coefficients with respect to $N_B$, for a NACA0012 hydrofoil in flapping motion with parameters $X_R/c = 0.3$, $TSR = 0.125\%$, $h_0/c = 0.25$, $\theta_0 = 10, °20°, 40°$, and $Str = 0.1, 0.2, 0.4$.

Finally in Fig. 21, the evolution of pressure coefficient is presented, for different number of panels on the foil, $X_R/c = 0.3$, $TSR = 0.125\%$, and for a case of intermediate flapping motion $h_0/c = 0.5$, $\theta_0 = 20°$, and $Str = 0.2$, during the $5^{th}$ period of oscillation. It is clear that convergence is achieved for $N_B \geq 120$. We also notice that a finite (non-zero) pressure difference occurs at the trailing edge, see the discussion after Eq. (2.9) in Sec 2.3.

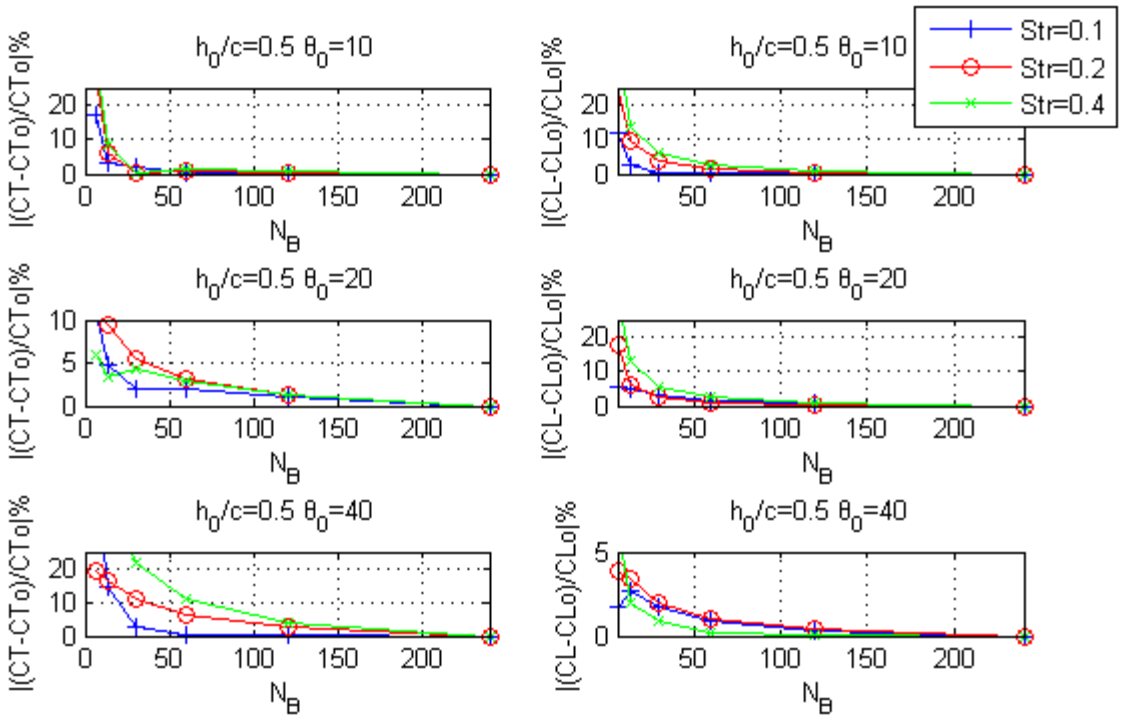


Figure 19: Convergence of Thrust and Lift Coefficients with respect to $N_B$, for NACA0012, $X_R/c=0.3$, $TSR=0.125\%$, $h_0/c=0.5$, $\theta_0=10,°20°,40°$, and $Str=0.1,0.2,0.4$.

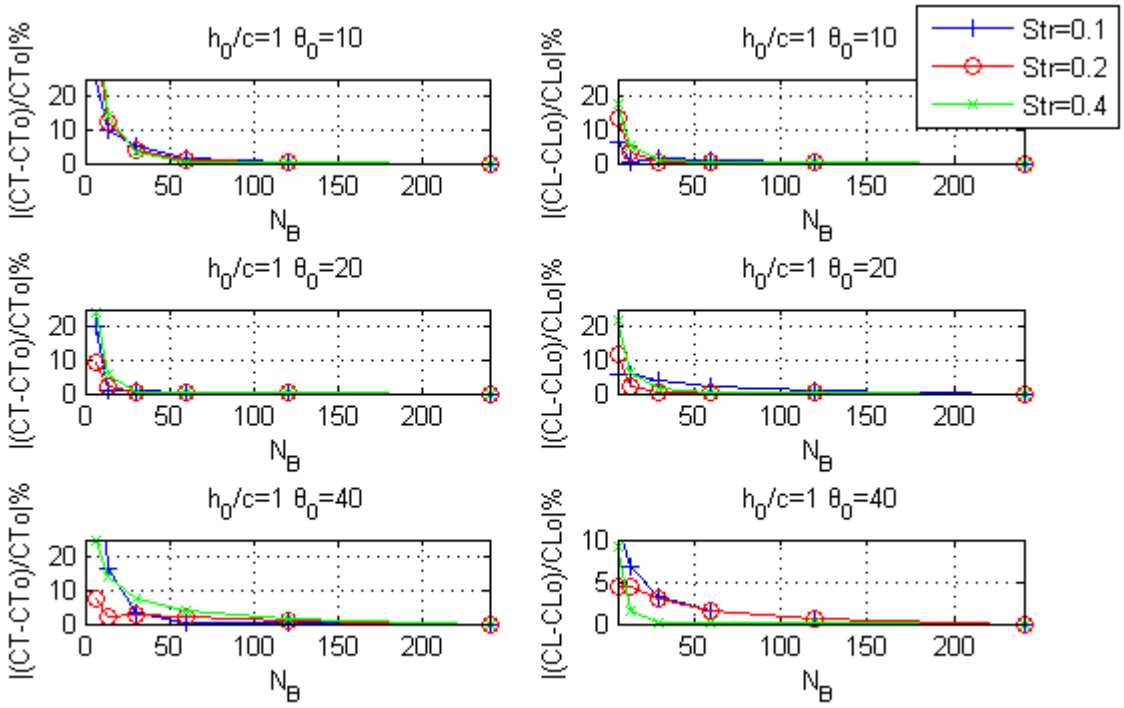


Figure 20: Convergence of Thrust and Lift Coefficients with respect to $N_B$, for NACA0012, $X_R/c=0.3$, $TSR=0.125\%$, $h_0/c=1$, $\theta_0=10,°20°,40°$, and $Str=0.1,0.2,0.4$.

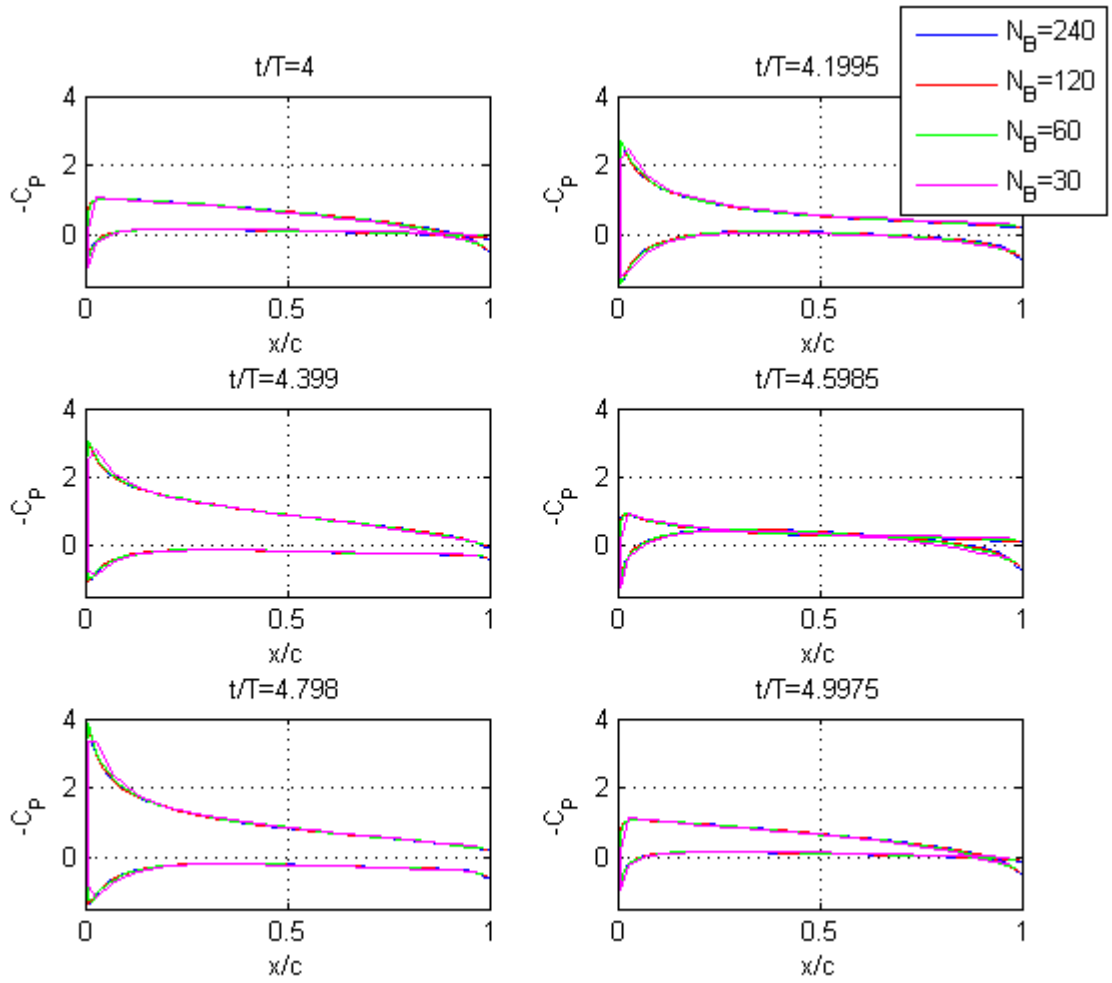


Figure 21: Convergence of boundary-pressure field with respect to $N_B$, for a NACA0012 hydrofoil, in flapping motion with $X_R / c = 0.3$, $TSR = 0.125\%$, $h_0 / c = 0.5$, $\theta_0 = 20°$, and $Str = 0.2$, during the 5th period of oscillation.

To summarize, stability and convergence of the present scheme has been studied by extensive numerical investigation. For the range of motion parameters that we have tested i.e. Strouhal number $(St = 0.1 \div 0.4)$ reduced frequency $(k_r = 0.1 \div 3.8)$, heaving $(h_0 / c = 0.25 \div 1)$ and pitching $(\theta_0 = 10° \div 40°)$ amplitudes, the numerical scheme is unconditionally stable. The above analysis also results in that a minimum number of $N_B = 120$ panels on the hydrofoil is required, while for harmonic motion the time step must be $\Delta t / T < 0.125\%$ (more than 800 time steps per period of oscillation). Finally, according to the efficiency of the scheme we have to mention that the reduction of problem's dimension from 2D to 1D, due to BEM, results in reduction of the computational cost, orders of magnitude less than other space-discretisation based numerical methods e.g. FDM's, FEM's. In addition, even more efficient higher order BEM's could be applied, see e.g. Cottrel et al (2009), Lee and Kerwin (2003), Belibassakis et al, (2013), and this is left as a subject for future extension.

### 2.9.2 Hydrofoil in steady motion

Numerical computations and results for a cambered NACA4412 (Fig.21) hydrofoil at a stationary angle of attack $a$ are shown in Figs.23-25. Present method results are based on $N_B = 120$ panels and the time step is $\Delta t U / c = 4\%$. Due to the initial acceleration, a starting vortex is generated behind of the trailing edge, whose intensity equals the initial value of circulation around the foil (Kelvin's theorem). That vortex induces a downwash at the foil which influences the value of circulation and the lift force acting it. As the distance between the vortex and the hydrofoil grows, the influence of the vortex reduces and the flow tend to become steady. When the starting vortex has gone far enough of the foil (after a distance of more than 10 chord lengths) the motion becomes time independent. For smooth transition from rest to steady state a filter function has been used in the sense of Eq. (2.70). In steady state condition, pressure distribution and lift force can be compared with results from steady panel methods as well as with experimental measurements from the literature.

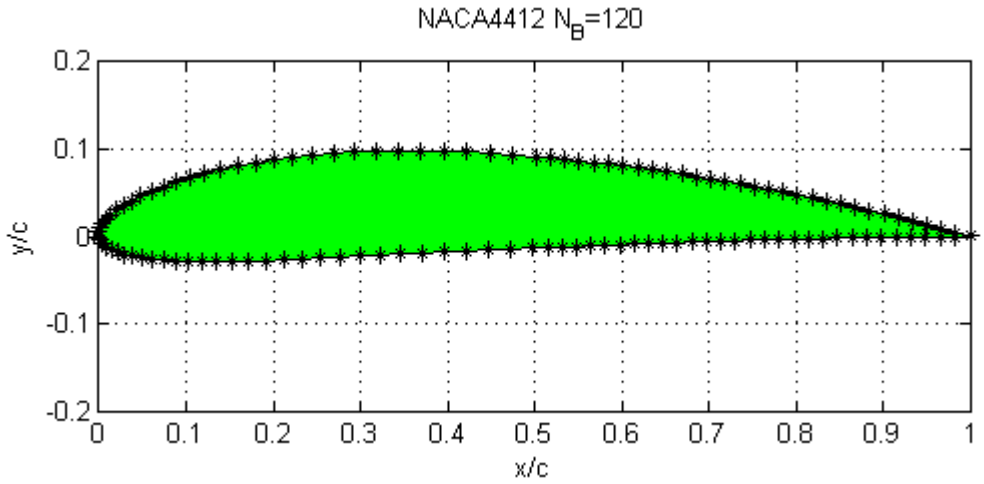


Figure 22: Geometry of a NACA0012 hydrofoil and discretization with non-uniform iso-cosine grid denser at the leading edge.

In Figure 23 we can see the time history of dipole intensity on the wake for a NACA0012 at $a = 4°$. Dipole intensity is analogous to the length of the quivers. From Morino condition (2.9) and relation (2.18) dipole intensity equals the circulation which is analogous to the lift force according to Kutta-Joukowski theorem see e.g. Batchelor (1967), Kundu and Cohen (2004) or another introductory book to fluid mechanics. As we expected Lift force, which in the rest is zero, gradually rises to a constant value at the steady state condition. Therefore, after more than 10 chord lengths lift coefficient and other quantities such as the velocity and pressure distribution can be compared with results from steady panel methods.

In the following figures velocity and pressure distributions for a NACA4412 hydrofoil at an angle of attack $a = 4°$ after 10 & 100 chord lengths are compared with steady boundary element methods which is described in bibliography, see e.g. Moran (1984) and Filippas (2011). The first method is the equivalent with the scheme described in the present work, steady, indirect, potential based panel method developed by Morino and Kuo in 1974, see also Moran Ch.4 (1984).

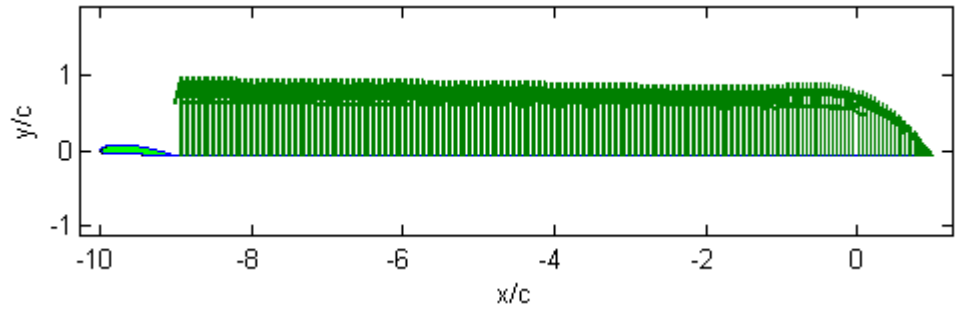


Figure 23: History of dipole intensity on the wake, for NACA4412 at an angle of attack $a = 4°$.

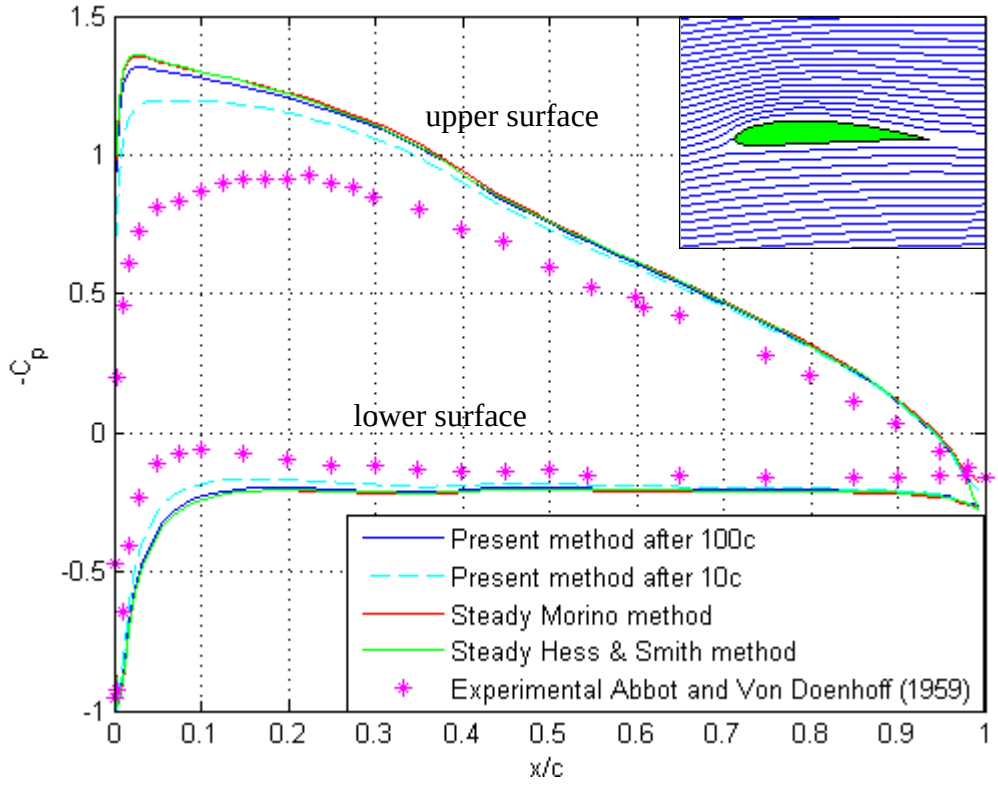


Figure 24: -Cp distribution for NACA 4412 at angle of attack a=4 after 10 & 100 chord lengths in comparison with steady panel methods and experimental results. On the upper right corner a streamline plot is presented.

The second one is an indirect source and vortex based panel method, the so called Douglas-Neumann method, developed by Hess & Smith in 1966, see also Moran (1984) and Filippas (2011). Comparison with experimental results from Abbot and Von Doenhoff (1959) is also presented.

The form of pressure distribution (Fig.24) is as expected from the fundamental laws of hydrodynamics. Acceleration of flow at the upper side of leading edge (due to conservation of mass) results in dropping pressure (Bernoulli's theorem).

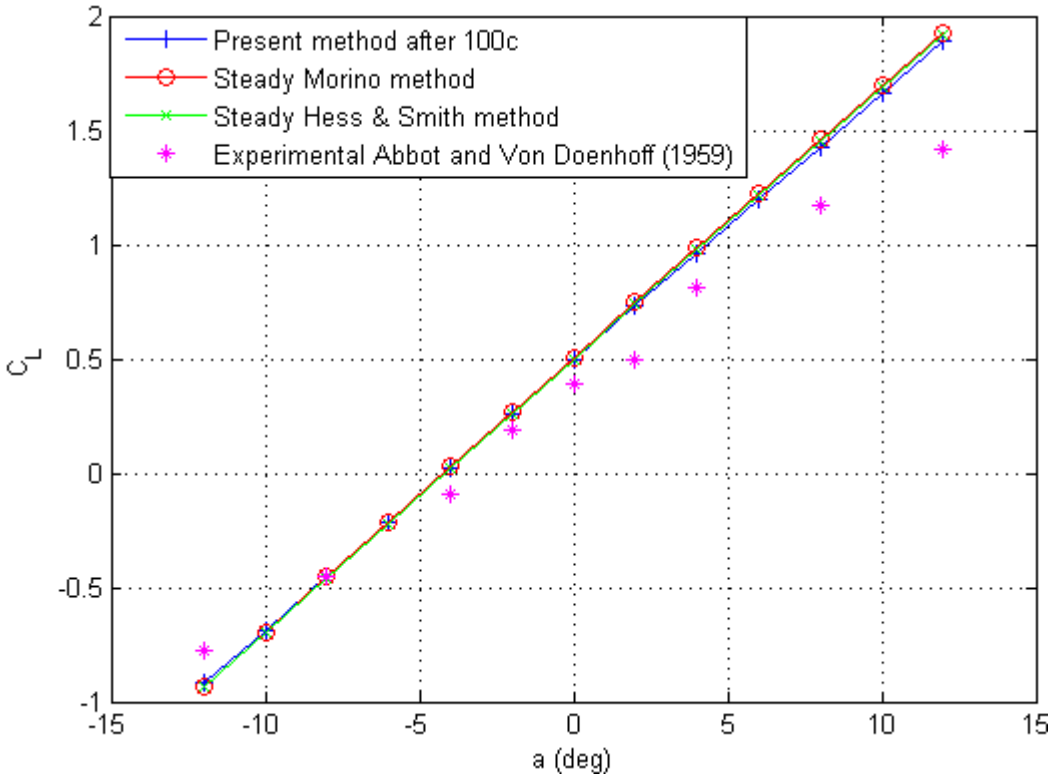


Figure 25: CL for NACA 4412 at different angle of attacks after 100 chord lengths, in comparison with steady panel methods and experimental results.

The opposite behavior is noticed on the lower side due to the geometry and the angle of attack, leading to fluid compression in this area, see also streamline plot. Comparison between the three methods is very satisfying. Small differences occur at the trailing edge where the two methods applying Morino condition results in pressure distribution with little but not zero pressure difference at the trailing edge. On the contrary pressure distribution is closed at the trailing edge on Hess & Smith method, due to the fact that a pressure-type Kutta condition has been applied. We notice that the unsteady hydrofoil has to cover a distance of order $100c$ in order to obtain the exact steady result.

In Figure 25 we present the values of lift coefficient of a NACA4412 hydrofoil for a range of angles of attack $a$ calculated with unsteady and steady panel methods against experimental results by Abbot and Von Doenhoff (1959). The comparison with steady potential theory applied by panel methods is very satisfactory. The deviation between present method and experimental results that occurs at large angles, is due to effects of viscosity. At higher angles the loss of lift due to separation of flow and static stall phenomenon cannot be predicted by an inviscid theory like the present one. Hybrid boundary layer and BEM's can be used in order to model leading edge separation and improve the above predictions at large angle of attack, see Lewis (1991), Politis & Belibassakis (1999), Riziotis and Voutsinas (2007), Belibassakis (2010), such an extension is left as a subject for future work.

### 2.9.3 Hydrofoil in heaving motion

We have already seen that our method is compatible with steady potential theory and can give satisfying predictions against experimental results in steady state condition. For simplicity, before we study the efficient thrust producing flapping motion, we will present results in the two following subsections concerning pure linear or rotational oscillations of hydrofoil at forward constant speed motion. In this section, numerical results are presented concerning an unsteady heaving hydrofoil in infinite submergence. Except of forward translation with constant speed $U$, the hydrofoil also performs vertical (heaving) oscillations. Heaving oscillation is important, as one of the two independent motions of thunniform swimming mode that is used by cetaceans, like dolphins, whales etc. and leads to efficient thrust production. For validation purposes, in the next we present comparisons, concerning lift coefficient, with unsteady linear hydrofoil theory.

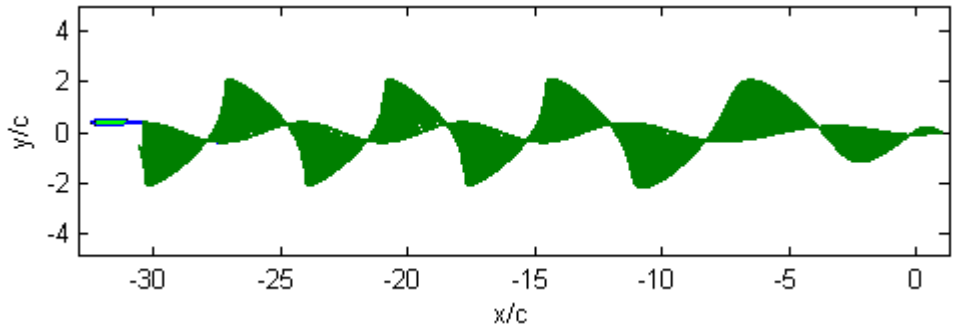


Figure 26: History of dipole intensity on the wake, for a NACA0012 hydrofoil in heaving motion with $k_r = 1$ and $h_0 / c = 0.2$.

In the framework of linearized asymptotic theory the hydrofoil is assumed very thin. Furthermore, the angle of attack and the amplitudes of oscillatory motions are small. Under the above assumptions the foil and the shear layer can be collapsed onto a cut in the x-axis. For a detailed study in asymptotic methods in fluid dynamics, see e.g. Newman (1977) or Van Dyke (1975). According to the linear theory (Appendix C) the lift coefficient is given by:

$$C_L(t) = C_{L0}\cos(\omega t) = \mathrm{Re}\left\{\dot{C}_{Lo} e^{i\omega t}\right\}, \tag{2.78}$$

where

$$\dot{C}_{Lo} = -4\pi i k_r \frac{h_0}{c}\cdot C(k_r) - 2\pi i^2 k_r^2 \frac{h_0}{c}. \tag{2.79}$$

In the above, $k_r = \omega c / 2U$ denotes the reduced frequency. In the present section length is nondimensionalised using half chord length $c/2$, which in appendix C is considered to be $c/2 = 1$.

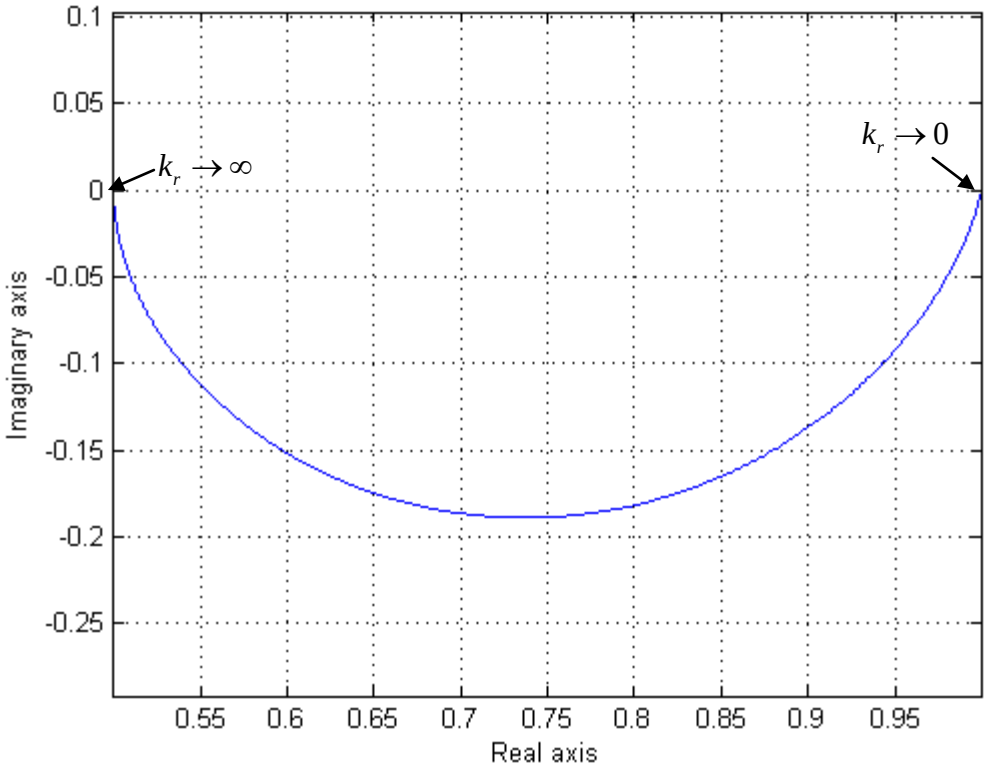


Figure 27: Argand diagram of Theodorsen function, reduced frequency raises from zero to infinite along the complex curve with clockwise direction.

The second term in (2.79), which is analogous to the linear acceleration, is the added mass term of lift coefficient. Notice that it is analogous to $k_r^2$, and thus for small frequencies it is negligible, while for high unsteadiness it has the major contribution. Also, $C(k_r)$ is the Theodorsen function defined as a ratio of Hankel functions of second kind, zero and first order

$$C(k_r) = \frac{H_1^{(2)}(k_r)}{H_1^{(2)}(k_r) + iH_0^{(2)}(k_r)}. \tag{2.80}$$

Function $C(k_r)$ encompasses the memory effects due to the unsteady wake, and for low frequencies its limiting value is 1 which is compatible with the steady result $dC_L / da = 2\pi$. The Argand diagram of Theodorsen function is presented in Figure 27.

In Figs.28 & 39 we compare integrated results concerning the amplitude of lift coefficient obtained by the present method against predictions by linearised theory for thin hydrofoil. A symmetrical NACA0012 hydrofoil is simulated in small and moderate oscillations, i.e. $h_0 / c = 0.05 \div 0.4$. Number of panel on hydrofoil's boundary are $N_B = 120$ and $TSR = 0.125$, i.e. one period contains 800 time steps.

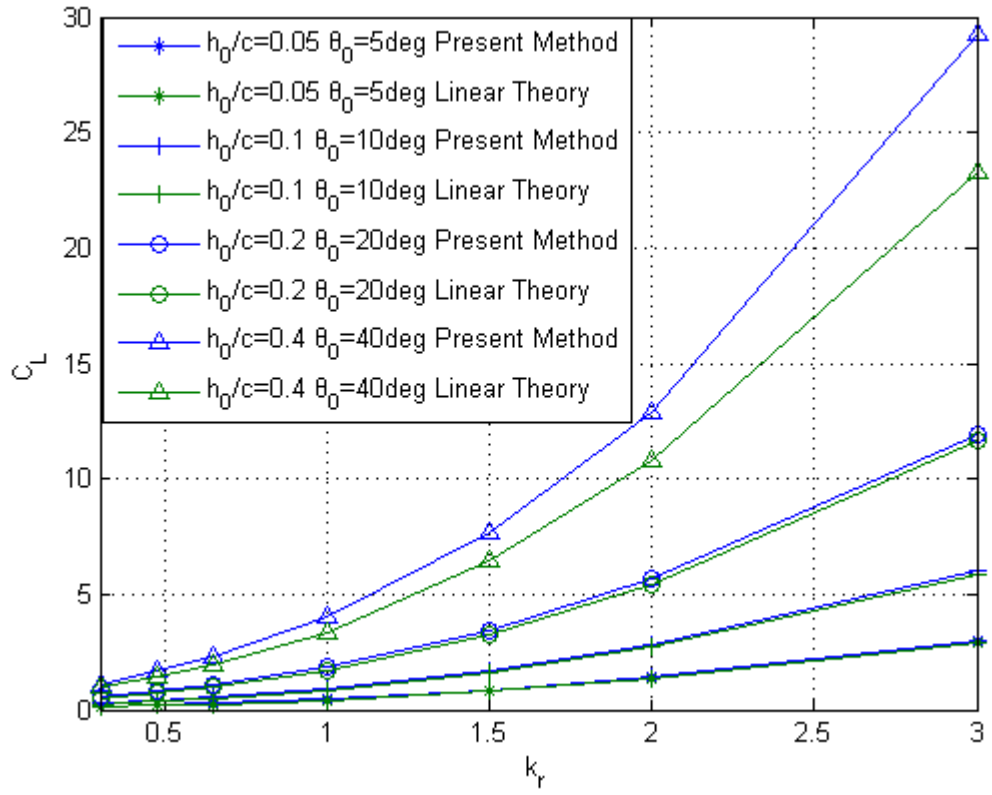


Figure 28: Amplitude of lift coefficient for a NACA0012 hydrofoil in heaving motion with $h_0 / c = 0.05 \div 0.4$, evaluated by the present method and compared with theoretical asymptotic results.

We can see that our predictions are in good agreement with thin hydrofoil theory for a satisfyingly wide range of reduced frequency $k_r$ when heave and pitch amplitude are small to moderate, i.e. $h_0 / c = 0.05 \div 0.2$, and in moderate frequencies $k_r < 2$ for larger amplitudes.

Figure 29 demonstrates also that the predictions for phase lag are compatible with linear theory. Only in the case of $h_0 / c = 0.2$ and $k_r = 1$ a small difference appears in between the maximum values of lift coefficient, due non-linear effects of large amplitude motion and non-linearised wake (wake is assumed to be steady but still it is not linearized and collapsed onto x axis), this non-linearities are not taken into account by linear thin hydrofoil theory. According to the above our numerical scheme is valid for small and moderate oscillations in the framework of potential theory. Furthermore it is obvious that for accurate predictions of hydrodynamic quantities in larger oscillatory amplitude and more unsteady character, linear theory is provide good results and it is necessary to resort to numerical methods like the present one.

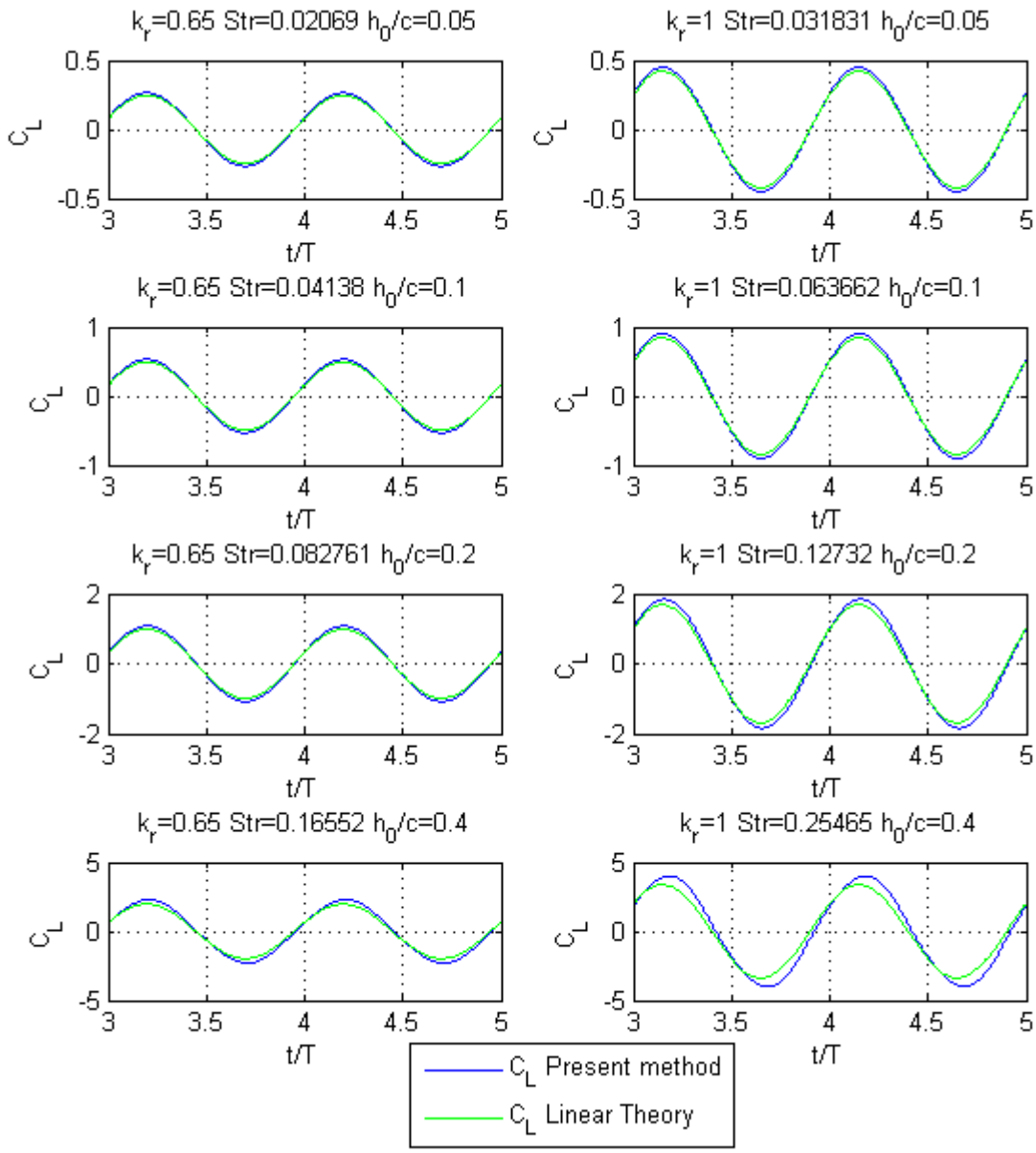


Figure 29: Time history of lift coefficient for a NACA0012 hydrofoil in heaving motion with $h_0 / c = 0.05 \div 0.4$, and $k_r = 0.65,1$ evaluated by the present method and compared with theoretical asymptotic results. Resulting Strouhal number, $Str = \omega h / \pi U = \left(2h / \pi c\right) k_r$, varies from 0.02 to 0.25.

### 2.9.4 Hydrofoil in pitching motion

In this case the hydrofoil moves with constant forward speed while performs rotating oscillations (pitching) around the midchord. This is a required step before we study the more complex flapping motion. In the following, we present comparisons, concerning lift coefficient, with unsteady linearized hydrofoil theory in the same way as in previous section.

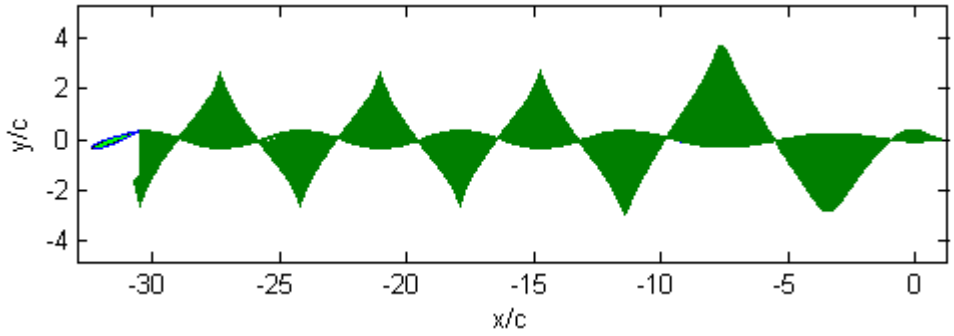


Figure 30: History of dipole intensity on the wake, for a NACA0012 hydrofoil in pitching motion with $k_r = 1$ and $\theta_0 = 20°$.

According to the linear theory (Appendix C) the lift coefficient is:

$$C_L(t) = C_{L0}\cos(\omega t) = \mathrm{Re}\left\{\dot{C}_{Lo}e^{i\omega t}\right\}, \tag{2.81}$$

where

$$\dot{C}_{Lo} = 2\pi(1+\frac{1}{2}ik_r)\theta_0 \cdot C(k_r) + \pi i k_r \theta_0. \tag{2.82}$$

The second term in (2.82) is the added inertia, due to rotation, component of lift coefficient, that is important for large reduced frequencies. We can notice that when $k_r \to 0 \Rightarrow C(k_r) \to 1$ the lift coefficient converges to the expected from steady thin hydrofoil theory value, i.e. $C_L \to 2\pi\theta_0$.

In Figs.31 & 32 we compare integrated results concerning the amplitude of lift coefficient obtained by the present method against predictions by linearised theory for thin hydrofoil. A thin symmetrical NACA0012 hydrofoil is simulated in small and moderate oscillations, i.e. $\theta_0 = 5° \div 40°$. Number of panel on hydrofoil's boundary are $N_B = 120$ and $TSR = 0.125$, i.e. 800 time steps pre period of oscillation.

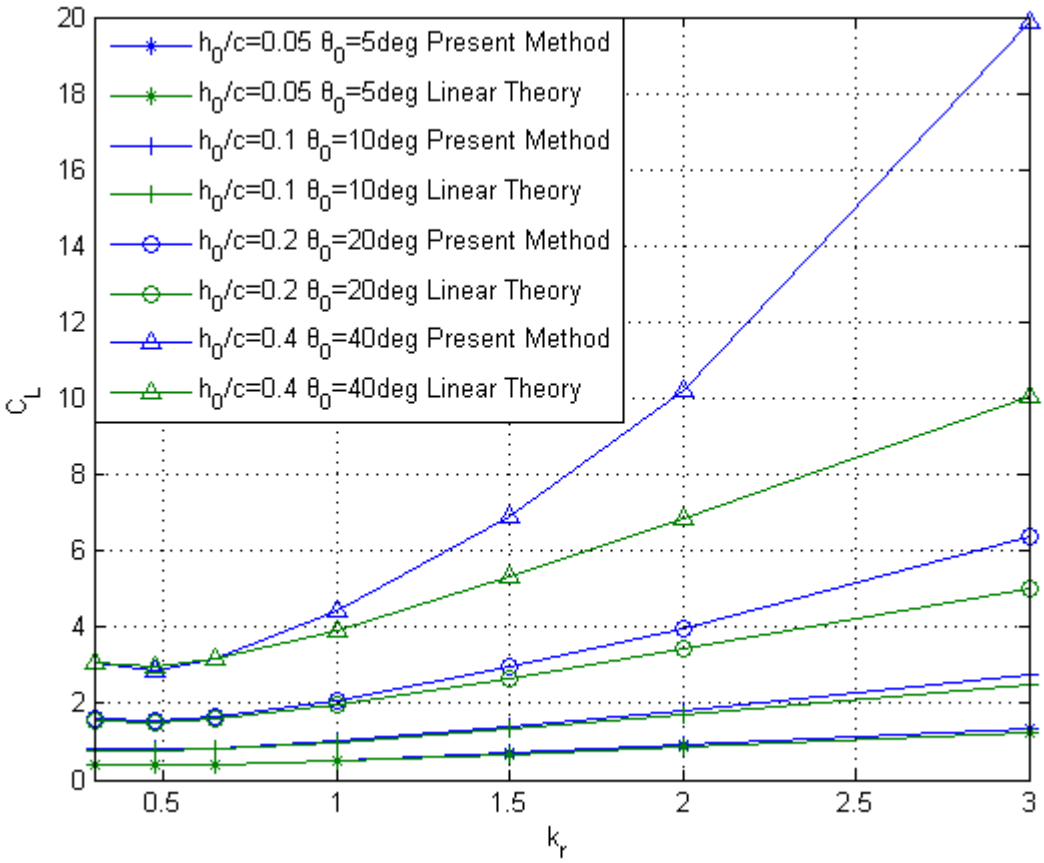


Figure 31: Amplitude of lift coefficient for a NACA0012 hydrofoil in pitching motion $\theta_0 = 5° \div 40°$, evaluated by the present method and compared with theoretical asymptotic results.

Again our predictions are in good agreement with thin hydrofoil theory for a wide range of reduced frequency when heave and pitch amplitude are small to moderate i.e., $\theta_0 = 5° \div 20°$ and in moderate frequencies $k_r < 1.5$ for larger amplitudes.

In Figure 32 time evolution of lift coefficient is presented in comparison with linear theory, demonstrating also that the predictions for phase lag are compatible with linear theory for pitching motion too. As we can notice from time evolution of lift coefficient (Fig.32), in the case of $\theta_0 = 40°$ and $k_r = 1$, effects associated with wake shape that are neglected by linear theory, change the mode of $C_L(t)$ as calculated by the present method. According to the above analysis our numerical scheme is valid for small and moderate oscillations in the framework of potential theory in both cases of pure heaving or pitching oscillations.

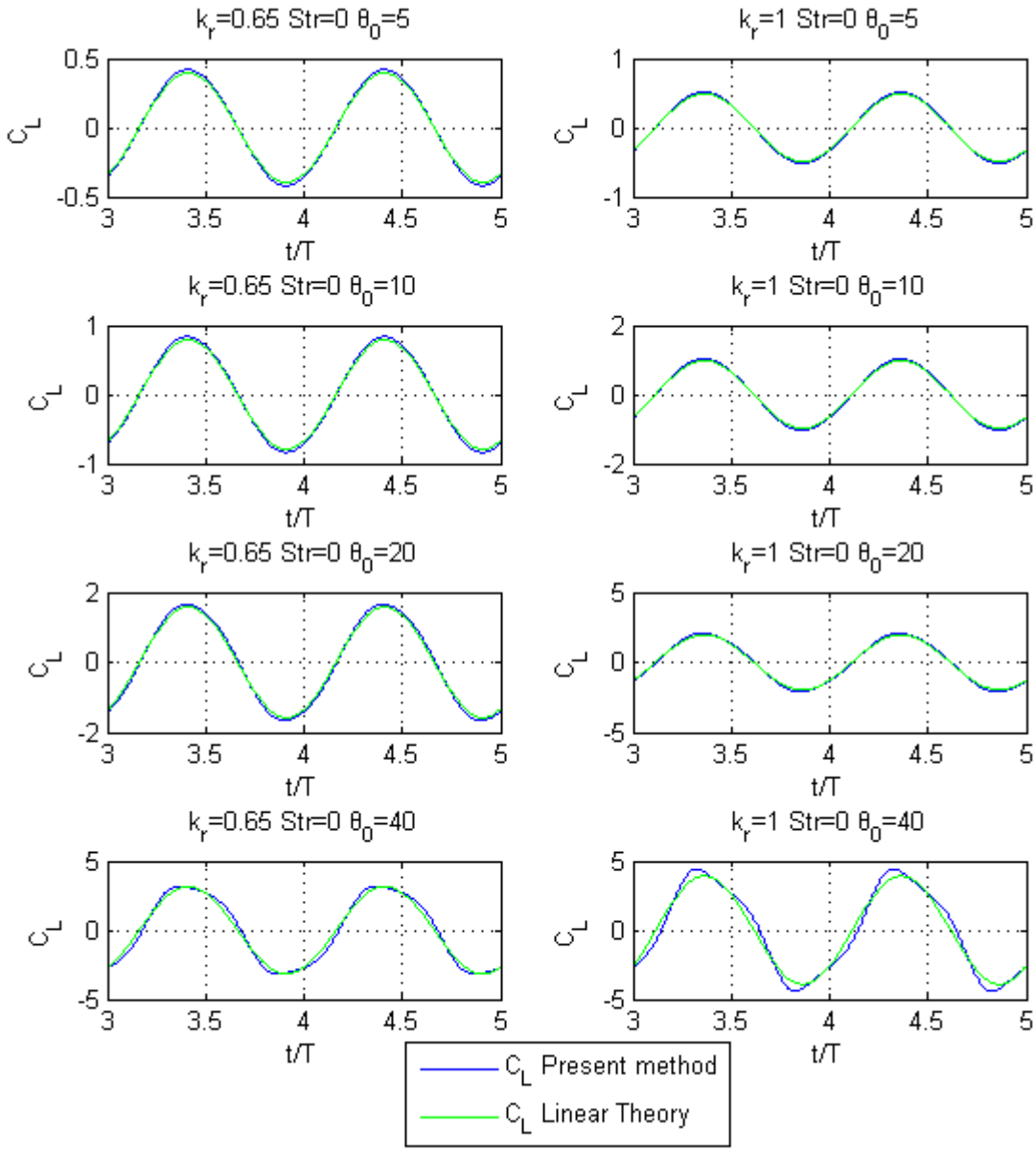


Figure 32: Time history of lift coefficient for NACA0012 hydrofoil in pitching motion $\theta_0 = 5° \div 40°$, evaluated by the present method and compared with theoretical asymptotic results.

### 2.9.5 Hydrofoil in flapping motion

In this section numerical results are presented concerning a flapping hydrofoil in infinite domain. Except of forward translation with constant speed $U$, the hydrofoil also performs combined vertical (heaving) and rotational (pitching) oscillatory motions, the latter with respect to a pivot axis located at a specific distance $X_R$ from the leading edge. The phase difference between pitching and heaving motion is appropriate selected at $90°$, see e.g. Rozhdestvensky & Ryzhov (2003). That kinematics, simulate the motion of the fin that hydrobionts use in order to produce thrust efficiently. As we have mentioned in Chapter 1 many theoretical and experimental studies has been published related to biomimetic systems and have demonstrated that flapping foils can be used as high efficient propulsion systems. In the first part of the present section we present comparisons with unsteady linear hydrofoil theory and in the second one with experimental results by Schouveiler et al (2005).

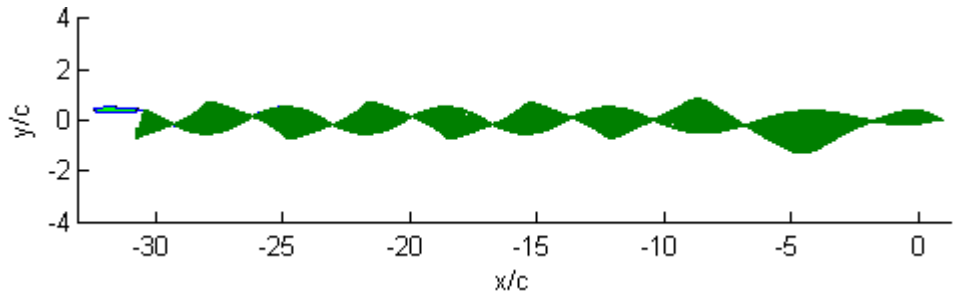


Figure 33: History of dipole intensity on the wake, for a NACA0012 hydrofoil in flapping motion with $k_r = 1, h_0 / c = 0.2$, $\theta_0 = 20°$ and $\psi = -90°$.

According to the linear theory, Appendix C and Newman (1977), the lift coefficient can be evaluated

$$C_L(t) = C_{L0}\cos(\omega t) = \mathrm{Re}\left\{\dot{C}_{Lo} e^{i\omega t}\right\}, \tag{2.83}$$

where the complex amplitude can be evaluated from (2.79) and (2.82) using the principle of linear superposition

$$\dot{C}_{Lo} = 2\pi\left[-2ik_r\frac{h_0}{c} + \left(1+\frac{1}{2}ik_r\right)\theta_0\right]\cdot e^{i\psi}\cdot C(k_r) + 2\pi\left(-i^2k_r^2\frac{h_0}{c} + i\frac{k_r}{2}\theta_0 e^{i\psi}\right), \tag{2.84}$$

$C(k)$ is the Theodorsen function and the second order in (2.84) is the added mass term of lift coefficient.

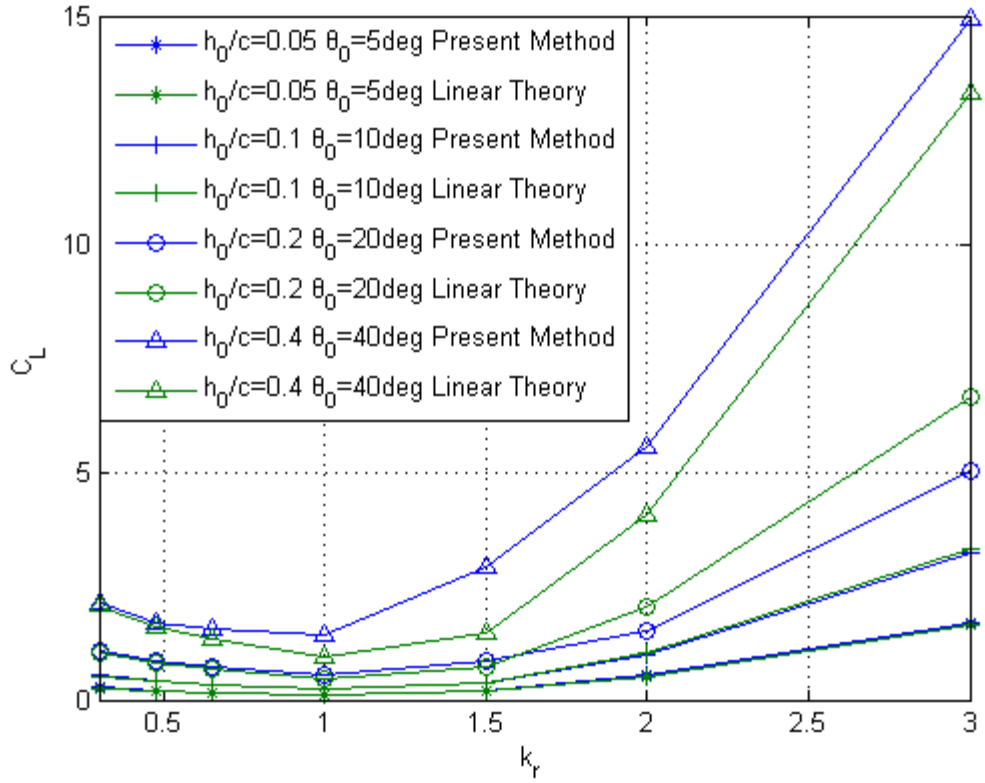


Figure 34: Amplitude of lift coefficient for a NACA0012 in flapping motion with $h_0/c = 0.05 \div 0.4$, $\theta_0 = 5° \div 40°$, $\psi = -90°$, $X_R/c = 0.5$ evaluated by the present method and compared with theoretical asymptotic results.

In Figs. 34 & 35 we compare integrated results concerning the amplitude of lift coefficient obtained by the present method against predictions by linearised theory for thin hydrofoil. A symmetrical NACA0012 hydrofoil is performing small and moderate oscillations i.e. $h_0/c = 0.05 \div 0.4$, $\theta_0 = 5° \div 40°$ and $X_R/c = 0.5$. Number of panels on hydrofoil's boundary is $N_B = 120$ and $TSR = 0.125$, i.e. one period contains 800 time steps.

We can see that our predictions are in good agreement with thin hydrofoil theory, for a wide range of reduced frequency $k_r$ when heave & pitch amplitudes are small and moderate i.e. $h_0/c = 0.05 \div 0.2$, $\theta_0 = 5° \div 20°$ and in moderate frequencies $k_r < 1$ for larger amplitudes.

Figure 35 demonstrates also that present predictions concerning phase lag are compatible with linear theory. Again we can notice from time evolution of lift coefficient in Fig.32, that in the case of $h_0/c = 0.05 \div 0.2$ and $k_r = 1$, non-linear effects of large amplitude motion and non-linearised wake change the mode of $C_L(t)$, which is not well predicted by linear thin hydrofoil theory. According to the above our numerical scheme is valid for small and moderate oscillations in the framework of potential theory.

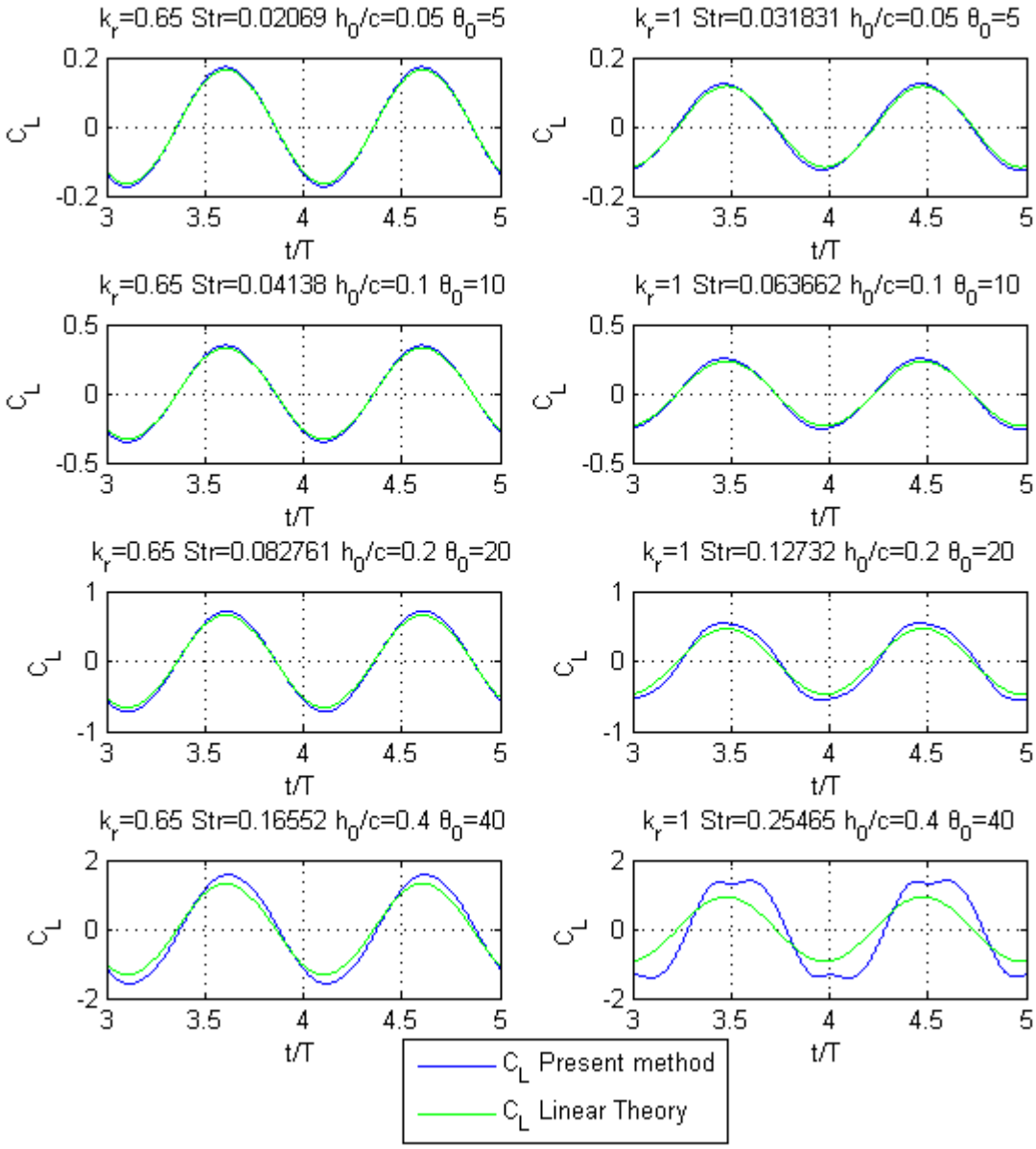


Figure 35: Time history of lift coefficient for a NACA0012 hydrofoil in flapping motion with $h_0/c = 0.05 \div 0.4$, $\theta_0 = 5° \div 40°$, $\psi = -90°$, $X_R/c = 0.5$ evaluated by the present method and compared with theoretical asymptotic results. Resulting Strouhal number, $Str = \omega h/\pi U = (2h/\pi c)k_r$, varies from 0.02 to 0.25.

A further comparison between the present potential flow method and computational results by Schouveiler et al (2005) is presented in Figs.36 & 37. These results concern efficient thrust production cases in large amplitude oscillations and high unsteadiness. In Fig.36 we present the evolution in time of lift and thrust coefficients for NACA0012 hydrofoil in flapping motion with $h_0/c = 0.75$, $\theta_0 = 23.3°$, $\psi = -90°$, $a_{\max} = 20°$, $X_R/c = 0.33$. In this case our results are found in good agreement with the experimental measurements.

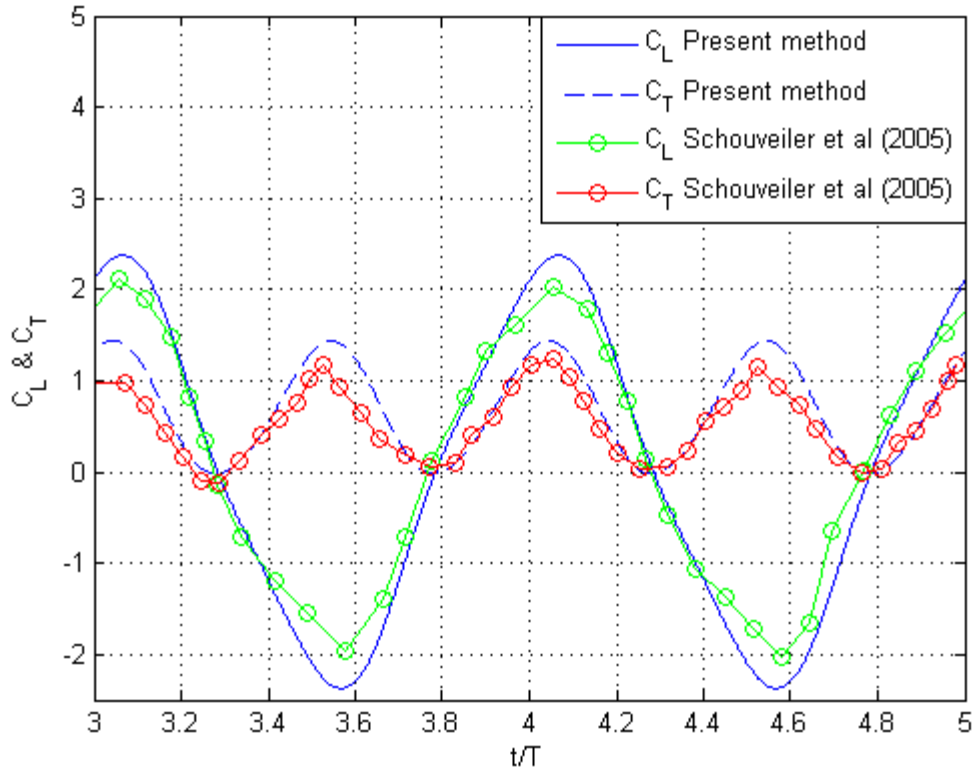


Figure 36: Time history of lift and thrust coefficients for a NACA0012 hydrofoil in flapping motion with $h_0/c=0.75$, $\theta_0=23.3°$, $\psi=-90°$, $a_{\max}=20°$, $X_R/c=0.33$. Comparison between present-method results and experimental data from Schouveiler et al (2005).

Furthermore, in Fig.37 we present results concerning average thrust coefficient for the case of NACA0012 hydrofoil in flapping motion with $h_0/c=0.75$, $\theta_0=23.3°$, $\psi=-90°$, $a_{\max}=20°$, $X_R/c=0.33$. We can see that for small and moderate angles of attack, where leading edge separation and dynamic stall effects are not manifested, the modes of the curves are similar, while for large angles, i.e. $a_{\max}>25°$, present method over-predicts $C_T$, and that is due to viscous effects, like dynamic stall that are omitted by inviscid, potential theory. Although, our results are in good agreement with linear theory, deviation occurs between our numerical results about thrust coefficient and experimental, in that high amplitude case $(h_0/c=0.75)$, especially in higher unsteadiness and angles of attack i.e. $Str>0.2$ and $a_{\max}>20°$. That is due to the following reasons:

- Non linear effect that have neglected due to the linearization of the wake (frozen wake) and linearization of pressure Kutta condition (Morino condition).
- Viscous flow effects, like the presence of frictional and viscous pressure drag that are opposite to thrust force are not taken into account.
- Viscous flow effects, like leading edge separation and dynamic stall that reduces the value of thrust coefficient and they are not predicted from the present method.
- 3-D effects that may appear in experimental measurements are neglected by our 2-D method.

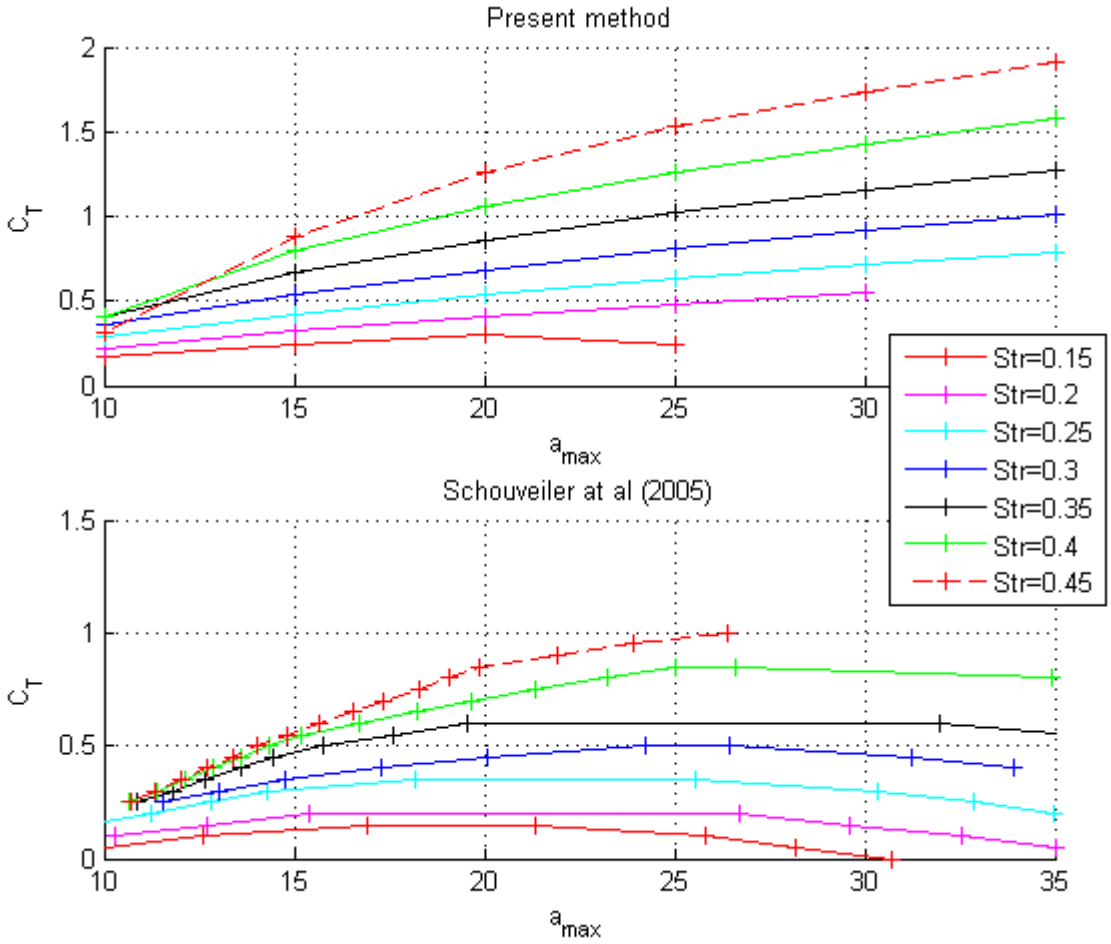


Figure 37: Average thrust coefficient for a NACA0012 hydrofoil in flapping motion with $h_0/c = 0.75$, $\theta_0 = 2° \div 68°$, $\psi = -90°$, $a_{\max} = 10° \div 35°$, $Str = 0.15 \div 0.45$, $X_R/c = 0.33$, evaluated by the present method and compared with experimental results by Schouveiler et al (2005).

In Fig. 37 we notice that the thrust coefficient increases with the Strouhal number, while it first rises then decreases when the maximum of the angle of attack increases. For increasing $Str$, we observe a continuous evolution from a drag-producing to a thrust-producing motion. Thus in the parameter region under consideration, negative values of the mean horizontal force have been obtained for $\alpha_{\max} > 30°$ and low Strouhal $Str < 0.15$. In experimental results the maximum of the thrust is reached at a value of angle of attack which evolves from $a_{\max} = 15°$ for $Str = 0.1$ to $a_{\max} = 30°$ for $Str = 0.45$. And the maximum thrust coefficient measured is $C_T = 1.05$ at $Str = 0.45$ & $a_{\max} = 30°$ while the hydromechanical efficiency is $\eta_h = F_{x,av}U / P_{av} = 0.42$, where $P_{av}$ is the mean value of power absorbed by the foil, Schouveiler at al (2005).

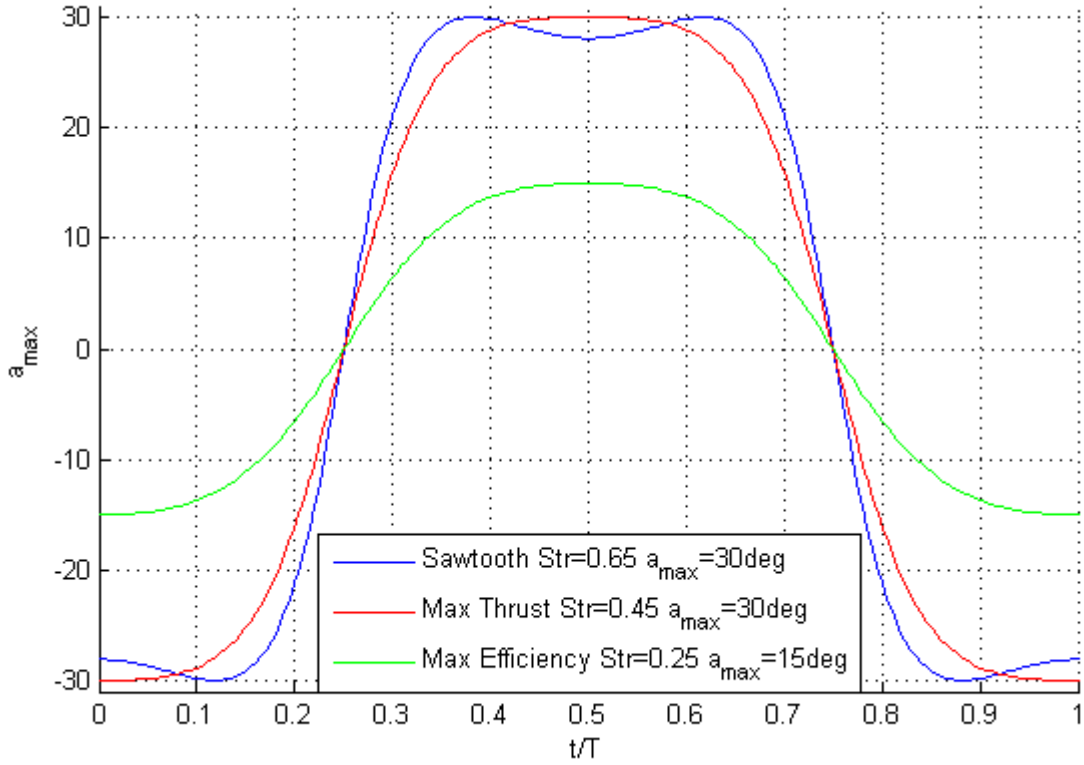


Figure 38: Angle of attack for a NACA0012 hydrofoil in flapping motion with $h_0 / c = 0.75$, $\psi = -90°$, for $Str = 0.45 \& a_{\max} = 30°$ and $Str = 0.25 \& a_{\max} = 15°$ that correspond to the maximum thrust and efficiency respectively, in the present parameter domain, according to experimental results by Schouveiler et al (2005).

Also, Schouveiler at al (2005) mentioned that efficiency presents a well-defined unique peak in the considered parameter range. The highest value of the efficiency has been measured for, $Str = 0.25$ & $a_{\max} = 15°$ and is $\eta_h = 0.73$. It is associated with a moderate thrust coefficient $C_x = 0.32$.

For use as a propulsion system, the conditions of high efficiency together with high thrust are required. These two conditions are not encountered outside of the parameter range we explored for the present study. In fact, if Fig. 37 shows that higher thrust can be expected when increasing the Strouhal number and/or the maximum of the angle of attack, these high thrusts would be associated with low efficiency: no more than 40% (see Schouveiler, 2005). The present parameter domain includes the maximum of efficiency and the condition of high thrust together with high efficiency when the maximum angle of attack or Strouhal number is increased.

It is also worth to mention that experiments of Hover et al (2004), consisted of measuring the propulsive performance of a foil oscillating with an imposed angle of attack profile. They report that the most efficient situation is achieved with a cosine profile (although highest thrusts are found with a sawtooth-profile), see also Fig.38.

### 2.9.6 Hydrofoil in the presence of a sinusoidal background field (gust)

We have already studied one type of unsteadiness that appears in lifting flow problems, i.e. the time dependent oscillating motions of the hydrofoil. Another example of unsteady motion occurs when the hydrofoil is moving with constant forward speed in a fluid which is non uniform i.e. a disturbed background field exists, for example a sinusoidal gust. The last problem has been studied by many scientist like Sears and Kerwin using theoretical or numerical methods, see e.g. Appendix C, Newman (1977), Belibassakis (1993). Practical examples of this are the motion of a hydrofoil ship in waves, an airplane in turbulence or the motion of the propeller blades in a spatially non uniform ship's wake. Also, energy extraction from non-uniform internal wavy flows using biomimetc flapping-foil systems, could be another very interesting application.

In the present subsection we will consider a hydrofoil in steady motion and on a sinusoidal background field in order to obtain results and compare with thin hydrofoil theory developed by Sears, see Appendix C and Newman (1977).

According to the linear theory the lift coefficient is given by the following equation

$$C_L(t) = C_{L0}\cos(\omega_g t) = \mathrm{Re}\left\{\dot{C}_{Lo} e^{i\omega_g t}\right\}, \tag{2.85}$$

where

$$\dot{C}_{Lo} = 2\pi \frac{V_g}{U} \underbrace{\left[ \frac{\dfrac{2i}{\pi k_{r,g}}}{H_1^{(2)}(k_{r,g}) + iH_0^{(2)}(k_{r,g})} \right]}_{S(k_{r,g})}. \tag{2.86}$$

In the above, $k_{r,g} = \omega_g c / 2U$ denotes gust's reduced frequency, $\omega_g$ is gust's radial frequency and $V_g$ is the amplitude of gust velocity. Also, $S(k_{r,g})$ is the Sears function, defined in terms of Hankel functions of second kind, zero and first order:

$$S\left(k_{r,g}\right) = \frac{2i/\pi k_{r,g}}{H_1^{(2)}(k_{r,g}) + iH_0^{(2)}(k_{r,g})}. \tag{2.87}$$

Function $C(k_r)$ encompasses the memory effects due to the unsteady wake, and for low frequencies its limiting value is 1. The Argand diagram of Theodorsen function is presented in Figure 39.

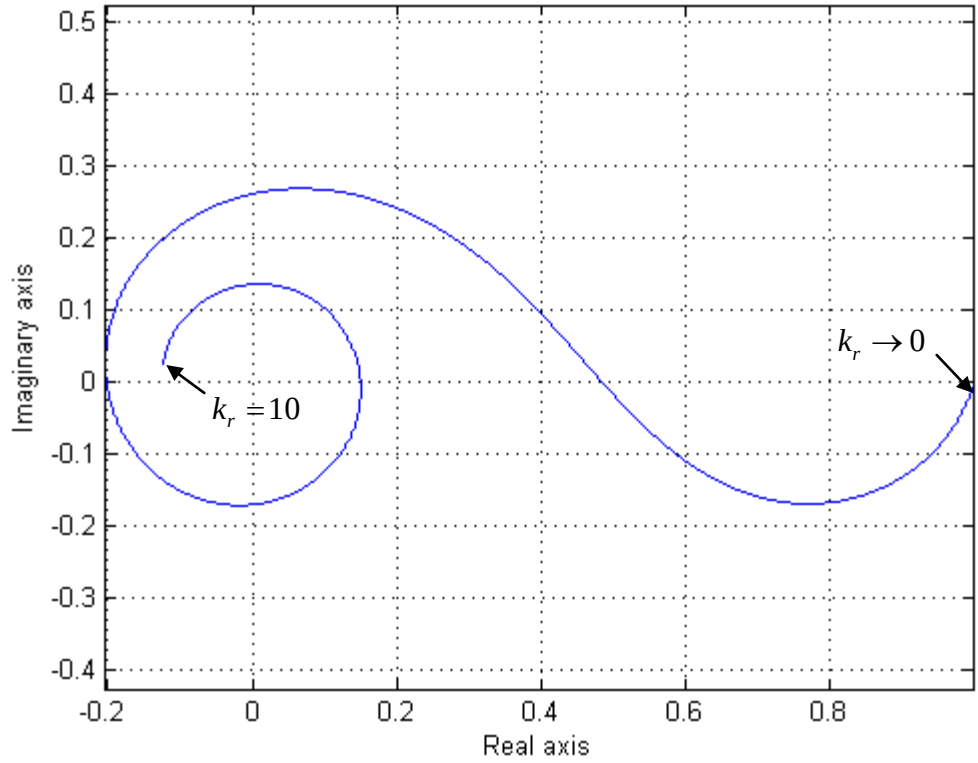


Figure 39: Argand diagram of Sears function, reduced frequency raises from zero to infinite along the complex curve.

If the foil has an angle of attack or performs heaving and/or pitching motion, the problem can be solved using linear superposition and the appropriate terms from (2.84) must be added in (2.86).

Results for the magnitude of $C_L$ for NACA0012 at zero angle of attack with $V_g = 0.05V$ in comparison with linear theory are presented in the following figures.

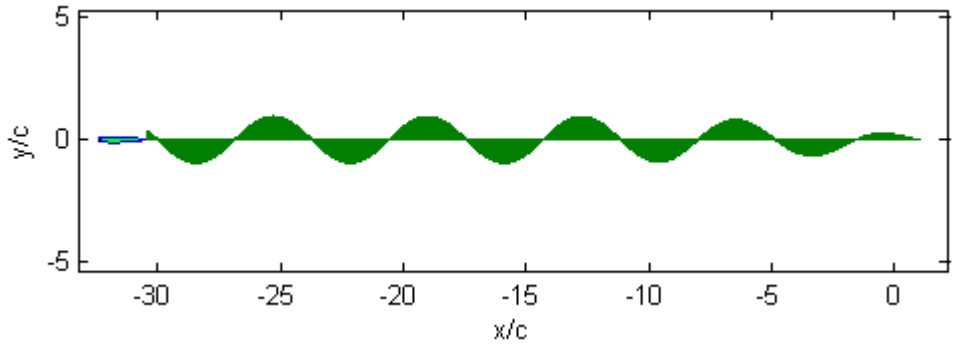


Figure 40: History of dipole intensity on the wake, for a NACA0012 in forward motion with constant speed $U$ and at zero angle of attack, in the presence of a sinusoidal gust with $V_g / U = 0.2$ and $k_{r,g} = 1$.

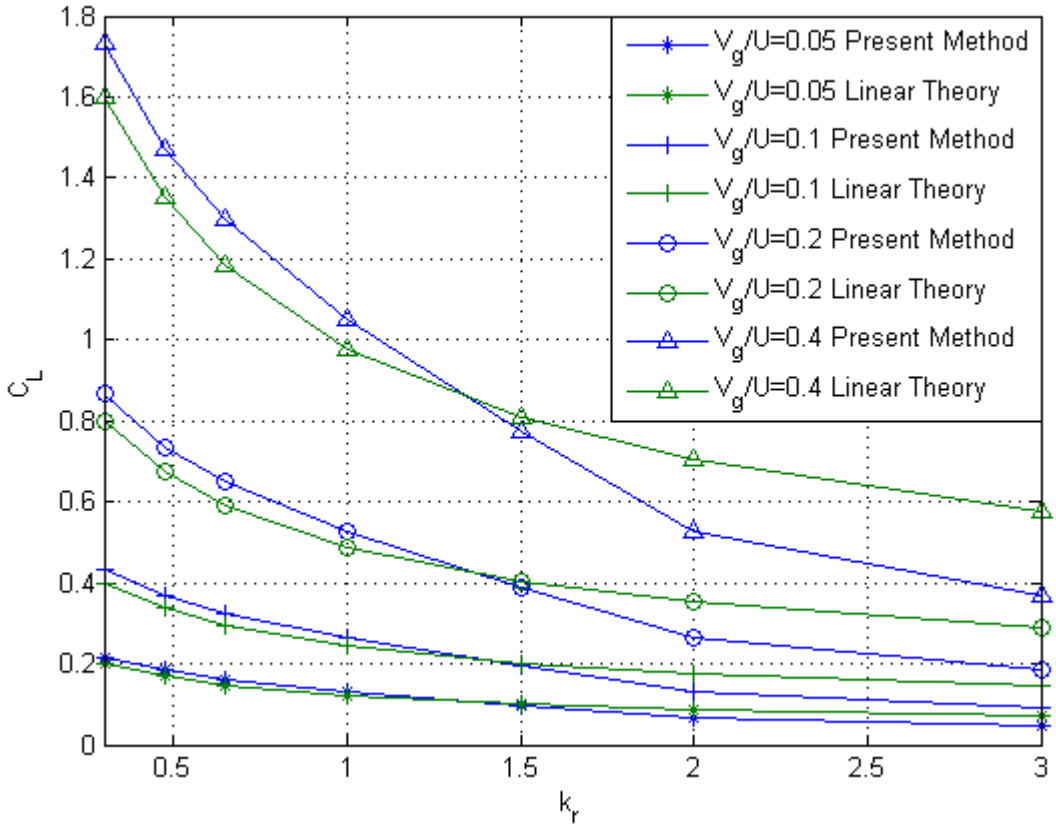


Figure 41: Amplitude of lift coefficient for a NACA0012 in forward motion with constant speed $U$ and at zero angle of attack, in the presence of a sinusoidal gust with $V_g / U = 0.05 \div 0.4$, evaluated by the present method and compared with theoretical asymptotic results.

In Figs. 41 & 42 we present results concerning the amplitude of lift coefficient obtained by the present method compared with predictions by linear thin hydrofoil theory. A symmetrical NACA0012 hydrofoil is performing forward motion with constant speed $U$ and at zero angle of attack, in the presence of a sinusoidal gust with $V_g / U = 0.05 \div 0.4$. Number of panels on hydrofoil's boundary is $N_B = 120$ and $TSR = 0.125$, i.e. one period contains 800 time steps.

We can see that our predictions are in good agreement with thin hydrofoil theory, especially when gust velocity is moderate and small i.e. $V_g / U = 0.05 \div 0.2$ and in small frequencies $k_{r,g} < 1$ for larger velocity amplitudes.

In Figure 42 evolution of $C_L$ is presented for different frequencies corresponding to $k_{r,g} = 0.65,1$ and various gust velocities in the range $V_g / U = 0.05 \div 0.4$. It is demonstrated that present-method predictions concerning phase lag are also in very good agreement with linear theory. According to the above our numerical scheme is accurate for small and moderate gust velocities and compatible with linear potential theory.

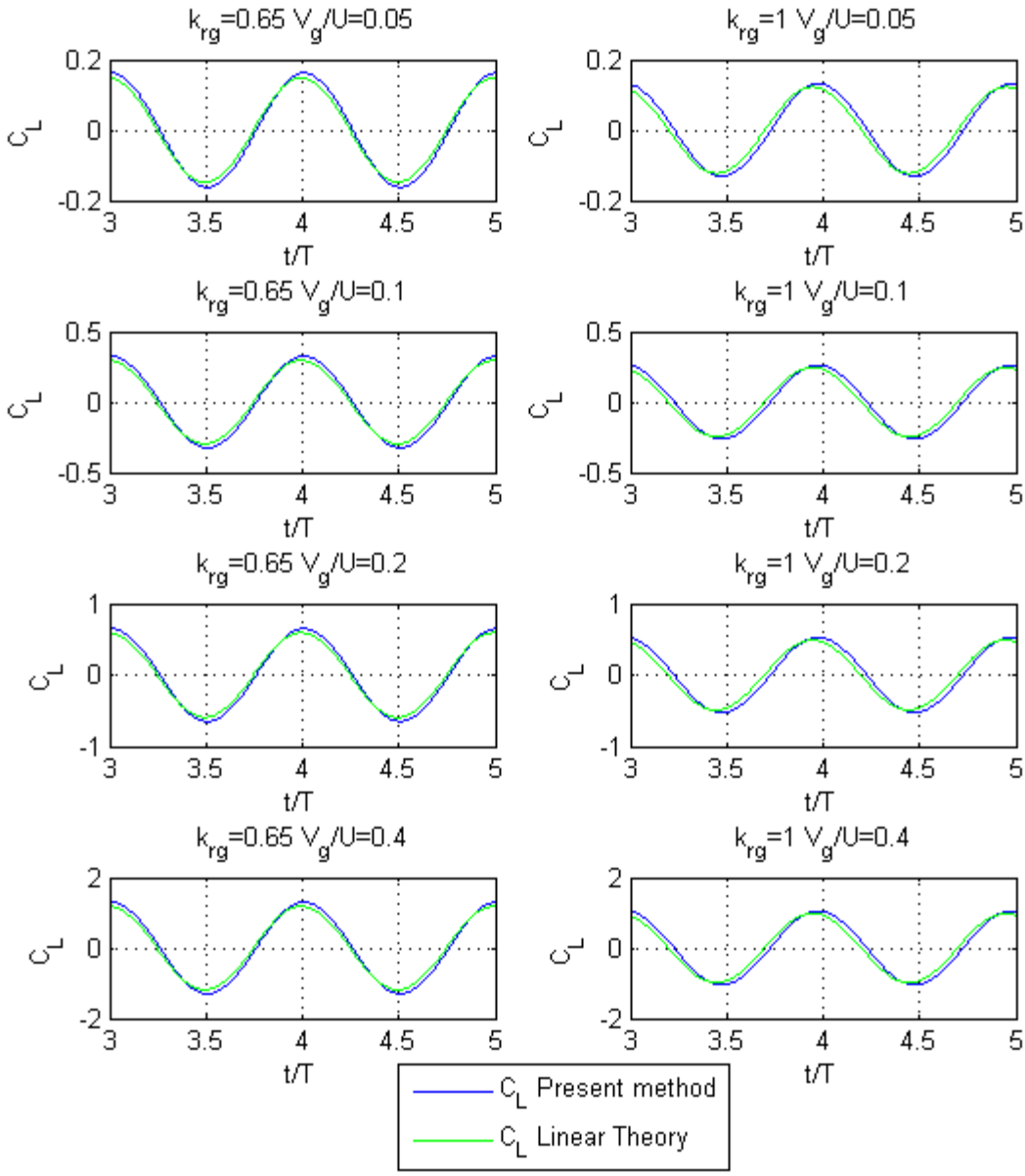


Figure 42: Time history of lift coefficient for a NACA0012 in forward motion with constant speed $U$ and at zero angle of attack, in the presence of a sinusoidal gust with $V_g / U = 0.05 \div 0.4$ and $k_{r,g} = 0.3, 0.475$, evaluated by the present method and compared with theoretical asymptotic results.

## 2.10 Conclusions and suggestions for future work

In the first part of the present thesis an unsteady Boundary Element Method is developed for the general unsteady problem of flow around lifting bodies of general shape in unbounded domain. Also effects of a nonuniform background velocity field (gust) are modeled.

The method is applied to the hydrodynamic analysis of hydrofoils in several conditions as ranging from the simple steady case of cambered hydrofoil in constant angle of attack to the more complex situation of thrust producing flapping hydrofoil and the case of hydrofoil in the presence of a sinusoidal gust. Present work supplements the evidence of previous studies (see Section 1.1) that such biomimetic systems when operate at optimum conditions could achieve high thrust and efficiency levels and maneuvering capacity. Results are obtained, illustrating the numerical performance of the developed BEM and validating its accuracy through comparisons with other methods and experimental data. Numerical predictions include lift and thrust coefficients of the system, over a range of motion parameters, as reduced frequency, Strouhal number, maximum angle of attack.

Future extensions include the introduction and modeling of the non-linear effects of the wake using a free wake model in conjunction with enhanced non-linear pressure-type Kutta condition, in order to achieve better predictions in cases of higher unsteadiness. Furthermore, treatment of leading edge separation and dynamic stall effects would extend method's applicability to operation conditions corresponding to large angles of attack. Also, friction resistance could be taken into account using boundary layer theory and experimental and empirical coefficients, see e.g. Blevins (1984). All the above extensions would provide in the future even better comparison with experimental measurements, and support the derivation of systematic results for the detailed investigation of various arrangements of flapping hydrofoil systems operating in stationary fluid or in nonuniform background fields. Finally, we conclude that the present method, with the appropriate extensions, can serve as a useful tool for assessment and the preliminary design and control of biomimetic systems such as flapping foils for efficient marine propulsion and maneuvering.

# 3 Hydrodynamic analysis of moving non-lifting bodies beneath the free surface

## 3.1 Summary

In this subsection, we concentrate ourselves to the investigation of the hydrodynamic behavior of submerged oscillating bodies. In particular, we study the problem of an oscillating non-lifting body of smooth but arbitrary geometry beneath the free surface. This problem includes as subproblems of special interest the wave resistance problem in the case of a body with constant forward speed and the enforced radiation problem due to body's oscillatory motions. Then in Chapter 4 the whole methodology is extended to the case of unsteady lifting bodies beneath the free surface and in the presence of waves. At first stage of development, we consider moderate submergence and relatively low speeds permitting us to approximately neglect effects due to breaking waves and cavitation. Thus, the amplitude of the free-surface waves is small in comparison with the wave length, in conformity with linear free-surface wave theory. However the motions and the geometry of the body are not linearized. In addition, effect of flat bottom is taken into account. The mathematical formulation is based, again, on potential theory and the problem is treated in the framework of a fast and robust BEM for the numerical estimation of hydrodynamic quantities of interest, as well as the examination of the effects of basic geometrical and physical parameters. Representation theorem is applied on both the free surface and the body boundaries providing us with a Dirichlet-to-Neumann map $(DtN)$ of the boundary values of potential an its normal derivative. That integral map will be used together with the free-surface boundary conditions to construct an integro-differencial equation for the evolution of the dynamical system. A higher order Adams-Bashford-Moulton predictor-corrector method is applied for the solution of the discrete form of the above equation, that is obtained applying a collocation scheme. In addition a Perfectly Matched Layer (PML) model is used for the implementation of conditions at infinity. Finally, stability convergence efficiency of the numerical scheme and the performance of the PML is studied through numerical results concerning the free-surface elevation over a range of parameters including non-dimensional frequency parameter and depth to wave length ratio.

## 3.2 Definition of the Problem

The studied configuration is depicted in Fig. 43. The domain of definition of the problem is an open semi-bounded domain $D \subseteq \mathbb{R}^2$ with boundary $\partial D$ which is supposed to be smooth. The problem is time dependent and the oscillating body is represented by a moving boundary $\partial D_B(t)$ in the earth-fixed frame of reference. The amplitude of the free-surface waves is assumed to be small in comparison with the wave length, permitting, as a first approximation, linearization of the free-surface boundary conditions on the mean level. However, the present analysis could be directly extended to treat the non-linear problem and this task is left as subject for future work. A Cartesian coordinate system is introduced with y-axis pointing upwards and its origin at the point on the mean free surface (y=0).

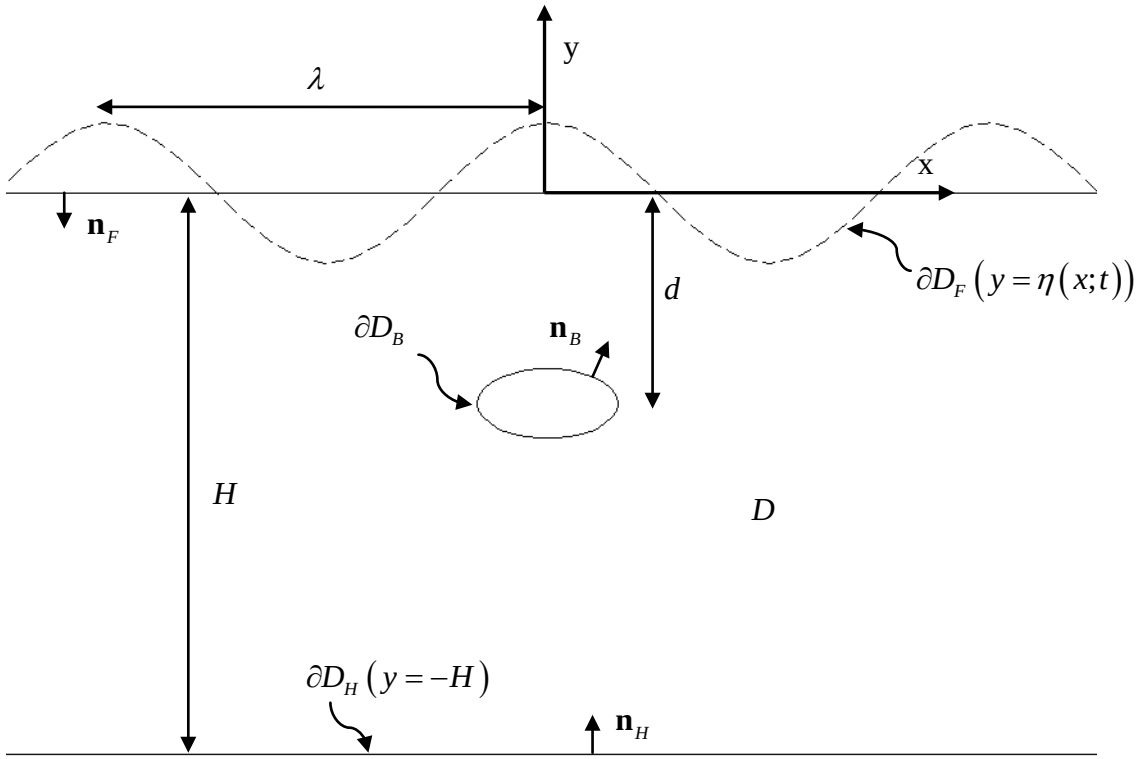


Figure 43: Definition of the studied problem in the case of a non-lifting body oscillating beneath the free surface in mean depth $d$ .

The wave potential $\Phi(x,y;t)$ satisfies the Laplace equation

$$\Delta\Phi(x,y;t)=0\ ,\ (x,y)\in D. \tag{3.1}$$

A Neumann-type, no entrance boundary condition must be satisfied on the body and on the hard bottom

$$\frac{\partial\Phi_B(x,y;t)}{\partial n_B}=\boldsymbol{V}_B(x,y;t)\cdot\boldsymbol{n}_B(x,y;t)\doteq b(x,y;t)\ ,\ (x,y)\in\partial D_B, \tag{3.2}$$

$$\frac{\partial\Phi_H(x,y;t)}{\partial y}=0\ ,\ y=-H, \tag{3.3}$$

where $\mathbf{V}_B$ denotes the general body velocity at $(x_B,y_B)\in\partial D_B$ .

The linearized dynamic and kinematic boundary conditions should be satisfied on the free surface

$$\frac{\partial \Phi_F(x,y;t)}{\partial t} = -g\eta(x;t) \ , \ y=0, \tag{3.4}$$

$$\frac{\partial \Phi_F(x,y;t)}{\partial n} = -\frac{\partial \eta(x;t)}{\partial t} \ , \ y=0, \quad \text{where } \frac{\partial}{\partial n} = -\frac{\partial}{\partial y}. \tag{3.5}$$

The dynamic boundary condition of the free surface (3.4), is similar to the one applied on the free wake of a lifting body examined in Chapter 2, and in the present case, it requires that the hydrodynamic pressure as approaching the free surface equals the atmospheric pressure. This assumption using Bernoulli's theorem and linearization leads to relation (3.4). The kinematic boundary condition (3.5), is also of the same type as the one used in the modeling of the free wake, it necessitates that the normal velocities of the fluid and of the free-surface boundary must be equal and thus $D(y-\eta)/Dt = 0$, where $D/Dt$ is the material derivative. Last relation, after linearization leads to (3.5). For details concerning the linear free-surface wave theory see e.g. Batchelor (1967), Newman (1977), Kundu & Cohen (2004).

We treat the above as an initial value problem and we assume that the potential and its derivatives vanish at large distance from the body

$$\lim_{r\to\infty} \Phi \ \text{ and } \ \nabla\Phi = 0, \qquad r = \sqrt{\left(x-x_B\right)^2 + \left(y-y_B\right)^2}. \tag{3.6}$$

In the above equations indices $\{B,F,H\}$ denote values of the wave field $\Phi(x,y;t)$ on body's contour, on the free surface and the seabed. Furthermore, $\eta(x,t)$ is the free-surface elevation, $g$ is the acceleration of gravity, $\boldsymbol{n}$ is the unit vector normal to the boundary pointing into $D$, $H$ is the constant depth (that could be finite), $d$ is the mean submergence of the body and $\lambda$ is the wavelength of the radiation wave, see Figure 43.

According to the theory of linear systems, the harmonic state (after the full transition from rest) of a linear system, due to harmonic excitation with radial frequency $\omega$, is harmonic oscillatory motion with the same frequency. Knowing the frequency of the responding wave we can evaluate the corresponding wave length using dispersion relation

$$\omega^2 = kg\tanh(kH), \ k = \frac{2\pi}{\lambda}. \tag{3.7}$$

where $k$ is the wave length. In this way, using linear theory an approximate prediction of the wave can be provided.

### 3.3 Boundary integral formulation for non-lifting flows

Applying the representation theorem (Appendix A) to our problem Eqs.(3.1-3.6), concerning a non-lifting body, we obtain the following formula for the evaluation of the potential on points in $D$ from the boundary values of it and its normal derivative on the boundaries

for $(\mathbf{x}_0) \in D$:

$$\Phi(\mathbf{x}_0;t) = \int_{\partial D_B(t)} \underbrace{(\boldsymbol{V}_B \cdot \boldsymbol{n}_B)}_{b(\mathbf{x};t)} G_m(\mathbf{x}_0,\mathbf{x}) - \Phi_B(\mathbf{x};t)\frac{\partial G_m(\mathbf{x}_0\,|\,\mathbf{x})}{\partial n} ds(\mathbf{x}) + \int_{\partial D_F(t)} \frac{\partial \Phi_F(\mathbf{x}_0\,|\,\mathbf{x})}{\partial n} G_m(\mathbf{x}_0\,|\,\mathbf{x}) - \Phi_F(\mathbf{x};t)\frac{\partial G_m(\mathbf{x}_0\,|\,\mathbf{x})}{\partial n} ds(\mathbf{x}). \tag{3.8}$$

In the above relation we have used the Green's function consisted of the singularity/fundamental solution of 2D Laplace equation corresponding to a Rankine source and a regular part corresponding to a mirror source with respect to the bottom $(y=-H)$

$$G_m(\mathbf{x}_0\,|\,\mathbf{x}) = \frac{\ln r(\mathbf{x}_0\,|\,\mathbf{x})}{2\pi} + \frac{\ln r(\mathbf{x}_0\,|\,\mathbf{x}_m)}{2\pi}\ ,\ r(\mathbf{x}_0\,|\,\mathbf{x}) = \left|\mathbf{x}_0 - \mathbf{x}\right|, \tag{3.9}$$

where $\mathbf{x}_0 = (x_0, y_0)$ is the field point, $\mathbf{x} = (x, y)$ is the integration point and $\mathbf{x}_m = (x, -y-2H)$ its image with respect to $\partial D_H$ (Fig. 44). The normal derivative on the boundary is easily derived by differentiating

$$\frac{\partial G_m(\mathbf{x}_0\,|\,\mathbf{x})}{\partial n} = -\frac{1}{2\pi}\frac{\boldsymbol{n}\cdot\boldsymbol{r}(\mathbf{x}_0\,|\,\mathbf{x})}{\left[r(\mathbf{x}_0\,|\,\mathbf{x})\right]^2} - \frac{1}{2\pi}\frac{\boldsymbol{n}\cdot\boldsymbol{r}(\mathbf{x}_{0,m}\,|\,\mathbf{x})}{\left[r(\mathbf{x}_{0,m}\,|\,\mathbf{x})\right]^2}\ ,\ \mathbf{r}(\mathbf{x}_0,\mathbf{x}) = \left\{(x_0 - x) - (y_0 - y)\right\}, \tag{3.10}$$

where $\mathbf{x}_{0,m} = (x_0, -y_0 - 2H)$ is the image of $\mathbf{x}_0 = (x_0, y_0)$ with respect to $\partial D_H$ (Fig. 44). In this way the bottom boundary condition is identically satisfied (Fig. 45) and the corresponding boundary term of the integral representation is dropped.

In a similar way as in Chapter 2, applying the representation theorem (Appendix A) for points at the free surface and the body contour, respectively, we obtain a system of two equations, one for $\Phi_B$ and one for $\Phi_F$, written compactly as follows

$$\frac{1}{2}\Phi_{B/F}(\mathbf{x}_0;t) = \int_{\partial D_B(t)} b(\mathbf{x};t)\, G_m(\mathbf{x}_0,\mathbf{x}) - \Phi_B(\mathbf{x};t)\frac{\partial G_m(\mathbf{x}_0\,|\,\mathbf{x})}{\partial n} ds(\mathbf{x}) + \int_{\partial D_F(t)} \frac{\partial \Phi_F(\mathbf{x}_0\,|\,\mathbf{x})}{\partial n} G_m(\mathbf{x}_0\,|\,\mathbf{x}) - \Phi_F(\mathbf{x};t)\frac{\partial G_m(\mathbf{x}_0\,|\,\mathbf{x})}{\partial n} ds(\mathbf{x}),\ (\mathbf{x}_0) \in \partial D_{B/F}. \tag{3.11}$$

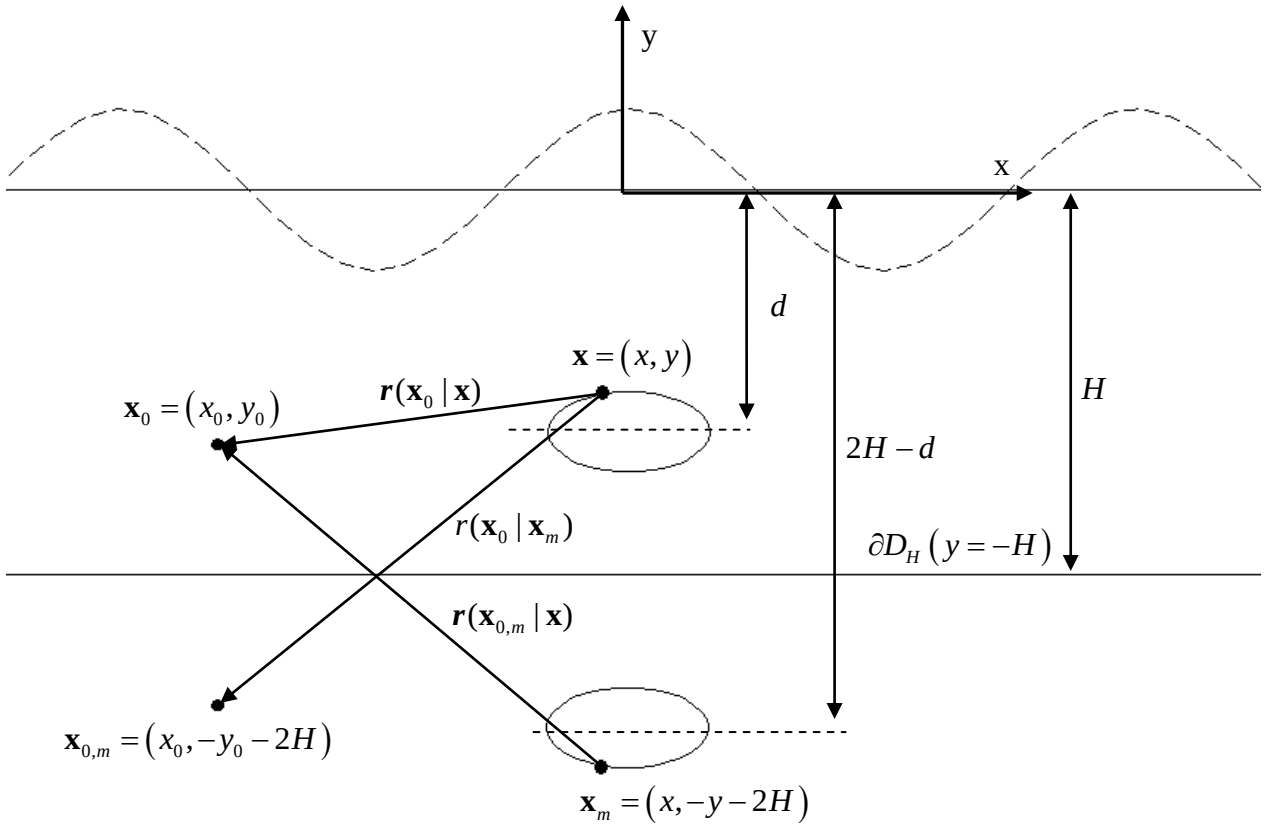


Figure 44: Notation for the definition of flat bottom's partial Green functions using the method of images.

The above relations are weakly singular integral equations for the unknown boundary values of $\Phi$ and $\frac{\partial \Phi}{\partial n}$. In this case the values of the derivative are also not known in the free surface. Eqs.(3.11) will be used to set-up a Dirichlet-to-Neumann map (DtN) of the boundary values $\Phi_B$ and $\Phi_F$ and its normal derivatives. The latter integral map can be used together with the free-surface boundary conditions (3.4) & (3.5), treated as a dynamical system, providing us with an integro-differential equation that governs the evolution of the unknown free surface at the specified level of approximation. In the following section we will apply a collocation scheme and we will describe how numerical solution can be obtained, using the discrete DtN map and the discrete form of the free-surface boundary conditions applied on collocation points.

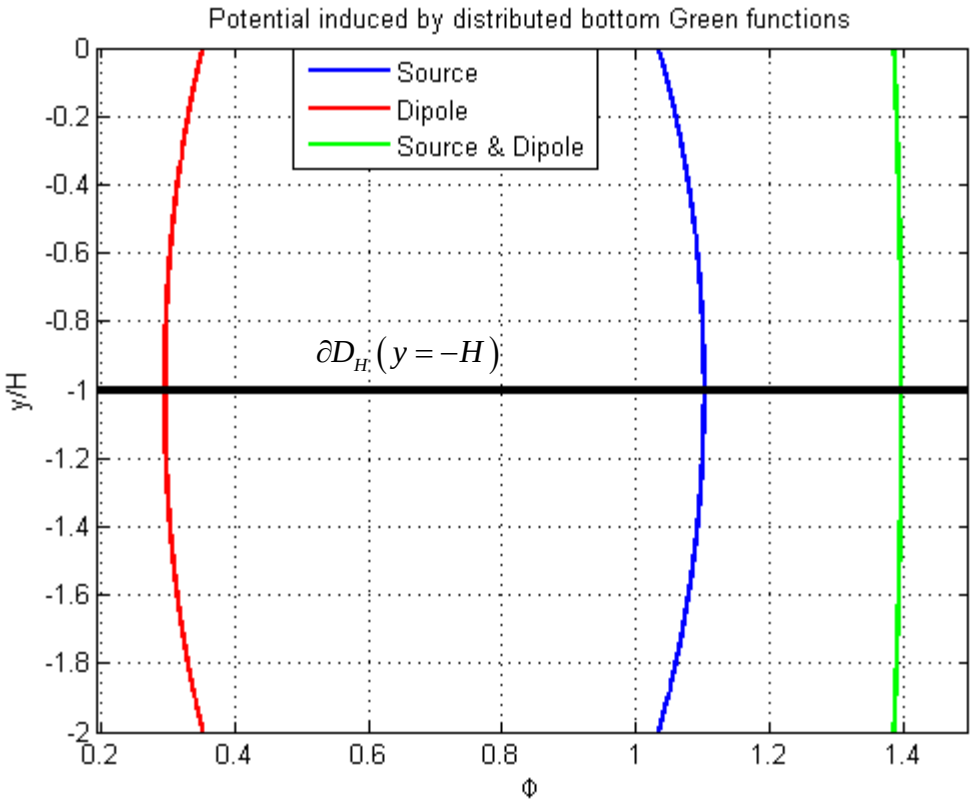


Figure 45: Potential through the seabed, induced by flat bottom Green functions distributed on a panel on the mean free-surface level, at $x \in (-1,1)$, $y = 0$. Notice that the normal to the bottom derivative of potential is zero, i.e. Neumann condition (3.3) is valid by definition.

### 3.4 Construction of the discrete DtN map

Following a low-order panel method, the body contour is replaced by a closed polygonal line (with $N_B$ denoting the number of panels), the free surface is also approximated by $N_F$ straight-line panels. The potential and its normal derivative, at each time step, are approximated by piecewise constant distributions, as follows

$$\Phi_B(x,y;t) = \Phi_{Bi}, \text{ at panel i, i=1,...,N}_B, \tag{3.12}$$

$$\Phi_F(x,y;t) = \Phi_{Fi}, \text{ at panel i, i=1,...N}_{F,} \tag{3.13}$$

$$\frac{\partial \Phi_B(x,y;t)}{\partial n} = \frac{\partial \Phi_{Bi}}{\partial n} = (\boldsymbol{V}_B \cdot \boldsymbol{n}_B)_i = b_i, \text{ at panel i, i=1,...,N}_B, \tag{3.14}$$

$$\frac{\partial \Phi_F(x,y)}{\partial n} = \frac{\partial \Phi_{Fi}}{\partial n}, \text{ at panel i, i=1,...,N}_F, \tag{3.15}$$

Also the free-surface elevation is similarly approximated as

$$\eta(x) = \eta_i, \text{ at panel i, i=1,...,N}_F. \tag{3.16}$$

Applying a collocation scheme, using the center of each panel as collocation point where Eqs.(3.11) are satisfied, the following discretized equations are obtained

$\text{for}\,(x_i, y_i)\ ,\ i = 1,..., N_B$ :

$$\sum_{j=1}^{N_B} \underbrace{\left( \frac{\delta_{ij}}{2} + B_{ij}^m \right)}_{\{a_{11}\}_{ij}} \Phi_{Bj} + \sum_{j=1}^{N_F} \underbrace{\left( -A_{ij}^m \right)}_{\{a_{12}\}_{ij}} \frac{\partial \Phi_{Fj}}{\partial n} = \sum_{j=1}^{N_B} \underbrace{\left( A_{ij}^m \right)}_{\{s_{11}\}_{ij}} \underbrace{\left( \mathbf{V}_B \cdot \mathbf{n} \right)_j}_{b_j} + \sum_{j=1}^{N_F} \underbrace{\left( -B_{ij}^m \right)}_{\{s_{12}\}_{ij}} \Phi_{Fj}, \tag{3.17}$$

$\text{for}\,(x_i, y_i)\ ,\ i = 1,..., N_F$ :

$$\sum_{j=1}^{N_B} \underbrace{\left( B_{ij}^m \right)}_{\{a_{21}\}_{ij}} \Phi_{Bj} + \sum_{j=1}^{N_F} \underbrace{\left( -A_{ij}^m \right)}_{\{a_{22}\}_{ij}} \frac{\partial \Phi_{Fj}}{\partial n} = \sum_{j=1}^{N_B} \underbrace{\left( A_{ij}^m \right)}_{\{s_{21}\}_{ij}} \underbrace{\left( \mathbf{V}_B \cdot \mathbf{n} \right)_j}_{b_j} + \sum_{j=1}^{N_F} \underbrace{\left( -\frac{\delta_{ij}}{2} - B_{ij}^m \right)}_{\{s_{22}\}_{ij}} \Phi_{Fj}, \tag{3.18}$$

where $\delta_{ij}$ is Kronecker's delta. The quantities $A_{ij}^m$ and $B_{ij}^m$ are induced factors and represent the potential at collocation point $i$ due to a unit source or dipole distribution at panel $j$ (taking into account the seabed boundary condition), defined as

$$A_{ij}^m = \int_{panel\ j} G_m(x_i, y_i \mid x_j, y_j) ds(x_j, y_j), \tag{3.19}$$

$$B_{ij}^m = \int_{panel\ j} \frac{\partial G_m(x_i, y_i \mid x_j, y_j)}{\partial n} ds(x_j, y_j). \tag{3.20}$$

As we have seen in Section 2.5, in the case of low order BEMs, the above integrals can be calculated analytically, an example have already been presented in Figure 45.

Equations (3.17) & (3.18) consists a set of $N_B + N_F$ equations which can be written in matrix form:

$$\underbrace{\begin{bmatrix} \{a_{11}\}_{N_B \times N_B} & \{a_{12}\}_{N_B \times N_F} \\ \{a_{21}\}_{N_F \times N_B} & \{a_{22}\}_{N_F \times N_F} \end{bmatrix}}_{A} \begin{bmatrix} \{\Phi_B\}_{N_B \times 1} \\ \left\{ \frac{\partial \Phi_F}{\partial n} \right\}_{N_F \times 1} \end{bmatrix} = \underbrace{\begin{bmatrix} \{s_{11}\}_{N_B \times N_B} & \{s_{12}\}_{N_B \times N_F} \\ \{s_{21}\}_{N_F \times N_B} & \{s_{22}\}_{N_F \times N_F} \end{bmatrix}}_{S} \begin{bmatrix} \{b\}_{N_B \times 1} \\ \{\Phi_F\}_{N_F \times 1} \end{bmatrix}. \tag{3.21}$$

Multiplying the above equation with $\mathbf{A}^{-1}$ we get:

$$\begin{bmatrix} \{\Phi_B\}_{N_B \times 1} \\ \left\{ \frac{\partial \Phi_F}{\partial n} \right\}_{N_F \times 1} \end{bmatrix} = \mathbf{D} \cdot \begin{bmatrix} \{V_B \cdot n_B\}_{N_B \times 1} \\ \{\Phi_F\}_{N_F \times 1} \end{bmatrix} = \begin{bmatrix} \mathbf{D}_{11} & \mathbf{D}_{12} \\ \mathbf{D}_{21} & \mathbf{D}_{22} \end{bmatrix} \begin{bmatrix} \{b\}_{N_B \times 1} \\ \{\Phi_F\}_{N_F \times 1} \end{bmatrix}, \tag{3.22}$$

where $\mathbf{D} = \mathbf{D}(t) = \mathbf{A}^{-1}\mathbf{S}$ is the discrete *DtN* operator which connects at each point on the boundaries $\partial D_B$ and $\partial D_F$ the potential with its normal derivative. We assume that this matrix is invertible. Replacing Eq. (3.22) in the discrete form of the free-surface boundary conditions (3.4) & (3.5)

$$\frac{\partial \Phi_{Fi}}{\partial t} = -g\eta_i \ , \ i = 1,..., N_{F,} \tag{3.23}$$

$$\frac{\partial \eta_i}{\partial t} = -\frac{\partial \Phi_{Fi}}{\partial n} \ , \ i = 1,..., N_F, \tag{3.24}$$

we obtain the following system of ODEs describing the evolution of the discrete system

$$\frac{\partial \mathbf{U}}{\partial t} = \mathbf{f}(\mathbf{U}), \text{ where } \mathbf{U} = \begin{bmatrix} \{\Phi_F\}_{N_F \times 1} \\ \{\eta\}_{N_F \times 1} \end{bmatrix}, \tag{3.25}$$

where the vector function $\mathbf{f}$ is defined as follows

$$\mathbf{f}(\mathbf{U}) = \begin{bmatrix} \mathbf{0} & \mathbf{-gI} \\ \mathbf{-D_{22}} & \mathbf{0} \end{bmatrix} \cdot \mathbf{U} + \begin{bmatrix} \mathbf{0} \\ \mathbf{-D_{21}b} \end{bmatrix}. \tag{3.26}$$

Equation (3.26) can be numerically integrated to calculate current values of $\{\Phi_F, \eta\}$ on the basis of information concerning $\left\{\Phi_B, \Phi_F, \frac{\partial \Phi_B}{\partial n}, \frac{\partial \Phi_F}{\partial n}, \eta\right\}$ at previous time steps. Subsequently, the *DtN* map (3.22) is used to calculate $\left\{\Phi_B, \frac{\partial \Phi_F}{\partial n}\right\}$. Recall that $\left\{\frac{\partial \Phi_B}{\partial n}\right\} = \{b\}$ is known at every time step from no entrance boundary condition.

### 3.5 Numerical time-integration of the system

Starting from an prescribed initial condition e.g. from the rest, a time step method can be applied to obtain the solution. After the evaluation of different methods we have found that a higher order Adams-Bashford-Moulton predictor-corrector method provides the required accuracy, stability and efficiency; see also Longuet-Higgins-Cokelet (1976) and Johannessen & Swan (1997). The used system requires calculation of only two derivative equations at each time-step, while other single step methods requires one evaluation per order of accuracy. The error associated with this scheme is of order $\left(\Delta t^5\right)$ where $\Delta t$ is the time step, ensuring that quick convergence is achieved.

To be more precise, if we know $\mathbf{U}(t)$ we have at the corrector step

$$\mathbf{U}(t+\Delta t)=\mathbf{U}(t)+\frac{\Delta t}{24}\left[9\mathbf{f}_{pre}(t+\Delta t)+19\mathbf{f}(t)-5\mathbf{f}(t-\Delta t)+\mathbf{f}(t-2\Delta t)\right], \tag{3.27}$$

with predictor

$$\mathbf{f}_{pre}(t+\Delta t)=\mathbf{f}_{t+\Delta t}\left(\mathbf{U}_{pre}(t+\Delta t)\right), \tag{3.28}$$

where

$$\mathbf{U}_{pre}(t+\Delta t)=\mathbf{U}(t)+\frac{\Delta t}{24}\left[55\mathbf{f}(t)-59\mathbf{f}(t-\Delta t)+37\mathbf{f}(t-2\Delta t)-9\mathbf{f}(t-3\Delta t)\right]. \tag{3.29}$$

Notice that, the calculation of $\mathbf{U}$ at time step $t+\Delta t$ requires the values of derivatives $\frac{\partial \mathbf{U}}{\partial t}$ evaluated at three time steps in the past and a prediction of $\frac{\partial \mathbf{U}}{\partial t}$ at the future time step. For the last one we use $\mathbf{U}_{pre}$ from equation (3.29) and equation (3.26) with the DtN map at the future time step, as the index in (3.28) denotes, which can be calculated because the motion of the foil is prescribed.

In the following, we will present two examples of calculation, relevant with two problems of special interest for Offshore and Marine Engineering. First of all, the wave generation due to an oscillating non-lifting body in prescribed motion, i.e. the enforced radiation problem is considered. Subsequently, the wave generation due to a hydrodynamically shaped body, moving with constant speed beneath the free surface, i.e. the wave resistance problem is studied.

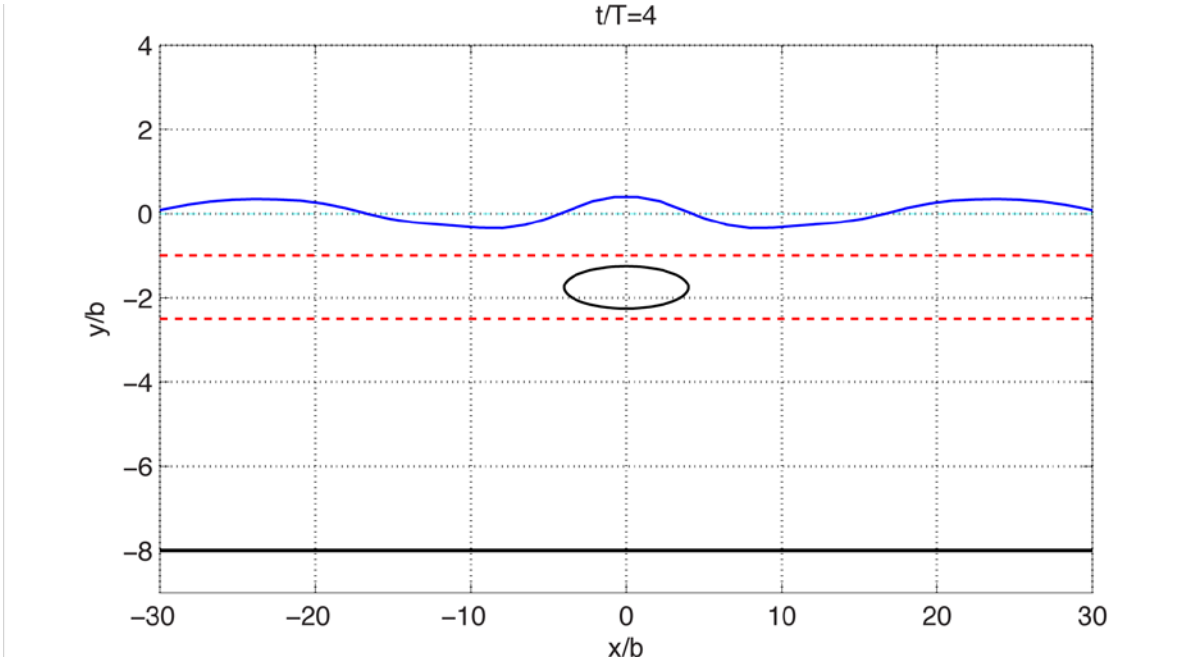


Figure 46: Radiation problem. Free-surface elevation generated by large amplitude oscillations of an elliptically shaped, fully immersed body at $\omega^2 \mathrm{H}/g = 1.63$. The upper and lower limit of heaving motion are shown using dashed lines.

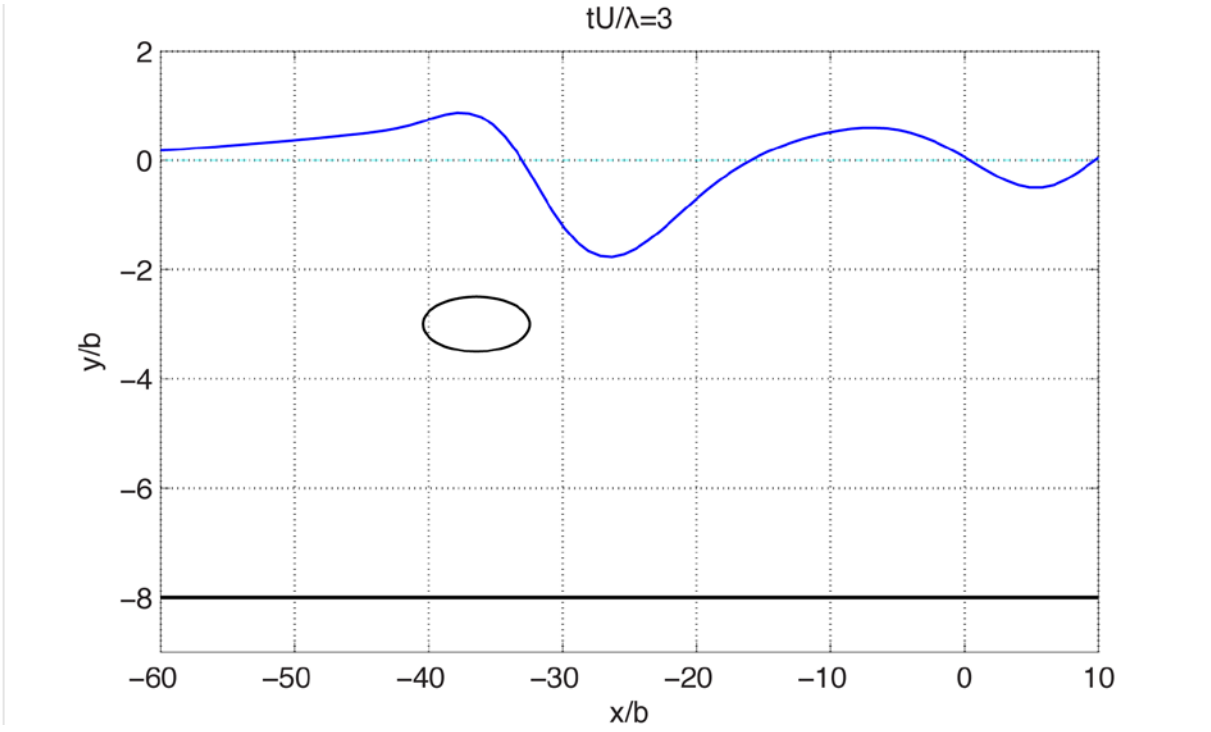


Figure 47: Wave resistance problem. Free-surface elevation generated by forward motion of an elliptically shaped, fully immersed body at $Fn = U/\sqrt{ga} = 1$.

To proceed, we present in Figs. 46 and 48 the calculated free-surface elevation in the case of an elliptically-shaped, fully immersed body of axis ratio $a/b=8$ (where $a$ is the length and $b$ the height of the body), performing oscillations in heaving motion with large amplitude $h/b=0.25$, in water of dept $H/b=8$, after 4 periods starting from rest. The mean submergence is $d/b=1.75$ and thus, the vertical oscillation is limited in the interval $-2.5<y/b<-1$, shown using dashed lines in Fig.46. In the examined case the frequency parameter is $\omega^2 \mathrm{H}/g=1.63$ corresponding to intermediate wave conditions $H/\lambda=0.27$, where H is water depth and $\lambda$ the wavelength of free waves in the water strip at the examined frequency predicted by linear theory Eq. (3.7). Furthermore, the time history of calculated free-surface elevation is plotted in Fig.48 for all over the horizontal domain for the first 4 periods of oscillation starting from rest. We clearly observe the generation of symmetrical waves propagating to both directions with phase speed $C$ in compatibility with linearized theory.

The free surface elevation for another example is presented in Figure 47 and 49. In that case, the same elliptical body performs forward motion with constant speed $U$, and corresponding Froude number $Fn=U/\sqrt{ga}=1$, submergence $d/b=3$, in water of dept $H/b=8$ and corresponding bathymetric Froude number $Fn_H=U/\sqrt{gH}=0.71$, starting from rest. The depth is intermediate with $H/\lambda=0.33$, where $\lambda$ is the wavelength of free waves in the water strip at the examined velocity predicted by linear theory, $U^2=g/k\tanh(kH)$, $k=2\pi/\lambda$. Furthermore, the time history of calculated free-surface elevation is plotted in Fig.49 all over the horizontal domain and from $t=0$ to $t=3\lambda/U$. We clearly observe the generation of a trough over the high pressure region near the bow, followed by a crest. The main wave is propagating with phase speed $U$, in compatibility with linearized theory.

Stability and convergence of the present scheme has been studied by extensive numerical investigation in cases of oscillatory motion with respect to both degrees of freedom (heave, pitch), as well as in cases of to steady forward motion. The above analysis results in that a minimum number of $N_F=25$ panels per wavelength on the free surface is required, while for harmonic motion the time step must be $\Delta t<0.04T$ (4 % of the period of oscillation). Numerical stability is achieved when a of Courant-Friedrichs-Lewy (CFL-type) condition is satisfied, as follows

$$\frac{C\Delta t}{\Delta x}\ll 1, \tag{3.30}$$

where C is the celerity of the generated free-surface waves. The exact critical value is frequency dependent and it is smaller for lower frequencies, it is also a function of Froude number in the case where forward motion dominates.

In the previous example we did not left the radiation wave field to reach at the limits of the domain and thus we obtained natural solutions that were not affected by reflection on the end of truncated domain. An important task concerning the present time-domain scheme deals with the treatment of infinite domain and the implementation of appropriate radiation-type conditions at infinity.

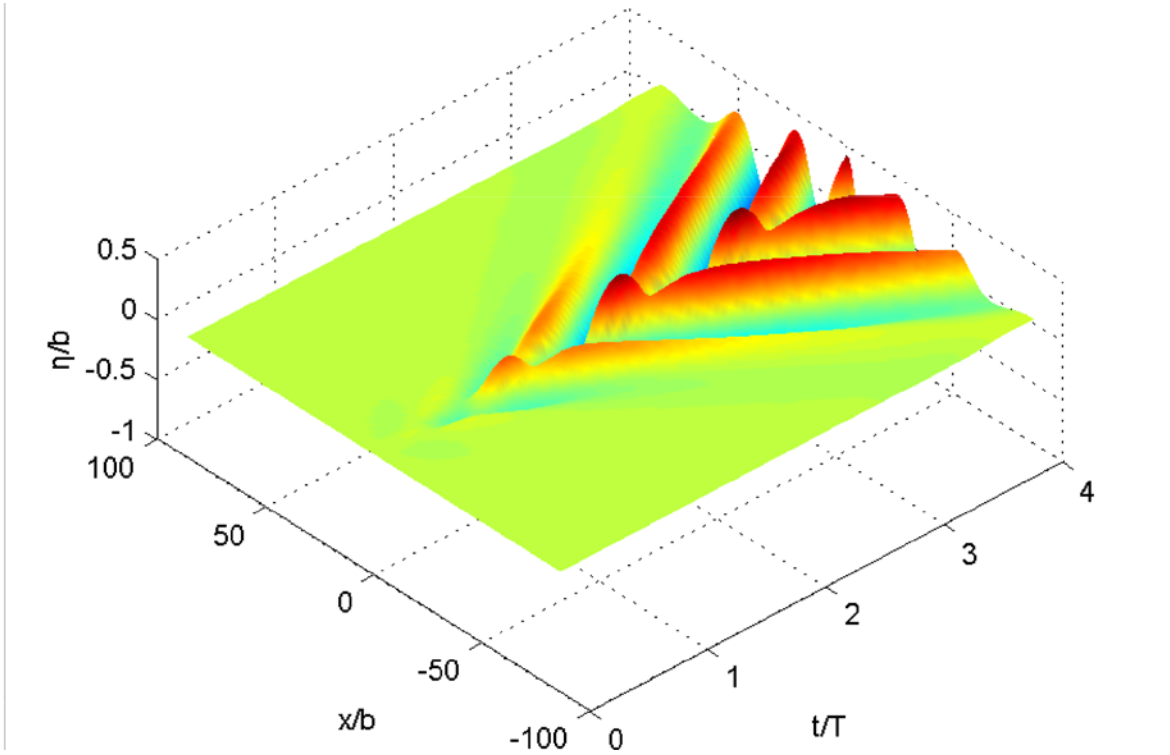


Figure 48. Time history of free surface for the example of Fig. 46.

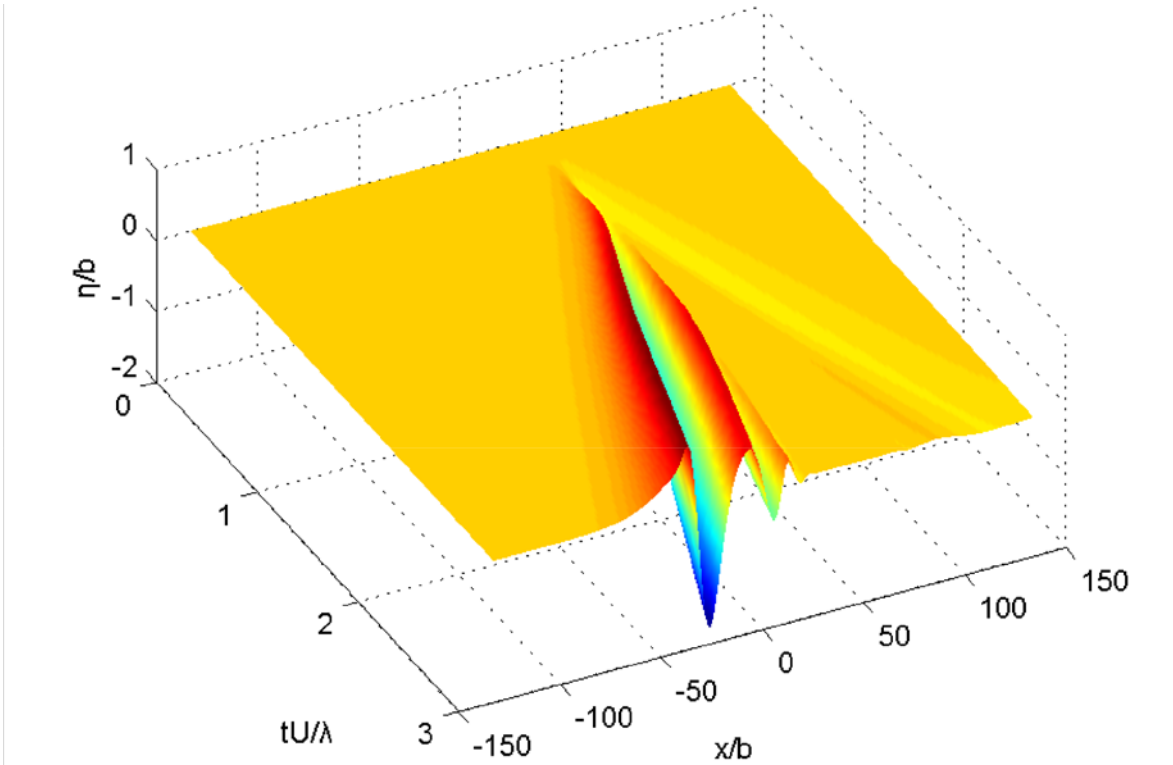


Figure 49. Time history of free surface for the example of Fig. 47.

### 3.6 Conditions at infinity - Implementation of PML model

Although in the case of purely linear waves, conditions at infinity could be treated by using the appropriate time-dependent Green function, the present work is based on the truncation of the domain and on the implementation of Perfectly Matched Layer (PML) model, as e.g. described by Berenger (1994) and Turkel & Yefet (1998). The latter model permits the numerical absorption of the waves reaching the left $(x=a)$ and right $(x=b)$ termination ends of the truncated domain with minimum reflection. This selection is motivated by the fact that PML model supports the efficient extension of the present numerical scheme to treat generation and propagation of nonlinear waves excited due to large motion(s) of floating body at low submergence depths; see also Belibassakis and Athanassoulis (2011). Such an extension is left to be the subject of future work.

In order to apply the above PML-type absorbing layer the time-derivative operator in the left hand-side of (3.25) is substituted by the following mixed-type operator:

$$\frac{d\mathbf{U}}{dt}+\sigma(x)\mathbf{U}=f(\mathbf{U}), \tag{3.31}$$

where the PML-parameter $\sigma(x)$ is a positive absorption coefficient with support extended over several wavelengths from the artificial end-type boundaries $(x=a, x=b)$ used to truncate the computational domain. In the present work we use selection of the PML coefficients, as described by Collino and Monk (1998) and applied by Belibassakis et al (2001) and Belibassakis and Athanassoulis (2011) to water wave problems. In accordance with the previous works the optimum distribution of the absorption coefficient is of the form:

$$\sigma(x)=\begin{cases} \sigma_0\left|\dfrac{x-a-l}{l}\right|^p, & if\ x<a+l \\ 0, & if\ a+l<x<b-l, \\ \sigma_0\left|\dfrac{x-b+l}{l}\right|^p, & if\ x>b-l \end{cases} \tag{3.32}$$

where $\sigma_0$ is a positive parameter controlling the magnitude of the $\sigma(x)$ distribution, $l$ adjusts the support of $\sigma(x)$ and is comparable to the characteristic wave length of the generated wave and $p$ is a positive parameter that controls the rate of absorption in the PML.

To investigate the performance of the PML we used the example of Figs.46 and 48 of an elliptically-shaped body of axis ratio $a/b=8$, performing heaving oscillations with large amplitude $h/b=0.25$, in water of dept $H/b=8$. The mean submergence is $d/b=1.75$ and the vertical oscillation is limited in the interval $-2.5<y/b<-1$. The frequency parameter varies $\Omega=\omega^2\mathrm{H}/g=0.41\div6.5$ corresponding to wave conditions $H/\lambda=10\%\div103\%$.

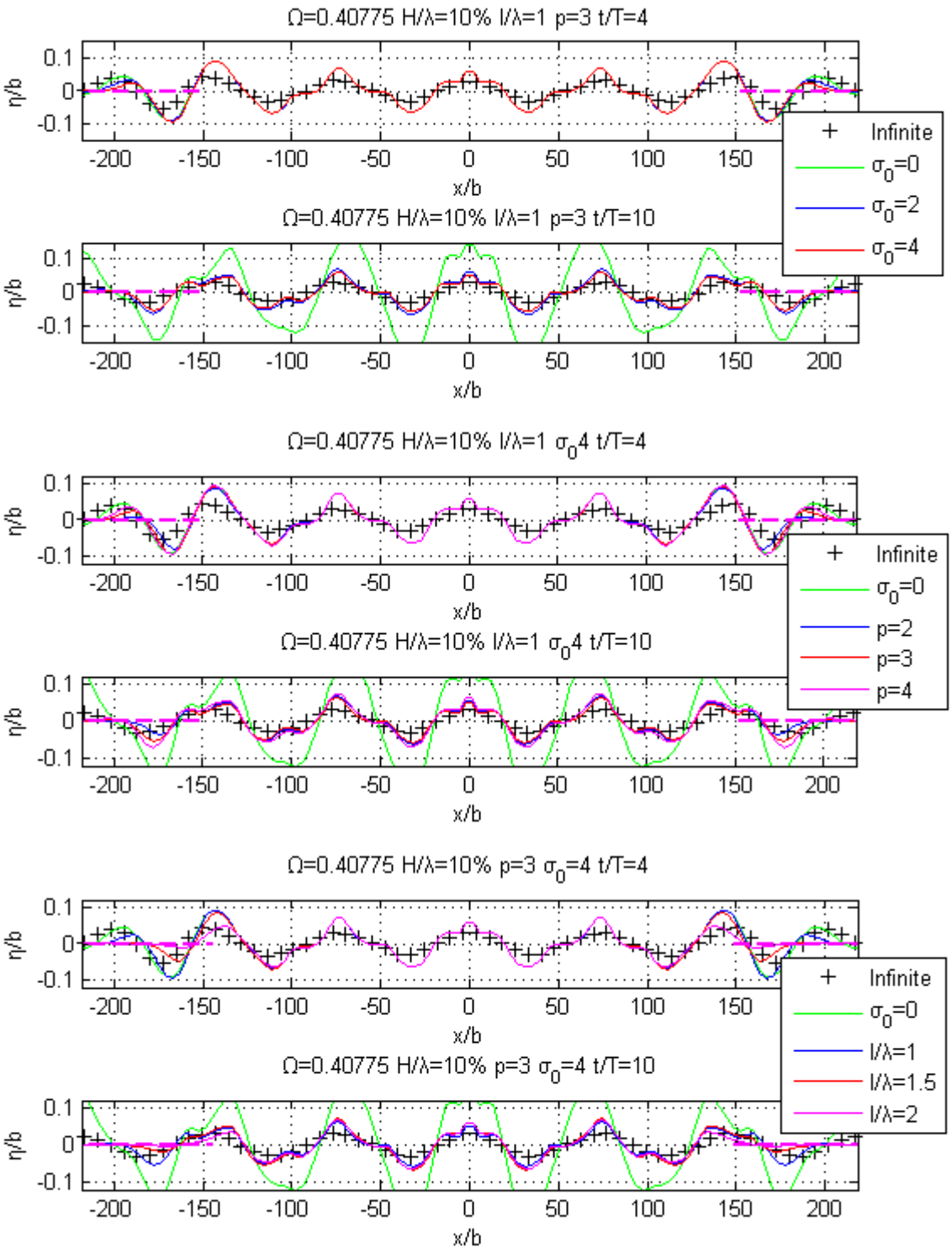


Figure 50: Implementation of the PML for $\omega^2 \mathrm{H}/g = 0.41$ & $\mathrm{H}/\lambda = 10\%$. The position of PML is indicated by magenta dashed lines.

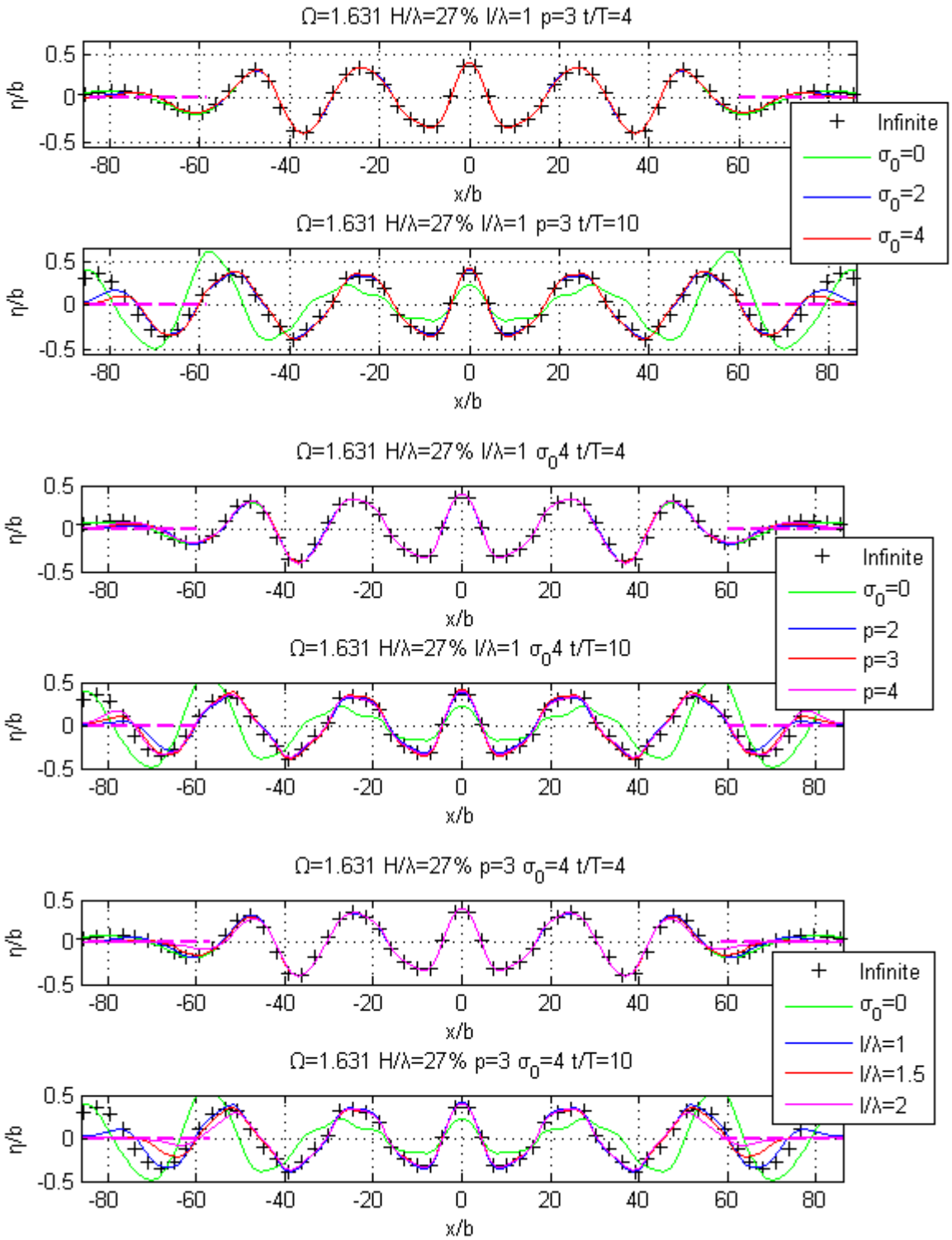


Figure 51: Implementation of the PML for $\omega^2 H / g = 1.63$ & $H / \lambda = 27\%$. The position of PML is indicated by magenta dashed lines.

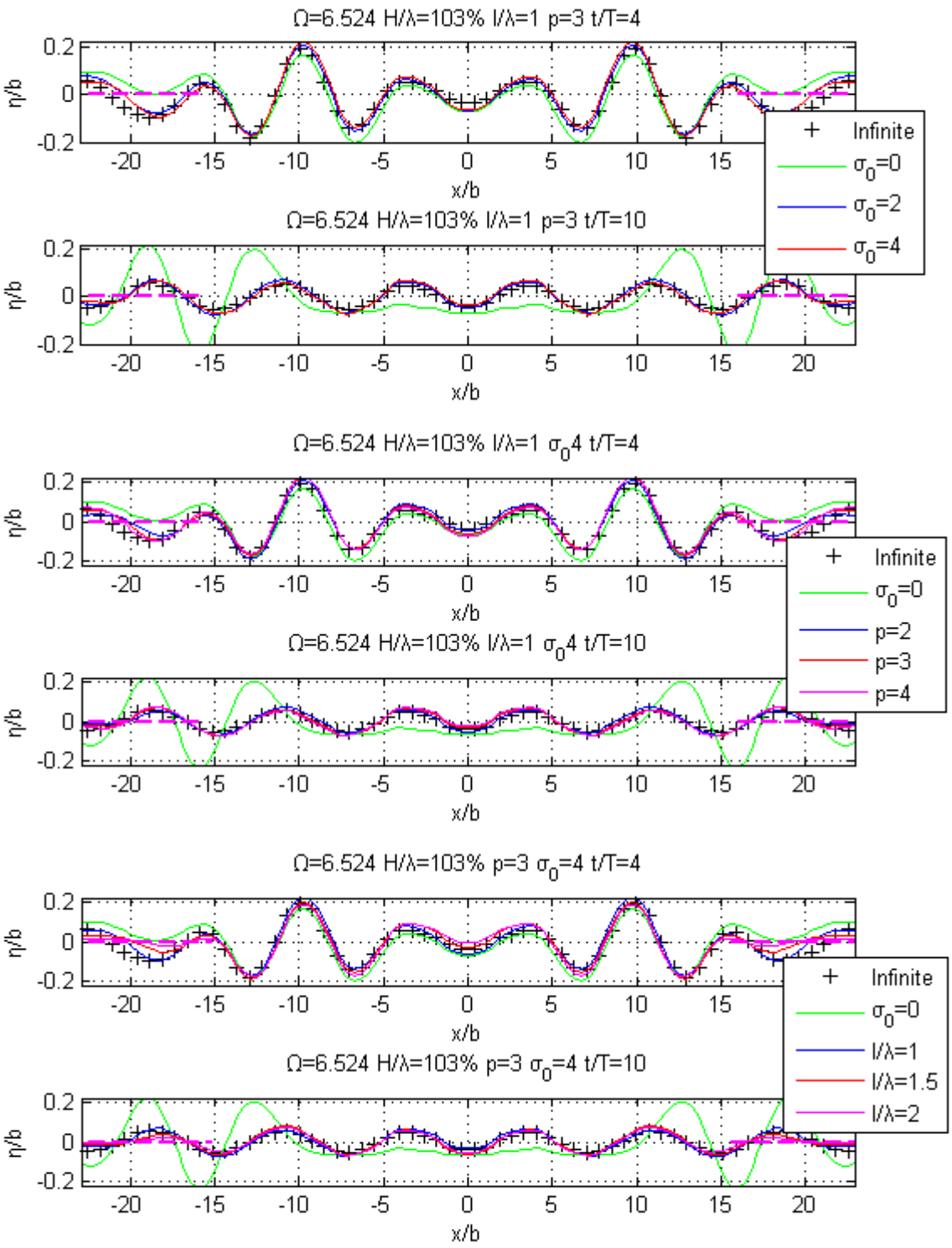


Figure 52: Implementation of the PML for $\omega^2 H / g = 6.52$ & $H / \lambda = 103\%$. The position of PML is indicated by magenta dashed lines.

For these cases of moderate and deep water, we present in Figs. 50-53 the performance of the PML model, with parameters $l/\lambda = 1, 1.5, 2$, $p = 2, 3, 4$ and $\sigma_0 = 2, 4$. In particular, the calculated free-surface elevation after 4 and 8 periods is plotted in the upper and lower subplots, as obtained by using the absorbing layer. In addition, in the same figure the previous results are compared against a reference numerical solution (indicated by crosses) obtained by using a very long (characterized as infinite) computational domain ensuring that the generated wave disturbance has not reached its horizontal ends at the two times considered $t/T = 4 \& 8$. In order to punctuate the importance of PML in truncated domains, a solution with $\sigma_0 = 0$ were added in every plot, leading to denaturized free-surface elevations due to reflection. We clearly observe in the above Figs. that the wave decays within the PML while the numerical solution remains in very good compatibility to the reference solution outside the absorbing layer. Based on extensive numerical evidence we conclude that the following PML parameters are suitable for the studied problem: $\ell/\lambda = 1 \div 2$, $p = 2 \div 4$ and $\sigma_0 = 2 \div 4$.

### 3.7 Conclusions and suggestions for future work

An unsteady potential-based Boundary Element Method is developed and applied to the analysis of translating and oscillating non-lifting bodies operating beneath the free surface at prescribed motion. The modeling includes finite-depth effects. The potential representation theorem is applied to the body contour and the free surface for the construction of a *DtN* map that connects Dirichlet to Neumann boundary data of the potential. The latter map is applied to formulate the free surface boundary conditions with respect to the dynamical variables leading to set of ODEs. The solution of the dynamical system is obtained by means of a higher order Adams-Bashford-Moulton predictor-corrector scheme. For the implementation of conditions at infinity the domain is truncated and the PML model is applied to absorb the waves reaching the ends with minimum reflection. The performance of the PML in the present problem is numerically studied by simulations and the appropriate values of its numerical parameters were identified.

The present study is concentrated on the modeling of free surface and finite depth, whose effects for relatively low submergence and depth, respectively, could become quite important. We examined problems of enforced radiation due to oscillating non-lifting bodies of arbitrary geometry and the wave resistance of non-lifting bodies advancing with constant forward speed. Results were shown illustrating the numerical performance of the developed BEM. Numerical predictions are presented demonstrating the evolution of free-surface elevation over a range of motion parameters, such as non-dimensional frequency for the radiation and Froude number & bathymetric Froude number for the wave resistance problem, in moderate and deep water.

Future extensions and enhancements include the introduction and modeling of non-linear free-surface boundary conditions, effects of shallow water and also non-uniform bathymetry, for the study of engineering applications near the coastal zone. The first one can be done quite straightforward due to the choice of truncation of the domain and the implementation of condition at infinity with the absorbing layer model.

# 4 Hydrodynamic analysis of lifting bodies beneath the free surface and in waves

## 4.1 Summary

In the final section, the problem of unsteady lifting bodies beneath the free surface and in waves is considered. That problem have been also studied, using extended Theodorsen's and Sears's unsteady linear hydrofoil theory (Newman, 1977), by Grue & Palm (1988). For the detailed investigation of the effects of free surface on the unsteady-body hydrodynamics, the potential based panel method, that has been developed in the first chapter for lifting bodies in unbounded domain and in the second for non-lifting bodies beneath the free surface, is extended in order to treat the more complex problem of unsteady 2D lifting bodies operating beneath the free surface in the presence of incoming waves. In the same way as in previous chapters, we consider moderate submergence and relatively low speeds permitting us to approximately neglect effects due to breaking waves and cavitation. However, no linearization has been applied on the motions and the geometry of the body. We begin with the definition of the problem and the derivation of the Boundary Integral Equation on the free surface and on the body contour. Thereafter, we present the construction of the discrete $DtN$ map and the solution of the free-surface boundary conditions that describe the evolution of the dynamical system. Finally, an appropriate form of Bernoulli's theorem is derived for the calculation of pressure boundary values on the body. Numerical performance of the scheme is tested through plenty simulations concerning the thrust coefficient and the efficiency of the system over a range of motion parameters, including Froude number, non dimensional submergence of the body and bathymetry, reduced frequency, Strouhal number, feathering parameter. Results are compared against corresponding calculations in infinite fluid. Also, comparisons against other methods are presented and discussed. Our results indicate that good performance can be obtained under optimal operating conditions. Moreover, the free-surface effects are important for moderated to large Froude numbers and low submergence and have to be taken into account. Thus, the present method after enhancements can serve as a useful tool for assessment and the preliminary design and control of such systems extracting energy from sea waves for marine propulsion.

## 4.2 Formulation of the problem

Consider a 2D lifting body, e.g. a hydrofoil operating in unsteady motion beneath the free surface and in the presence of incoming waves (Figure 53). The domain of definition of the problem is an open semi-bounded domain $D \subseteq \mathbb{R}^2$ with smooth boundary $\partial D$. The problem is time dependent and the oscillating body is represented by a moving boundary $\partial D_B(t)$ in the earth-fixed frame of reference. The amplitude of the free-surface waves is assumed to be small in comparison with the wave length permitting as a first approximation, linearization of the free-surface boundary conditions on the mean free-surface level (shown in Fig.53 using a dashed line). However, the present analysis could be directly extended to treat the non-linear problem and this task is left to be subject for future work. A Cartesian coordinate system is introduced with y-axis pointing upwards and tits origin at the point on the mean free surface ($y$=0).

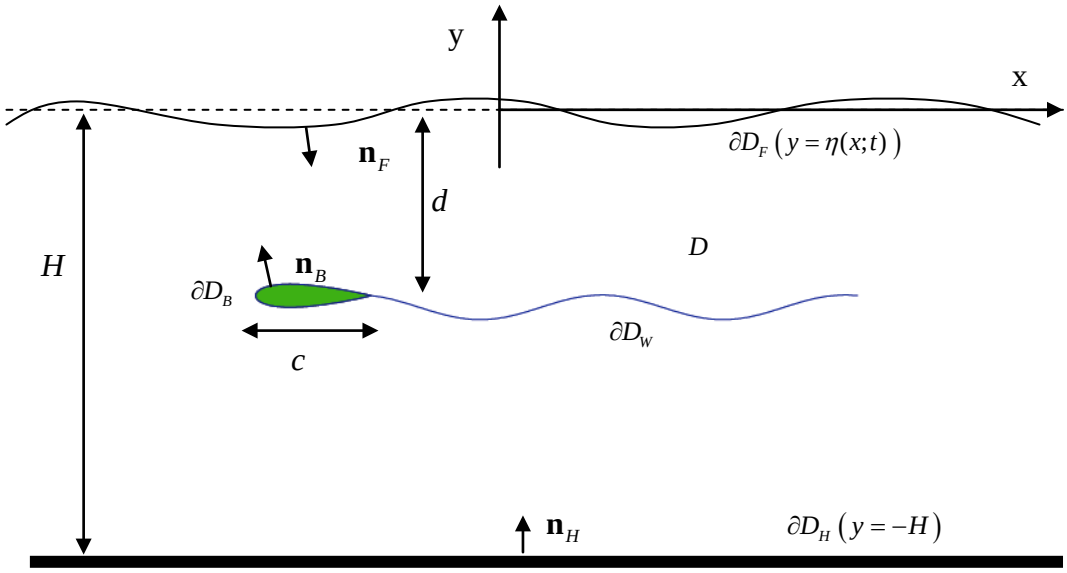


Figure 53: Definition of the studied problem in the case of hydrofoil (of chord $c$) moving under the free surface (at mean submergence $d$)

Let $\Phi_T(x,y;t)$ the total wave potential that consists of the incident wave potential $\Phi_I(x,y;t)$ which is assumed to be known and the disturbance potential $\Phi(x,y;t)$ which can be decomposed to the enforced radiation and the diffraction potential field. Also, $\eta(x;t)$ denotes the free-surface elevation associated with the disturbance field, $g$ the acceleration of gravity, $H$ the constant depth, $d$ the mean submergence of the body, $\boldsymbol{V}_B$ the body's motion derivative and $\boldsymbol{V}_I = \nabla\Phi_I$ the derivative of the incident wave field. Finally, $\boldsymbol{n}$ denotes the unit normal vector pointing into the interior of $D$.

The non-lifting part of the problem is written (as we have discuss in the previous chapter) for the total wave potential as follows

$$\Delta\Phi_T(x,y;t) = 0 \ , \ (x,y) \in D, \tag{4.1}$$

$$\frac{\partial\Phi_T(x,y;t)}{\partial n_B} = \boldsymbol{V}_B \cdot \boldsymbol{n}_B \ , \ (x,y) \in \partial D_B, \tag{4.2}$$

$$\frac{\partial\Phi_T(x,y;t)}{\partial y} = 0 \ , \ y = -H, \tag{4.3}$$

$$\frac{\partial\Phi_T(x,y;t)}{\partial t} = -g\eta_T(x;t) \ , \quad \text{on} \ \ y = 0, \tag{4.4}$$

$$\frac{\partial\Phi_T(x,y;t)}{\partial n} = -\frac{\partial\eta_T(x;t)}{\partial t} \ , \ y = 0, \tag{4.5}$$

$$\lim_{x\to\pm\infty}\Phi_T=\Phi_I \text{ and } \lim_{x\to\pm\infty}\nabla\Phi_T=\nabla\Phi_I. \tag{4.6}$$

The governing equation is Laplace equation (4.1), supplemented by the body boundary condition (4.2) and the hard bottom no-entrance boundary condition (4.3). The linearized dynamic (4.4) and kinematic (4.5) boundary conditions are satisfied on the mean free surface. We treat the above as an initial value problem and we the disturbance potential and its derivatives vanish at large distance from the body (4.6).

Furthermore, we assume that the incident wave field $\Phi_I$ is a harmonic function that satisfies the equations of the linear free-surface boundary value problem with the absence of the body i.e. Eqs. (4.1), (4.3), (4.4), (4.5), hold for $\Phi_I$ too. Thus, the disturbance wave potential must satisfy the following equations:

$$\Delta\Phi(x,y;t)=0 \ , \ (x,y)\in D, \tag{4.7}$$

$$\frac{\partial\Phi_B(x,y;t)}{\partial n_B}=\left[\boldsymbol{V}_B\left(x,y;t\right)-\boldsymbol{V}_I\left(x,y;t\right)\right]\cdot\boldsymbol{n}_B\left(x,y;t\right)\doteq b\left(x,y;t\right) \ , \ (x,y)\in\partial D_B, \tag{4.8}$$

$$\frac{\partial\Phi_H(x,y;t)}{\partial y}=0 \ , \ y=-H, \tag{4.9}$$

$$\frac{\partial\Phi_F(x,y;t)}{\partial t}=-g\eta(x;t) \ , \quad \text{on} \ \ y=0, \tag{4.10}$$

$$\frac{\partial\Phi_F(x,y;t)}{\partial n}=-\frac{\partial\eta(x;t)}{\partial t} \ , \ y=0, \tag{4.11}$$

$$\lim_{x\to\pm\infty}\Phi \text{ and } \nabla\Phi=0. \tag{4.12}$$

Moreover, in the case of lifting flows around sharp-ended bodies like a hydrofoil, the problem is supplemented by the following equations

$$\lim_{(x,y)\to(x_{TE},y_{TE})}\left(\Phi_B^u-\Phi_B^l\right)=\mu_W(x_{TE},y_{TE}) \ , \ (x,y)\in\partial D_B, \tag{4.13}$$

$$p_W^u(x,y;t)=p_W^l(x,y;t) \ , \ (x,y)\in\partial D_W, \tag{4.14}$$

$$\frac{\partial\Phi_W^u(x,y;t)}{\partial n_w}=\frac{\partial\Phi_W^l(x,y;t)}{\partial n_w} \ , \ (x,y)\in\partial D_W, \tag{4.15}$$

$$\frac{D\mu_W\left(x,y;t\right)}{Dt}=0, \quad (x,y)\in\partial D_W. \tag{4.16}$$

The indices $\{B,H,F,W\}$ are used to denote values of the disturbance field $\Phi(x,y;t)$ on the body surface, the seabed, on the free surface and the wake of the hydrofoil, respectively and $\mu_W = \Phi_W^u - \Phi_W^l$ denotes the potential jump (the dipole intensity) on the free wake and $\frac{D}{Dt} = \frac{\partial}{\partial t} + \boldsymbol{V}_{T,m} \cdot \nabla$ is the material derivative based on the mean total velocity $\boldsymbol{V}_{T,m} = \frac{\nabla\Phi_{T,W}^u + \nabla\Phi_{T,W}^l}{2}$ on the trailing vortex sheet.

Recalling form Chapter 2 that equation (4.13) is the Morino type Kutta condition on the trailing edge that demands continuity of the potential jump at the intersection of the body contour and the trailing vortex sheet. Moreover, equations (4.14) & (4.15) are the dynamic and kinematic conditions on the trailing vortex sheet, stating that the pressure and the normal to the boundary velocity are continuous through $\partial D_W$. Eq.(4.16) can be derived from (4.14) & (4.15) and expresses Kelvin's law, i.e. the conservation of circulation (expressed by $\mu_W$) along a material curve. As we have discuss, that relation states that $\partial D_W$ evolves in time, moving with the mean velocity. Enforcement of the Kutta condition, in conjunction with the Eq.(4.16) and linearization, leads to the following expression concerning the potential jump on the trailing vortex sheet

$$\mu_W(\mathbf{x};t) = \mu_W(\mathbf{x} + \mathbf{V}_{TE}\Delta t; t - \Delta t), \qquad \mathbf{x} = (x,y) \in \partial D_W, \tag{4.17}$$

where $\mathbf{V}_{TE}$ denotes an appropriate velocity determined from the motion derivative of the foil trailing edge.

As we have discuss in Chapter 2, the above approximation permits the calculation of vorticity transport on the free trailing vortex sheet, which is geometrically modeled by the path of the motion of trailing edge of the hydrofoil ("frozen wake model", see Politis 2011). Future extensions of the present work will include a fully nonlinear free wake model, in conjunction with enhanced pressure-type Kutta condition requiring that the pressure difference at the trailing edge to be zero, see e.g. Bose (1992) and Politis (2011).

### 4.3 Representation theorem for boundary values of potential - Boundary integral equation

In the case of lifting flows around unsteady bodies under the free surface, and in the additional presence of incoming waves, the representation theorem (3.8) concerning the disturbance potential should be extended in order to include the contribution from the trailing vortex sheet $\partial D_W$. Also, the right-hand side of the body boundary condition (4.8) includes the effect of incoming wave potential. Thus, the representation theorem, Eq. (3.8) is modified by adding an extra (last) term (that appears in the representation in the case of lifting flows in unbounded domain Eq.2.17) in the right-hand side as follows

for $(\mathbf{x}_0) \in D$:

$$\begin{aligned}\Phi(\mathbf{x}_0;t) = &\int_{\partial D_B(t)} \underbrace{\left[(\boldsymbol{V}_B - \boldsymbol{V}_I)\cdot \boldsymbol{n}_B\right]}_{b(\mathbf{x};t)} G_m(\mathbf{x}_0,\mathbf{x}) - \Phi_B(\mathbf{x};t)\frac{\partial G_m(\mathbf{x}_0\,|\,\mathbf{x})}{\partial n} ds(\mathbf{x}) \\ &+ \int_{\partial D_F(t)} \frac{\partial \Phi_F(\mathbf{x}_0\,|\,\mathbf{x})}{\partial n} G_m(\mathbf{x}_0\,|\,\mathbf{x}) - \Phi_F(\mathbf{x};t)\frac{\partial G_m(\mathbf{x}_0\,|\,\mathbf{x})}{\partial n} ds(\mathbf{x}). \\ &- \int_{\partial D_W(t)} [\![\Phi_W]\!](\mathbf{x};t)\frac{\partial G_m(\mathbf{x}_0\,|\,\mathbf{x})}{\partial n} ds(\mathbf{x}),\end{aligned} \tag{4.18}$$

where $[\![\Phi_W]\!] = \Phi_W^u - \Phi_W^l = \mu_W$ is the potential jump or the dipole intensity at the wake.

In the same way, the BIEs (3.11) are modified

for $(\mathbf{x}_0) \in \partial D_{B/F}$:

$$\begin{aligned}\frac{1}{2}\Phi_{B/F}(\mathbf{x}_0;t) = &\int_{\partial D_B(t)} b(\mathbf{x};t) G_m(\mathbf{x}_0,\mathbf{x}) - \Phi_B(\mathbf{x};t)\frac{\partial G_m(\mathbf{x}_0\,|\,\mathbf{x})}{\partial n} ds(\mathbf{x}) \\ &+ \int_{\partial D_F(t)} \frac{\partial \Phi_F(\mathbf{x}_0\,|\,\mathbf{x})}{\partial n} G_m(\mathbf{x}_0\,|\,\mathbf{x}) - \Phi_F(\mathbf{x};t)\frac{\partial G_m(\mathbf{x}_0\,|\,\mathbf{x})}{\partial n} ds(\mathbf{x}). \\ &- \int_{\partial D_W(t)} [\![\Phi_W]\!](\mathbf{x};t)\frac{\partial G_m(\mathbf{x}_0\,|\,\mathbf{x})}{\partial n} ds(\mathbf{x}).\end{aligned} \tag{4.19}$$

Eqs. (4.19) and Morino condition (4.13) can be used to set-up the modified *DtN* map of the boundary values $\Phi_B$ and $\Phi_F$ and its normal derivatives. The latter integral map can be used together with the free-surface boundary conditions (4.10) & (4.11), treated as a dynamical system, providing us with an integro-differential equation that governs the evolution of the unknown free surface at the specified level of approximation. In the following section we will apply a collocation scheme and we will see how numerical solution can be obtained, using the discrete DtN map and the discrete form of the free-surface boundary conditions applied on collocation points.

### 4.4 Construction of the discrete DtN map

A low order panel method is applied again, the body contour is replaced by a closed polygonal line (with $N_B$ denoting the number of panels), the free surface is approximated by $N_F$ straight-line panels. Potential, derivatives, potential jump on the wake and the free-surface elevation are approximated by piecewise constant distributions, as follows

$$\Phi_B(x,y;t) = \Phi_{Bi},\ \text{at panel i},\ \text{i=1,...,N}_B, \tag{4.20}$$

$$\Phi_F(x,y;t) = \Phi_{Fi},\ \text{at panel i},\ \text{i=1,...N}_{F,} \tag{4.21}$$

$$[\![\Phi_W]\!](x,y;t) = [\![\Phi_W]\!]_i = \mu_{Wi},\ \text{at panel i},\ \text{i=1,...N}_{W,} \tag{4.22}$$

$$\frac{\partial \Phi_B(x,y;t)}{\partial n} = \frac{\partial \Phi_{Bi}}{\partial n} = \left[(\boldsymbol{V}_B - \boldsymbol{V}_I)\cdot \boldsymbol{n}_B\right]_i = b_i,\ \text{at panel i},\ \text{i=1,...,N}_B, \tag{4.23}$$

$$\frac{\partial \Phi_F(x,y)}{\partial n} = \frac{\partial \Phi_{Fi}}{\partial n},\ \text{at panel i},\ \text{i=1,...,N}_F, \tag{4.24}$$

$$\eta(x) = \eta_i,\ \text{at panel i},\ \text{i=1,...,N}_F. \tag{4.25}$$

Applying a collocation scheme, using the center of each panel as collocation point where Eqs. (4.19) are satisfied, the following discretized equations are obtained

$\text{for}\,(x_i, y_i)\ ,\ i = 1,...,N_B$ :

$$\sum_{j=1}^{N_B}\left(\frac{\delta_{ij}}{2} + B_{ij}^m\right)\Phi_{Bj} + \sum_{j=1}^{N_F}\left(-A_{ij}^m\right)\frac{\partial \Phi_{Fj}}{\partial n} = \sum_{j=1}^{N_B}\left(A_{ij}^m\right)\underbrace{\left[(\boldsymbol{V}_B - \boldsymbol{V}_I)\cdot \boldsymbol{n}_B\right]_j}_{b_j} + \sum_{j=1}^{N_F}\left(-B_{ij}^m\right)\Phi_{Fj} + \sum_{j=1}^{N_W}\left(-B_{ij}^m\right)\mu_{Wj}, \tag{4.26}$$

$\text{for}\,(x_i, y_i)\ ,\ i = 1,...,N_F$ :

$$\sum_{j=1}^{N_B}\left(B_{ij}^m\right)\Phi_{Bj} + \sum_{j=1}^{N_F}\left(-A_{ij}^m\right)\frac{\partial \Phi_{Fj}}{\partial n} = \sum_{j=1}^{N_B}\left(A_{ij}^m\right)\underbrace{\left[(\boldsymbol{V}_B - \boldsymbol{V}_I)\cdot \boldsymbol{n}_B\right]_j}_{b_j} + \sum_{j=1}^{N_F}\left(-\frac{\delta_{ij}}{2} - B_{ij}^m\right)\Phi_{Fj} + \sum_{j=1}^{N_w}\left(-B_{ij}^m\right)\mu_{Wj}. \tag{4.27}$$

And in the lifting problem we have the discretised form of Morino condition (4.13)

$$\mu_{W1} = \Phi_{\mathrm{BN_B}} - \Phi_{\mathrm{B1}}. \tag{4.28}$$

Recall that, the quantities $A_{ij}^m$ and $B_{ij}^m$, which can be evaluated analytically (Section 2.5), are induced factors and represent the potential at collocation point $i$ due to a unit source or dipole distribution at panel $j$

$$A_{ij}^{m} = \int_{panel\ j} G_m(x_i, y_i \mid x_j, y_j) ds(x_j, y_j), \tag{4.29}$$

$$B_{ij}^{m} = \int_{panel\ j} \frac{\partial G_m(x_i, y_i \mid x_j, y_j)}{\partial n} ds(x_j, y_j). \tag{4.30}$$

Relation (4.28) can be replaced in (4.26) and (4.27):

for $(x_i, y_i)$ , $i = 1,..., N_B$ :

$$\sum_{j=1}^{N_B} \underbrace{\left( \frac{\delta_{ij}}{2} + \delta_{N_B j} B_{N_B j}^{s} - \delta_{1j} B_{1j}^{s} + B_{ij}^{s} \right)}_{\{a_{11}\}_{ij}} \Phi_{Bj} + \sum_{j=1}^{N_F} \underbrace{\left( -A_{ij}^{s} \right)}_{\{a_{12}\}_{ij}} \frac{\partial \Phi_{Fj}}{\partial n}$$

$$= \sum_{j=1}^{N_B} \underbrace{\left( A_{ij}^{s} \right)}_{\{s_{11}\}_{ij}} b_j + \sum_{j=1}^{N_F} \underbrace{\left( -B_{ij}^{s} \right)}_{\{s_{12}\}_{ij}} \Phi_{Fj} + \sum_{j=2}^{N_W} \underbrace{\left( -B_{ij}^{s} \right)}_{\{w_1\}_{ij}} \mu_{Wj}, \tag{4.31}$$

for $(x_i, y_i)$ , $i = 1,..., N_F$ :

$$\sum_{j=1}^{N_B} \underbrace{\left( \delta_{N_B j} B_{N_B j}^{s} - \delta_{1j} B_{1j}^{s} + B_{ij}^{s} \right)}_{\{a_{21}\}_{ij}} \Phi_{Bj} + \sum_{j=1}^{N_F} \underbrace{\left( -A_{ij}^{s} \right)}_{\{a_{22}\}_{ij}} \frac{\partial \Phi_{Fj}}{\partial n}$$

$$= \sum_{j=1}^{N_B} \underbrace{\left( A_{ij}^{s} \right)}_{\{s_{21}\}_{ij}} b_j + \sum_{j=1}^{N_F} \underbrace{\left( -\frac{\delta_{ij}}{2} - B_{ij}^{s} \right)}_{\{s_{22}\}_{ij}} \Phi_{Fj} + \sum_{j=2}^{N_W} \underbrace{\left( -B_{ij}^{s} \right)}_{\{w_2\}_{ij}} \mu_{Wj}. \tag{4.32}$$

Similarly as in the previous chapter, the above equations are put in matrix form as follows

$$\underbrace{\begin{bmatrix} \{a_{11}\}_{N_B \times N_B} & \{a_{12}\}_{N_B \times N_F} \\ \{a_{21}\}_{N_F \times N_B} & \{a_{22}\}_{N_F \times N_F} \end{bmatrix}}_{A} \begin{bmatrix} \{\Phi_B\}_{N_B \times 1} \\ \left\{ \frac{\partial \Phi_F}{\partial n} \right\}_{N_F \times 1} \end{bmatrix} = \underbrace{\begin{bmatrix} \{s_{11}\}_{N_B \times N_B} & \{s_{12}\}_{N_B \times N_F} \\ \{s_{21}\}_{N_F \times N_B} & \{s_{22}\}_{N_F \times N_F} \end{bmatrix}}_{S} \begin{bmatrix} \{b\}_{N_B \times 1} \\ \{\Phi_F\}_{N_F \times 1} \end{bmatrix}$$

$$+ \underbrace{\begin{bmatrix} \{w_1\}_{N_B \times (N_W - 1)} \\ \{w_2\}_{N_F \times (N_W - 1)} \end{bmatrix}}_{W} \{\mu_W\}_{(N_W - 1) \times 1}. \tag{4.33}$$

Therefore, in the present case, the *DtN* map becomes

$$\begin{bmatrix} \{\Phi_B\}_{N_B\times 1} \\ \left\{\frac{\partial \Phi_F}{\partial n}\right\}_{N_F\times 1} \end{bmatrix} = \mathbf{D}\cdot\begin{bmatrix} \{b\}_{N_B\times 1} \\ \{\Phi_F\}_{N_F\times 1} \end{bmatrix} + \mathbf{P}(\mu_W), \tag{4.34}$$

with

$$\mathbf{D} = \begin{bmatrix} \mathbf{D}_{11} & \mathbf{D}_{12} \\ \mathbf{D}_{21} & \mathbf{D}_{22} \end{bmatrix} = \mathbf{A}^{-1}\mathbf{S}, \tag{4.35}$$

and

$$\mathbf{P}(\mu_W) = \begin{bmatrix} \mathbf{P}_1 \\ \mathbf{P}_2 \end{bmatrix} = \mathbf{A}^{-1}\cdot\left(\mathbf{W}\cdot\left[\{\mu_W\}_{(N_W-1)\times 1}\right]\right). \tag{4.36}$$

Thus, in the case of lifting flows beneath the free surface, the system of ODEs, describing the evolution of the discrete system is

$$\frac{d\mathbf{U}}{dt} = \mathbf{f}(\mathbf{U}), \tag{4.37}$$

where

$$\mathbf{U} = \begin{bmatrix} \{\Phi_F\}_{N_F\times 1} \\ \{\eta\}_{N_F\times 1} \end{bmatrix}, \tag{4.38}$$

and

$$\mathbf{f}(\mathbf{U}) = \begin{bmatrix} \mathbf{0} & \mathbf{-gI} \\ \mathbf{-D_{22}} & \mathbf{0} \end{bmatrix}\cdot\mathbf{U} + \begin{bmatrix} \mathbf{0} \\ \mathbf{-D_{21}b} \end{bmatrix} + \begin{bmatrix} \mathbf{0} \\ \mathbf{-P}_2(\mu_W) \end{bmatrix}. \tag{4.39}$$

We observe in the above equation that the effect of the trailing wake is taken into account through $\mathbf{P}_2(\mu_W)$ and the effect of the incident wave through the component $\mathbf{V}_I = \partial\Phi_I / \partial n_B$ in $\mathbf{b}$.

### 4.5 Calculation of pressure - Bernoulli's Theorem

In the present section we will present the derivation of an appropriate form of Bernoulli's theorem for the calculation of pressure distribution on the boundary of a body in unsteady lifting flow beneath the free surface and in the presence of waves modeled by an harmonic incident wave field $\Phi_I$. In contrary with the case of gust velocity that was a rotational field, the present incident wave field is irrotational and thus Bernoulli's theorem can be applied. Therefore, conservation of energy along a stream line in a free-surface flow can be written

$$\frac{\partial \Phi_T}{\partial t} + \frac{1}{2}\left(\nabla \Phi_T\right)^2 + \frac{p - p_{atm}}{\rho} + gy = C(t), \ (x, y) \in D, \tag{4.40}$$

where $C(t)$ can be set to zero with redefinition of the potential, i.e.

$$\frac{p - p_{atm}}{\rho} = -\frac{\partial \Phi_T}{\partial t} - \frac{1}{2}\left(\nabla \Phi_T\right)^2 - gy, \tag{4.41}$$

where $p(x, y)$ is the pressure at $(x, y) \in D$ and $p_{atm}$ is the atmospheric pressure on the free surface, ρ is the density of the fluid $g$ is the acceleration of gravity and the last term is the hydrostatic component. Also, $\Phi_T = \Phi + \Phi_I$ is the total wave potential consists of the disturbance potential $\Phi$ (enforced radiation and diffraction potential field) and the incident wave potential $\Phi_I$. Also, $\frac{\partial \Phi}{\partial t}$ denotes time rate of potential according to a fixed observer with regard to an inertia reference frame.

As we have already seen, using BEM's we can evaluate the trace $\Phi^*$ of the disturbance potential on the boundary and differentiating we can calculate the rate of change according to a body-fixed reference frame, denoted by $\frac{d\Phi^*}{dt}$. Recall now from Section 2.7 relation (2.56)

$$\frac{d\Phi^*}{dt} = \nabla \Phi \cdot \boldsymbol{V}_B + \frac{\partial \Phi}{\partial t}, \tag{4.42}$$

The above equation connects the inertia rate of change $\frac{\partial \Phi}{\partial t}$ of the disturbance potential, which is required in Bernoulli's equation with the body-fixed rate of change of the potential's trace $\frac{d\Phi^*}{dt}$ which is calculated using BEMs. Using (4.42), (4.41) becomes

$$\frac{p - p_{\inf}}{\rho} = -\frac{\partial \Phi_I}{\partial t} - \frac{d\Phi^*}{dt} + \nabla \Phi \cdot \boldsymbol{V}_B - \frac{1}{2}\left(\nabla \Phi_I + \nabla \Phi\right)^2 - gy. \tag{4.43}$$

In relation (4.43), the term $\nabla\Phi$ is the space gradient of the disturbance potential $\Phi$. But using BEM we calculate the surface gradient $\nabla\Phi^*$ of the trace $\Phi^*$. Recall also relation (2.61)

$$\nabla\Phi = \nabla\varphi + \left(\boldsymbol{n}\cdot\nabla\Phi\right)\boldsymbol{n}. \tag{4.44}$$

The above relation connects the space gradient of the disturbance potential with the surface gradient of the trace of the disturbance potential on the boundary. But the normal to the boundary derivative is known from the no entrance boundary condition (4.8), thus replacing (4.8) into (4.44), it follows

$$\nabla\Phi = \nabla\Phi^* + \underbrace{\left(\boldsymbol{V}_B\cdot\boldsymbol{n}_B - \nabla\Phi_I\cdot\boldsymbol{n}_B\right)}_{b}\boldsymbol{n}_B. \tag{4.45}$$

Substituting relation (4.45) into (4.43) we obtain the final form of Bernoulli's equation which is required for the calculation of pressure distribution on the boundary:

$$\frac{p-p_{atm}}{\rho} = -\frac{\partial\Phi_I}{\partial t} - \frac{d\Phi^*}{dt} + \left(\nabla\Phi^* + b\cdot\boldsymbol{n}_b\right)\cdot\boldsymbol{V}_B - \frac{1}{2}\left(\nabla\Phi_I + \nabla\Phi^* + b\cdot\boldsymbol{n}_b\right)^2 - gy. \tag{4.46}$$

Or using the definition of the non-dimensional pressure coefficient:

$$C_p = \frac{p-p_{atm}}{\frac{1}{2}\rho U^2}, \tag{4.47}$$

where $U$ is a characteristic velocity of the motion of the body e.g. the forward velocity,

we get:

$$C_P = \frac{-\frac{\partial\Phi_I}{\partial t} - \frac{d\Phi^*}{dt} + \left(\nabla\Phi^* + b\cdot\boldsymbol{n}_b\right)\cdot\boldsymbol{V}_B - \frac{1}{2}\left(\nabla\Phi_I + \nabla\Phi^* + b\cdot\boldsymbol{n}_b\right)^2 - gy}{\frac{1}{2}U^2}, \tag{4.48}$$

or in discrete form:

$\text{for}\,(x_i, y_i)\in\bar{D}$:

$$C_{Pi} = \frac{-\frac{\partial\Phi_{Ii}}{\partial t} - \frac{d\Phi_i^*}{dt} + \left[\nabla\Phi_i^* + \left(b\cdot\boldsymbol{n}_b\right)_i\right]\cdot\boldsymbol{V}_{Bi} - \frac{1}{2}\left[\nabla\Phi_{Ii} + \nabla\Phi_i^* + \left(b\cdot\boldsymbol{n}_b\right)_i\right]^2 - gy_i}{\frac{1}{2}U^2}. \tag{4.49}$$

### 4.6 Free-surface effects on wave-powered propulsion using flapping-foil biomimetic systems

As we have discussed in section 1.2 biomimetic propulsors is the subject of extensive investigation, first of all because they could used as the main propulsion system providing efficient thrust production for marine purposes and secondly, due to the fact that they are ideally suited for converting directly environmental (sea wave) energy to useful thrust.

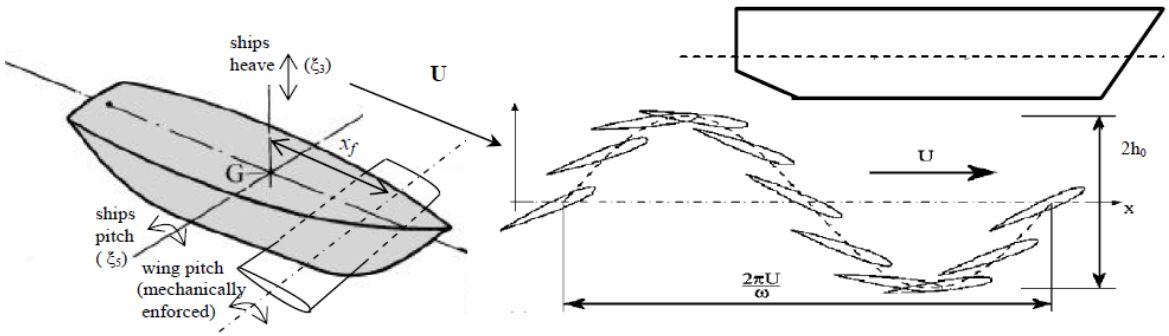


Figure 54. Sketch of a flapping-wing system used for augmenting ship propulsion in waves

More specifically, ongoing research is focused on the hydrodynamic analysis of flapping wings located beneath the ship's hull, operating in random motion; see Fig.54. The wing undergo a combined transverse and rotational oscillatory motion, while the ship is steadily advanced in the presence of waves, modeled by directional spectrum. The present system is investigated as an unsteady thrust production mechanism, augmenting the overall propulsion system of the ship. The horizontal wing undergoes a combined vertical and angular (pitching) oscillatory motion, while travelling at constant forward speed. The vertical motion is induced by the random motion of the ship in waves, essentially due to ship heave and pitch, at the station where the flapping wing is located. Wing-pitching motion is controlled as a proper function of wing-vertical motion and it is imposed by an external mechanism.

In the present work we focus to the effects of free surface and incoming waves to the thrust production of flapping-foil propulsor systems. A reference to the famous Gray's paradox and an explanation, related to wave energy extraction, is given in Subsection 4.6.1. In Subsection 4.6.2 Numerical results are presented and discussed concerning hydrofoils in flapping motion under the free surface and in finite depth, in order to examine the rate of convergence, stability and efficiency of the numerical scheme. Subsequently, comparisons are presented with other methods from the literature, in order to examine the range of applicability, as well as the limitations of the developed method. In particular, in Subsec. 4.6.3 the hydrofoil in steady motion beneath the free surface is examined focusing on the wave resistance problem and the effects of free surface on lift production, also the effect of the angle of attack and the direction of circulation on the form of the generated wave is noticed. In Subsec. 4.6.4. the additional effects of oscillatory motion(s) are presented. In the same Subsection the behavior of hydrodynamic quantities as the Froude number decreases and the boundaries moving away of the flapping foil is examined, testing also compatibility with the method developed in Chapter 2, concerning the same problem in infinite domain. Finally in Subsec. 4.6.5, results are presented for the system operating as unsteady thruster in incoming waves.

Consider a flapping hydrofoil beneath the free surface and in the presence of incoming waves (Fig. 54). The flapping motion of the foil consists of a forward motion

$$s(t) = -U \cdot t \cdot F(t), \tag{4.50}$$

a linear (heaving) oscillatory motion in y-direction

$$h(t) = h_0 \cos(\omega t + \varphi) \cdot F(t) = \mathrm{Re}\left\{\dot{h}_o e^{i\omega t + \varphi}\right\} \cdot F(t), \tag{4.51}$$

and rotational (pitching) oscillations about a pivot axis

$$\theta(t) = \theta_0 \cos(\omega t + \psi + \varphi) = \mathrm{Re}\left\{\dot{\theta}_o e^{i\omega t + \psi + \varphi}\right\} \cdot F(t), \tag{4.52}$$

where $h_0$ and $\dot{h}_o$ are the amplitude and the complex amplitude of heaving motion, $\theta_0$ and $\dot{\theta}_o$ are the amplitude and the complex amplitude of the pitching rotation, which is positive counterclockwise, pitching is considered around hydrofoil's pivot axis which is located on the chord and at distance $X_R$ from the leading edge, $\psi$ is the phase difference between the heave and pitch which in the following analysis is selected $\psi = 90°$, $\varphi$ is the phase difference between the heaving motion and the free-surface elevation due to the incident wave, $\omega$ is the radial frequency which is set same for the two oscillatory motions and $i$ is the imaginary unit. Also $d$ is the submergence of the foil and $H$ is the distance between the bottom and the mean free-surface level. In addition, $F(t) = 1 - \exp\left[-f_0 (t/T)^2\right]$ is a filter function permitting smooth transition from rest to the harmonic oscillatory motion.

Thus every point B of the hydrofoil with initial position according to an inertia coordinate system $(x_{B0}, y_{B0})$ is moving along the curve:

$$x_B(t) = x_{B0} \cos\theta(t) - y_{B0} \sin\theta(t) - s(t), \tag{4.53}$$
$$y_B(t) = x_{B0} \sin\theta(t) + y_{B0} \cos\theta(t) + h(t). \tag{4.54}$$

In the context of linearized free-surface wave theory, the incident wave is modeled by the following expressions concerning the free surface elevation and the associated potential

$$\eta_I(x;t) = \eta_0 \cos(kx - \omega)\, F(t), \tag{4.55}$$

and

$$\Phi_I(\mathbf{x};t) = -\frac{g\eta_0}{\omega_1} \frac{\cosh(k(y+H))}{\cosh(kH)} \sin(kx - \omega_1 t)\, F(t), \tag{4.56}$$

where $\eta_0$ is the corresponding amplitude of free-surface elevation, $\omega_1^2 = kg\tanh(kH)$ is the angular frequency of the incident wave.

The ratio of inertial to gravitational forces that controls the effects of the waves generated from the forward motion of the foil is expressed by Froude number $F_n = U/\sqrt{cg}$ . The unsteadiness of the motion is measured by the non-dimensional reduced frequency $k_r = \omega c/2U$, where $c$ is the chord length of the hydrofoil, which can be used both in the cases where heaving motion exists or not. In the case of heaving or flapping motion we can use Strouhal number $St = \omega h/\pi U = (2h/\pi c)k_r$ . Another motion parameter is the feathering parameter $\varepsilon = \theta_0 U/\omega h_0$, introduced by Lighthill (1970). This non-dimensional number provides a measure of the relative magnitude of pitch and heave oscillations. The maximum angle of attack $a_{\max}$ in still water, is also considered. The instantaneous angle of attack can be evaluated:

$$a(t) = \tan^{-1}\left(\frac{dh/dt}{ds/dt}\right) - \theta. \tag{4.57}$$

Of course the angle of attack is affected by the downwash induced from the wake and also by wave velocity and these effects are not taken into account in the above expession.

As we have seen in the previous chapter, using linear theory, an approximate prediction of the wave length can be provided. According to the theory of linear systems, the oscillatory motion of the foil with radial frequency $\omega$, produce waves with the same frequency. Knowing the frequency of the responding wave, we can evaluate the corresponding wave length, using dispersion relation

$$\omega^2 = k_{osc} g\tanh(k_{osc}H),\ k_{osc} = \frac{2\pi}{\lambda_{osc}}, \tag{4.58}$$

where $\lambda_{osc}$ and $k_{osc}$ are the wave length and the wave number due to the oscillatory motion of the foil.

Moreover, assuming that the wave travels with the same velocity $U$ with the hydrofoil we have

$$U^2 = g/k_{for}\tanh(k_{for}H),\ k_{fro} = \frac{2\pi}{\lambda_{for}}, \tag{4.59}$$

where $\lambda_{for}$ and $k_{for}$ are the wave length and the wave number due to the forward motion of the foil.

In the following analysis we consider as a characteristic wave length of the radiation wave the maximum of the above two, i.e. $\lambda = \max(\lambda_{osc}, \lambda_{for})$.

Moreover, the parameters that control the space and time discretization are, $N_B$ the number of panels on the body contour, Time Sampling Ratio $(TSR)$ defined as the percentage of the period that equals to the time step

$$TSR = \frac{dt}{T} \cdot 100. \tag{4.60}$$

Space Sampling Ratio $(SSR)$ defined as the percentage of, the predicted from the linear theory, radiation wave length that equals to panel length on the free surface

$$SSR = \frac{dx}{\lambda} \cdot 100. \tag{4.61}$$

A wake model is applied to linearize free wake dynamics and the corresponding discretization parameter $N_W(t)$ is a function of $N_B$ and $TSR$ in the same manner as discussed in Chapter 2. In the following analysis we choose $N_B = 120$, exploiting results of subsection 2.9.1.

Finally, the implementation of conditions at infinity is based on the PML model described in Section 3.6. The PML parameters that will be used in the following numerical analysis are $\sigma_0 = 3$, $p = 3$ and $l/\lambda = 1$. The length of the domain, including absorbing layer zone is $L = U \cdot N_T \cdot T + 8\lambda$, where $N_T$ denotes the number of periods considered, and the initial position of the foil is $X_f = L/2 - 4\lambda$.

Before proceeding to the numerical investigation of the problem, we will present a brief reference to the famous Gray's paradox (1936) that was the threshold for intense research in the field of marine propulsion and of wave energy extraction, using biomimetic systems.

### 4.6.1 Gray's paradox

Modern research on biomimetic foil and wave-powered propulsion begins in 30's with Gray's paradox, by which, estimations of sea mammals resistance based on drag coefficient result in power requirements exceeding those that can be accomplished by the structure and mass of their muscle system. In 1936 J. Gray made experiments in order to study fish motion and thrust production. He used a flexible model or a dead fish and an appropriate apparatus to enforce fish-like wave motions of the body. Gray calculated the total resistance of a dolphin, using turbulent boundary layer theory and estimated, among other things, that the required power for thrust production, in order to overcome total drag, was possibly about seven times the estimated muscular power available. This yields the famous Gray's paradox, which in the following decades were considered by a large number of investigators.

One direction that researcher investigated, in order to explain that paradox, was the influence of the swimming motion on the resistance of the body. In 1999, Barret et al carried out experiments using a robotic-tuna mechanism. He noticed that drag reduction of order 50%-70% occurred when the phase speed of the travelling wave on the body was larger than the swimming speed. He mentioned that the reduction in total resistance may occurs because of the laminarization of the boundary layer by the motion of the body or the appropriate interaction of fin's trailing edge vortex's with others from the leading edge's and the body.

In addition, Blake (1983) mentioned that some other mechanisms relevant with the material and the topography of fishes' skin ought to be taken into account. To be more specific, the drag-reducing mucus or fish slime and a viscous or dynamic damping capacity of the skin, have to be considered.

Another possible explanation is the following. The fin of hydrobionts such as dolphins and whales is located in a horizontal plane, enables in this way, efficiently utilization of wave flows' energy. Relevant examples mentioned by Rozhdestvensky & Ryzhov (2003) are "sliding" of cetaceans on the waves and their motion in the region of the bow pressure wave of ships. Moreover, studies demonstrate that some types of cetaceans, e.g. whale Balaenoptera physalus, can save up to 40% of the propulsion power while moving beneath the wavy free surface, see. Bose & Lien (1989),(1990). Extraction of energy from non-uniform (wavy) flows can tackle the well-known Gray paradox and explain the effect that the cetaceans can develop greater speeds than those, their muscular capability allows.

### 4.6.2 Numerical performance

Numerical stability, convergence and efficiency of the scheme has been tested using as an example, a submerged symmetric NACA0012 hydrofoil (Fig.55) flapping in calm sea. Rotation axis is considered to be at $X_R / c = 0.3$, moreover $\psi = -90°$, in submergence $(d / c = 1.5 \div 24)$ over a range of flapping motion's and free surface's parameters, i.e., Froude number $(Fn = 0.25 \div 2)$, Strouhal number $(St = 0.1 \div 0.4)$, reduced frequency $(k_r = 0.1 \div 3.8)$, heaving $(h_0 / c = 0.25 \div 1)$ and pitching $(\theta_0 = 10° \div 40°)$ amplitude, in shallow, moderate and deep water $(H / \lambda = 4\% \div 700\%)$.

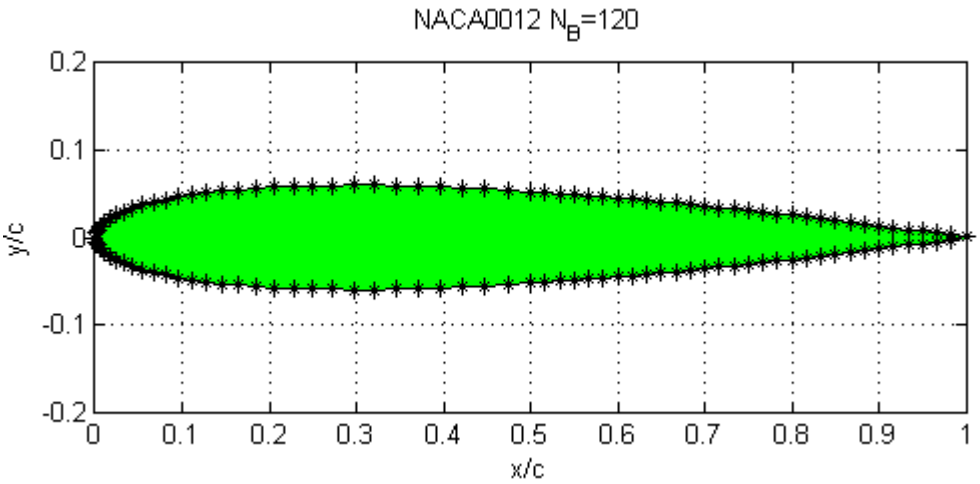


Figure 55: Geometry of a NACA0012 hydrofoil and discretization with non-uniform iso-cosine grid denser at the leading edge.

Results concern hydrodynamic quantities, both integrated like non-dimensional Lift $\left(C_L = F_Y / 0.5\rho U^2 c\right)$ and Thrust $\left(C_T = -F_X / 0.5\rho U^2 c\right)$ coefficients and distributed such as pressure coefficient $\left(C_P = p / 0.5\rho U^2\right)$ and non-dimensional free surface elevation $(\eta / c)$. Transition from rest to harmonic state condition has been accomplished after the third period of oscillation. Average force coefficient is $C_{F,av} = 1/T \int_{4T}^{5T} C_F(t) dt$ and the amplitude of force coefficients is calculated by $C_{F,amp} = 0.5\left[\max\left\{C_F(t),\ t \in (4T, 5T)\right\} - \min\left\{C_F(t),\ t \in (4T, 5T)\right\}\right]$.

A non-uniform discretisation has been applied on the hydrofoil's boundary in the sense of Fig.55. The grid is denser at the leading edge where the profile changes abruptly and becomes uniform to the trailing edge, so as the panels in the vicinity of the trailing edge to have comparable length with the wake's panels, the total number of panels on the body contour is $N_B = 120$. A uniform grid of $N_f$ panels has replace the mean line of the free surface. In the following figures the mean value of Trust coefficient and the amplitude of Lift coefficient are presented. Finally the values of PML parameters are $\sigma_0 = 3$, $p = 3$, $l / \lambda = 1$, exploiting the results of Sec. 3.6.

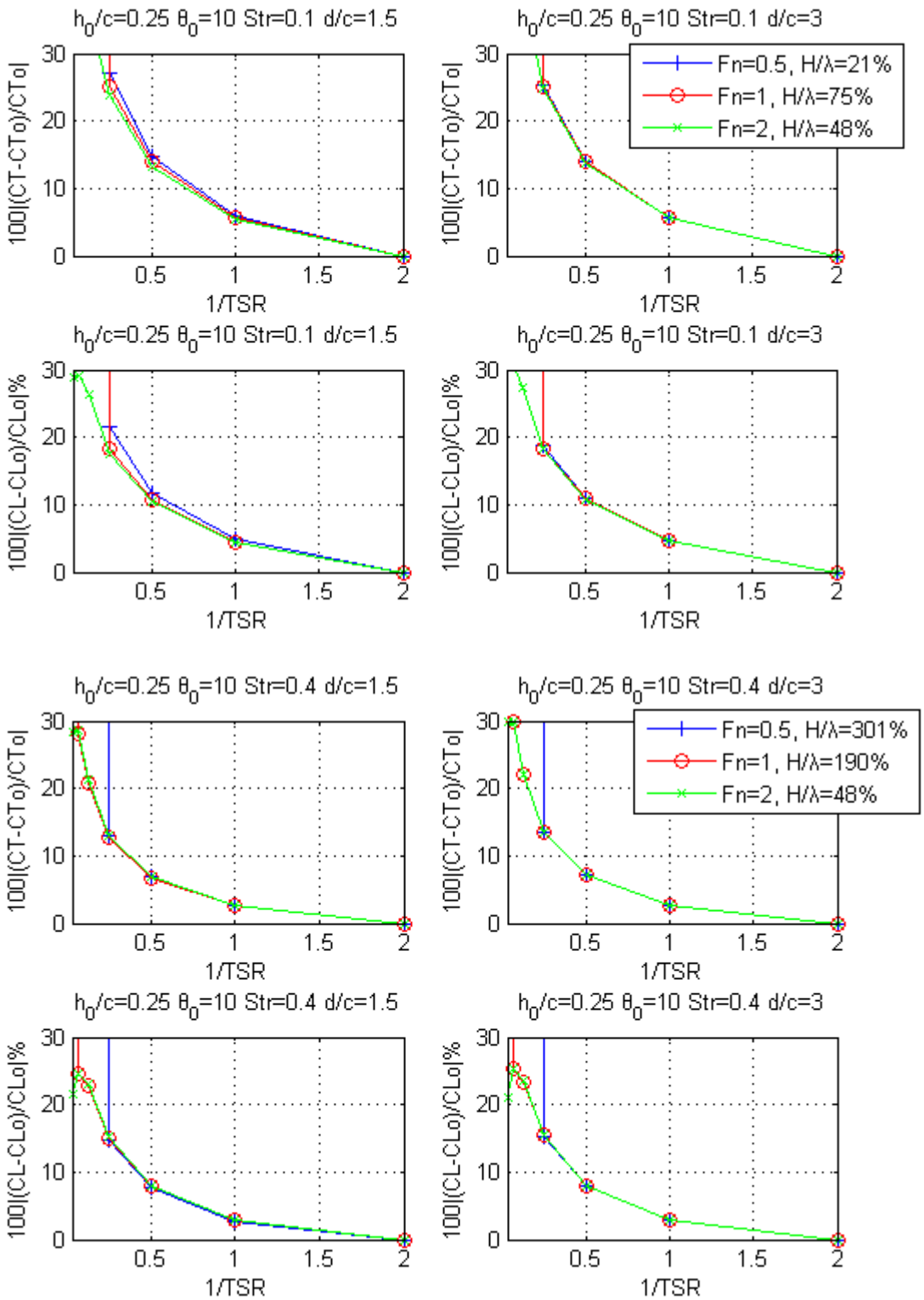


Figure 56: Convergence of $C_T$ & $C_L$ with respect to $1/TSR$, for a NACA0012 hydrofoil in flapping motion with $X_R/c=0.3$, $N_B=120$, $h_0/c=0.25$, $\theta_0=10°$, $Str=0.1,0.4$ and beneath the free surface with $SSR=4$, $d/c=1.5,3$, $Fn=0.5,1,2$ and $H/\lambda=21\%\div301\%$.

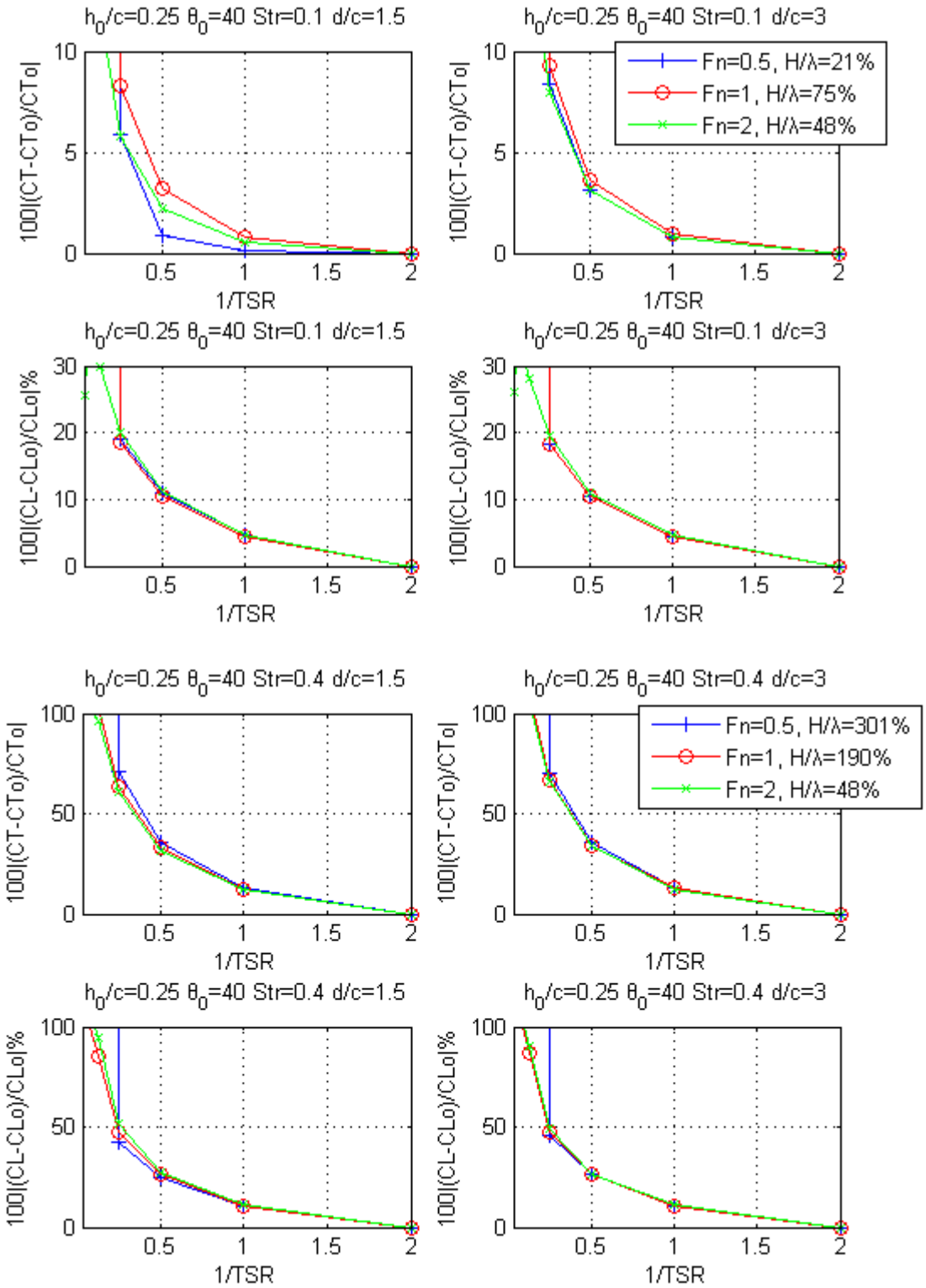


Figure 57: Convergence of $C_T$ & $C_L$ with respect to $1/TSR$, for a NACA0012 hydrofoil in flapping motion with $X_R / c = 0.3$, $\mathrm{N_B} = 120$, $h_0 / c = 0.25$, $\theta_0 = 40°$, $Str = 0.1, 0.4$ and beneath the free surface with $SSR = 4$, $d / c = 1.5, 3$, $Fn = 0.5, 1, 2$ and $H / \lambda = 21\% \div 301\%$.

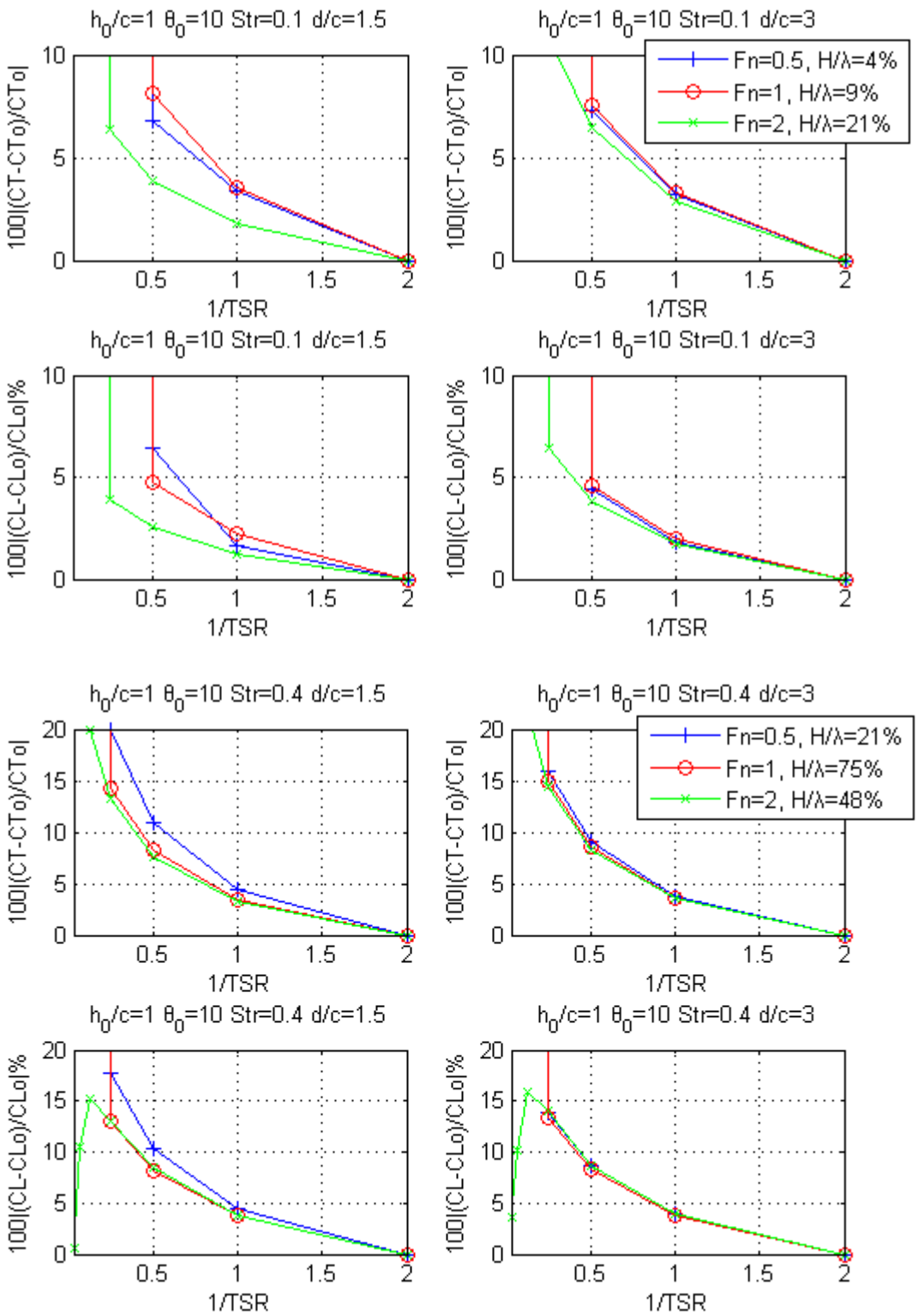


Figure 58: Convergence of $C_T$ & $C_L$ with respect to $1/TSR$, for a NACA0012 hydrofoil in flapping motion with $X_R/c=0.3$, $N_B=120$, $h_0/c=1$, $\theta_0=10°$, $Str=0.1,0.4$ and beneath the free surface with $SSR=4$, $d/c=1.5,3$, $Fn=0.5,1,2$ and $H/\lambda=4\%\div75\%$.

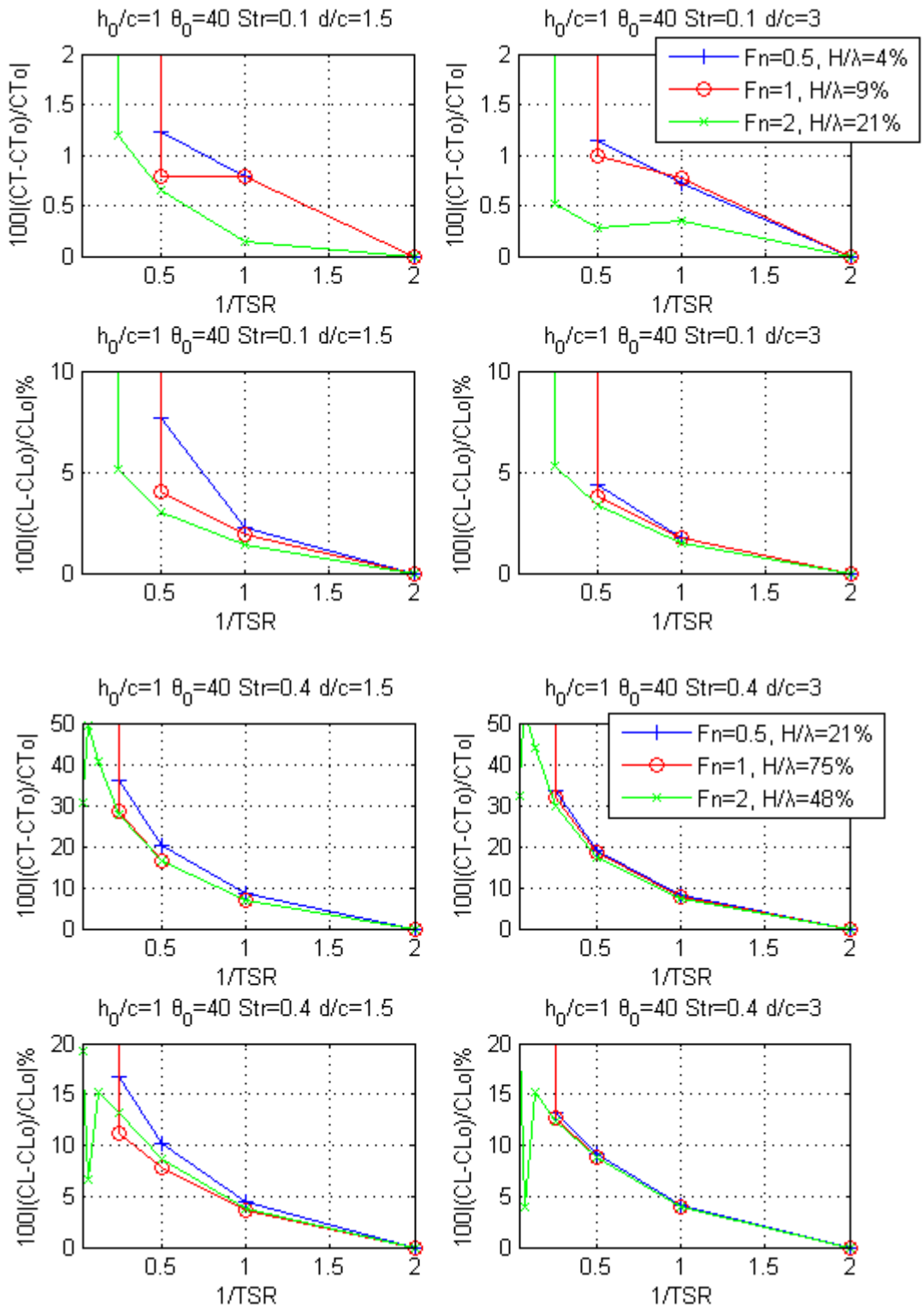


Figure 59: Convergence of $C_T$ & $C_L$ with respect to $1/TSR$, for a NACA0012 hydrofoil in flapping motion with $X_R/c=0.3$, $N_B=120$, $h_0/c=1$, $\theta_0=40°$, $Str=0.1,0.4$ and beneath the free surface with $SSR=4$, $d/c=1.5,3$, $Fn=0.5,1,2$ and $H/\lambda=4\%\div75\%$.

In Figs. 56 to 59 convergence characteristics of the numerical scheme concerning integrated force, i.e. average thrust force and lift amplitude, coefficients against time step, expressed by $1/TSR$ for a range of kinematic parameters, are demonstrated. We can see that the relevant error $100\left|\left(C_F - C_{F0}\right)/C_{F0}\right|$ is less than 5% for $TSR \le 1\%$, which corresponds to more than 100 time steps per period of oscillation. The relevant error is measured with respect to the value of the coefficient $C_{F0}$ for $TSR = 0.5\%$. Notice that the use of the higher order Adams-Bashford-Moulton predictor-corrector method reduces significantly the time steps per period that are required for convergence in comparison with numerical results presented in Chapter 2, concerning the problem in infinite domain in the same range of parameters. In this way, the addition computational cost due to the discretization of the free-surface boundary is balanced and the time for computation remains of the same order of magnitude.

Also in Figs. 60 to 63 convergence of the numerical scheme with respect to panel number on the free surface , expressed by $1/SSR$ is tested, for a range of kinematic parameters. We can see that the relevant error $100\left|\left(C_F - C_{F0}\right)/C_{F0}\right|$, concerning integrated force coefficients, is less than 5% for $SSR \le 4\%$, which corresponds to more than 25 panels per wavelength. The relevant error is measured again with respect to the value of the coefficient $C_{F0}$ for the maximum panel number tested that corresponds to $SSR = 2\%$.

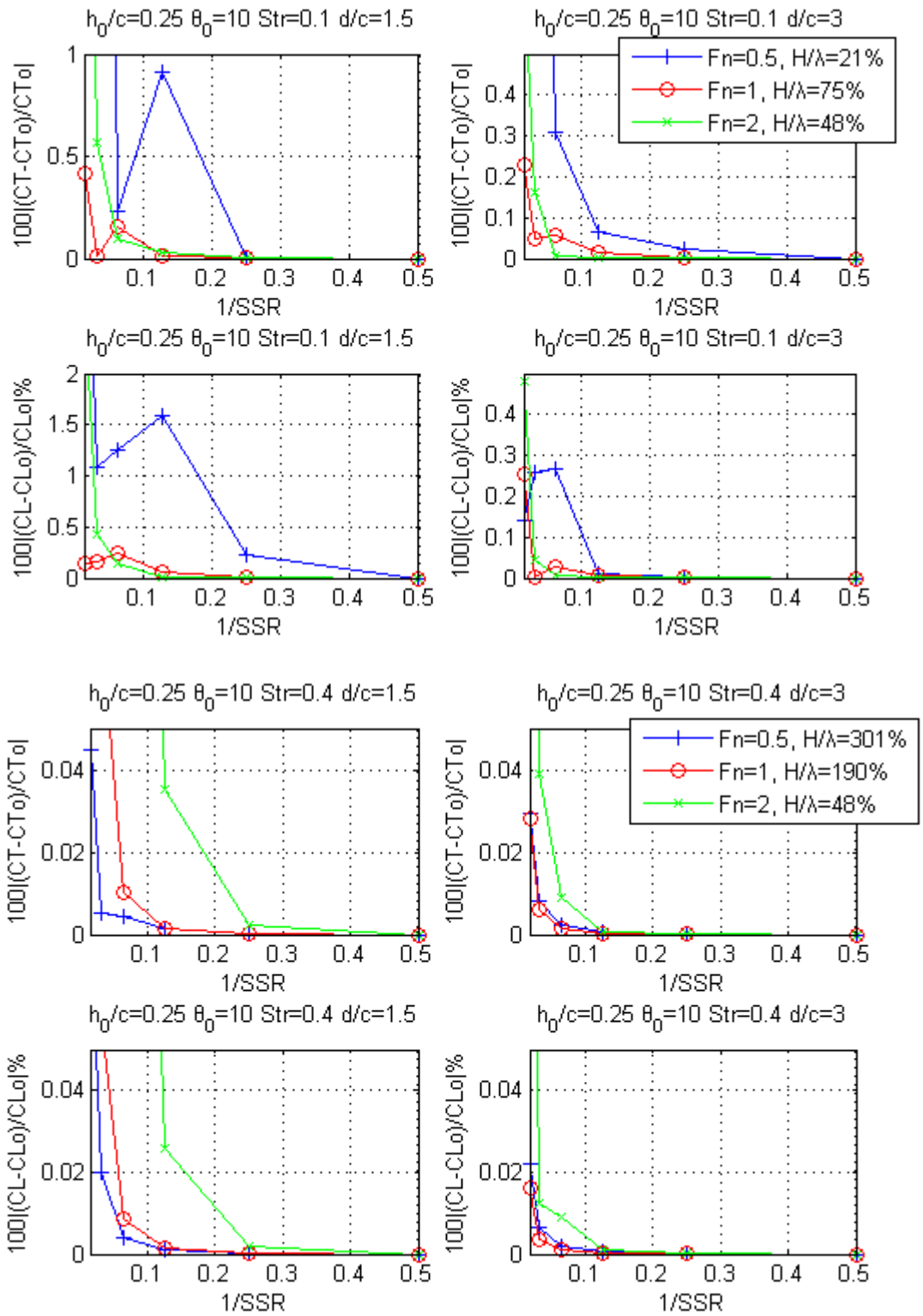


Figure 60: Convergence of $C_T$ & $C_L$ with respect to $1/SSR$, for a NACA0012 hydrofoil in flapping motion with $X_R/c=0.3$, $\mathrm{N_B}=120$, $h_0/c=0.25$, $\theta_0=10°$, $Str=0.1,0.4$ and beneath the free surface with $TSR=1$, $d/c=1.5,3$, $Fn=0.5,1,2$ and $H/\lambda=21\%\div301\%$.

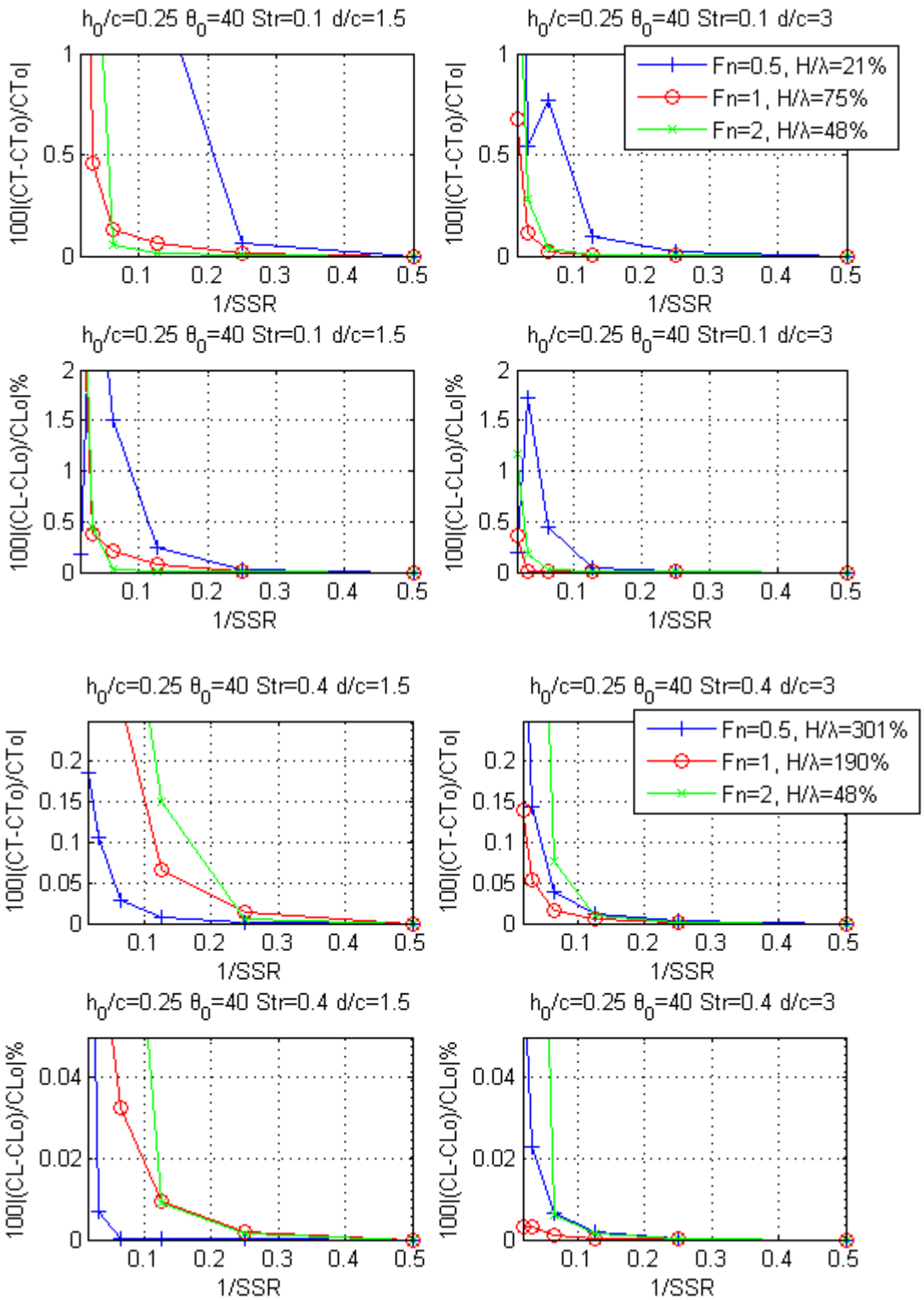


Figure 61: Convergence of $C_T$ & $C_L$ with respect to $1/SSR$, for a NACA0012 hydrofoil in flapping motion with $X_R/c=0.3$, $\mathrm{N_B}=120$, $h_0/c=0.25$, $\theta_0=40°$, $Str=0.1,0.4$ and beneath the free surface with $TSR=1$, $d/c=1.5,3$, $Fn=0.5,1,2$ and $H/\lambda=21\%\div301\%$.

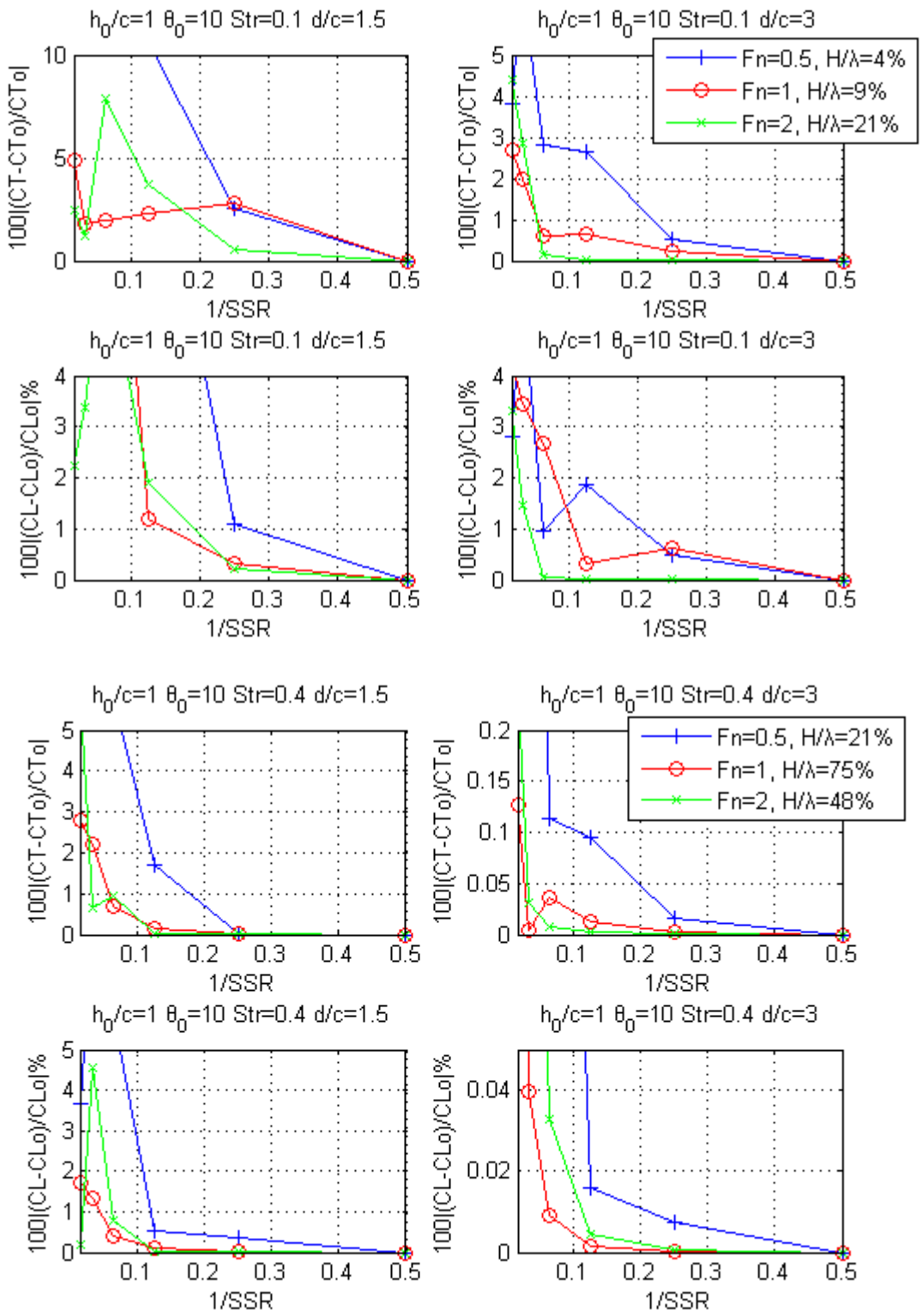


Figure 62: Convergence of $C_T$ & $C_L$ with respect to $1/SSR$, for a NACA0012 hydrofoil in flapping motion with $X_R/c=0.3$, $\mathrm{N_B}=120$, $h_0/c=1$, $\theta_0=10°$, $Str=0.1,0.4$ and beneath the free surface with $TSR=1$, $d/c=1.5,3$, $Fn=0.5,1,2$ and $H/\lambda=4\%\div75\%$.

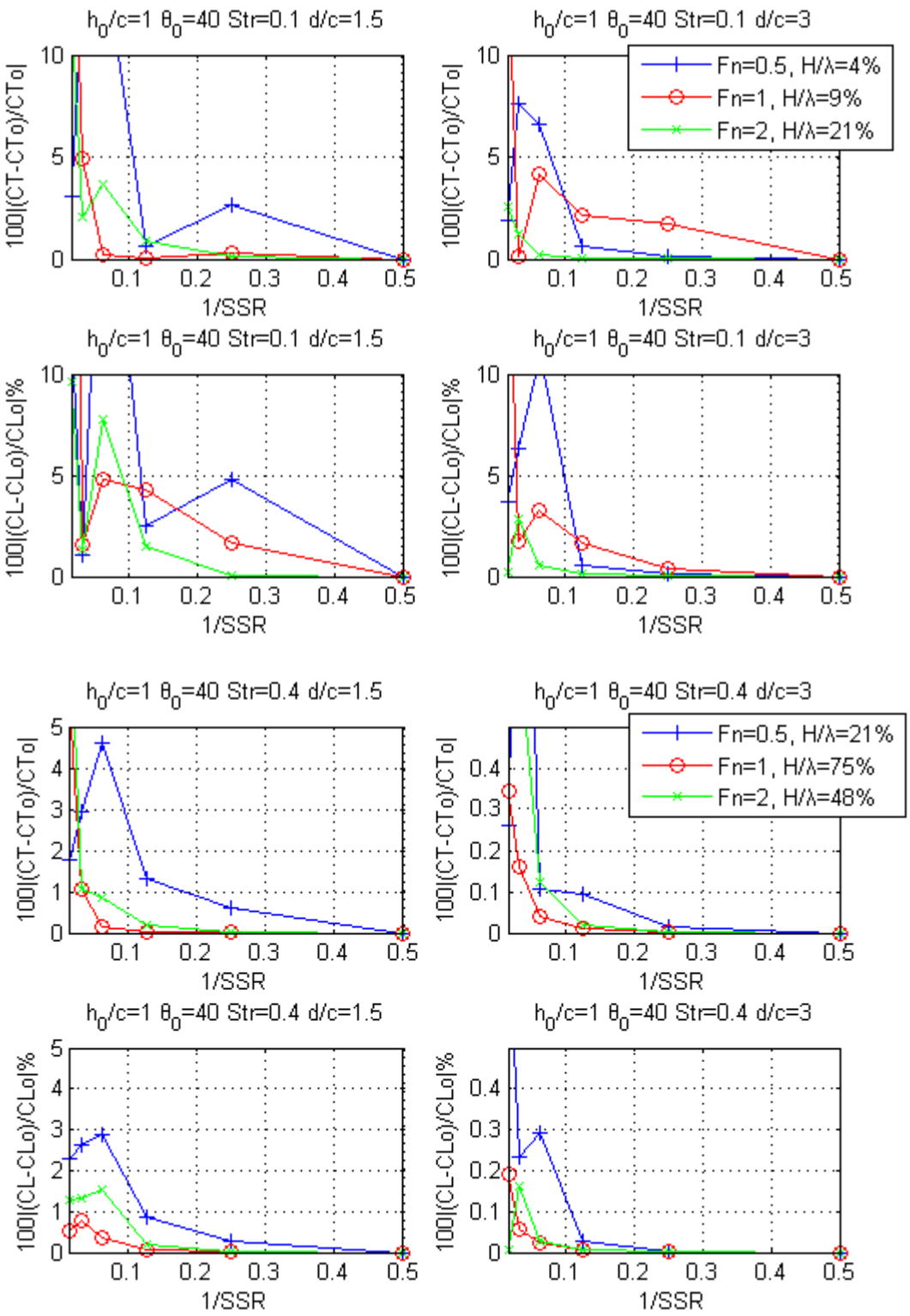


Figure 63: Convergence of $C_T$ & $C_L$ with respect to $1/SSR$, for a NACA0012 hydrofoil in flapping motion with $X_R/c=0.3$, $\mathrm{N_B}=120$, $h_0/c=1$, $\theta_0=40°$, $Str=0.1,0.4$ and beneath the free surface with $TSR=1$, $d/c=1.5,3$, $Fn=0.5,1,2$ and $H/\lambda=4\%\div75\%$.

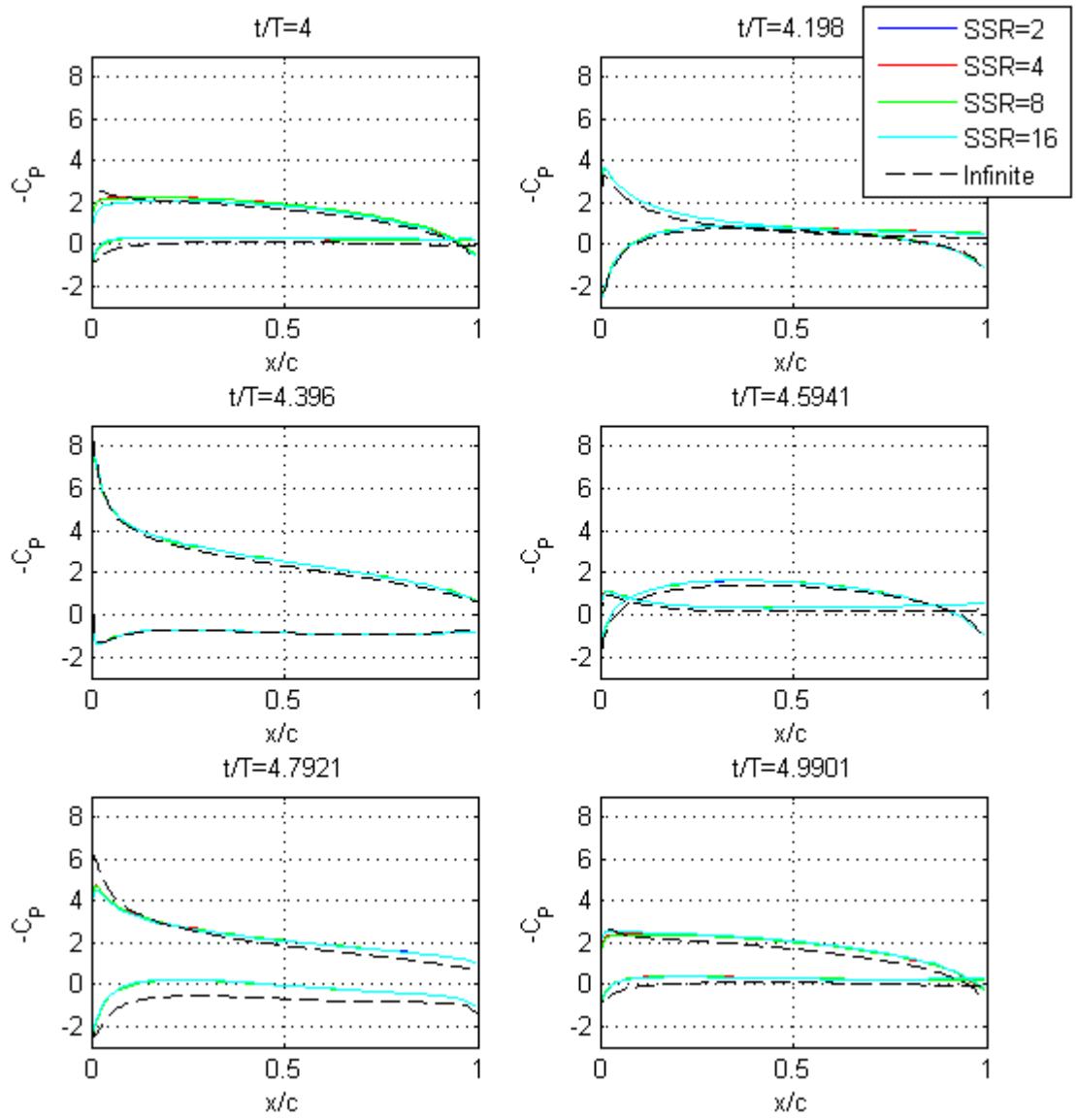


Figure 64: Convergence of $C_P(x;t)$ with respect to $SSR$, for a NACA0012 hydrofoil in flapping motion with $X_R/c=0.3$, $N_B=120$, $TSR=1$, $h_0/c=1$, $\theta_0=40°$, $Str=0.4$ and beneath the free surface with $d/c=1.5$, $Fn=2$ and $H/\lambda=48\%$, during the 5th period of oscillation and comparison with corresponding results in infinite domain (dashed line).

Moreover, in Fig. 64, the evolution pressure coefficient is presented for different number of panels on the free surface, $TSR=1\%$, $N_B=120$, for intense flapping motion with $h_0/c=1$, $\theta_0=40°$, and $Str=0.4$, $X_R/c=0.3$, during the 5th period of oscillation. It is clear that convergence is achieved for $SSR\geq 4$. To illustrate the free-surface effects we compare with results in infinite domain. The variation in pressure distribution leads to an increase in average thrust coefficient form $C_{T,\inf}=0.72$ to $C_T=0.76$ and a small decrease in lift amplitude from $C_{L,\inf}=2.96$ to $C_L=2.95$.

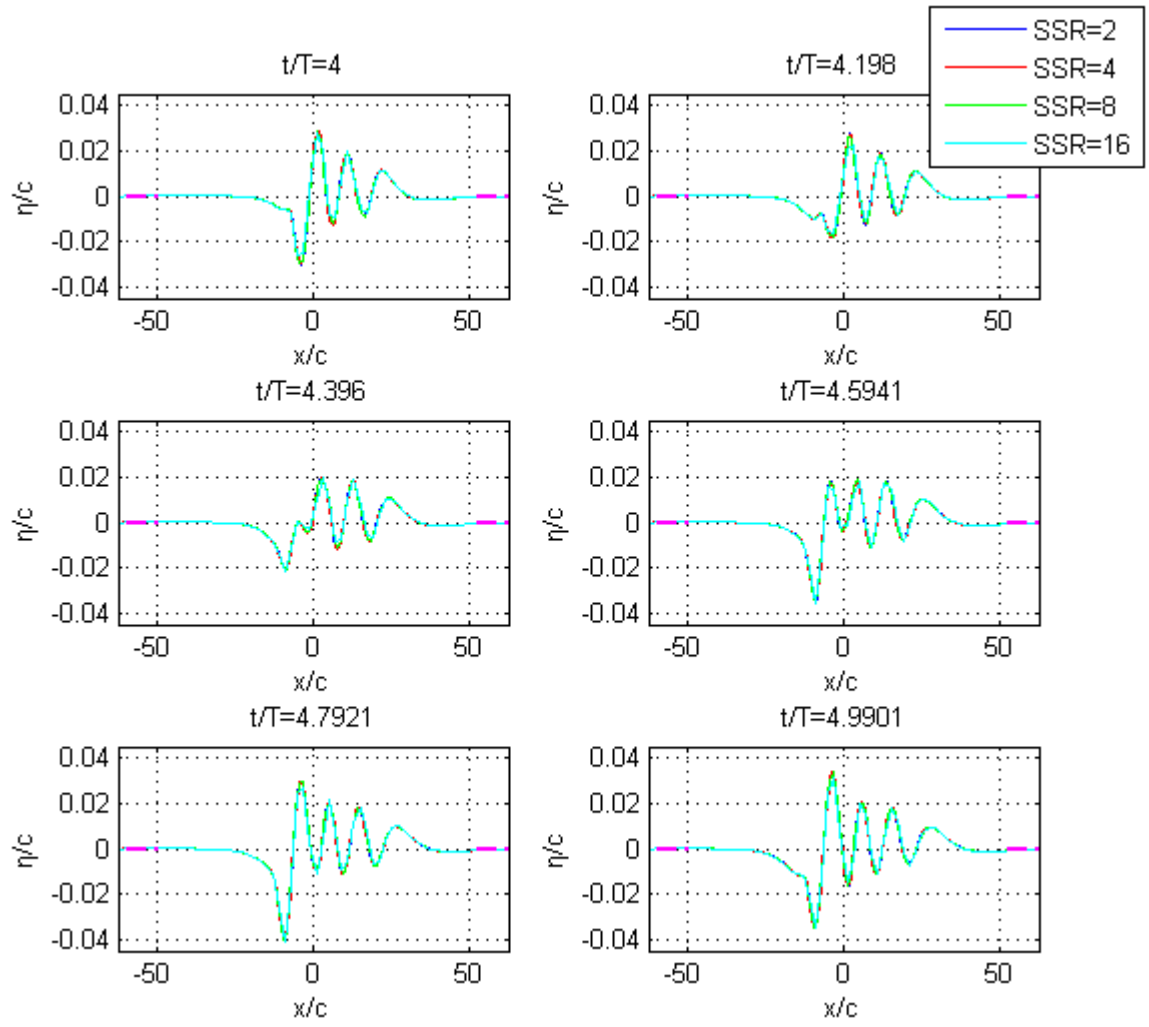


Figure 65: Convergence of $\eta(x;t)$ with respect to $SSR$, for a NACA0012 hydrofoil in flapping motion with $X_R/c=0.3$, $N_B=120$, $TSR=1$, $h_0/c=0.25$, $\theta_0=10°$, $Str=0.1$ and beneath the free surface with $d/c=3$, $Fn=2$ and $H/\lambda=48\%$, during the 5th period of oscillation.

In addition, in Fig. 65, the evolution free surface-elevation is presented for different values of $SSR$, $TSR=1\%$, $N_B=120$, for light flapping motion with $h_0/c=0.25$, $\theta_0=10°$, and $Str=0.1$, $X_R/c=0.3$, during the 5th period of oscillation. It is clear that convergence is achieved for $SSR\geq 4$. A wave that travels with the speed of the foil is generated; the decrease of pressure at the leading edge leads to a through followed by a crest that consist the main wave pattern which has time varying amplitude due to the oscillating motion. The wave, generated at the state of transition, gradually decays and thus transition to harmonic state occurs after 4 periods of oscillation. Notice that our result about the wavelength is in good agreement with the prediction from linear theory, i.e. $\lambda/c=12.5$. In that case the wave length due to the forward motion dominates, from Eq.(4.42) we have $\lambda_{for}/c=12.5$, while the wave length from oscillatory motion is small but not negligible, from Eq.(4.41) we have $\lambda_{osc}/c=2$, thus the resulting wave is steady in x-direction but oscillatory in y, with respect to the hydrofoil-fixed reference frame.

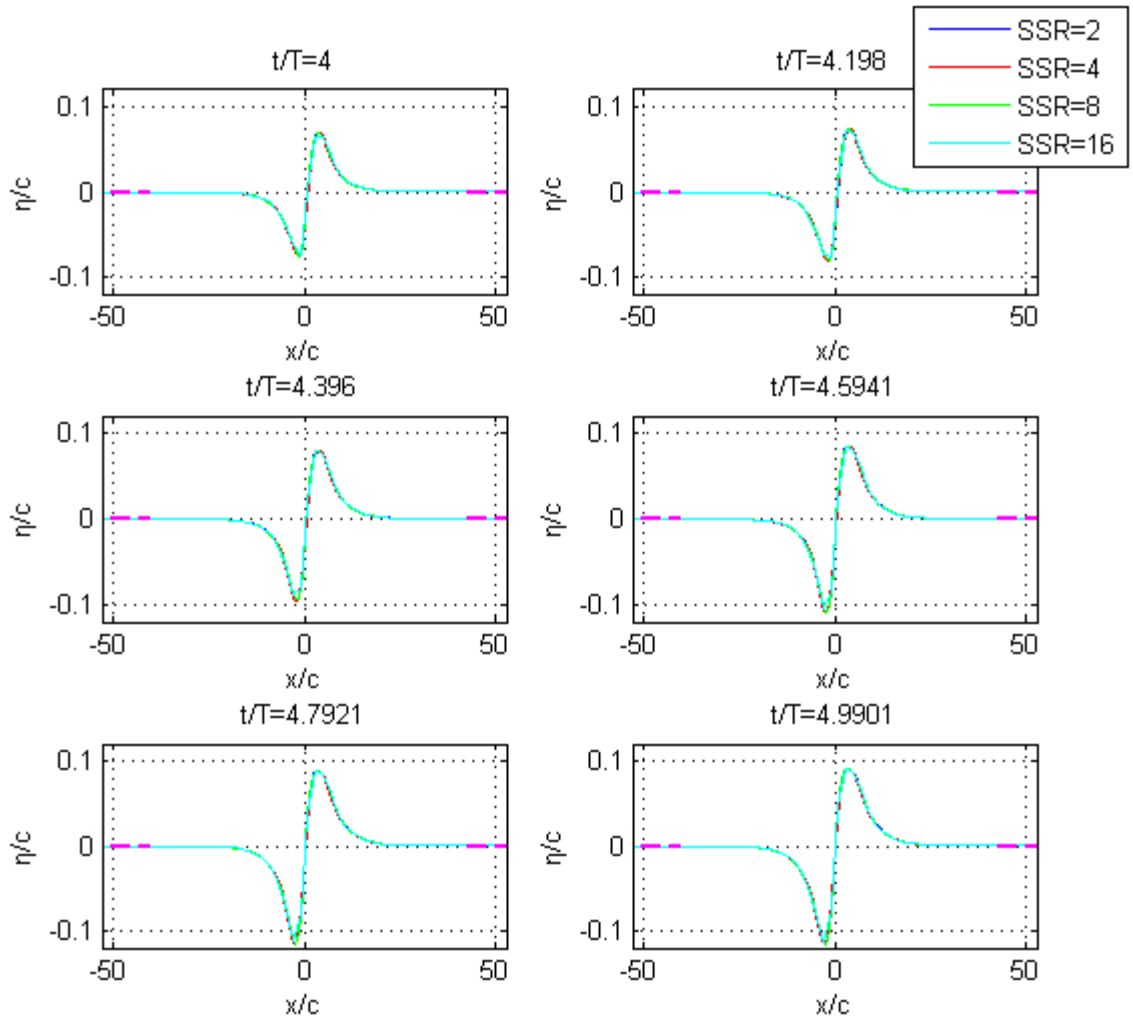


Figure 66: Convergence of $\eta(x;t)$ with respect to $SSR$, for a NACA0012 hydrofoil in flapping motion with $X_R/c=0.3$, $N_B=120$, $TSR=1$, $h_0/c=0.25$, $\theta_0=10°$, $Str=0.4$ and beneath the free surface with $d/c=3$, $Fn=2$ and $H/\lambda=48\%$, during the 5th period of oscillation.

Furthermore, in Fig. 66, the evolution free surface-elevation, during the 5th period of oscillation, is presented for the same case as in Fig. 65 but with $Str=0.4$. Again convergence is achieved for $SSR\geq 4$. In that case of higher $Str$ only one wave pattern that travels with the speed of the foil, is generated. In that case the wave length due to the forward motion dominates, from Eq.(4.42) we have $\lambda_{for}/c=12.5$, while the wave length from oscillatory motion is significantly smaller, from Eq.(4.41) we have $\lambda_{osc}/c=0.12$, thus the resulting wave is almost steady with respect to the hydrofoil-fixed reference frame.

To summarize, stability and convergence of the present scheme has been studied by extensive numerical investigation. For the range of motion parameters that we have tested i.e. $(d/c=1.5\div 3)$, Froude number $(Fn=0.25\div 2)$, Strouhal number $(St=0.1\div 0.4)$, reduced

frequency $\left(k_r = 0.1 \div 3.8\right)$, heaving $\left(h_0 / c = 0.25 \div 1\right)$ and pitching $\left(\theta_0 = 10° \div 40°\right)$ amplitude, in shallow, moderate and deep water $\left(H / \lambda = 4\% \div 300\%\right)$ a minimum number of $N_B = 120$ panels on the hydrofoil is required, while for harmonic motion the time step must be $\Delta t / T < 1\%$ (more than 100 time steps per period of oscillation) and the panel length on the free surface $\Delta x / \lambda < 4\%$ (more than 35 panels per wave length).

Stability of the numerical scheme had also been tested and we have found that it is achieved when a of Courant-Friedrichs-Lewy (CFL-type) condition is satisfied, as follows

$$\frac{C\Delta t}{\Delta x} \ll 1, \tag{4.62}$$

where C is the celerity of the generated free-surface waves. The exact critical value is frequency dependent and it is smaller for lower frequencies. A detailed study for the effects of other parameters on critical Courant number must be done, and this is left as a subject for future work.

Moreover, according to the efficiency of the scheme its is demonstrated that the application of the higher order Adams-Bashford-Moulton predictor-corrector method reduces significantly the required time step per period that are required for convergence in comparison with numerical results presented in Chapter 2 concerning the problem in infinite domain in the same range of parameters. In this way, the addition computational cost due to the discretization of the free-surface boundary is balanced and the time for computation remains of the same order of magnitude. In general, the reduction of problem's dimension from 2D to 1D due to BEM resulting in reduction of the computational cost, orders of magnitude less than other space-discretisation based numerical methods e.g. FDM's, FEM's. In addition, even more efficient higher order BEM's could be applied, see e.g. Cottrel et al (2009), Lee and Kerwin (2003), Belibassakis et al, (2013), and this is left as a subject for future extension.

### 4.6.3 Hydrofoil in steady motion under the free surface

Numerical computations and results for NACA4412 hydrofoil at a stationary angle of attack $5°$ and a variety of Froude numbers $Fn = U / \sqrt{gc}$ and submergences $d / c$ of the foil are shown in Figs. 67-70. In all cases deep water conditions $(H / \lambda >> 0.5)$ are assumed. Present method results are based on $N_B = 120$ panels on the body, the number of free-surface panels per wavelength is $N_F / \lambda = 25$, and the time step $U\Delta t / \lambda = 4\%$. Transition from rest to steady state condition has been accomplished after a distance of 10 chord lengths.

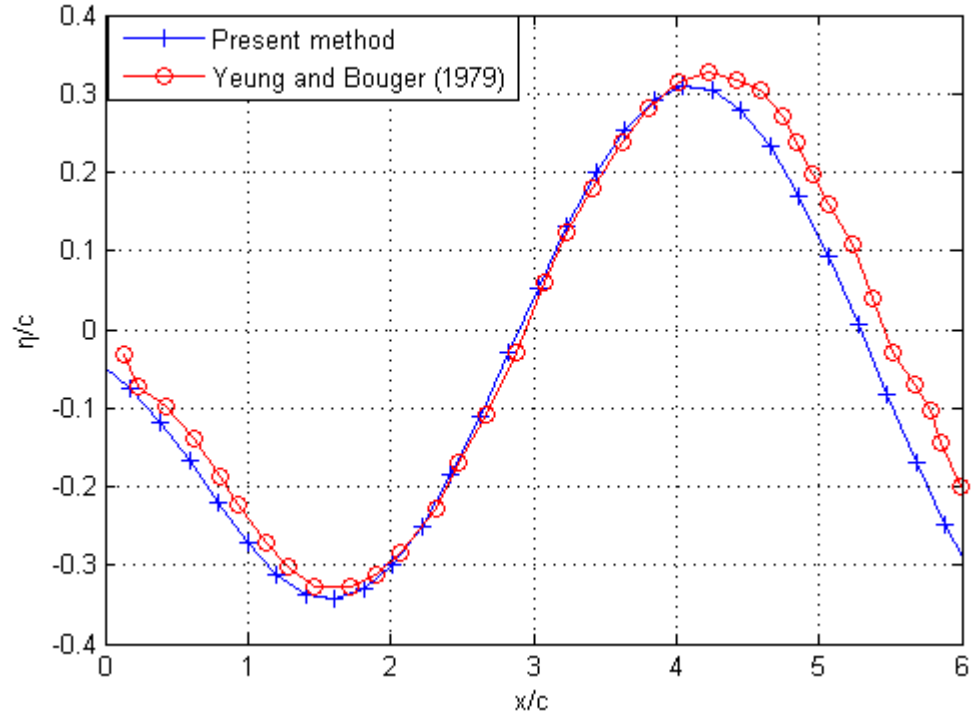


Figure 67: Free-surface elevation for a NACA4412 hydrofoil, at $5°$ angle of attack, for $Fn = 0.9$ and submergence $d / c = 1$ (with respect to the trailing edge of the foil).

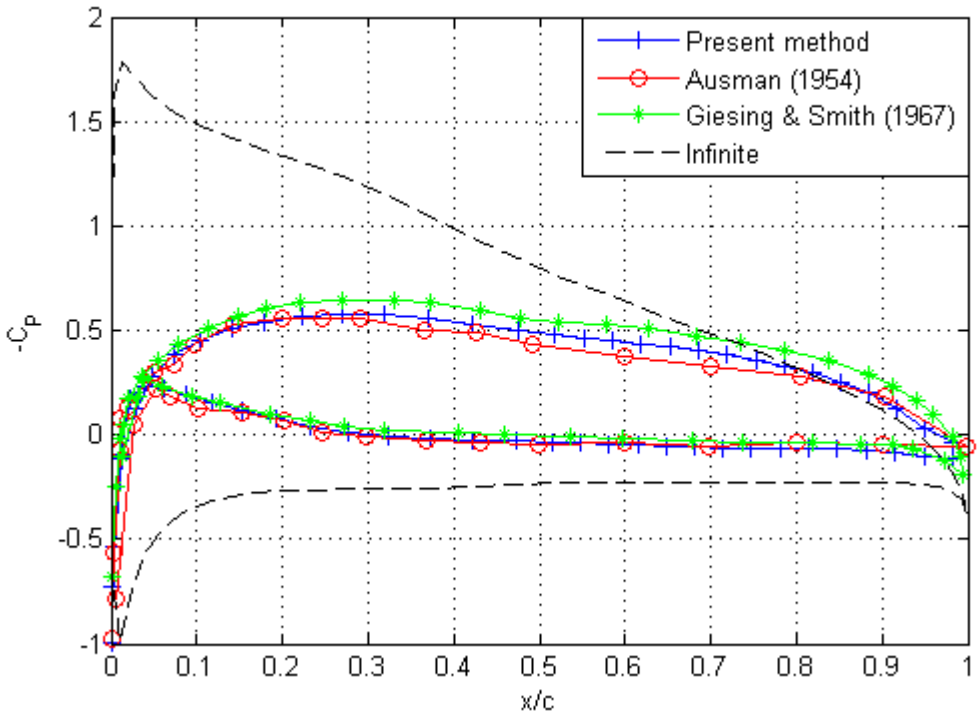


Figure 68: Pressure coefficient for a NACA4412 at $5°$ $Fn = 1.03$ and submergence $d / c = 0.6$ (with respect to the midchord of the foil).

Results for both distributed and integrated quantities are presented in comparison with numerical results from steady state panel methods by various authors (denoted in the figures) and experimental measurements by Ausman (1954). In particular, the wave elevation for $Fn = 0.9$ and $d/c = 1$ is shown in Fig.67. Also, the pressure coefficient at somewhat greater Froude number $Fn = 1.03$ and smaller submergence of the foil $d/c = 0.6$ is plotted in Fig.68. In both cases we observe that present results are in good agreement with other methods and experimental data. To illustrate the effects of the free surface on the generation of the lift, we include in Fig.72 a calculation with the foil in infinite domain. We notice that free-surface effects result in significant decrease of pressure jump on the foil and reduction of suction force at the leading edge. The latter is, in general, responsible for the loss of lift and the increase of the wave resistance.

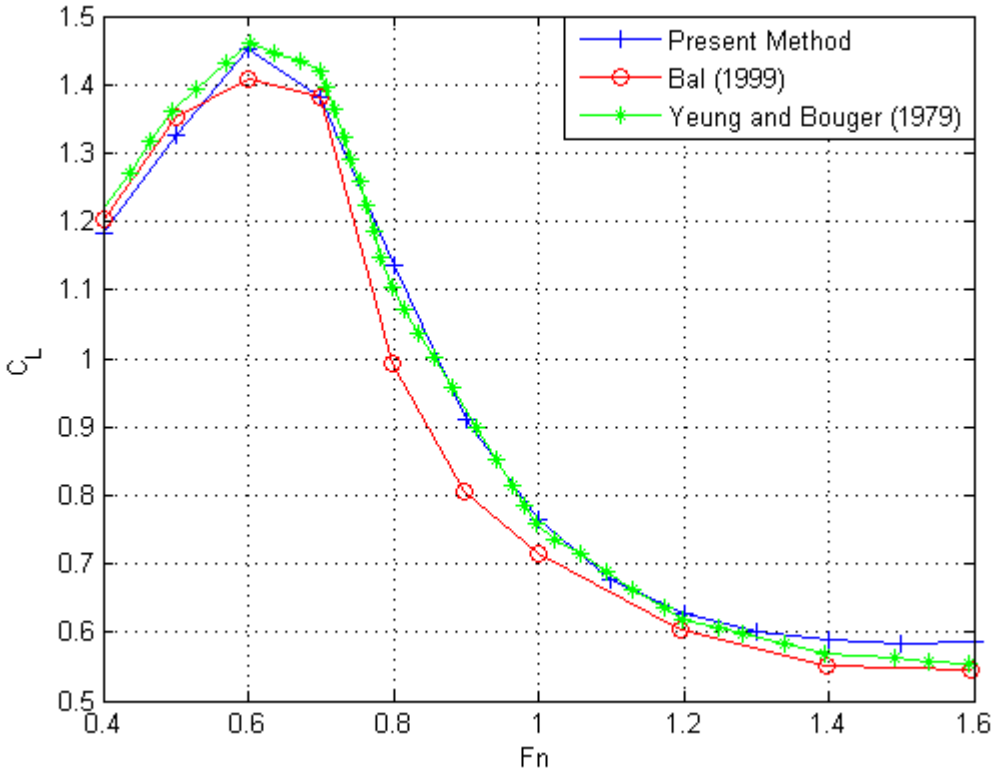


Figure 69: Lift coefficient for a NACA4412 hydrofoil, at $5°$ angle of attack, for submergence $d/c = 1$ (with respect to the trailing edge of the foil), against Froude number.

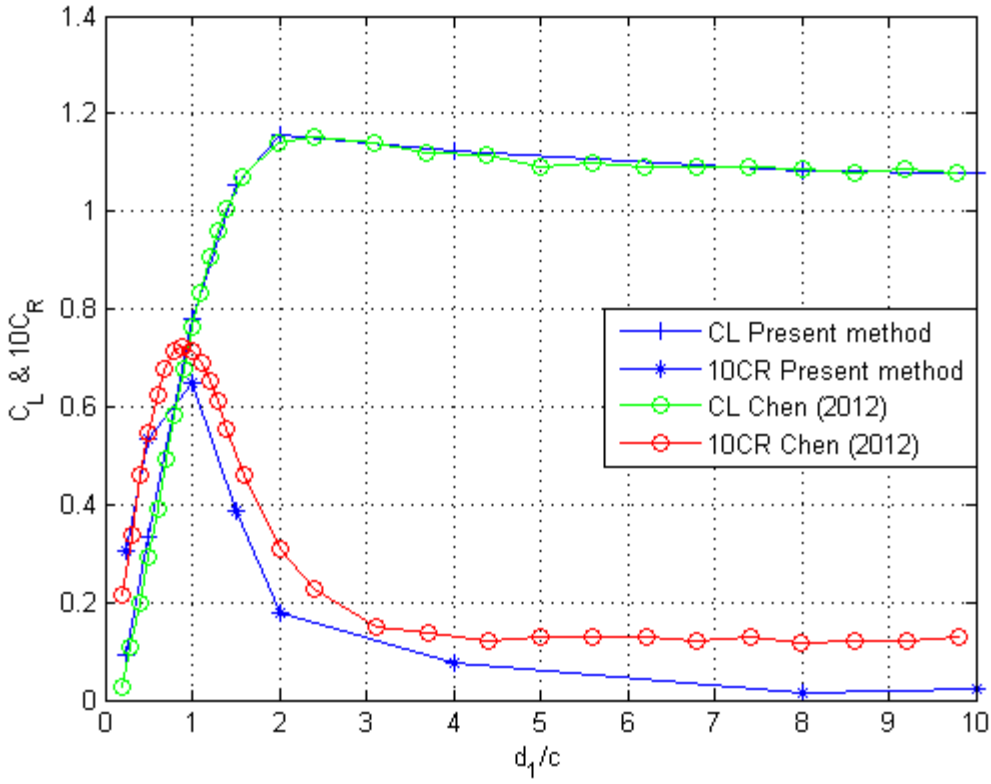


Figure 70: Lift and wave resistance coefficients for NACA4412 hydrofoil at 5° and $Fn=1$, against submergence (with respect to the midchord of the foil).

Furthermore, in Fig. 69 the effect of Froude number on the lift coefficient for foil submergence $d/c=1$ is shown, and compared with predictions by Bal (1999) and Yeung & Bouger (1979). It is seen that the free surface causes a drop in $C_L$ as Froude number Increases. The effect of free surface on lift and wave resistance coefficient ($C_R = F_X / 0.5\rho U^2 c$), for $Fn=1$, is presented in Fig.70 and compared with predictions by Chen (2012). We observe in this figure that as submergence increases the lift converges to its value in infinite domain and that wave resistance tends to zero, as expected.

Finally, an interesting observation concerns the shape of the induced waveform by hydrodynamically shaped bodies advancing with forward speed beneath the free surface. Notice that significant differences occurs between the wave generated by the elliptically shaped non-lifting body in Figure 47 of Section 3.5 and by the hydrofoil NACA4412 in Fig. 67. In particular the wave generated by the non-lifting body consists of a crest, over the high pressure vicinity on the bow, followed by a trough, while in the case of lifting hydrofoil the wave form is antisymmetric. Obviously the difference is due to the circulation that is developed in the lifting case which removes the stagnation point that is responsible causes the compression.

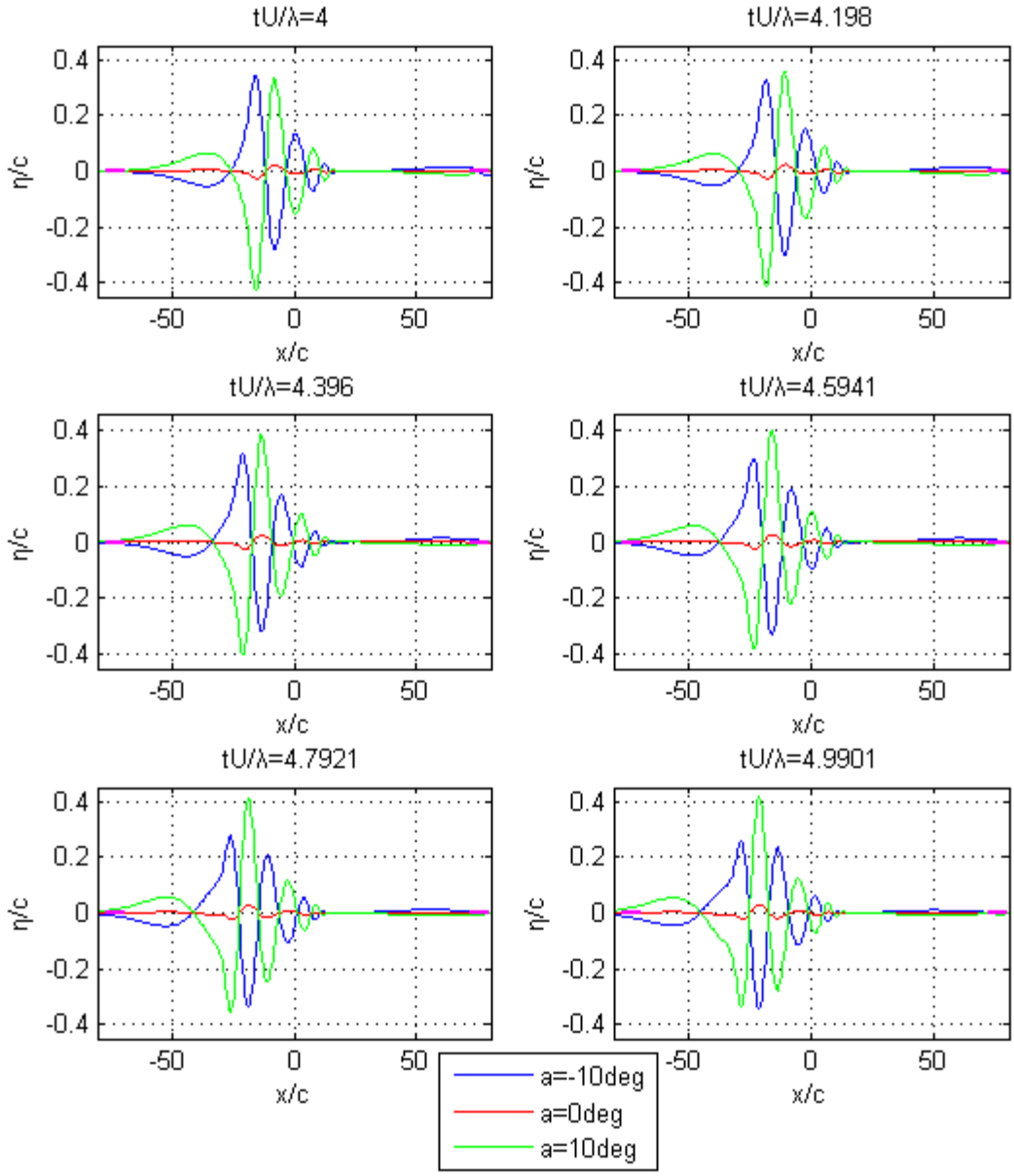


Figure 71: Free-surface elevation generated by a symmetric NACA0012 hydrofoil advancing at $Fn = 2$, for different angles of attack $(a = -10°, 0°, 10°)$, at $d / c = 3$ and $H / \lambda = 48\%$.

To demonstrate that, we plot in Fig. 71 the free-surface elevation generated by a symmetric NACA0012 hydrofoil advancing at $Fn = 2$, for different angles of attack $(a = -10°, 0°, 10°)$, at $d / c = 3$ and $H / \lambda = 48\%$.

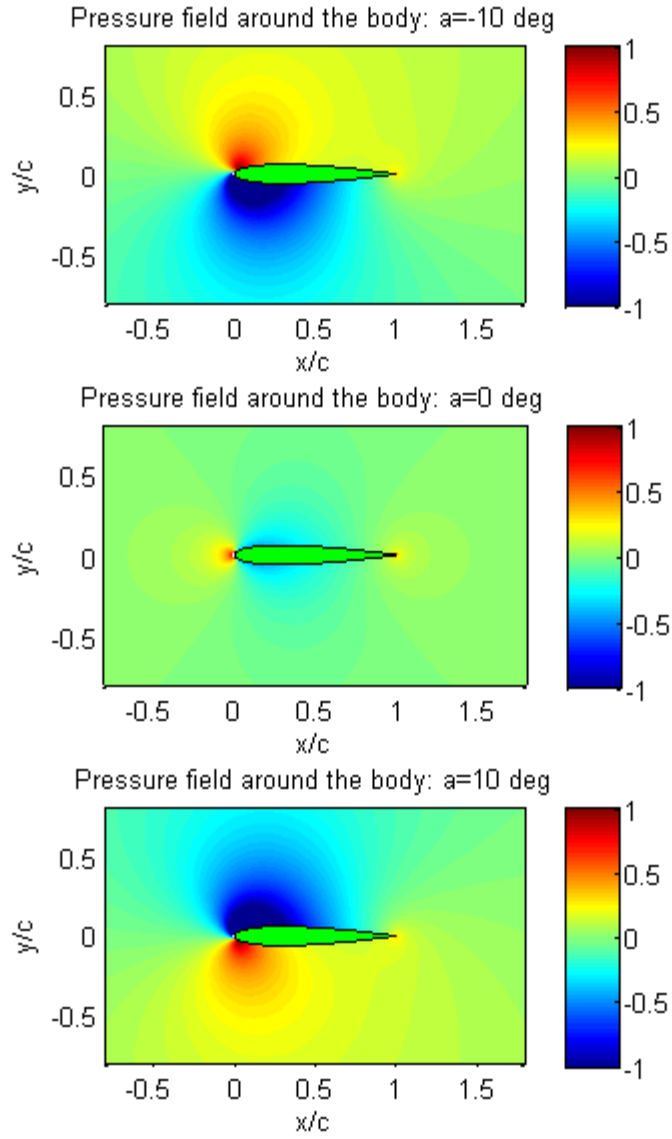


Figure 72: Pressure field around a NACA0012 hydrofoil in steady motion at different angles of attack $a = -10°, 0°, 10°$, in infinite domain. the induced circulation moves the maximum pressure point in different places on the upper or the lower side of the foil.

Also for better understanding, in Fig. 72 the pressure field for NACA0012 in the same angles of attack is presented, calculated in infinite domain by steady BEMs (Filippas, 2011). Notice that negative angles of attack leads to a stagnation point and a maximum pressure point on the upper surface and in that case a similar to the non-lifting case wave-pattern, starting with crest is observed. When the angle of attack is zero or positive, clockwise circulation leads to acceleration and drop of pressure on the upper side of the hydrofoil and thus a trough is generated in that vicinity, followed by a crest.

### 4.6.4 Free-surface effects on flapping foil thruster

In this section numerical results are presented concerning a flapping hydrofoil under the free surface. Except of forward translation with constant speed $U$, the hydrofoil also performs combined vertical (heaving) and rotational (pitching) oscillatory motions, the latter with respect to a pivot axis located at a specific distance $X_R$ from the leading edge. The phase difference between pitching and heaving motion is denoted by is appropriately selected $\psi = -90\,\text{deg}$; see e.g. Rozhdestvensky and Ryzhov (2003). The Strouhal number of the hydrofoil is $St = \omega h / \pi U = (2/\pi) k (h/c)$, with $k_r = \omega c / 2U$ the reduced frequency, and $\varepsilon = \theta_0 U / \omega h_0$ is the feathering parameter. The numerical parameters are kept the same as in the previous section.

In Fig. 73 we compare integrated results concerning a thrust coefficient defined as $T / \rho g h_0^2$ (where $T$ is the trust and $h_0$ the heave amplitude) obtained by the present method against predictions by linearised theory for thin uncambered hydrofoil developed by Grue et al (1988). The latter model is based on oscillating flat plate beneath the free surface. For compatibility in the comparison a thin symmetrical NACA0006 hydrofoil is simulated in small-amplitude oscillations. Results have been obtained for heaving oscillatory and flapping motion, respectively, and are plotted in Fig.73 against the non-dimensional frequency $\Omega = \omega^2 c / 2g$. We can see present method predictions are in good agreement with thin hydrofoil theory.

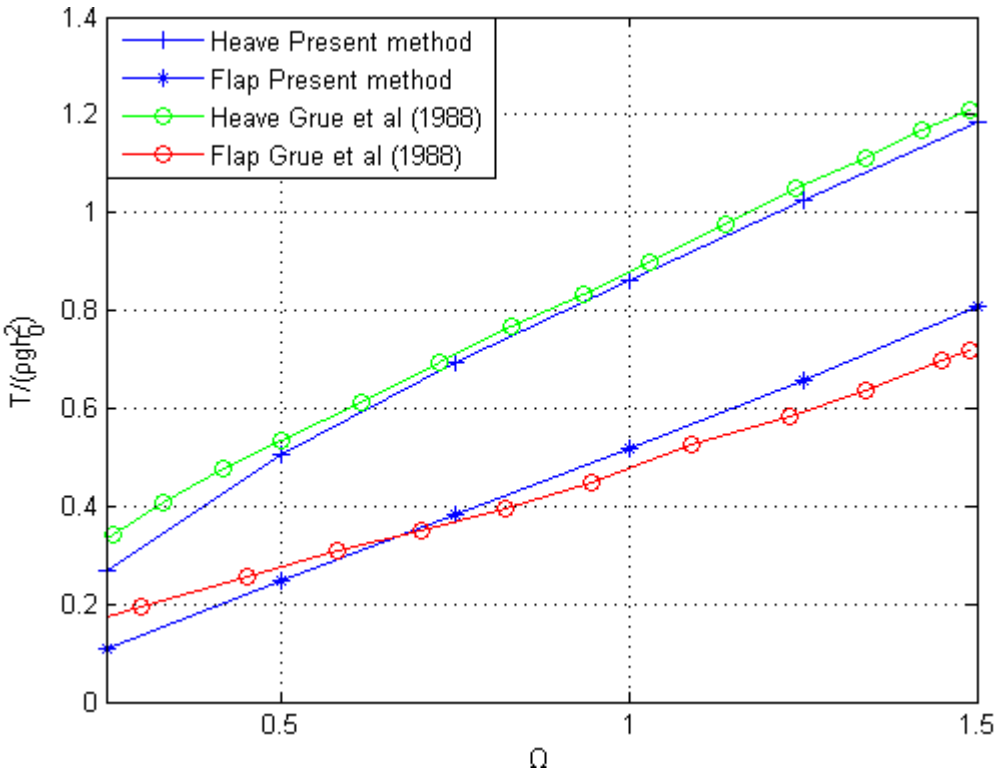


Figure 73: Thrust coefficient $T / \rho g h_0^2$ against non dimensional frequency $\Omega$, for NACA0006 hydrofoil at $d/c = 0.5$, in heaving and flapping motions. Feathering parameter $\varepsilon = 0.6$, pivot point $X_R / c = 0.5$, and heave-pitch phase lag $\psi = -90°$.

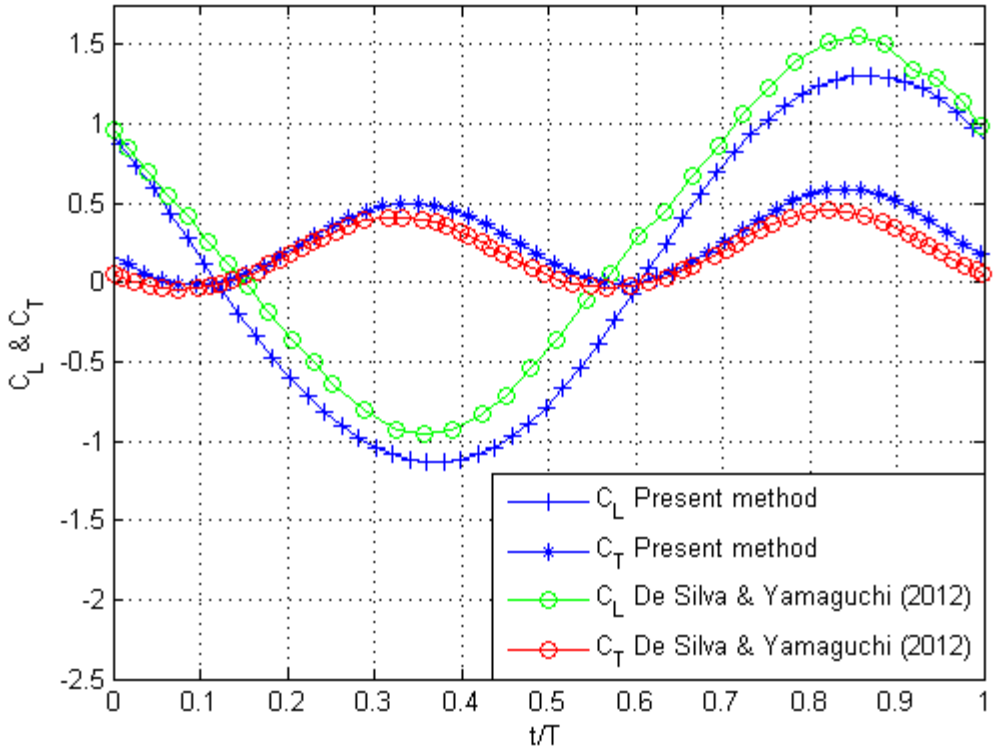


Fig. 74 Lift and thrust coefficients for NACA0015 at $Fn = 0.87$ and submergence $d/c = 1.28$. In this case $St = 0.18$, $h_0/c = 0.6$, $\theta_0 = 15.2°$, pivot point $X_R/c = 0.3$ and phase lag $\psi = -105°$.

A further comparison between the present potential flow method and recent computations by De Silva & Yamaguchi (2012) based on CFD solver (FLUENT) is presented in Fig. 74. Our results concerning the lift coefficient of a NACA0015 section at $Fn = 0.87$ are found in very good agreement with the viscous solver. On the other hand, more increased differences concerning the thrust coefficient are observed, attributed to viscosity effects that are not taken into account. In any case the present method is again found to be able to provide reasonable predictions, at least in the examined examples which are characterized by small and moderate angles of attack, where leading edge separation and dynamic-stall effects are not manifested.

In the second part of the present subsection we choose the example of intense flapping motion with $h_0/c = 1$, $\theta_0 = 40°$, and $Str = 0.4$, $X_R/c = 0.3$, to study the effects of Froude number $(Fn = 0.25 \div 2)$ and of the additional boundaries i.e. free surface & seabed and also to test compatibility with results concerning the same problem in infinite domain as the Froude number decreases and as the boundaries moves away from the flapping foil. For that purpose the submergence of the foil is $d/c = H/2c = Dist$ and raises from 1.5 to 48. The numerical scheme's parameters are $N_B = 120$, $TSR = 1$, $SSR = 4$, $\sigma_0 = 3$, $p = 3$, $l/\lambda = 1$.

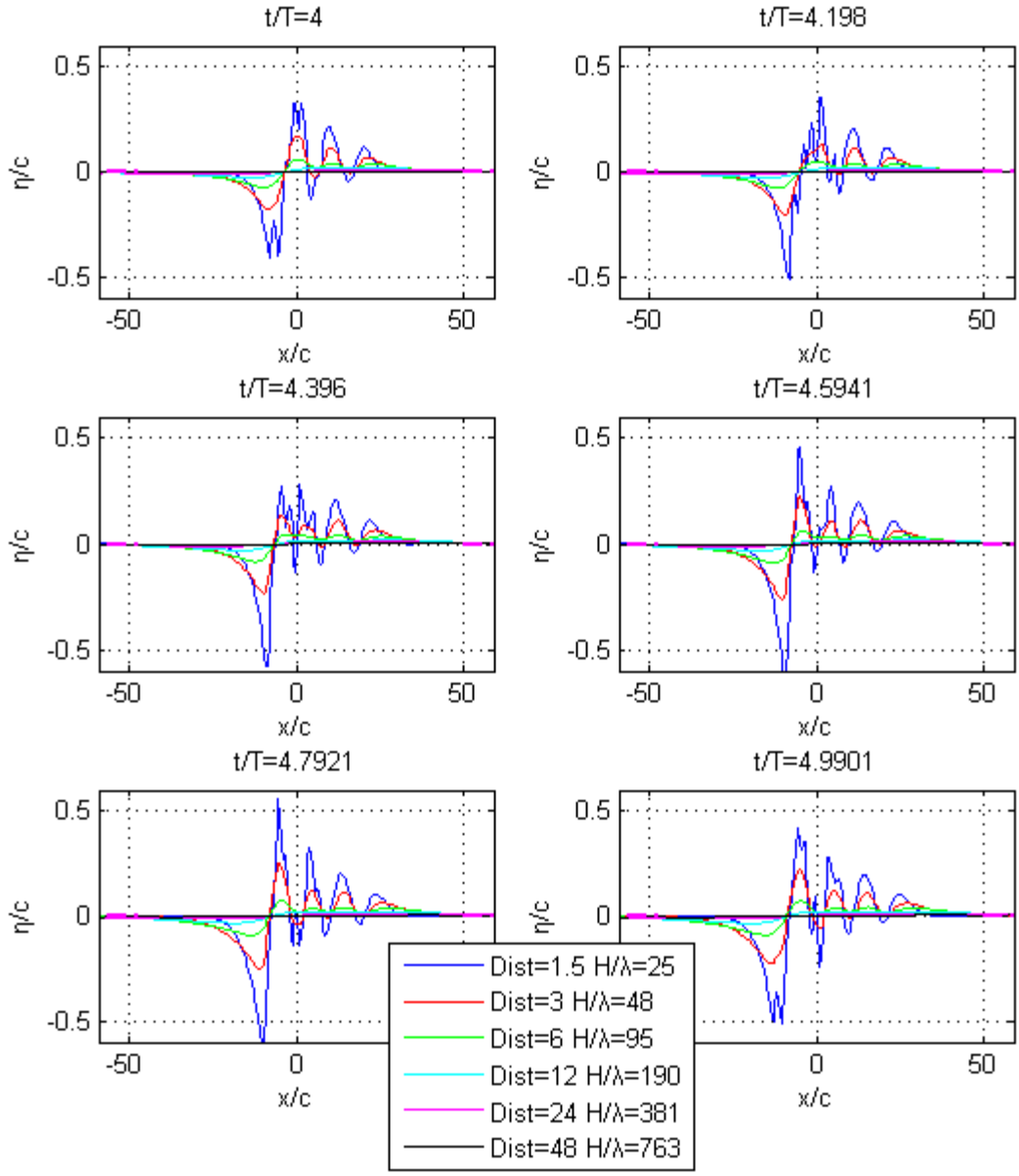


Figure 75: Free surface elevation for increasing distance between the foil and the boundaries, for a NACA0012 hydrofoil in flapping motion with $X_R / c = 0.3$, $\mathrm{N_B} = 120$, $TSR = 1$, $h_0 / c = 1$, $\theta_0 = 40°$, $Str = 0.4$, $Fn = 2$ during the $5^{\text{th}}$ period of oscillation.

In Figure 75, the free surface elevation during the last period is presented for increasing distance $(Dist = 1.5 \div 48)$ between the hydrofoil and the boundaries. Notice that as the boundaries moves away the wave tends to a small amplitude harmonic wave, in compatibility with linear fee-surface wave theory, and for even larger distances $Dist > 12$ there is practically no wave generation.

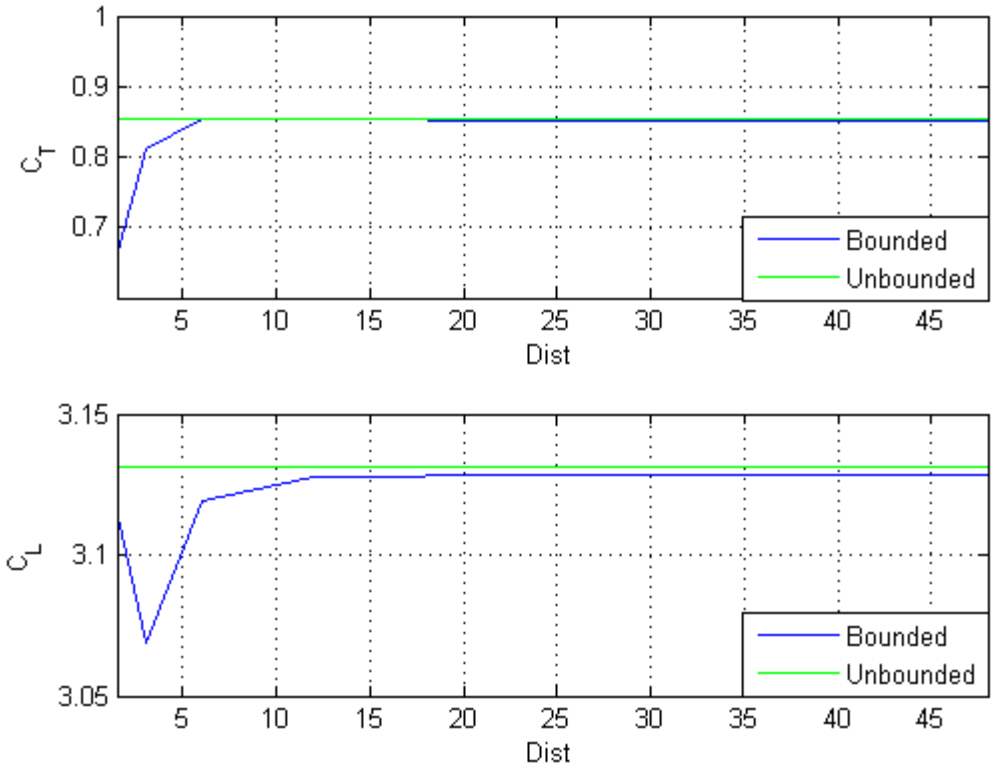


Figure 76: Thrust and lift coefficients with respect to the distance between the foil and the boundaries, for a NACA0012 hydrofoil in flapping motion with $X_R / c = 0.3$, $\mathrm{N_B} = 120$, $TSR = 1$, $h_0 / c = 1$, $\theta_0 = 40°$, $Str = 0.4$, $Fn = 2$, averaged over the 5th period of oscillation.

Additionally, in Figure 76, integrated characteristics are presented for increasing distance $(Dist = 3,12,48)$ between the hydrofoil and the free surface and bottom. Also, comparison with the result in infinite domain is given. Notice that as the boundaries moves away average thrust coefficient and amplitude of lift coefficient tend to the corresponding to infinite domain results.

Moreover, in Figure 77 we present calculations concerning the average thrust coefficient and the average and amplitude of lift coefficient for three cases $d / c = 1.5, 3, 4.5$ for low intermediate and deep submergence. In the last case the hydrofoil performs in a very close distance to the bottom and the effect of that solid boundary dominates. Notice that a mean lift force appears as the foil approaches the free surface while for infinite domain average lift force is zero for symmetrical foils in symmetrical flapping motion. This is due to the acceleration of flow (conservation of mass) in the narrow area between the leading edge and sea surface, when the leading edge is at the highest position of its trajectory. That acceleration leads to fall of pressure on the upper side of the foil that is greater than the corresponding fall on the lower side when the leading edge reaches the lowest level of it trajectory. A similar phenomenon is mentioned when the foil approached the bottom and a negative average lift occurs. In general, when the foil operates near the bottom the forces increase. Notice also that the average values of integrated forces decreases for increasing Froude numbers and that decrease is more significant for lower submergence.

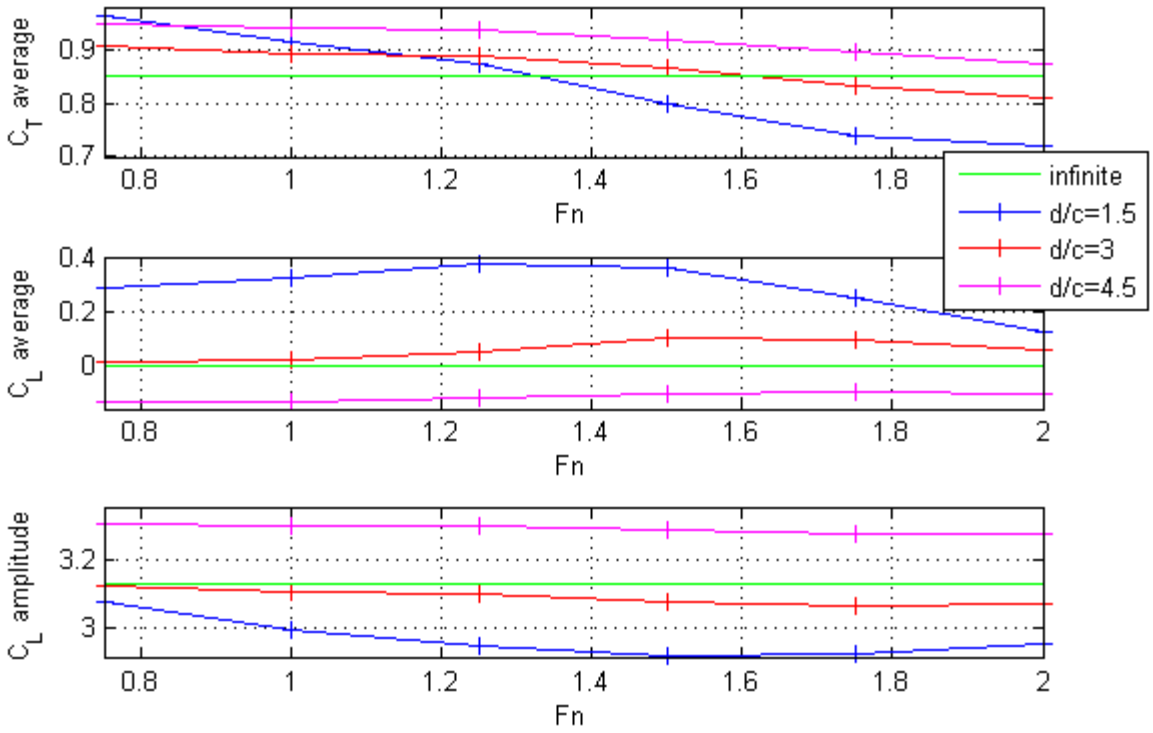


Figure 77: Integrated characteristics against Froude number, for a NACA0012 hydrofoil in flapping motion with $X_R / c = 0.3$, $\mathrm{N_B} = 120$, $TSR = 1$, $h_0 / c = 1$, $\theta_0 = 40°$, $Str = 0.4$, for submergence $d / c = 1.5, 3, 4.5$ and depth $H / \lambda > 43\%$ in comparison with results in infinite domain.

Furthermore, the effects of free surface and bottom weaken as the distance between the foil and the boundaries increases (case of $d_1 / c = 3$) and the results tend to approach their values in infinite domain.

Finally, in Fig 78 we focus to the effect of bottom, using the same example of intense flapping motion with $h_0 / c = 1$, $\theta_0 = 40°$, and $Str = 0.4$, $X_R / c = 0.3$ in low submergence $d / c = 1.5$. Integrated results are presented, concerning average thrust coefficient and amplitude of lift coefficient against $H / \lambda$ that varies from moderate to deep water. The effect of bottom is significant, as expected, in the region of moderate depth $H / \lambda < 0.5$, while for deep water $\left(H / \lambda > 0.5\right)$ the value of forces on the foil remains practically constant. In general, amplitude of $C_L$ increases while average $C_T$ decreases, in moderate depth.

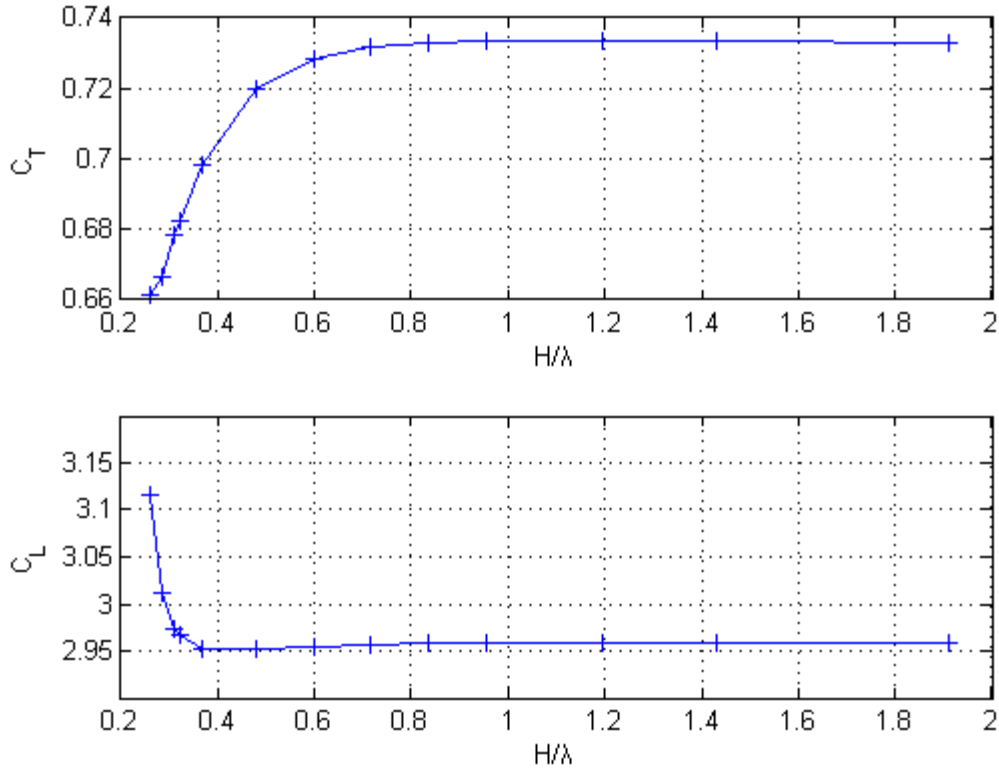


Figure 78: Integrated characteristics against sea depth, for a NACA0012 hydrofoil in flapping motion with $X_R / c = 0.3$, $\mathrm{N_B} = 120$, $TSR = 1$, $h_0 / c = 1$, $\theta_0 = 40°$, $Str = 0.4$, for submergence $d / c = 1.5$

It is clear from the above, that the method developed in Chapters 3 and 4 for hydrodynamic analysis of unsteady bodies beneath the free surface and over flat bottom is compatible with the method described in Chapter 2 concerning the same problem in infinite domain. In the following paragraphs, comparisons with other numerical methods and experimental results from the literature are presented, in order to demonstrate the range of applicability and the limitations of the present method.

### 4.6.5 Flapping foil thruster in waves

Finally, we present numerical results in the case of flapping foil of chord $c = 7m$ operating in waves of frequency $\omega_I = 0.66\,rad/s$, in deep water conditions studied by De Silva & Yamaguchi (2012). The phase difference between incident wave and foil heaving motion is $\varphi = -90°$, the wave amplitude is $\eta_0 / c = 0.14$ and the corresponding frequency of encounter is $\omega_{en} = \omega_I + kU = 0.98\,rad/s$, which is equal to the frequency of oscillation $(\omega)$. The Strouhal

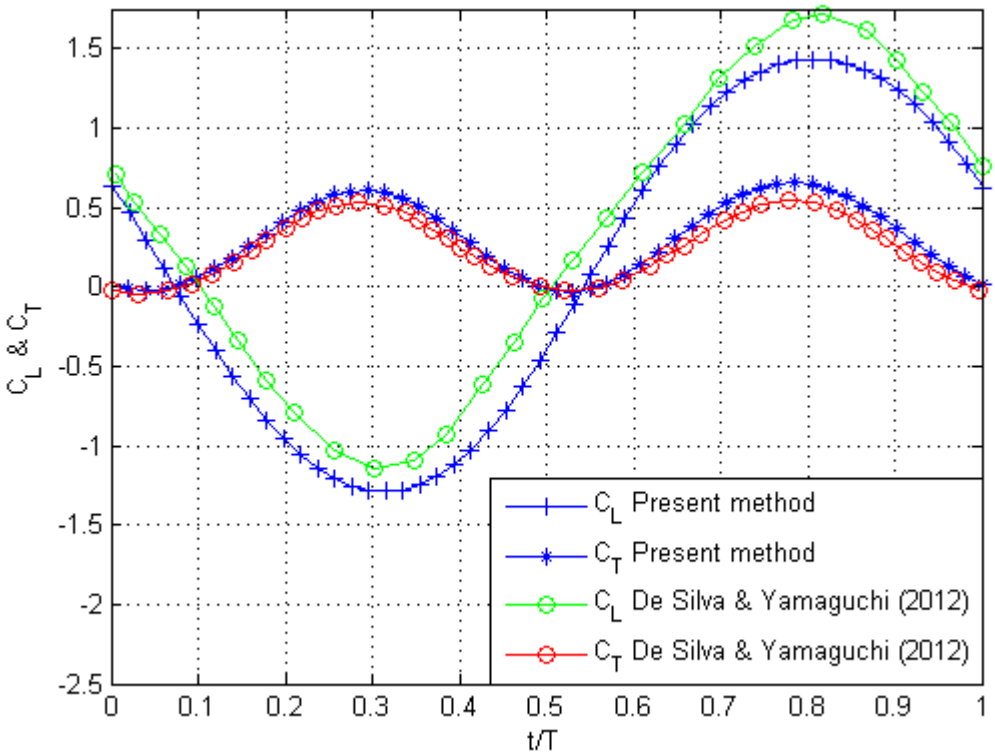


Figure 79. Same as in Fig.74 for a hydrofoil of chord $c = 7m$, in the presence of incident waves: $\eta_0 / c = 1/7$, $\omega_I = 0.66$ and $\varphi = -90°$.

number and rest parameters remains the same as in the previous case. Comparisons concerning lift and thrust coefficient against predictions by De Silva & Yamaguchi (2012) are shown in Fig.79. Again, for the particular conditions, present BEM is shown to provide satisfactory predictions, however, the computational cost is order(s) of magnitude less, making the present method, after enhancements and extensions a useful tool for the design and performance of flapping foil thrusters in waves.

Finally in Fig. 80 we demonstrated the effect of phase difference between the heaving motion and the incoming wave. The example is about a NACA0012 hydrofoil at $Fn = 2$ and submergence $d / c = 3$, in intense thrust producing flapping motion, with $Str = 0.4$, $h_0 / c = 1$, $\theta_0 = 40°$, pivot point $X_R / c = 0.3$ and phase lag between heaving and pitching motion $\psi = -90°$. In the presence of incident waves with $\eta_0 / c = h_0 / c = 1$, $\omega_{en} h / \pi U = Str = 0.4$.

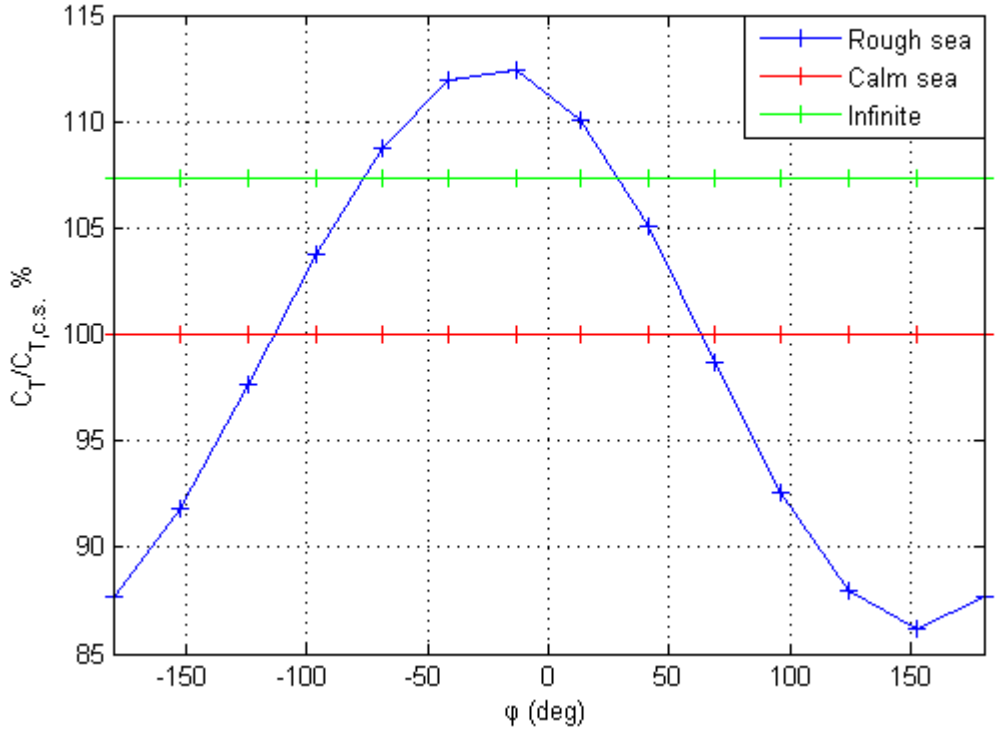


Figure 80: Average thrust coefficient against phase difference $\varphi$ between incident free-surface elevation wave and heaving motion, for a NACA0012 hydrofoil at $Fn = 2$ and submergence $d/c = 3$ in moderate to deep water $\mathrm{H}/\lambda = 48\%$. In intense flapping motion with $Str = 0.4$, $h_0/c = 1$, $\theta_0 = 40°$, pivot point $X_R/c = 0.3$ and phase lag between heaving and pitching motion $\psi = -90°$. In the presence of incident waves with $\eta_0/c = h_0/c = 1$, $\omega_{en}h/\pi U = Str = 0.4$.

Notice that the effect of free surface boundary in that case causes a reduction 7.3% of thrust force, due to wave generation (wave resistance and radiation), in comparison with the thrust production in very large submergence (infinite domain), where the thrust coefficient is predicted $C_{T,\inf} = 0.87$ (recall from Section 2.9 that our method in infinite domain for high amplitudes and frequencies, overpredicts thrust, however a very interesting qualitative study can be done). However, there exist a region, $\varphi = -113.4° \div 63°$, where energy extraction from waves raises the total thrust free of cost at a maximum percentage of 12.4% of its value in calm sea at $\varphi = -13°$. Moreover in the region $\varphi = -77° \div 28.5°$, wave energy extraction overcomes the losses due to wave generation and the values of thrust are even larger of the corresponding in infinite domain.

It is expected that even greater amounts of energy could be extracted from waves using proper control of flapping motion, possibly increasing the hydrodynamic efficiency of the flapping-foil propulsor in comparison with conventional propellers. Taking into account that the most energy-absorbing motion (i.e. foil's heave) for the propulsion is induced free of cost by the motions of the ship (reducing simultaneously undesirable ship's pitching), the efficiency of the system could reach levels over 100%, providing concurrently a more enjoyable voyage

### 4.7 Conclusions and suggestions for future work

An unsteady Boundary Element Method is developed and applied to the analysis of flapping hydrofoils operating beneath the free surface, and in the presence of incident waves. The modelling includes finite-depth effects. Previous studies concerning flapping foils have shown that such systems, at optimum operating conditions, could achieve high thrust levels and efficiency. The present study has been focused on studying the effects of the free surface and the bottom, which for relatively low submergence and depth respectively, could become quite important.

Results are shown illustrating the numerical performance of the developed BEM and validating it through comparisons with other methods and experimental data. Numerical predictions include lift, thrust and resistance coefficients, and also distributed quantities such as free-surface elevation and boundary pressure coefficient of the system, over a range of motion parameters, such as reduced frequency, Strouhal number, feathering parameter and free-surface parameters such as Froude number, nondimensional frequency $\Omega$, depth to wavelength ratio.

Future extensions include the introduction and modelling of various non-linearities associated with the evolution of the free surface and the trailing vortex sheets. Furthermore, treatment of leading edge separation and dynamic stall effects would extend its applicability to operation conditions corresponding to large angles of attack.

## Epilogue

Biomimetic systems such as flapping wings located beneath the hull of the ship are investigated at NTUA as an unsteady thruster, augmenting the overall propulsion of the ship and offering dynamic stabilization. In this direction, an unsteady Boundary Element Method is developed in the present thesis and applied to the solution of the potential flow problem around 2D lifting bodies of general shape performing a general, prescribed motion in stationary fluid and in incoming waves.

The present study is focused on studying the effects of the free surface and the bottom, which for relatively low submergence and depth respectively, could become quite important. For the detailed investigation of the effects of the free surface a potential-based panel method has been developed for the hydrodynamic analysis of 2D nonlifting bodies and hydrofoils, undergoing heaving (vertical) and pitching oscillations while moving with constant forward speed. The instantaneous angle of attack is influenced by the foil oscillatory motion and by the incident waves. At a first stage of development we consider moderate submergence and relatively low speeds permitting us to approximately linearise the free surface conditions and neglect effects due to breaking waves and cavitation.

Various specific extensions and further enhancements of the present model have been proposed in the last sections of Chapters 2, 3 and 4 and are left to be examined in the next period. An important, more demanding direction for future work is the extension of the present numerical scheme and investigation to 3D, supporting the study of the propulsive performance generally shaped wings taking into account finite span and interaction with the hull of the ship. Another direction deals with the implementation of high-order BEMs using B-Splines or NURBS for the representation of the geometry and the unknown distributions of singularities on the boundary, accelerating the convergence and leading to increased numerical efficiency.

## Appendix A - Representation theorem for the potential

The theory of the integral equations is based on the representation of the potential in terms of boundary values of the potential and its derivative. Here we are going to present the proof of a useful formula and next, the construction of the boundary integral equation whose solution provides the boundary values of the potential and its derivative. In this way only boundary values is required for the knowledge of the potential all over the domain.

Let $(x_0, y_0) \in \mathbb{R}^2 \setminus D$ and $(x, y) \in D$ and thus $(x, y) \neq (x_0, y_0)$, in this case it holds:

$$\Delta\left[\ln r(x, y \mid x_0, y_0)\right] = 0, \ \forall (x_0, y_0) \in \mathbb{R}^2 \setminus D \ \text{ and } \ (x, y) \in D, \tag{A.1}$$

where $r(x, y \mid x_0, y_0) = \sqrt{(x - x_0)^2 + (y - y_0)^2}$ .

Furthermore since $\Delta \ln r$ is a well defined function on $D$, we can take its surface integral:

$$\iint_D \Delta\left[\ln r(x, y \mid x_0, y_0)\right] dxdy = 0. \tag{A.2}$$

Let now $(x_0, y_0) \in D$. In this case in the integration region exists a point $(x, y) \in D$ so as to $(x, y) = (x_0, y_0)$ therefore the previous process cannot be applied directly. In order to perform a similar process we surround $(x_0, y_0)$ with a circular disk with radius R (Figure 81). We define in this way a circular vicinity $D_0$ around $(x_0, y_0)$ such as $(x, y) \notin D_0$:

$$D = (D \setminus D_0) \cup D_0. \tag{A.3}$$

Now $\Delta \ln r$ is well defined and harmonic in $D \setminus D_0$ and thus:

$$\iint_{D \setminus D_0} \Delta\left[\ln r(x, y \mid x_0, y_0)\right] dxdy = 0, \tag{A.4}$$

therefore

$$\iint_D \Delta\left[\ln r(x, y \mid x_0, y_0)\right] dxdy = \iint_{D_0} \nabla\left[\nabla \ln r(x, y \mid x_0, y_0)\right] dxdy. \tag{A.5}$$

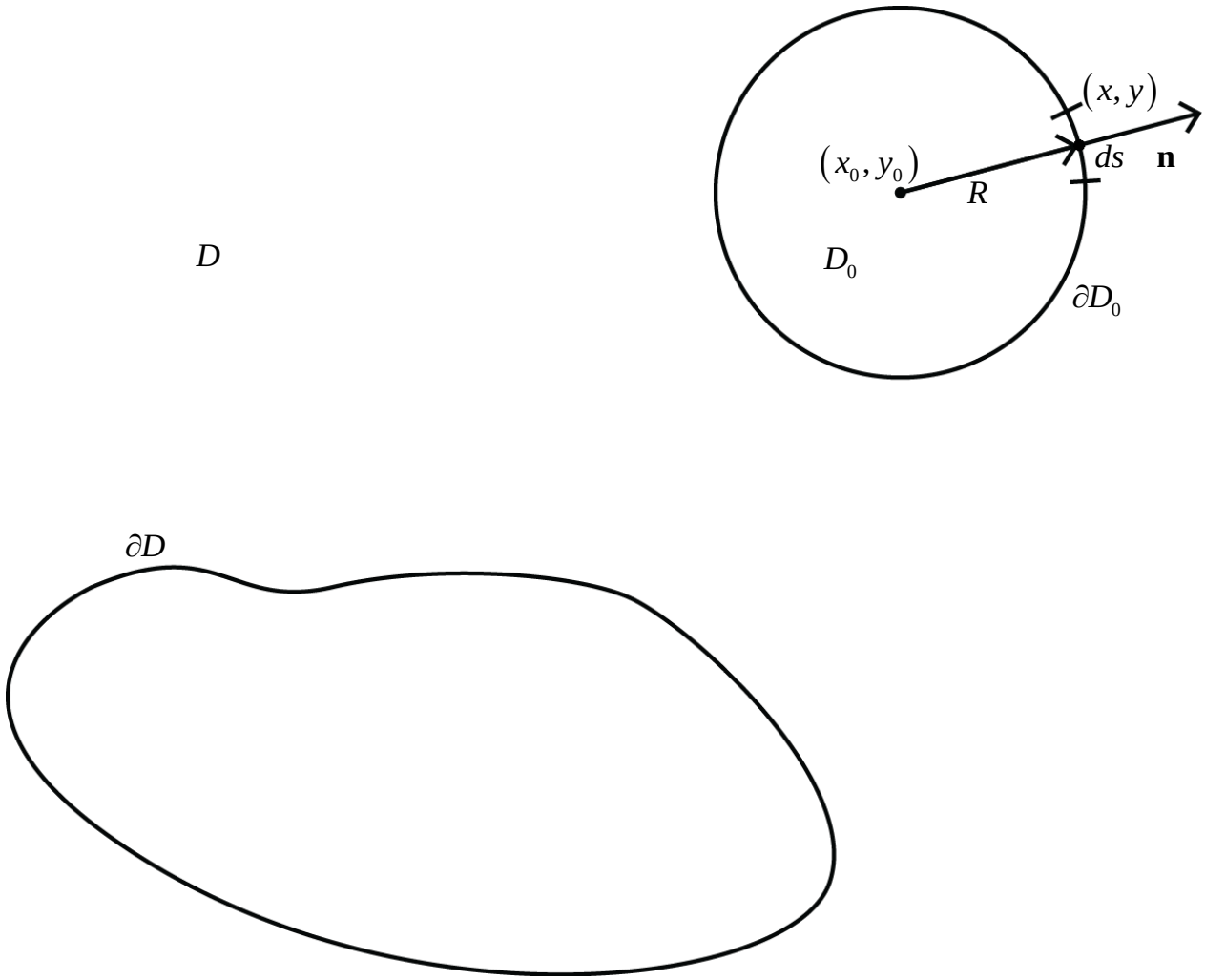


Figure 81: Application of Gauss's theorem in the case that $(x_0, y_0) \in D$.

Appling Gauss theorem:

$$\iint_{D_0} \nabla\left[\nabla \ln r(x, y \mid x_0, y_0)\right] dxdy = -\int_{\partial D_0} \frac{\partial \ln r(x, y \mid x_0, y_0)}{\partial n} ds(x, y) \tag{A.6}$$

$$\Rightarrow \iint_{D_0} \Delta\left[\ln r(x, y \mid x_0, y_0)\right] dxdy = -\int_{\partial D_0} \frac{\mathbf{r}}{r^2} \cdot \mathbf{n} r d\theta = -2\pi. \tag{A.7}$$

Summarizing we have:

$$\Delta\left[-\frac{\ln r(x, y \mid x_0, y_0)}{2\pi}\right] = 0, \ \ \forall (x_0, y_0) \in D_0, (x, y) \in D \setminus D_0, \tag{A.8}$$

and

$$\iint_D \Delta\left[-\frac{\ln r(x,y\,|\,x_0,y_0)}{2\pi}\right]dxdy = 1, \tag{A.9}$$

therefore the function in the brackets

$$G(x,y\,|\,x_0,y_0) = -\frac{1}{2\pi}\ln r(x,y\,|\,x_0,y_0), \tag{A.10}$$

is the fundamental solution of the Laplace operator or the infinite space Green function and satisfies the following equation:

$$\Delta\left[-\frac{\ln r(x,y\,|\,x_0,y_0)}{2\pi}\right] = \delta(x,y\,|\,x_0,y_0),\ \ \forall\left(x_0,y_0\right)\in D_0,(x,y)\in D\setminus D_0, \tag{A.11}$$

where $\delta(x,y\,|\,x_0,y_0)$ is the Dirac delta function at point $\left(x_0,y_0\right)$. A very important property of delta function is its sampling property:

$$\iint_D \Phi\left(x,y\right)\delta(x,y\,|\,x_0,y_0)dxdy = \Phi\left(x_0,y_0\right). \tag{A.12}$$

In the theory of generalized functions the above relation is the definition of Dirac function. In this case it is a functional which is defined by it action on another function, for a more detailed study in generalized functions see e.g. Vladimirov (1979).

Let now $\left(x_0,y_0\right)\in\partial D$. In this case the neighborhood of $\left(x_0,y_0\right)$ is a half circular disk (Figure 82). Working as previously, but with $D_0$ a half circular disk we get:

$$\Delta\left[-\frac{\ln r(x,y\,|\,x_0,y_0)}{2\pi}\right] = \frac{1}{2}\delta(x,y\,|\,x_0,y_0),\ \ \forall\left(x_0,y_0\right)\in\partial D,(x,y)\in\partial D. \tag{A.13}$$

Lets apply now the second Green's identity, see e.g. Kress (1989):

$$\iint_D\left[\left[-\frac{\ln r(x,y\,|\,x_0,y_0)}{2\pi}\right]\cdot\Delta\Phi(x,y)-\Phi(x,y)\Delta\left[-\frac{\ln r(x,y\,|\,x_0,y_0)}{2\pi}\right]\right]dxdy =$$
$$\int_{\partial D}\left[\left[-\frac{\ln r(x,y\,|\,x_0,y_0)}{2\pi}\right]\frac{\partial\Phi(x,y)}{\partial n}-\Phi(x,y)\frac{\partial\left[-\frac{\ln r(x,y\,|\,x_0,y_0)}{2\pi}\right]}{\partial n}\right]ds(x,y), \tag{A.14}$$

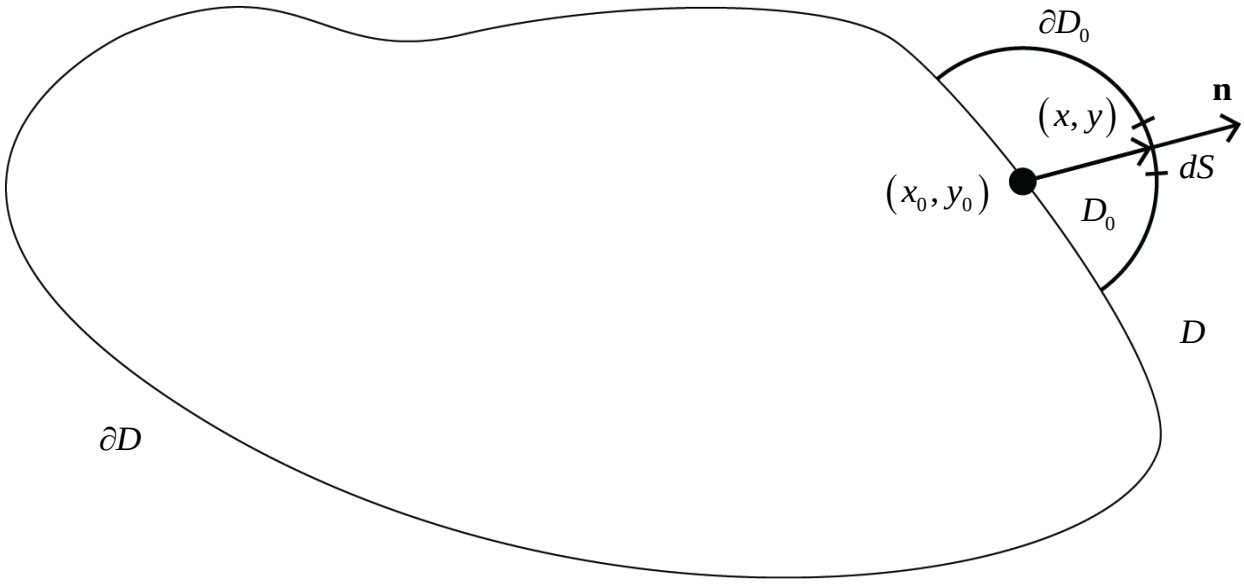


Figure 82: Application of Gauss's theorem in the case that $(x_0, y_0) \in \partial D$.

therefore

$$\iint_D \left[ \left[ -\frac{\ln r(x,y \mid x_0,y_0)}{2\pi} \right] \cdot \Delta\Phi(x,y) - \Phi(x,y)\delta(x,y \mid x_0,y_0) \right] dxdy =$$
$$\int_{\partial D} \left[ \left[ -\frac{\ln r(x,y \mid x_0,y_0)}{2\pi} \right] \frac{\partial\Phi(x,y)}{\partial n} + \Phi(x,y) \frac{1}{2\pi} \frac{\mathbf{r}(x,y \mid x_0,y_0)}{r^2(x,y \mid x_0,y_0)} \mathbf{n} \right] ds(x,y), \qquad \text{(A.15)}$$

$$\Rightarrow \Phi(x_0,y_0) = -\iint_D \frac{\ln r(x,y \mid x_0,y_0)}{2\pi} \cdot \Delta\Phi(x,y) dxdy$$
$$\int_{\partial D} \left[ \frac{\ln r(x,y \mid x_0,y_0)}{2\pi} \frac{\partial\Phi(x,y)}{\partial n} - \Phi(x,y) \frac{1}{2\pi} \frac{\mathbf{r}(x,y \mid x_0,y_0)}{r^2(x,y \mid x_0,y_0)} \mathbf{n} \right] ds(x,y). \qquad \text{(A.16)}$$

Assuming that $\Phi$ is harmonic in $D$ we finally get:

$$\Phi(x_0,y_0) = \int_{\partial D} \left[ \frac{\ln r(x,y \mid x_0,y_0)}{2\pi} \frac{\partial\Phi(x,y)}{\partial n} - \Phi(x,y) \frac{1}{2\pi} \frac{\mathbf{r}(x,y \mid x_0,y_0)}{r^2(x,y \mid x_0,y_0)} \mathbf{n} \right] ds(x,y), \qquad \text{(A.17)}$$

and using the property of reciprocity of Green functions we can also write

$$\Phi(x_0,y_0) = \int_{\partial D} \left[ \frac{\ln r(x_0,y_0 \mid x,y)}{2\pi} \frac{\partial\Phi(x,y)}{\partial n} + \Phi(x,y) \frac{1}{2\pi} \frac{\mathbf{r}(x_0,y_0 \mid x,y)}{r^2(x_0,y_0 \mid x,y)} \mathbf{n} \right] ds(x,y). \qquad \text{(A.18)}$$

Finally, defining the Green functions in the following way:

$$G(x_0, y_0 \mid x, y) = \frac{1}{2\pi} \ln r(x_0, y_0 \mid x, y) \ , \ (x, y) \in \mathbb{R}^2, (x_0, y_0) \in \mathbb{R}^2, \tag{A.19}$$

and

$$\frac{\partial G(x_0, y_0 \mid x, y)}{\partial n} = -\frac{1}{2\pi} \frac{\boldsymbol{n} \cdot \boldsymbol{r}(x_0, y_0 \mid x, y)}{\left[ r(x_0, y_0 \mid x, y) \right]^2} \ , \ (x, y) \in \mathbb{R}^2, (x_0, y_0) \in \mathbb{R}^2, \tag{A.20}$$

where

$$r(x_0, y_0 \mid x, y) = \left[ (x_0 - x)^2 + (y_0 - y)^2 \right]^{1/2}, \tag{A.21}$$

the representation theorems are put in the form

for $(x_0, y_0) \in D$:

$$\Phi(x_0, y_0) = \int_{\partial D} \frac{\partial \Phi(x, y)}{\partial n} G(x_0, y_0 \mid x, y) - \Phi(x, y) \frac{\partial G(x_0, y_0 \mid x, y)}{\partial n} ds(x, y). \tag{A.22}$$

Working similarly for $(x_0, y_0) \in \partial D$ and using (A.13) we get the next Fredholm 2nd kind weakly singular boundary integral equation that can be solved for the unknown boundary values:

$$\frac{1}{2} \Phi(x_0, y_0) = \int_{\partial D} \frac{\partial \Phi(x, y)}{\partial n} G(x_0, y_0 \mid x, y) - \Phi(x, y) \frac{\partial G(x_0, y_0 \mid x, y)}{\partial n} ds(x, y). \tag{A.23}$$

The last form of representation theorem eq. (A.22) or (A.23) is appropriate for a physical interpretation. The first order in the integral is the potential induced at $(x_0, y_0)$ from a distribution of sources (singularities) with intensity $\frac{\partial \Phi(x, y)}{\partial n}$ located on the boundary, while the second one is the potential from a distribution of dipoles parallel to $\boldsymbol{n}$ (singularities), with intensity $\Phi(x, y)$.

## Appendix B - Singular integrals

Consider the boundary integral equation (A.23) for $(x_0, y_0) \in \partial D$:

$$\frac{1}{2}\Phi(x_0, y_0) = \int_{\partial D} \frac{\partial \Phi(x, y)}{\partial n} G(x_0, y_0 \mid x, y) - \Phi(x, y) \frac{\partial G(x_0, y_0 \mid x, y)}{\partial n} ds(x, y). \tag{B.1}$$

The integrals appeared in the above relation are singular, since $(x_0, y_0) \in \partial D$ there is a point at the domain of integration where $(x_0, y_0) \equiv (x, y) \Rightarrow r = 0$. At this point the integrands become infinite and has no meaning in the usual Riemann sense. These integrals are called singular and in the present section we will try to present a way to be determined as the limit of a well defined regular integral.

Integrals on the r.h.s. of (B.1) are of the general form:

$$I_1(x_0, y_0) = \int_C f(x, y) \ln r(x_0, y_0 \mid x, y) ds(x, y), \tag{B.2}$$

and

$$I_2(x_0, y_0) = \int_C \boldsymbol{f}(x, y) \frac{\boldsymbol{r}(x_0, y_0 \mid x, y)}{\left[r(x_0, y_0 \mid x, y)\right]^2} ds(x, y), \tag{B.3}$$

where f and **f** are continuous scalar or vector functions of $(x, y)$. Consider now a Cartesian coordinate system tangent to $C$ with origin at $(x_0, y_0)$ and a partition of the integration domain $C$ into the following subdomains $C_1$, $C_{12} = C_{12}^l \cup C_{12}^r$ and $C_2 = C_2^l \cup C_2^r$ centered at $(x_0, y_0)$ as shown on Figure 83. The subdomains are bounded by the points $A_1 \equiv (-\rho_1^l, 0)$, $B_1 \equiv (\rho_1^r, 0)$ and $A_2 \equiv (-\rho_2, 0)$, $B_2 \equiv (\rho_2, 0)$ respectively.

Then:

$$C = C_1 \cup C_{12} \cup C_2, \tag{B.4}$$

also

$$C = \left( \lim_{\substack{\rho_1^l \to 0 \\ \rho_1^r \to 0}} C_{12} \right) \cup C_2. \tag{B.5}$$

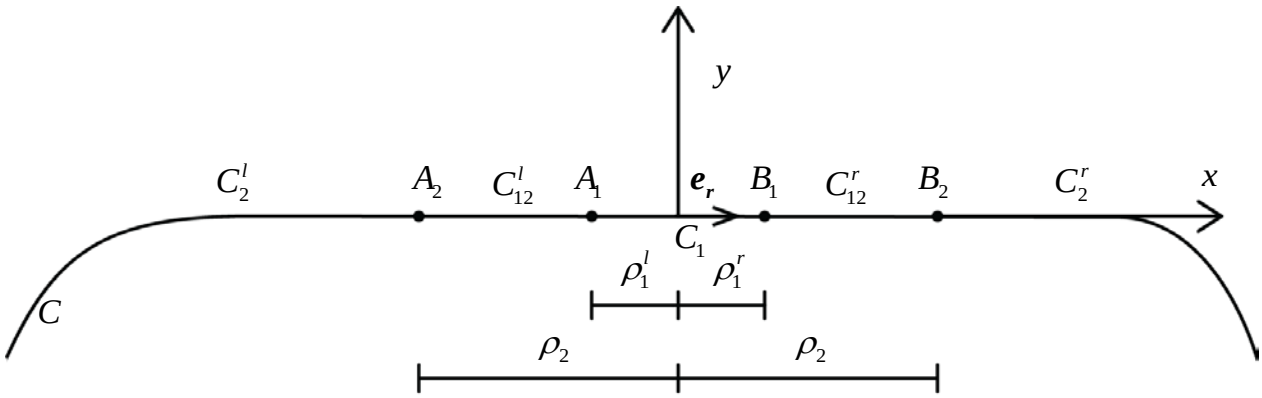


Figure 83: Decomposition of singular integrals' integration domain.

Integrals (B.2) and (B.3) are regular in $C_2$ and in $C_{12}$ since $(x_0, y_0) \neq (x, y)$, but singular in $C_1$. We shall try to define them as the limit: $\rho_1^l \to 0 \wedge \rho_1^r \to 0$, with integration domain $C_{12} \cup C_2$.

Let work with the singular part of (B.2):

$$I_1^{'}(x_0, y_0) = \int_{C_{12}} f(x, y) \ln r(x_0, y_0 \mid x, y) ds(x, y). \tag{B.6}$$

For small $\rho_1^l$ and $\rho_1^r$ we have from Taylor formula:

$$f(x, y) = f(x_0, y_0) + \nabla f(x_0, y_0) \cdot \boldsymbol{r} = f(x_0, y_0) + \nabla f(x_0, y_0) \cdot \boldsymbol{e_r} \cdot r, \tag{B.7}$$

where $\boldsymbol{e}_r$ is the parallel at C unit vector and $\boldsymbol{r} = \boldsymbol{e}_r \cdot r$.

Then relation (B.6) becomes:

$$\begin{aligned} I_1^{'}(x_0, y_0) &= \int_{C_{12}} f(x_0, y_0) \ln r(x_0, y_0 \mid x, y) ds(x, y) \\ &+ \int_{C_{12}} \nabla f(x_0, y_0) \cdot \boldsymbol{e_r} \cdot r \cdot \ln r(x_0, y_0 \mid x, y) dS(x, y), \end{aligned} \tag{B.8}$$

$$\Rightarrow I_1^{'}(x_0, y_0) = f(x_0, y_0) \left( \int_{\rho_2}^{\rho_1^l} \ln r dr + \int_{\rho_1^r}^{\rho_2} \ln r dr \right)$$

$$+\nabla f(x_0,y_0)\cdot \boldsymbol{e_r}\left(\int_{\rho_2}^{\rho_1^l} r\cdot\ln r dr+\int_{\rho_1^r}^{\rho_2} r\cdot\ln r dr\right), \tag{B.9}$$

$$\Rightarrow I_1^{'}(x_0,y_0)=f(x_0,y_0)\begin{bmatrix}\left(\rho_1^l-\rho_2^l\right)-\left(\rho_1^l\ln\rho_1^l-\rho_2^l\ln\rho_2^l\right)\\+\left(\rho_2^r-\rho_1^r\right)-\left(\rho_2^r\ln\rho_r^r-\rho_1^r\ln\rho_1^r\right)\end{bmatrix}$$

$$+\nabla f(x_0,y_0)\cdot\frac{1}{4}\begin{bmatrix}-\left(\rho_1^l\right)^2\left(2\ln\rho_2-1\right)+\left(\rho_2\right)^2\left(2\ln\rho_2-1\right)\\+\left(\rho_2\right)^2\left(2\ln\rho_2-1\right)-\left(\rho_1^r\right)^2\left(2\ln\rho_1^r-1\right)\end{bmatrix} \tag{B.10}$$

since

$$\lim_{r\to0} r\cdot\ln r=\lim_{r\to0}\frac{\ln r}{\frac{1}{r}}\overset{deL'Hospital}{=}\lim_{r\to0}\frac{\frac{1}{r}}{-\frac{1}{r^2}}=-\lim_{r\to0} r=0, \tag{B.11}$$

and

$$\lim_{r\to0} r^2\cdot\ln r=\lim_{r\to0}\frac{\ln r}{\frac{1}{r^2}}\overset{deL'Hospital}{=}\lim_{r\to0}\frac{\frac{1}{r}}{-\frac{2}{r^3}}=-2\lim_{r\to0} r^2=0, \tag{B.12}$$

it holds:

$$\lim_{\substack{\rho_1^l\to0\\ \rho_1^r\to0}} I_1^{'}(x_0,y_0)=0, \tag{B.13}$$

therefore $I_1^{'}$ and $I_1$ are well defined and unique. Singular integrals that their value is independent from the way that their support $C_1$ reduces to zero, are referred as weakly singular integrals.

Lets now try to apply the same procedure to the singular part of (B.3):

$$I_2^{'}(x_0,y_0)=\int_{C_{12}}\boldsymbol{f}(x,y)\frac{\boldsymbol{r}(x_0,y_0\,|\,x,y)}{\left[r(x_0,y_0\,|\,x,y)\right]^2}ds(x,y). \tag{B.14}$$

For small $\rho_1^l$ and $\rho_1^r$ we have from Taylor formula:

$$\boldsymbol{f}(x,y)=\boldsymbol{f}(x_0,y_0)+(\boldsymbol{r}\cdot\nabla)\boldsymbol{f}(x_0,y_0), \tag{B.15}$$

and

$$\begin{aligned} \boldsymbol{f}(x,y)\cdot\boldsymbol{r} &= \left[\boldsymbol{f}(x_0,y_0)+r\cdot(\boldsymbol{e}_r\cdot\nabla)\boldsymbol{f}(x_0,y_0)\right]r\cdot\boldsymbol{e}_r \\ &= \boldsymbol{f}(x_0,y_0)\cdot\boldsymbol{e}_r\cdot r+\left[(\boldsymbol{e}_r\cdot\nabla)\boldsymbol{f}(x_0,y_0)\cdot\boldsymbol{e}_r\right]\cdot r^2. \end{aligned} \tag{B.16}$$

Letting:

$$A=\int_{C_{12}}\frac{\boldsymbol{f}(x_0,y_0)\cdot\boldsymbol{e}_r\cdot r(x_0,y_0\,|\,x,y)}{r^2(x_0,y_0\,|\,x,y)}ds(x,y), \tag{B.17}$$

$$B=\int_{C_{12}}\frac{\left[(\boldsymbol{e}_r\cdot\nabla)\boldsymbol{f}(x_0,y_0)\cdot\boldsymbol{e}_r\right]\cdot r^2(x_0,y_0\,|\,x,y)}{r^2(x_0,y_0\,|\,x,y)}ds(x,y), \tag{B.18}$$

we have $I_2^{'}(x_0,y_0)=A+B.$

Working on A, we have:

$$A=\int_{\rho_2}^{\rho_1^l}\frac{\boldsymbol{f}(x_0,y_0)\cdot\boldsymbol{e}_r}{r}dr+\int_{\rho_1^r}^{\rho_2}\frac{\boldsymbol{f}(x_0,y_0)\cdot\boldsymbol{e}_r}{r}dr, \tag{B.19}$$

$$\Rightarrow A=\boldsymbol{f}(x_0,y_0)\cdot\boldsymbol{e}_r l\,\mathrm{n}\frac{\rho_1^l}{\rho_2^r}. \tag{B.20}$$

Working on B, we have:

$$B=\int_{\rho_2}^{\rho_1^l}\left[(\boldsymbol{e}_r\cdot\nabla)\boldsymbol{f}(x_0,y_0)\cdot\boldsymbol{e}_r\right]\frac{r^2}{r^2}dr+\int_{\rho_1^r}^{\rho_2}\left[(\boldsymbol{e}_r\cdot\nabla)\boldsymbol{f}(x_0,y_0)\cdot\boldsymbol{e}_r\right]\frac{r^2}{r^2}dr \tag{B.21}$$

$$\Rightarrow B=\left[(\boldsymbol{e}_r\cdot\nabla)\boldsymbol{f}(x_0,y_0)\cdot\boldsymbol{e}_r\right]\left(\rho_1^l-\rho_1^r\right). \tag{B.22}$$

Finally we can notice that $\lim_{\substack{\rho_1^l\to 0\\ \rho_1^r\to 0}} B=0,$ thus B is well defined.

Things are more complicated for A, which is singular because of the $1/r$ singularity in the kernel. If we assume that $\rho_1^l$ is not going to zero independently of $\rho_1^r$ and that a relationship between them exists:

$$\frac{\rho_1^l}{\rho_2^r}=a, \tag{B.23}$$

is this case we have

$$\lim_{\substack{\rho_1^l \to 0 \\ \rho_1^r \to 0}} A = \boldsymbol{f}(x_0, y_0) \cdot \boldsymbol{e}_r \ln a. \tag{B.24}$$

Therefore A can take any finite value by properly selecting α, to get this finite value, $\rho_1^l$ should not going to zero independently of $\rho_1^r$, but in the way that a relation like eq.(B.21) demands. Finally if we assume for symmetry that $\rho_1^l = \rho_1^r$ then A=0. Integrals which converge only for such specialized contraction schemes of the integration region are termed Cauchy principal value integrals or we say that their convergence is in the Cauchy principal value sense.

Therefore we have seen that the first integral in (B.1), that is of the general form of equation (B.2) is weakly singular. The second on is of course of the general for of (B.3) but it also has a peculiarity. The rate of divergence when $(x, y) \to (x_0, y_0)$ is weakened due to the special form of $\boldsymbol{f}(x, y) = \mathbf{n}(x, y)$. In particular when $(x, y) \to (x_0, y_0)$, $\boldsymbol{r}(x_0, y_0 \mid x, y)$ becomes tangent to $d\mathbf{s}$ and thus transverse to $\boldsymbol{f}(x, y) = \mathbf{n}(x, y)$, in this way the nominator $\mathbf{n}(x, y) \cdot \boldsymbol{r}(x_0, y_0 \mid x, y)$ tends to zero with a rate of order of $x^{-1}$, and thus the Cauchy principal value integral becomes weakly singular. However, Cauchy principal value integrals appear in the representation theorem of the velocity from potential and potential's derivative boundary values. That theorem is necessary for the calculation of the velocities on the wake and for the extension to the fully non-linear model.

More extended study in singular integral have been done by many scientists such as Muskhelishvili (1953), Mikhlin (1965), Polyanin & Manzhirov (2008).

# Appendix C - Linear unsteady hydrofoil theory

## C.1 Formulation of the thin unsteady hydrofoil problem

In the present section we will present the 2D unsteady thin hydrofoil theory described in Newman's text book "Marine Hydrodynamics" (1977), which we will follow in a strong abridged way.

The problem will be treated in the framework of linear perturbation theory. Consider an unsteady 2D hydrofoil traveling with constant velocity $U$ in unbounded domain. Assume that the foil is thin and at a small angle of attack, performing unsteady perturbations around its mean position. The lifting problem is unsteady and thus a trailing vortex sheet is generated from the trailing edge. Vorticity is generated in foil's wake in such a way as the total circulation around it, is opposite to the circulation of the foil at every time step in conformity with Kelvin's theorem. However, both the body contour and the trailing vortex sheet are considered to be linearised and thus they collapse onto a cut in the x-axis. The problem is treated with respect to a body-fixed reference frame, i.e. the oscillating body, which is considered stationary in x-direction, is encountering a uniform flow.

Moreover, we consider incompressible and irrotational flow, thus a total velocity potential $\Phi_T(x,y;t)$ can be defined that consists of the constant uniform flow potential $\Phi_I(x,y)$, with $\nabla\Phi_I(x,y)=\{-U,0\}$, and the perturbation potential $\Phi(x,y;t)$ that vanishes at infinity. Furthermore no entrance boundary condition must be satisfied on the body, also an appropriate Kutta condition must be valid necessitating finite velocity at the trailing edge, while dynamic and kinematic boundary conditions must be applied on the wake, demanding continuity of the pressure and of the, normal to the boundary velocity, through x-axis. Finally, as we have stated before, total circulation along a material curve must be constant in time and thus, on the assumption that the motion has arisen from an initial state of rest, the total circulation about the foil and the wake must vanish.

Using the principle of linear superposition, we will decompose the thickness and the lifting (camber and angle of attack) effects separately. Thickness is constant and thus the first problem is unsteady, on the other side an unsteady problem is considered, a foil with zero thickness with varying camber line and angle of attack.

In the present Chapter we will focus to the unsteady lifting problem. Let $y_c(x;t)$ denoting the camber line of the foil, according to the no entrance boundary condition of the lifting problem the camber line must be a material curve

$$\frac{D(y-y_c)}{Dt}=\frac{\partial(y-y_c)}{\partial t}+\nabla\Phi_T\cdot\nabla(y-y_c)=0 \tag{C.1}$$

$$\Rightarrow -\frac{\partial y_c}{\partial t}+\left(-U+\frac{\partial\Phi}{\partial x}\right)\cdot\left(-\frac{\partial y_c}{\partial x}\right)+\left(\frac{\partial\Phi}{\partial y}\right)\cdot\left(1-\frac{\partial y_c}{\partial y}\right)=0 \tag{C.2}$$

$$\Rightarrow \frac{\partial \Phi}{\partial y} - \frac{\partial y_c}{\partial t} + U \frac{\partial y_c}{\partial x} - \frac{\partial \Phi}{\partial x}\frac{\partial y_c}{\partial x} - \frac{\partial \Phi}{\partial y}\frac{\partial y_c}{\partial y} = 0, \tag{C.3}$$

in the above relation the last two terms are second order and can be neglected, thus the no entrance boundary condition leads to the following Neumann boundary condition

$$\frac{\partial \Phi}{\partial y} = \frac{\partial y_c}{\partial t} - U_I \frac{\partial y_c}{\partial x}. \tag{C.4}$$

Applying the above boundary condition on the cut we get for the derivative of the disturbance potential

$$\frac{\partial \Phi}{\partial y}(x,0;t) = b(x;t) \doteq \frac{\partial y_c}{\partial t}(x;t) - U_I \frac{\partial y_c(x;t)}{\partial x}, \;\; x \in (-1,1). \tag{C.5}$$

Where we have non-dimensionalised the hydrofoil with respect to the half chord, and thus the hydrofoil extends from -1 to 1 and the wake from $-\infty$ to 1.

Using knowledge from the thin hydrofoil theory, see. e.g. Newman (1977) Chapter 5, we represent the foil and the wake with a distribution of vortices with intensity $\gamma(x;t)$ and in that case the disturbance potential derivatives on the upper (denoted by "+") and the lower (denoted by "-") surfaces of the foil and the wake will be

$$\frac{\partial \Phi_{\pm}(x;t)}{\partial x} = \mp \frac{1}{2}\gamma(x;t), \;\; x \in (-\infty,1), \tag{C.6}$$

and

$$\frac{\partial \Phi_{\pm}(x;t)}{\partial y} = -\frac{1}{2\pi}\int_{-\infty}^{1} \frac{\gamma(\xi;t)}{\xi - x} d\xi, \;\; x \in (-\infty,1). \tag{C.7}$$

We mention that the above integral is singular i.e. it explodes when $\xi \to x$.

As we have mentioned before total circulation around the foil $\Gamma(t)$ and its wake must be zero and thus

$$\int_{-\infty}^{1} \gamma(x;t)\,dx = \int_{-\infty}^{-1} \gamma(\zeta;t)\,d\zeta + \Gamma(t) = 0. \tag{C.8}$$

Dynamic boundary condition on the trailing vortex sheet denotes that it cannot carry loading, in order to apply that we need an expression for the pressure difference on the wake. Consider a streamline extending from infinite to a point near the hydrofoil, unsteady Bernoulli's theorem is

$$\frac{\partial \Phi_T}{\partial t}+\frac{1}{2}\left(\nabla \Phi_T\right)^2+\frac{p}{\rho}=\frac{\partial \Phi_I}{\partial t}+\frac{1}{2}U^2+\frac{p_\infty}{\rho} \tag{C.9}$$

$$\Rightarrow \frac{\partial\left(\Phi_I+\Phi\right)}{\partial t}+\frac{1}{2}\left(\frac{\partial \Phi}{\partial x}-U\right)^2+\frac{1}{2}\left(\frac{\partial \Phi}{\partial y}\right)^2+\frac{p}{\rho}=\frac{\partial \Phi_I}{\partial t}+\frac{1}{2}U^2+\frac{p_\infty}{\rho} \tag{C.10}$$

$$\Rightarrow \frac{\partial \Phi}{\partial t}-U\frac{\partial \Phi}{\partial x}+\frac{p-p_\infty}{\rho}+\frac{1}{2}\left[\left(\frac{\partial \Phi}{\partial x}\right)^2+\left(\frac{\partial \Phi}{\partial y}\right)^2\right]=0, \tag{C.11}$$

where the last quadratic perturbation velocity term is of second order and can be neglected, therefore linearised unsteady Bernoulli's theorem can be written

$$p\left(x,y;t\right)-p_\infty=-\rho\left[\frac{\partial \Phi\left(x,y;t\right)}{\partial t}-U\frac{\partial \Phi}{\partial x}\left(x,y;t\right)\right]. \tag{C.12}$$

Applying the above on the upper and the lower surface of the wake and abstracting we get

$$p_+-p_-=-\rho\left[\frac{\partial\left(\Phi_+-\Phi_-\right)}{\partial t}-U\left(\frac{\partial \Phi_+}{\partial x}-\frac{\partial \Phi_-}{\partial x}\right)\right]. \tag{C.13}$$

Dynamic boundary condition on the wake requires that

$$p_+-p_-=0\ ,\ x\in\left(-\infty,-1\right) \tag{C.14}$$

$$\Rightarrow \frac{\partial\left(\Phi_+-\Phi_-\right)}{\partial t}-U\left(\frac{\partial \Phi_+}{\partial x}-\frac{\partial \Phi_-}{\partial x}\right)=0\ ,\ x\in\left(-\infty,-1\right), \tag{C.15}$$

differentiating with respect to x we get

$$\Rightarrow \frac{\partial\left(\frac{\partial \Phi_+}{\partial x}-\frac{\partial \Phi_-}{\partial x}\right)}{\partial t}-U\frac{\partial\left(\frac{\partial \Phi_+}{\partial x}-\frac{\partial \Phi_-}{\partial x}\right)}{\partial x}=0\ ,\ x\in\left(-\infty,-1\right), \tag{C.16}$$

and finally using (C.6) we conclude to the following form of dynamic boundary condition expresses in terms of distributed vorticity

$$\Rightarrow \frac{\partial \gamma\left(x;t\right)}{\partial t}-U\frac{\partial \gamma\left(x;t\right)}{\partial x}=0\ ,\ x\in\left(-\infty,-1\right). \tag{C.17}$$

The above partial differential equation is of unidirectional wave type and its solutions represents waves traveling with celerity $-U$ from -1 to $-\infty$

$$\gamma\left(x;t\right)=\gamma\left(x+Ut\right)\ ,\ x\in\left(-\infty,-1\right). \tag{C.18}$$

Applying now a pressure-type condition we demand that the pressure difference must be zero at the trailing edge, i.e.

$$p_+ - p_- = 0 \ , \ x = -1, \tag{C.19}$$

following the same procedure as before we get

$$\Rightarrow \frac{\partial \gamma(-1;t)}{\partial t} - U \frac{\partial \gamma(-1;t)}{\partial x} = 0. \tag{C.20}$$

Moreover differentiating (C.8) with respect to time we have

$$\frac{d\Gamma(t)}{dt} = -\int_{-\infty}^{-1} \frac{\partial \gamma(\zeta;t)}{\partial t} d\zeta, \tag{C.21}$$

replacing (C.20) to (C.21) and integrating we conclude

$$\frac{d\Gamma(t)}{dt} = -U\gamma(-1;t). \tag{C.22}$$

The above relation is an expression of unsteady Kutta condition for the unknown value of vortex intensity at the trailing edge. The rate of change in foils circulation is proportional to the intensity of the produced vorticity, in this way hydrofoil's circulation has unsteady character, nevertheless Kelvin's conservation of total circulation remains valid. Taking now into account relations (C.18) and (C.22) we conclude that every fluid particle on foil's vortex wake carries vorticity's strength that equals its strength from the time that it was at the trailing edge.

We can now use relation (C.7) and equation (C.18) to contact a representation theorem for the y-component of the disturbance velocity on x-axis from vorticity boundary distributions

$$\frac{\partial \Phi_{\pm}(x;t)}{\partial y} = -\frac{1}{2\pi}\int_{-1}^{1} \frac{\gamma(\xi;t)}{\xi - x} d\xi - \frac{1}{2\pi}\int_{-\infty}^{-1} \frac{\gamma(\zeta + Ut)}{\zeta - x} d\zeta, \ y = 0. \tag{C.23}$$

Before we proceed it is noteworthy to give a description of the unsteady lifting problem using the knowledge gained until now:

a) Circulation around the foil changes in time as a function of the total velocity field

b) The total velocity field consists of the undisturbed component and the perturbation velocity field that is excited from the steady uniform velocity disturbed by the presence of the body and the unsteady motions of the foil.

c) The change of circulation in time is accompanied with free vorticity production at the trailing edge. That free vorticity is transferred invariable with fluid particles downstream of the flow.

d) A vorticity wave is propagating downstream on the wake as relation (C.18) demonstrates.

e) In this way the all the time history of the differential variations of circulation is stored in hydrofoil's wake (last term in C.21) and affects the total velocity field at every time step.

Appling now representation theorem (C.23) for points on the foil and imposing boundary condition we have

$$-\frac{1}{2\pi}\int_{-1}^{1}\frac{\gamma(\xi;t)}{\xi-x}d\xi = b(x;t)+\frac{1}{2\pi}\int_{-\infty}^{-1}\frac{\gamma(\zeta+Ut)}{\zeta-x}d\zeta,\ \ x\in(-1,1). \tag{C.24}$$

The above is a singular integral equation for the vortex strength, assuming that the r.h.s. is known it is a Fredholm integral equation of the first kind in which the unknown lies in the integrant of a singular integral that can be defined in the Cauchy principal value sense as described in Appendix B. In the following sections we will see how this type of equations can be solved.

## C.2 Solution of the singular integral equation in the steady case

A required sub-step before the solution of (C.24) is the solution of a simpler singular integral equation that appears in the corresponding lifting problem in steady thin hydrofoil theory

$$-\frac{1}{2\pi}\int_{-1}^{1}\frac{\gamma(\xi)}{\xi-x}d\xi = b_0(x),\ \ x\in(-1,1), \tag{C.25}$$

where the r.h.s. is supposed to be known.

In the next we will construct a solution of the above equation exploiting our physical understanding of the steady thin hydrofoil theory and the conjugate nature of thickness and lifting problems represented by conjugate source and vortex distributions.

Recalling the two conjugate problems, from steady thin hydrofoil theory

*Thickness problem*

$$\frac{\partial \Phi_{\pm}^{T}(x)}{\partial x} = -\frac{1}{2\pi}\int_{-1}^{1}\frac{q(\xi)}{\xi - x}d\xi, \tag{C.26}$$

$$\frac{\partial \Phi_{\pm}^{T}(x)}{\partial y} = \pm\frac{1}{2}q(x) = b_0(x). \tag{C.27}$$

Where $q(x)$ is the intensity of distributed sources on $(-1,1)$ that induce the velocity field associated with the thickness problem. From the above it is clear that x-component of disturbance velocity induced by constant strength sources distributed on x-axis is continuous through x-axis while y-component of the velocity is discontinuous. In that problem unknown source intensity is straightforward related with the known data $b_0(x)$, and thus the problem is solved, we can calculate $q(x)$ and $\frac{\partial \Phi_{\pm}^{T}(x)}{\partial y}$ from (C.27) and then $\frac{\partial \Phi_{\pm}^{T}(x)}{\partial x}$ replacing known source strength in (C.26). We notice that $\frac{\partial \Phi_{\pm}^{T}(x)}{\partial y}$ is zero outside the cut because there are not vortices distributed there.

*Lifting problem*

$$\frac{\partial \Phi_{\pm}^{L}(x)}{\partial x} = \mp\frac{1}{2}\gamma(x), \tag{C.28}$$

$$\frac{\partial \Phi_{\pm}^{L}(x)}{\partial y} = -\frac{1}{2\pi}\int_{-\infty}^{1}\frac{\gamma(\xi)}{\xi - x}d\xi = b_0(x). \tag{C.29}$$

On the contrary, concerning the lifting problem, it is clear that x-component of disturbance velocity induced by constant strength vortices distributed on x-axis is discontinuous through x-axis while y-component of the velocity is continuous. In that case solution cannot obtained in such a straightforward way, because known data are related with unknown $\gamma(x)$ through a singular integral equation identical to (C.25). In the following we will see how we can exploit the thickness problem in order to solved the more complex lifting problem. The only information that we have a priory is that $\frac{\partial \Phi_{\pm}^{L}(x)}{\partial x}$ is zero outside the cut because there are not vortices distributed there.

Let's consider the complex velocity field of the lifting problem defined as follows

$$w^{L} = \frac{\partial \Phi^{L}}{\partial x} - i\frac{\partial \Phi^{L}(x)}{\partial y}. \tag{C.30}$$

We multiply now with a suitable complex function e.g. $\left(1-z^2\right)^{1/2}$, that is real on the cut and pure imaginary on the remainder real axis. In this way the previous implicit lifting problem is mapped on an explicit one just like the thickness problem considered before.

From the previous procedure a new pseudo-velocity function has been defined by the transform of (C.30)

$$\tilde{w}^L = \frac{\partial \tilde{\Phi}^L}{\partial x} - i\frac{\partial \tilde{\Phi}^L(x)}{\partial y} = \left(\frac{\partial \Phi^L}{\partial x} - i\frac{\partial \Phi^L(x)}{\partial y}\right)\cdot\left(1-z^2\right)^{1/2}. \tag{C.31}$$

That function must satisfy the transformed form of conditions (C.28) and (C.29)

$$\frac{\partial \tilde{\Phi}^L_{\pm}(x)}{\partial y} = b_0(x)\cdot\left(1-x^2\right)^{1/2} \ , \ x\in(-1,1), \tag{C.32}$$

$$\frac{\partial \tilde{\Phi}^L_{\pm}(x)}{\partial y} = 0 \ , \ x\notin(-1,1), \tag{C.33}$$

where the second relation occurs from the fact that $\frac{\partial \Phi^L_{\pm}(x)}{\partial x}$ is zero outside the cut.

The above and the thickness problems are identical and thus the pseudo-velocity function can be generated with a source distribution, of strength given by a relation similar to (C.27)

$$\tilde{q}(x) = 2\frac{\partial \tilde{\Phi}^L_{\pm}(x)}{\partial y} = 2b_0(x)\cdot\left(1-x^2\right)^{1/2} \ , \ x\in(-1,1), \tag{C.34}$$

$$\tilde{q}(x) = 0 \ , \ x\notin(-1,1). \tag{C.35}$$

And the real part of the pseudo-velocity function is

$$\frac{\partial \tilde{\Phi}^L_{\pm}(x)}{\partial x} = -\frac{1}{\pi}\int_{-1}^{1}\frac{b_0(\xi)\cdot\left(1-\xi^2\right)^{1/2}}{\xi - x}d\xi. \tag{C.36}$$

Inverting now the transform applied before we get

$$\frac{\partial \Phi^L_{\pm}(x)}{\partial x} = -\frac{1}{\pi}\frac{1}{\left(1-x^2\right)^{1/2}}\int_{-1}^{1}\frac{b_0(\xi)\cdot\left(1-\xi^2\right)^{1/2}}{\xi - x}d\xi. \tag{C.37}$$

Finally from (C.28) we have

$$\gamma_p(x)=\frac{2}{\pi}\frac{1}{\left(1-x^2\right)^{1/2}}\int_{-1}^{1}\frac{b_0(\xi)\cdot\left(1-\xi^2\right)^{1/2}}{\xi-x}d\xi\ ,\ x\in(-1,1). \tag{C.38}$$

We have obtained a partial solution of the singular integral equation (C.25) that correspond to the solution of the steady thin hydrofoil lifting problem. However velocities calculated form (C.38) present a square-root singularity at the trailing edge and thus steady Kutta condition is not satisfied. In order to construct a solution compatible with Kutta condition we could use another transform in such a way that we would avoid singularity.

Using the complex function

$$\tilde{w}^L=\frac{\partial\tilde{\Phi}^L}{\partial x}-i\frac{\partial\tilde{\Phi}^L(x)}{\partial y}=\left(\frac{\partial\Phi^L}{\partial x}-i\frac{\partial\Phi^L(x)}{\partial y}\right)\cdot\left(\frac{1-z}{1+z}\right)^{1/2}, \tag{C.39}$$

we obtain a solution that leads to finite velocity at the trailing edge

$$\gamma_p(x)=\frac{2}{\pi}\left(\frac{1+x}{1-x}\right)^{1/2}\int_{-1}^{1}\left(\frac{1-\xi}{1+\xi}\right)^{1/2}\frac{b_0(\xi)}{\xi-x}d\xi\ ,\ x\in(-1,1). \tag{C.40}$$

We have obtained two partial solutions for the linear integral equation (C.25) in order to construct the general solution we have to add a partial solution the solution of the homogenous equation

$$\frac{1}{2\pi}\int_{-1}^{1}\frac{\gamma(\xi)}{\xi-x}d\xi=0,\ x\in(-1,1). \tag{C.41}$$

It is easy to prove that the difference of two partial solutions of a linear equation is a homogenous solution, therefore the solution of (C.41) can be obtained abstracting (C.38) from (C.40)

$$\gamma_h(x)=\frac{2}{\pi}\left(\frac{1+x}{1-x}\right)^{1/2}\int_{-1}^{1}\left(\frac{1-\xi}{1+\xi}\right)^{1/2}\frac{b_0(\xi)}{\xi-x}d\xi-\frac{2}{\pi}\frac{1}{\left(1-x^2\right)^{1/2}}\int_{-1}^{1}\frac{b_0(\xi)\cdot\left(1-\xi^2\right)^{1/2}}{\xi-x}d\xi\ ,\ x\in(-1,1) \tag{C.42}$$

$$\Rightarrow\gamma_h(x)=\frac{2}{\pi}\frac{1+x}{\left(1-x^2\right)^{1/2}}\int_{-1}^{1}\left(\frac{1-\xi}{1+\xi}\right)^{1/2}\frac{b_0(\xi)}{\xi-x}d\xi-\frac{2}{\pi}\frac{1}{\left(1-x^2\right)^{1/2}}\int_{-1}^{1}\frac{b_0(\xi)\cdot\left(1-\xi^2\right)^{1/2}}{\xi-x}d\xi \tag{C.43}$$

$$\Rightarrow\gamma_h(x)=\frac{2}{\pi}\frac{1}{\left(1-x^2\right)^{1/2}}\int_{-1}^{1}\frac{b_0(\xi)}{\xi-x}\left[(1+x)\left(\frac{1-\xi}{1+\xi}\right)^{1/2}-\left(1-\xi^2\right)^{1/2}\right]d\xi \tag{C.44}$$

$$\Rightarrow \gamma_h(x) = \frac{2}{\pi}\frac{1}{\left(1-x^2\right)^{1/2}}\int_{-1}^{1}\frac{b_0(\xi)}{\xi - x}\left(1-\xi^2\right)^{1/2}\left[(1+x)(1+\xi)^{-1/2}(1-\xi)^{-1/2}\left(\frac{1-\xi}{1+\xi}\right)^{1/2} - 1\right]d\xi \tag{C.45}$$

$$\Rightarrow \gamma_h(x) = \frac{2}{\pi}\frac{1}{\left(1-x^2\right)^{1/2}}\int_{-1}^{1}\frac{b_0(\xi)}{\xi - x}\left(1-\xi^2\right)^{1/2}\left[\frac{1+x}{1+\xi} - 1\right]d\xi \tag{C.46}$$

$$\Rightarrow \gamma_h(x) = \frac{2}{\pi}\frac{1}{\left(1-x^2\right)^{1/2}}\int_{-1}^{1}-\frac{b_0(\xi)}{x - \xi}\left(1-\xi^2\right)^{1/2}\frac{x-\xi}{1+\xi}d\xi \tag{C.47}$$

$$\Rightarrow \gamma_h(x) = -\frac{2}{\pi}\frac{1}{\left(1-x^2\right)^{1/2}}\int_{-1}^{1} b_0(\xi)\frac{(1-\xi)^{1/2}(1+\xi)^{1/2}}{1+\xi}d\xi \tag{C.48}$$

$$\Rightarrow \gamma_h(x) = -\frac{2}{\pi}\frac{1}{\left(1-x^2\right)^{1/2}}\int_{-1}^{1} b_0(\xi)\left(\frac{1-\xi}{1+\xi}\right)^{1/2}d\xi \tag{C.49}$$

$$\Rightarrow \gamma_h(x) = \frac{2}{\pi}\frac{C}{\left(1-x^2\right)^{1/2}}, \tag{C.50}$$

where

$$C = -\int_{-1}^{1} b_0(\xi)\left(\frac{1-\xi}{1+\xi}\right)^{1/2}d\xi. \tag{C.51}$$

We have obtained the homogenous solution, in order to find the general solution of linear integral equation (C.41) we add (C.38) and (C.51)

$$\gamma(x) = \gamma_h(x) + \gamma_p(x) = \frac{2}{\pi}\frac{1}{\left(1-x^2\right)^{1/2}}\left[\int_{-1}^{1}\frac{b_0(\xi)\cdot\left(1-\xi^2\right)^{1/2}}{\xi - x}d\xi + C\right],\ x\in(-1,1), \tag{C.52}$$

where $C$ now is an arbitrary constant.

From the definition of circulation we have

$$\Gamma = \int_{-1}^{1}\gamma(x)dx \tag{C.53}$$

$$\Rightarrow \Gamma = \int_{-1}^{1}\frac{2}{\pi}\frac{1}{\left(1-x^2\right)^{1/2}}\left[\int_{-1}^{1}\frac{b_0(\xi)\cdot\left(1-\xi^2\right)^{1/2}}{\xi - x}d\xi + C\right]dx \tag{C.54}$$

$$\Rightarrow \Gamma = \frac{2C}{\pi}\int_{-1}^{1}\frac{dx}{\left(1-x^2\right)^{1/2}} + \frac{2}{\pi}\int_{-1}^{1}\left[\int_{-1}^{1}\frac{1}{\left(1-x^2\right)^{1/2}}\frac{b_0(\xi)\cdot\left(1-\xi^2\right)^{1/2}}{\xi-x}d\xi\right]dx, \tag{C.55}$$

in the next section we will see that $\int_{-1}^{1}\frac{dx}{\left(1-x^2\right)^{1/2}} = \pi$ changing also the order of integration in the second integral we have

$$\Rightarrow \Gamma = 2C + \int_{-1}^{1}\left[\int_{-1}^{1}\frac{2}{\pi}\frac{1}{\left(1-x^2\right)^{1/2}}\frac{b_0(\xi)\cdot\left(1-\xi^2\right)^{1/2}}{\xi-x}dx\right]d\xi \tag{C.56}$$

$$\Rightarrow \Gamma = 2C + \int_{-1}^{1}\left(1-\xi^2\right)^{1/2} b_0(\xi) 4\left[-\frac{1}{2\pi}\int_{-1}^{1}\frac{1}{\left(1-x^2\right)^{1/2}}\frac{dx}{x-\xi}\right]d\xi, \tag{C.57}$$

notice now that in the brackets of (C.57), the l.h.s. of (C.41) has appeared; therefore we obtain

$$C = \frac{1}{2}\Gamma. \tag{C.58}$$

The constant $C$, that is related with the circulation, can be chosen in order to cancel the square-root infinity at the trailing edge i.e. when $x=-1$. This can be done if the term in brackets in (C.52) is zero at $x=-1$, therefore

$$C = \frac{1}{2}\Gamma = -\int_{-1}^{1}\frac{b_0(\xi)\cdot\left(1-\xi^2\right)^{1/2}}{\xi+1}d\xi \tag{C.59}$$

$$\Rightarrow C = -\int_{-1}^{1} b_0(\xi)\left(\frac{1-\xi}{1+\xi}\right)^{1/2} d\xi, \tag{C.60}$$

which is consistent with (C.51).

Summarizing, we solved the singular integral equation

$$\frac{1}{2\pi}\int_{-1}^{1}\frac{\gamma(\xi)}{\xi-x}d\xi = b_0(x), \quad x\in(-1,1), \tag{C.61}$$

that corresponds to the solution of the steady thin hydrofoil lifting problem, in such a way as steady Kutta condition, that the velocity at the trailing edge must be finite, is satisfied. The solution we have obtained is the following

$$\gamma(x)=\frac{2}{\pi}\frac{1}{\left(1-x^2\right)^{1/2}}\left[\int_{-1}^{1}\frac{b_0(\xi)\cdot\left(1-\xi^2\right)^{1/2}}{\xi-x}d\xi+\frac{1}{2}\Gamma\right],\ x\in(-1,1), \tag{C.62}$$

with

$$\Gamma=-2\int_{-1}^{1}b_0(\xi)\left(\frac{1-\xi}{1+\xi}\right)^{1/2}d\xi. \tag{C.63}$$

### C.3 Hilbert transforms

Before we proceed to the solution of the unsteady lifting problem we will consider the evaluation of some useful singular integrals known as Hilbert transforms. A we will see the calculation of this integrals is connected with the solution of lifting problems.

First of all, we consider the following category of elementary integrals

$$I_n=\int_{-1}^{1}\frac{x^n}{\left(1-x^2\right)^{1/2}}=\int_{0}^{\pi}(\cos\theta)^n\,d\theta=\begin{cases}0, & if\ \ n=2k+1\\ \pi\dfrac{(n-1)!}{n!}, & if\ \ n=2k\end{cases}. \tag{C.64}$$

Consider now the following integrals that is called Hilbert Transforms and appears in calculations of hydrodynamic quantities in thin hydrofoil theory

$$H_n(x)=\int_{-1}^{1}\frac{\xi^n d\xi}{(\xi-x)\left(1-\xi^2\right)^{1/2}}. \tag{C.65}$$

The above integrals are not elementary but they can evaluated using (C.64) and the following recursion formula

$$\mathrm{H}_n(x)=\int_{-1}^{1}\frac{\left[(\xi-x)\xi^{n-1}+x\xi^{n-1}\right]d\xi}{(\xi-x)\left(1-\xi^2\right)^{1/2}}=\int_{-1}^{1}\frac{\xi^n d\xi}{(\xi-x)\left(1-\xi^2\right)^{1/2}}=I_{n-1}+xH_{n-1}(x). \tag{C.66}$$

Let's consider some examples

for $n=0$

$$H_0(x)=\int_{-1}^{1}\frac{d\xi}{(\xi-x)\left(1-\xi^2\right)^{1/2}}=0. \tag{C.67}$$

The above relation is valid because $\left(1-\xi^2\right)^{-1/2}$ is the solution of eq.(C.41) as we have seen in the previous section.

for $n=1$

$$H_1(x)=\int_{-1}^{1}\frac{\xi d\xi}{(\xi-x)\left(1-\xi^2\right)^{1/2}}=I_o+xH_0(x)=\pi, \tag{C.68}$$

for $n=2$

$$H_2(x)=\int_{-1}^{1}\frac{\xi^2 d\xi}{(\xi-x)\left(1-\xi^2\right)^{1/2}}=I_1+xH_1(x)=\pi x. \tag{C.69}$$

We can see from the above that $H_n(x)$ is a polynomial of degree $n-1$.

The same formulas occurs for the case that the above integrals are considered on x-axis and outside the cut. Replacing x with complex variable and using analytic continuation and then considering the limiting value of z as imaginary part tends to zero we can see that recursive formula is valid and

$$H_0(\zeta)=\int_{-1}^{1}\frac{d\xi}{(\xi-\zeta)\left(1-\xi^2\right)^{1/2}}=\pi\left(\zeta^2-1\right)^{-1/2}. \tag{C.70}$$

For $n=1$

$$H_1(\zeta)=\int_{-1}^{1}\frac{\xi d\xi}{(\xi-\zeta)\left(1-\xi^2\right)^{1/2}}=I_o+\zeta H_0(\zeta)=\pi+\zeta\pi\left(\zeta^2-1\right)^{-1/2}=\pi\left[1+\zeta\left(\zeta^2-1\right)^{-1/2}\right], \tag{C.71}$$

for $n=2$

$$H_2(\zeta)=\int_{-1}^{1}\frac{\xi^2 d\xi}{(\xi-\zeta)\left(1-\xi^2\right)^{1/2}}=I_1+\zeta H_1(\zeta)=\pi\left[\zeta+\zeta^2\left(\zeta^2-1\right)^{-1/2}\right]. \tag{C.72}$$

### C.4 Solution of the singular integral equation in the unsteady case

Lets proceed now to the unsteady lifting problem and consider the singular integral equation for the unknown vortex distribution

$$-\frac{1}{2\pi}\int_{-1}^{1}\frac{\gamma(\xi;t)}{\xi-x}d\xi=b_{0,un}(x;t)\doteq b(x;t)+\frac{1}{2\pi}\int_{-\infty}^{-1}\frac{\gamma(\zeta+Ut)}{\zeta-x}d\zeta,\ \ x\in(-1,1). \tag{C.73}$$

The general solution of the above equation can be retrieved using Eqs. (C.61) - (C.63)

$$\gamma(x;t)=\frac{2}{\pi}\frac{1}{\left(1-x^2\right)^{1/2}}\left[\int_{-1}^{1}\frac{b_{0,un}(\xi;t)\cdot\left(1-\xi^2\right)^{1/2}}{\xi-x}d\xi+\frac{1}{2}\Gamma\right],\ x\in(-1,1) \tag{C.74}$$

$$\Rightarrow\gamma(x;t)=\frac{2}{\pi}\frac{1}{\left(1-x^2\right)^{1/2}}\left\{\int_{-1}^{1}\frac{\left(1-\xi^2\right)^{1/2}}{\xi-x}\left[b(\xi;t)+\frac{1}{2\pi}\int_{-\infty}^{-1}\frac{\gamma(\zeta+Ut)}{\zeta-\xi}d\zeta\right]d\xi+\frac{1}{2}\Gamma\right\}, \tag{C.75}$$

with

$$\Gamma(t)=-2\int_{-1}^{1}b_{0,un}(\xi;t)\left(\frac{1-\xi}{1+\xi}\right)^{1/2}d\xi. \tag{C.76}$$

Relation (C.75) can be written

$$\gamma(x;t)=\frac{2}{\pi}\frac{1}{\left(1-x^2\right)^{1/2}}\left\{\int_{-1}^{1}\frac{\left(1-\xi^2\right)^{1/2}}{\xi-x}b(\xi;t)d\xi+\underbrace{\int_{-1}^{1}\frac{\left(1-\xi^2\right)^{1/2}}{\xi-x}\left[\frac{1}{2\pi}\int_{-\infty}^{-1}\frac{\gamma(\zeta+Ut)}{\zeta-\xi}d\zeta\right]d\xi+\frac{1}{2}\Gamma}_{B(x;t)}\right\}. \tag{C.77}$$

Let's consider $B(x;t)$

$$B(x;t)=\int_{-1}^{1}\frac{1}{2\pi}\int_{-\infty}^{-1}\frac{\left(1-\xi^2\right)^{1/2}}{\xi-x}\frac{\gamma(\zeta+Ut)}{\zeta-\xi}d\zeta d\xi+\frac{1}{2}\Gamma, \tag{C.78}$$

and interchange integrals while using relation (C.8) we get

$$B(x;t)=-\frac{1}{2}\left\{\int_{-\infty}^{-1}\int_{-1}^{1}\frac{\left(1-\xi^2\right)^{1/2}}{\xi-x}\left[-\frac{1}{\pi}\frac{\gamma(\zeta+Ut)}{\zeta-\xi}\right]d\xi d\zeta+\int_{-\infty}^{1}\gamma(\zeta;t)d\zeta\right\} \tag{C.79}$$

$$\Rightarrow B(x;t)=-\frac{1}{2}\int_{-\infty}^{-1}\underbrace{\int_{-1}^{1}\frac{\left(1-\xi^2\right)^{1/2}}{\xi-x}\left[-\frac{1}{\pi}\frac{\gamma(\zeta+Ut)}{\zeta-\xi}\right]d\xi+\gamma(\zeta;t)}_{\mathrm{B_1}(x,\zeta;t)}d\zeta, \tag{C.80}$$

we will work now with the integrant of the exterior integral

$$\mathrm{B_1}(x,\zeta;t)=\int_{-1}^{1}\frac{\left(1-\xi^2\right)^{1/2}}{\xi-x}\left[-\frac{1}{\pi}\frac{\gamma(\zeta+Ut)}{\zeta-\xi}\right]d\xi+\gamma(\zeta;t) \tag{C.81}$$

$$\Rightarrow \mathrm{B}_1\left(x,\zeta;t\right)=-\frac{1}{\pi}\gamma\left(\zeta+Ut\right)\int_{-1}^{1}\frac{\left(1-\xi^2\right)^{1/2}}{\left(\xi-x\right)\left(\zeta-\xi\right)}d\xi+\gamma\left(\zeta;t\right), \tag{C.82}$$

recall that from relation (C.18) for point on the wake it holds $\gamma\left(\zeta;t\right)=\gamma\left(\zeta+Ut\right)$ thus

$$\mathrm{B}_1\left(x,\zeta;t\right)=\gamma\left(\zeta+Ut\right)\left[-\frac{1}{\pi}\int_{-1}^{1}\underbrace{\frac{\left(1-\xi^2\right)^{1/2}}{\left(\xi-x\right)\left(\zeta-\xi\right)}}_{B_2(x,\xi,\zeta)}d\xi+1\right], \tag{C.83}$$

consider the integrant of (C.83)

$$\mathrm{B}_2\left(x,\xi,\zeta\right)=\frac{\left(1-\xi^2\right)^{1/2}}{\left(\xi-x\right)\left(\zeta-\xi\right)}=-\frac{1-\xi^2}{\left(1-\xi^2\right)^{1/2}}\frac{1}{\left(\xi-x\right)\left(\xi-\zeta\right)}, \tag{C.84}$$

using partial fraction decomposition we get

$$\mathrm{B}_2\left(x,\xi,\zeta\right)=-\frac{1-\xi^2}{\left(1-\xi^2\right)^{1/2}}\left[\frac{1}{\left(\xi-x\right)\left(x-\zeta\right)}-\frac{1}{\left(\xi-\zeta\right)\left(x-\zeta\right)}\right] \tag{C.85}$$

$$\begin{aligned}\mathrm{B}_2\left(x,\xi,\zeta\right)=&-\frac{1}{\left(1-\xi^2\right)^{1/2}\left(x-\zeta\right)\left(\xi-x\right)}+\frac{\xi^2}{\left(1-\xi^2\right)^{1/2}\left(x-\zeta\right)\left(\xi-x\right)}\\&+\frac{1}{\left(1-\xi^2\right)^{1/2}\left(x-\zeta\right)\left(\xi-\zeta\right)}-\frac{\xi^2}{\left(1-\xi^2\right)^{1/2}\left(x-\zeta\right)\left(\xi-\zeta\right)}.\end{aligned} \tag{C.86}$$

We replace now (C.86) in (C.83), it follows

$$\begin{aligned}\mathrm{B}_1\left(x,\zeta;t\right)=\gamma\left(\zeta+Ut\right)\Bigg\{-\frac{1}{\pi}\int_{-1}^{1}\Bigg[&-\frac{1}{\left(1-\xi^2\right)^{1/2}\left(x-\zeta\right)\left(\xi-x\right)}+\frac{\xi^2}{\left(1-\xi^2\right)^{1/2}\left(x-\zeta\right)\left(\xi-x\right)}\\&+\frac{1}{\left(1-\xi^2\right)^{1/2}\left(x-\zeta\right)\left(\xi-\zeta\right)}-\frac{\xi^2}{\left(1-\xi^2\right)^{1/2}\left(x-\zeta\right)\left(\xi-\zeta\right)}\Bigg]d\xi+1\Bigg\}\end{aligned} \tag{C.87}$$

$$\Rightarrow \mathrm{B}_1\left(x,\zeta;t\right)=\gamma\left(\zeta+Ut\right)\left\{-\frac{1}{\pi}\frac{1}{\left(x-\zeta\right)}\left[-\int_{-1}^{1}\frac{d\xi}{\left(1-\xi^2\right)^{1/2}\left(\xi-x\right)}+\int_{-1}^{1}\frac{\xi^2 d\xi}{\left(1-\xi^2\right)^{1/2}\left(\xi-x\right)}\right.\right.$$
$$\left.\left.+\int_{-1}^{1}\frac{d\xi}{\left(1-\xi^2\right)^{1/2}\left(\xi-\zeta\right)}-\int_{-1}^{1}\frac{\xi^2 d\xi}{\left(1-\xi^2\right)^{1/2}\left(\xi-\zeta\right)}\right]+1\right\}, \qquad \text{(C.88)}$$

in the above equation we can recognize Hilbert transforms with respect to $x\in\left(-1,1\right)$ related with vortex distributions on the foil and generalized Hilbert transforms with respect to $\zeta\notin\left(-\infty,-1\right)$ related with vortex distributions on the trailing vortex sheet

$$\mathrm{B}_1\left(x,\zeta;t\right)=\gamma\left(\zeta+Ut\right)\left\{-\frac{1}{\pi}\frac{1}{\left(x-\zeta\right)}\left[-\mathrm{H}_0\left(x\right)+\mathrm{H}_2\left(x\right)+\mathrm{H}_0\left(\zeta\right)-\mathrm{H}_2\left(\zeta\right)\right]+1\right\} \qquad \text{(C.89)}$$

$$\Rightarrow \mathrm{B}_1\left(x,\zeta;t\right)=\gamma\left(\zeta+Ut\right)\left\{-\frac{1}{\pi}\frac{1}{\left(x-\zeta\right)}\left[\pi x+\pi\left(\zeta^2-1\right)^{-1/2}-\pi\left[\zeta+\zeta^2\left(\zeta^2-1\right)^{-1/2}\right]\right]+1\right\} \qquad \text{(C.90)}$$

$$\Rightarrow \mathrm{B}_1\left(x,\zeta;t\right)=\gamma\left(\zeta+Ut\right)\left\{1-\frac{x}{\left(x-\zeta\right)}-\frac{\left(\zeta^2-1\right)^{-1/2}}{\left(x-\zeta\right)}+\frac{\left[\zeta+\zeta^2\left(\zeta^2-1\right)^{-1/2}\right]}{\left(x-\zeta\right)}\right\} \qquad \text{(C.91)}$$

$$\Rightarrow \mathrm{B}_1\left(x,\zeta;t\right)=\gamma\left(\zeta+Ut\right)\left\{\frac{\left(\zeta^2-1\right)^{1/2}}{\left(\zeta-x\right)}\right.$$
$$\left.+\underbrace{1-\frac{x}{\left(x-\zeta\right)}-\frac{\left(\zeta^2-1\right)^{-1/2}}{\left(x-\zeta\right)}-\frac{\left(\zeta^2-1\right)^{1/2}}{\left(\zeta-x\right)}+\frac{\left[\zeta+\zeta^2\left(\zeta^2-1\right)^{-1/2}\right]}{\left(x-\zeta\right)}}_{\mathrm{B}_3\left(x,\zeta\right)}\right\}, \qquad \text{(C.92)}$$

after some algebra, it follows $B_3\left(x,\zeta\right)=0$. Thus relation (C.92) becomes

$$\mathrm{B}_1\left(x,\zeta;t\right)=\gamma\left(\zeta+Ut\right)\frac{\left(\zeta^2-1\right)^{1/2}}{\left(\zeta-x\right)}. \qquad \text{(C.93)}$$

Replacing (C.93) in (C.80) we obtain

$$B\left(x;t\right)=-\frac{1}{2}\int_{-\infty}^{-1}\gamma\left(\zeta+Ut\right)\frac{\left(\zeta^2-1\right)^{1/2}}{\left(\zeta-x\right)}d\zeta. \qquad \text{(C.94)}$$

Now the above expression of $B(x;t)$ is used in (C.77)

$$\gamma(x;t)=\frac{2}{\pi}\frac{1}{\left(1-x^2\right)^{1/2}}\left\{\int_{-1}^{1}\frac{\left(1-\xi^2\right)^{1/2}}{\xi-x}b(\xi;t)\,d\xi-\frac{1}{2}\int_{-\infty}^{-1}\gamma(\zeta+Ut)\frac{\left(\zeta^2-1\right)^{1/2}}{(\zeta-x)}d\zeta\right\}. \tag{C.96}$$

Again, the above solution is singular at the trailing edge $(x=-1)$ also through (C.6) infinite velocity occurs there. In order to avoid that singularity and satisfy Kutta condition the terms in brackets must vanish

$$\int_{-\infty}^{-1}\gamma(\zeta+Ut)\frac{\left(\zeta^2-1\right)^{1/2}}{(\zeta+1)}d\zeta=2\int_{-1}^{1}\frac{\left(1-\xi^2\right)^{1/2}}{\xi+1}b(\xi;t)\,d\xi \tag{C.97}$$

$$\Rightarrow\int_{-\infty}^{-1}\left(\frac{\zeta-1}{\zeta+1}\right)^{1/2}\gamma(\zeta+Ut)\,d\zeta=2\int_{-1}^{1}b(\xi;t)\left(\frac{1-\xi}{1+\xi}\right)^{1/2}d\xi. \tag{C.98}$$

The above relation is a singular integral equation for the wake vorticity. Notice that when the trailing vortex sheet reduces to a single vortex on the wake with strength $-\Gamma$ we obtain the steady state result for the circulation Eq. (C.63). In general that equation can be solved analytically using Laplace transform, Woods (1961), or numerically in a manner outlined by Frydenland & Kerwin (1977), Kerwin & Lee (1978) and Belibassakis (1993). In the present work we will present a solution for the case of sinusoidal oscillatory motions of the foil.

### C.5 Calculation of lift and moment

Before we proceed to the solution of (C.98) for the unknown wake vorticity, assuming harmonic oscillatory motion, we will obtain formulas for the calculation of force and moment in the general case.

Lift force and moment about $(x=0)$ can be calculated integrating pressure difference and its moment on the chord as follows

$$L=-\int_{-1}^{1}\left[p_{+}-p_{-}\right]dx, \tag{C.100}$$

and

$$M=-\int_{-1}^{1}\left[p_{+}-p_{-}\right]x\,dx, \tag{C.101}$$

where pressure difference can be evaluated from (C.13)

$$p_+ - p_- = -\rho\left[\frac{\partial\left(\Phi_+ - \Phi_-\right)}{\partial t} - U\left(\frac{\partial\Phi_+}{\partial x} - \frac{\partial\Phi_-}{\partial x}\right)\right]. \tag{C.102}$$

Working with lift force (C.100) we have

$$L = \int_{-1}^{1}\rho\left[\frac{\partial\left(\Phi_+ - \Phi_-\right)}{\partial t} - U\left(\frac{\partial\Phi_+}{\partial x} - \frac{\partial\Phi_-}{\partial x}\right)\right]dx = \int_{-1}^{1}\rho\frac{\partial\left(\Phi_+ - \Phi_-\right)}{\partial t} + U\gamma dx, \tag{C.103}$$

where relation (C.6) has been used.

Using integration by parts, we have

$$\int_{-1}^{1}\frac{\partial\Phi}{\partial t}dx = \int_{-1}^{1}\frac{\partial\Phi}{\partial t}d\left(x+1\right) = \left[\frac{\partial\Phi}{\partial t}\left(x+1\right)\right]_{-1}^{1} - \int_{-1}^{1}\frac{\partial^2\Phi}{\partial t\partial x}\left(x+1\right)dx - \int_{-1}^{1}\frac{\partial^2\Phi}{\partial t\partial x}\left(x+1\right)dx. \tag{C.104}$$

Where $\frac{\partial\Phi(1)}{\partial t} = 0$ because of the continuity along x-axis, i.e. $\frac{\partial\Phi(1)}{\partial t} = \lim_{x\to 1^+}\frac{\partial\Phi(x)}{\partial t}$, and the fact that the flow upstream to the leading edge is steady, i.e. $\frac{\partial\Phi(x)}{\partial t} = 0$ , $x > 1$. Using (C.104) and (C-6), relation (C.103) becomes

$$L = \rho\int_{-1}^{1}\left[\left(1+x\right)\frac{\partial\gamma}{\partial t} + U\gamma\right]dx. \tag{C.105}$$

Notice that the above equation for the steady case, leads to the known from Kutta-Joukowski theorem result $L_{st} = \rho U\Gamma$ .

Working in the same way we can obtain a similar result for moment

$$\mathrm{M} = \rho\int_{-1}^{1}\left[-\frac{1}{2}\left(1-x^2\right)\frac{\partial\gamma}{\partial t} + U\gamma x\right]dx. \tag{C.106}$$

Substituting vortex distribution (C.96) in (C.105) we have

$$L=\rho\int_{-1}^{1}(1+x)\frac{\partial}{\partial t}\left\{\frac{2}{\pi}\frac{1}{\left(1-x^2\right)^{1/2}}\left[\int_{-1}^{1}\frac{\left(1-\xi^2\right)^{1/2}}{\xi-x}b(\xi;t)\,d\xi-\frac{1}{2}\int_{-\infty}^{-1}\gamma(\zeta+Ut)\frac{\left(\zeta^2-1\right)^{1/2}}{(\zeta-x)}d\zeta\right]\right\}dx$$
$$+\rho\int_{-1}^{1}U\frac{2}{\pi}\frac{1}{\left(1-x^2\right)^{1/2}}\left\{\int_{-1}^{1}\frac{\left(1-\xi^2\right)^{1/2}}{\xi-x}b(\xi;t)\,d\xi-\frac{1}{2}\int_{-\infty}^{-1}\gamma(\zeta+Ut)\frac{\left(\zeta^2-1\right)^{1/2}}{(\zeta-x)}d\zeta\right\}dx \quad \text{(C.107)}$$

$$\Rightarrow L=\frac{2\rho}{\pi}\int_{-1}^{1}\left[\int_{-1}^{1}\frac{(1+x)}{\left(1-x^2\right)^{1/2}}\frac{\left(1-\xi^2\right)^{1/2}}{\xi-x}\frac{\partial b(\xi;t)}{\partial t}d\xi\right]dx$$
$$-\frac{\rho}{\pi}\int_{-1}^{1}\left[\int_{-\infty}^{-1}\frac{(1+x)}{\left(1-x^2\right)^{1/2}}\frac{\partial\gamma(\zeta+Ut)}{\partial t}\frac{\left(\zeta^2-1\right)^{1/2}}{(\zeta-x)}d\zeta\right]dx$$
$$+\frac{2\rho U}{\pi}\int_{-1}^{1}\left[\int_{-1}^{1}\frac{1}{\left(1-x^2\right)^{1/2}}\frac{\left(1-\xi^2\right)^{1/2}}{\xi-x}b(\xi;t)\,d\xi\right]dx$$
$$-\frac{\rho U}{\pi}\int_{-1}^{1}\left[\int_{-\infty}^{-1}\frac{1}{\left(1-x^2\right)^{1/2}}\gamma(\zeta+Ut)\frac{\left(\zeta^2-1\right)^{1/2}}{(\zeta-x)}d\zeta\right]dx \quad \text{(C.108)}$$

$$\Rightarrow L=\frac{2\rho}{\pi}\int_{-1}^{1}\left\{\int_{-1}^{1}\frac{1}{\left(1-x^2\right)^{1/2}}\frac{\left(1-\xi^2\right)^{1/2}}{\xi-x}\left[(1+x)\frac{\partial b(\xi;t)}{\partial t}+Ub(\xi;t)\right]d\xi\right\}dx$$
$$-\frac{\rho}{\pi}\int_{-1}^{1}\left\{\int_{-\infty}^{-1}\frac{1}{\left(1-x^2\right)^{1/2}}\frac{\left(\zeta^2-1\right)^{1/2}}{(\zeta-x)}\left[(1+x)\frac{\partial\gamma(\zeta+Ut)}{\partial t}+U\gamma(\zeta+Ut)\right]d\zeta\right\}dx, \quad \text{(C.109)}$$

Interchanging orders of integration we get

$$L=-\frac{2\rho}{\pi}\int_{-1}^{1}\left(1-\xi^2\right)^{1/2}\left\{\int_{-1}^{1}\frac{1}{(x-\xi)\left(1-x^2\right)^{1/2}}\left[(1+x)\frac{\partial b(\xi;t)}{\partial t}+Ub(\xi;t)\right]dx\right\}d\xi$$
$$+\frac{\rho}{\pi}\int_{-\infty}^{-1}\left(\zeta^2-1\right)^{1/2}\left\{\int_{-1}^{1}\frac{1}{(x-\zeta)\left(1-x^2\right)^{1/2}}\left[(1+x)\frac{\partial\gamma(\zeta+Ut)}{\partial t}+U\gamma(\zeta+Ut)\right]dx\right\}d\zeta \quad \text{(C.110)}$$

$$\Rightarrow L=-\frac{2\rho}{\pi}\int_{-1}^{1}\left(1-\xi^2\right)^{1/2}\left\{\frac{\partial b(\xi;t)}{\partial t}\int_{-1}^{1}\frac{(1+x)}{(x-\xi)\left(1-x^2\right)^{1/2}}dx+Ub(\xi;t)\int_{-1}^{1}\frac{1}{(x-\xi)\left(1-x^2\right)^{1/2}}dx\right\}d\xi$$

$$+\frac{\rho}{\pi}\int_{-\infty}^{-1}\left(\zeta^2-1\right)^{1/2}\left\{\frac{\partial\gamma(\zeta+Ut)}{\partial t}\int_{-1}^{1}\frac{(1+x)}{(x-\zeta)\left(1-x^2\right)^{1/2}}dx+U\gamma(\zeta+Ut)\int_{-1}^{1}\frac{1}{(x-\zeta)\left(1-x^2\right)^{1/2}}dx\right\}d\zeta. \tag{C.111}$$

In the above we can recognize the Hilbert transforms defined on the cut, i.e. $\xi\in(-1,1)$ and the generalized Hilbert transforms defined on the wake, i.e. $\zeta\in(-\infty,-1)$

$$L=-\frac{2\rho}{\pi}\int_{-1}^{1}\left(1-\xi^2\right)^{1/2}\left\{\frac{\partial b(\xi;t)}{\partial t}\left[H_0(\xi)+H_1(\xi)\right]+Ub(\xi;t)H_0(\xi)dx\right\}d\xi$$
$$+\frac{\rho}{\pi}\int_{-\infty}^{-1}\left(\zeta^2-1\right)^{1/2}\left\{\frac{\partial\gamma(\zeta+Ut)}{\partial t}\left[H_0(\zeta)+H_1(\zeta)\right]+U\gamma(\zeta+Ut)H_0(\zeta)\right\}d\zeta. \tag{C.112}$$

We can evaluate Hilbert transforms using Eqs. (C.67) and (C.68), using also using (C.8) and (C.18) we obtain

$$L=-2\rho\int_{-1}^{1}\left(1-\xi^2\right)^{1/2}\frac{\partial b(\xi;t)}{\partial t}d\xi+\rho U\Gamma$$
$$-\rho\int_{-\infty}^{-1}\left[1+\zeta+\left(\zeta^2-1\right)^{1/2}\right]\frac{\partial\gamma(\zeta+Ut)}{\partial t}d\zeta. \tag{C.113}$$

Notice that lift force consists of the quasi-steady lift component $L_{st}=\rho U\Gamma$, the lift due to body's motions and the last, memory term, that represents the effects of the wake where information of the whole history of circulation are stored.

Using (C.18) and substituting (C.17) in the last integral of (C.113), integrating by parts and then replacing (C.8), we obtain

$$-\rho\int_{-\infty}^{-1}\left[1+\zeta+\left(\zeta^2-1\right)^{1/2}\right]\frac{\partial\gamma(\zeta+Ut)}{\partial t}d\zeta$$
$$=-\rho U\int_{-\infty}^{-1}\left[1+\zeta+\left(\zeta^2-1\right)^{1/2}\right]\frac{\partial\gamma(\zeta;t)}{\partial\zeta}d\zeta$$
$$=-\lim_{\varepsilon\to-\infty}\rho U\left[\left[1+\zeta+\left(\zeta^2-1\right)^{1/2}\right]\gamma(\zeta;t)\right]_{\varepsilon}^{-1}+\rho U\int_{-\infty}^{-1}\left[1+\frac{\zeta}{\left(\zeta^2-1\right)^{1/2}}\right]\gamma(\zeta;t)d\zeta$$

$$= -\rho U\Gamma + \rho U \int_{-\infty}^{-1} \gamma(\zeta + Ut) \frac{\zeta d\zeta}{(\zeta^2 - 1)^{1/2}}. \tag{C.114}$$

Replacing (C.114) in (C.113) expression for lift force reduces to

$$L = -2\rho \int_{-1}^{1} (1-\xi^2)^{1/2} \frac{\partial b(\xi;t)}{\partial t} d\xi + \rho U \int_{-\infty}^{-1} \gamma(\zeta + Ut) \frac{\zeta d\zeta}{(\zeta^2 - 1)^{1/2}}. \tag{C.115}$$

In the same manner we obtain the following formula for the moment about the midchord $(x = 0)$

$$M = -\rho \int_{-1}^{1} \xi (1-\xi^2)^{1/2} \frac{\partial b(\xi;t)}{\partial t} d\xi - 2\rho U \int_{-1}^{-1} (1-\xi^2)^{1/2} b(\xi;t)\, d\xi + \frac{1}{2}\rho U \int_{-\infty}^{-1} \gamma(\zeta + Ut) \frac{d\zeta}{(\zeta^2 - 1)^{1/2}}. \tag{C.116}$$

In the above equations the first term expresses the added mass force and moment due to the linear and rotational acceleration of the foil, the second term in the moment equation is the quasi steady term and the last wake integral in both relations represent the memory effects stored in the trailing vortex sheet. Therefore, for a prescribed motion of hydrofoil's camber line, calculation of lift force and moment requires an expression for the wave-type vortex distribution on the wake, $\gamma(\zeta + Ut)$. That can be obtained solving equation (C.98).

### C.6 Harmonic time dependence

In the present section we will obtain analytical solution of equation (C.98) and calculation of lift force through (C.115) assuming for simplicity sinusoidal time dependence of the motion of camber line. Notice that, according to Fourier's theorem, every periodical wave-form can be obtained using simple harmonic forms and due to the linear character of the problem the solution equals the superposition of simple harmonic components.

Assuming harmonic motion of the mean camber line with radial frequency $\omega$ we have the following expression for the vertical velocity

$$b(x;t) = \mathrm{Re}\left\{ \dot{b}_0(x) e^{i\omega t} \right\}, \tag{C.117}$$

where $\dot{b}_0(x)$ is the complex amplitude of mean camber's velocity and $i$ is the complex unit.

According to the theory of linear systems the response must be harmonic both with respect to time and space, therefore

$$\gamma(x + Ut) = \mathrm{Re}\left\{ \dot{\gamma}_0 e^{i(\omega t + k_r x)} \right\}, \tag{C.118}$$

where $\dot{\gamma}_0$ is the complex amplitude of wave-type vorticity distribution and $k_r = \omega / U$ is the reduced frequency.

Lets substitute (C.117) and (C.118) in (C.98)

$$\int_{-\infty}^{-1}\left(\frac{\zeta-1}{\zeta+1}\right)^{1/2} \mathrm{Re}\left\{\dot{\gamma}_0 e^{i(\omega t+k_r\zeta)}\right\} d\zeta = 2\int_{-1}^{1} \mathrm{Re}\left\{\dot{b}_0(\xi) e^{i\omega t}\right\}\left(\frac{1-\xi}{1+\xi}\right)^{1/2} d\xi \tag{C.119}$$

$$\Rightarrow \mathrm{Re}\left\{\left[\int_{-\infty}^{-1}\left(\frac{\zeta-1}{\zeta+1}\right)^{1/2} \dot{\gamma}_0 e^{ik_r\zeta} d\zeta - 2\int_{-1}^{1}\dot{b}_0(\xi)\left(\frac{1-\xi}{1+\xi}\right)^{1/2} d\xi\right]\cdot e^{i\omega t}\right\} = 0, \tag{C.120}$$

using the known identity $\left(\mathrm{Re}\left\{ze^{ia}\right\} = 0 \Leftrightarrow z = 0 \ , \ a \in \mathbb{R}, z \in \mathbb{C}\right)$ from complex algebra, we have

$$\int_{-\infty}^{-1}\left(\frac{\zeta-1}{\zeta+1}\right)^{1/2} \dot{\gamma}_0 e^{ik_r\zeta} d\zeta = 2\int_{-1}^{1}\dot{b}_0(\xi)\left(\frac{1-\xi}{1+\xi}\right)^{1/2} d\xi \tag{C.121}$$

$$\Rightarrow \dot{\gamma}_0 = \frac{2\int_{-1}^{1}\left(\frac{1-\xi}{1+\xi}\right)^{1/2}\dot{b}_0(\xi) d\xi}{\int_{-\infty}^{-1}\left(\frac{\zeta-1}{\zeta+1}\right)^{1/2} e^{ik_r\zeta} d\zeta}. \tag{C.122}$$

Consider now the integral on denominator, if we assume as usual that harmonic wave is extended at all the support of the integral then the integrand is not absolute integrable. In order to avoid that, we assume that the motion starts abruptly from rest at $t_0 \ll t$ and thus $\gamma(x;t) = 0$ if $x < (t_0 - t)U$. Therefore (C.122) becomes

$$\Rightarrow \dot{\gamma}_0 = \frac{2\int_{-1}^{1}\left(\frac{1-\xi}{1+\xi}\right)^{1/2}\dot{b}_0(\xi) d\xi}{\lim\limits_{t_0\to-\infty}\underbrace{\int_{(t_0-t)U}^{-1}\left(\frac{\zeta-1}{\zeta+1}\right)^{1/2} e^{ik_r\zeta} d\zeta}_{A}}. \tag{C.123}$$

Working on A we have

$$A = \int_{(t_0-t)U}^{-1}\left(\frac{\zeta-1}{\zeta+1}\right)^{1/2} e^{ik_r\zeta} d\zeta \tag{C.124}$$

$$\Rightarrow A = \int_{(t_0-t)U}^{-1}\left(\frac{(\zeta-1)^2}{(\zeta+1)(\zeta-1)}\right)^{1/2} e^{ik_r\zeta} d\zeta \tag{C.125}$$

$$\Rightarrow A=\int_{(t_0-t)U}^{-1}\frac{|\zeta-1|}{\left(\zeta^2-1\right)^{1/2}}e^{ik_r\zeta}d\zeta \tag{C.126}$$

$$\Rightarrow A=-\int_{(t_0-t)U}^{-1}\frac{\zeta}{\left(\zeta^2-1\right)^{1/2}}e^{ik_r\zeta}d\zeta+\int_{(t_0-t)U}^{-1}\frac{1}{\left(\zeta^2-1\right)^{1/2}}e^{ik_r\zeta}d\zeta \tag{C.127}$$

$$\Rightarrow A=i\int_{(t_0-t)U}^{-1}\frac{i\zeta e^{ik_r\zeta}}{\left(\zeta^2-1\right)^{1/2}}d\zeta+\int_{(t_0-t)U}^{-1}\frac{1}{\left(\zeta^2-1\right)^{1/2}}e^{ik_r\zeta}d\zeta \tag{C.128}$$

$$\Rightarrow A=i\int_{(t_0-t)U}^{-1}\frac{\left(de^{ik_r\zeta}/dk_r\right)}{\left(\zeta^2-1\right)^{1/2}}d\zeta+\int_{(t_0-t)U}^{-1}\frac{1}{\left(\zeta^2-1\right)^{1/2}}e^{ik_r\zeta}d\zeta \tag{C.129}$$

$$\Rightarrow A=\left(i\frac{d}{dk_r}+1\right)\int_{(t_0-t)U}^{-1}\frac{1}{\left(\zeta^2-1\right)^{1/2}}e^{ik_r\zeta}d\zeta. \tag{C.130}$$

The limiting value of the above integral is proportional to the sum of Hankel function of zero order and second kind and its derivative i.e. Hankel function of first order and second kind (Fig.84).

They are defined by

$$H_0^{(2)}\left(k_r\right)\doteq J_n\left(k_r\right)-iY_n\left(k_r\right), \tag{C.131}$$

where $J_n\left(k_r\right)$ and $Y_n\left(k_r\right)$ is the Bessel functions of the first and second kind.

And the relation between them can be written

$$\frac{dH_0^{(2)}\left(k_r\right)}{dk_r}=iH_1^{(2)}\left(k_r\right). \tag{C.132}$$

In Figure 84 the Real and imagine part of Hankel functions of zero and first order and second kind are presented against reduced frequency $k_r$. Notice that, real part has a decaying wave character with rate $O\left(k_r^{-1/2}\right)$, while imagine part tends exponentially to zero, as $k_r$ raises, and thus only real part is important for moderate and large reduced frequencies. More information about Hankel and Bessel functions can be found in Abramowitz and Stegun (1964).

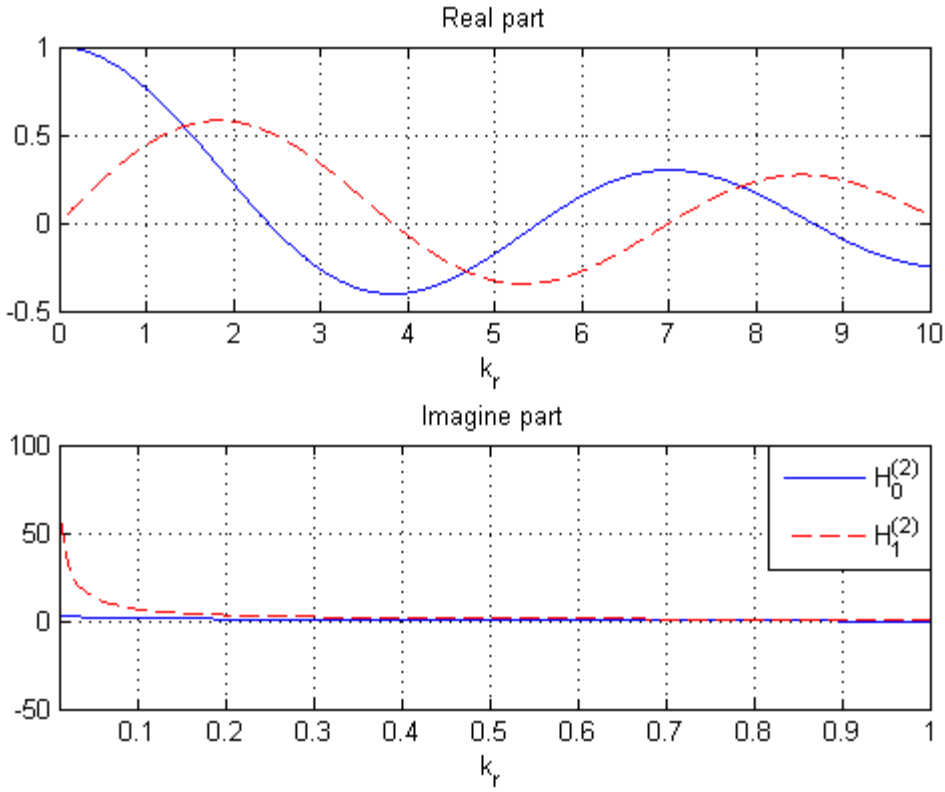


Figure 84: Real and imagine part of Hankel functions of zero and first order and second kind.

From the above we have

$$\lim_{t_0\to-\infty} A = \lim_{t_0\to-\infty}\left\{\left(i\frac{d}{dk_r}+1\right)\int_{(t_0-t)U}^{-1}\frac{1}{\left(\zeta^2-1\right)^{1/2}}e^{ik_r\zeta}d\zeta\right\} \tag{C.133}$$

$$\lim_{t_0\to-\infty} A = -\frac{\pi}{2}i\left(1+i\frac{d}{dk_r}\right)H_0^{(2)}\left(k_r\right) \tag{C.134}$$

$$\lim_{t_0\to-\infty} A = -\frac{\pi}{2}\left[iH_0^{(2)}\left(k_r\right)+H_1^{(2)}\left(k_r\right)\right]. \tag{C.135}$$

Finally, replacing (C.135) in (C.123), we obtain for complex vorticity

$$\Rightarrow \dot{\gamma}_0 = -\frac{4}{\pi}\frac{\int_{-1}^{1}\left(\frac{1-\xi}{1+\xi}\right)^{1/2}\dot{b}_0\left(\xi\right)d\xi}{\left[iH_0^{(2)}\left(k_r\right)+H_1^{(2)}\left(k_r\right)\right]}. \tag{C.136}$$

For the present linear system on harmonic excitation lifting force must be of sinusoidal time dependence

$$L(t) = \mathrm{Re}\left\{\dot{L}_0 e^{i\omega t}\right\}, \tag{C.137}$$

where $\dot{L}_0$ is the complex amplitude of lift force.

Replacing Eqs. (C.117), (C.118) in (C.115) and assuming that the motion starts abruptly from rest at $t_0 \ll t$ in the same manner with before, we obtain

$$L = -2\rho \int_{-1}^{1} \left(1-\xi^2\right)^{1/2} \frac{\partial\, \mathrm{Re}\left\{\dot{b}_0(\xi) e^{i\omega t}\right\}}{\partial t} d\xi + \lim_{t_0 \to -\infty} \left[ \rho U \int_{(t_0 - t)U}^{-1} \mathrm{Re}\left\{\dot{\gamma}_0 e^{i(\omega t + k_r \zeta)}\right\} \frac{\zeta\, d\zeta}{\left(\zeta^2 - 1\right)^{1/2}} \right] \tag{C.138}$$

and using (C.137), we have

$$\mathrm{Re}\left\{ \left[ \dot{L}_0 + 2\rho \int_{-1}^{1} \left(1-\xi^2\right)^{1/2} i\omega \dot{b}_0(\xi) d\xi - \lim_{t_0 \to -\infty} \left( \rho U \int_{(t_0 - t)U}^{-1} \dot{\gamma}_0 e^{ik_r \zeta} \frac{\zeta\, d\zeta}{\left(\zeta^2 - 1\right)^{1/2}} \right) \right] e^{i\omega t} \right\} = 0 \tag{C.139}$$

$$\Rightarrow \dot{L}_0 = -2\rho \int_{-1}^{1} \left(1-\xi^2\right)^{1/2} i\omega \dot{b}_0(\xi) d\xi + \lim_{t_0 \to -\infty} \left[ \rho U \int_{(t_0 - t)U}^{-1} \dot{\gamma}_0 e^{ik_r \zeta} \frac{\zeta\, d\zeta}{\left(\zeta^2 - 1\right)^{1/2}} \right]. \tag{C.140}$$

We can evaluate $\dot{\gamma}_0$ using (C.136), and thus

$$\dot{L}_0 = -2\rho \int_{-1}^{1} \left(1-\xi^2\right)^{1/2} i\omega \dot{b}_0(\xi) d\xi + \underbrace{\lim_{t_0 \to -\infty} \left( \rho U \int_{(t_0 - t)U}^{-1} \left\{ -\frac{4}{\pi} \frac{\int_{-1}^{1} \left(\frac{1-\xi}{1+\xi}\right)^{1/2} \dot{b}_0(\xi) d\xi}{\left[ i H_0^{(2)}(k_r) + H_1^{(2)}(k_r) \right]} \right\} e^{ik_r \zeta} \frac{\zeta\, d\zeta}{\left(\zeta^2 - 1\right)^{1/2}} \right)}_{\dot{\mathrm{B}}}. \tag{C.141}$$

Working with $\dot{\mathrm{B}}$ we have

$$\dot{\mathrm{B}} = -\frac{4\rho U}{\pi} \frac{1}{\left[ H_1^{(2)}(k_r) + i H_0^{(2)}(k_r) \right]} \lim_{t_0 \to -\infty} \left( \int_{(t_0 - t)U}^{-1} \left\{ \int_{-1}^{1} \left[ \frac{e^{ik_r \zeta} \zeta}{\left(\zeta^2 - 1\right)^{1/2}} \left(\frac{1-\xi}{1+\xi}\right)^{1/2} \dot{b}_0(\xi) \right] d\xi \right\} d\zeta \right), \tag{C.142}$$

interchanging orders of integration we have

$$\dot{\mathrm{B}} = -\frac{4\rho U}{\pi}\frac{1}{\left[iH_0^{(2)}(k_r)+H_1^{(2)}(k_r)\right]}\int_{-1}^{1}\left\{\left(\frac{1-\xi}{1+\xi}\right)^{1/2}\dot{b}_0(\xi)\left[\lim_{t_0\to-\infty}\int_{(t_0-t)U}^{-1}\frac{e^{ik_r\zeta}\zeta}{\left(\zeta^2-1\right)^{1/2}}d\zeta\right]\right\}d\xi \tag{C.143}$$

$$\Rightarrow \dot{\mathrm{B}} = \frac{4\rho U}{\pi}\frac{i}{\left[iH_0^{(2)}(k_r)+H_1^{(2)}(k_r)\right]}\int_{-1}^{1}\left\{\left(\frac{1-\xi}{1+\xi}\right)^{1/2}\dot{b}_0(\xi)\left[\lim_{t_0\to-\infty}\int_{(t_0-t)U}^{-1}\frac{i\zeta e^{ik_r\zeta}}{\left(\zeta^2-1\right)^{1/2}}d\zeta\right]\right\}d\xi \tag{C.144}$$

$$\Rightarrow \dot{\mathrm{B}} = \frac{4\rho U}{\pi}\frac{i}{\left[iH_0^{(2)}(k_r)+H_1^{(2)}(k_r)\right]}\int_{-1}^{1}\left\{\left(\frac{1-\xi}{1+\xi}\right)^{1/2}\dot{b}_0(\xi)\left[\lim_{t_0\to-\infty}\int_{(t_0-t)U}^{-1}\frac{\left(de^{ik_r\zeta}/dk_r\right)}{\left(\zeta^2-1\right)^{1/2}}d\zeta\right]\right\}d\xi \tag{C.145}$$

$$\Rightarrow \dot{\mathrm{B}} = \frac{4\rho U}{\pi}\frac{i}{\left[iH_0^{(2)}(k_r)+H_1^{(2)}(k_r)\right]}\int_{-1}^{1}\left\{\left(\frac{1-\xi}{1+\xi}\right)^{1/2}\dot{b}_0(\xi)\frac{d}{dk_r}\left[\lim_{t_0\to-\infty}\int_{(t_0-t)U}^{-1}\frac{e^{ik_r\zeta}}{\left(\zeta^2-1\right)^{1/2}}d\zeta\right]\right\}d\xi, \tag{C.146}$$

where the integral in the brackets is proportional to Hankel function of zero order and second kind

$$\dot{\mathrm{B}} = \frac{4\rho U}{\pi}\frac{i}{\left[iH_0^{(2)}(k_r)+H_1^{(2)}(k_r)\right]}\int_{-1}^{1}\left\{\left(\frac{1-\xi}{1+\xi}\right)^{1/2}\dot{b}_0(\xi)\left[-\frac{\pi}{2}i\frac{dH_0^{(2)}(k_r)}{dk_r}\right]\right\}d\xi, \tag{C.147}$$

using (C.132) we obtain

$$\dot{\mathrm{B}} = 2\rho U i\left(\frac{H_1^{(2)}(k_r)}{iH_0^{(2)}(k_r)+H_1^{(2)}(k_r)}\right)\int_{-1}^{1}\left\{\left(\frac{1-\xi}{1+\xi}\right)^{1/2}\dot{b}_0(\xi)\right\}d\xi. \tag{C.148}$$

Replacing $\dot{\mathrm{B}}$ in (C.141) and (C.141) into (C.137) we obtain

$$L(t) = -2\rho U\,\mathrm{Re}\left\{\left[ik_r\int_{-1}^{1}\left(1-\xi^2\right)^{1/2}\dot{b}_0(\xi)d\xi + \underbrace{\left(\frac{H_1^{(2)}(k_r)}{H_1^{(2)}(k_r)+iH_0^{(2)}(k_r)}\right)}_{C(k_r)}\int_{-1}^{1}\left\{\left(\frac{1-\xi}{1+\xi}\right)^{1/2}\dot{b}_0(\xi)\right\}d\xi\right]e^{i\omega t}\right\}, \tag{C.149}$$

where $C(k_r)$ is the Theodorsen function defined as a ratio of Hankel functions of second kind, zero and first order:

$$C(k_r)=\frac{H_1^{(2)}(k_r)}{H_1^{(2)}(k_r)+iH_0^{(2)}(k_r)}. \tag{C.150}$$

Function $C(k_r)$ encompasses the memory effects due to the unsteady wake, and for low frequencies its limiting value is 1. The Argand diagram of Theodorsen function is presented in Figure 85:

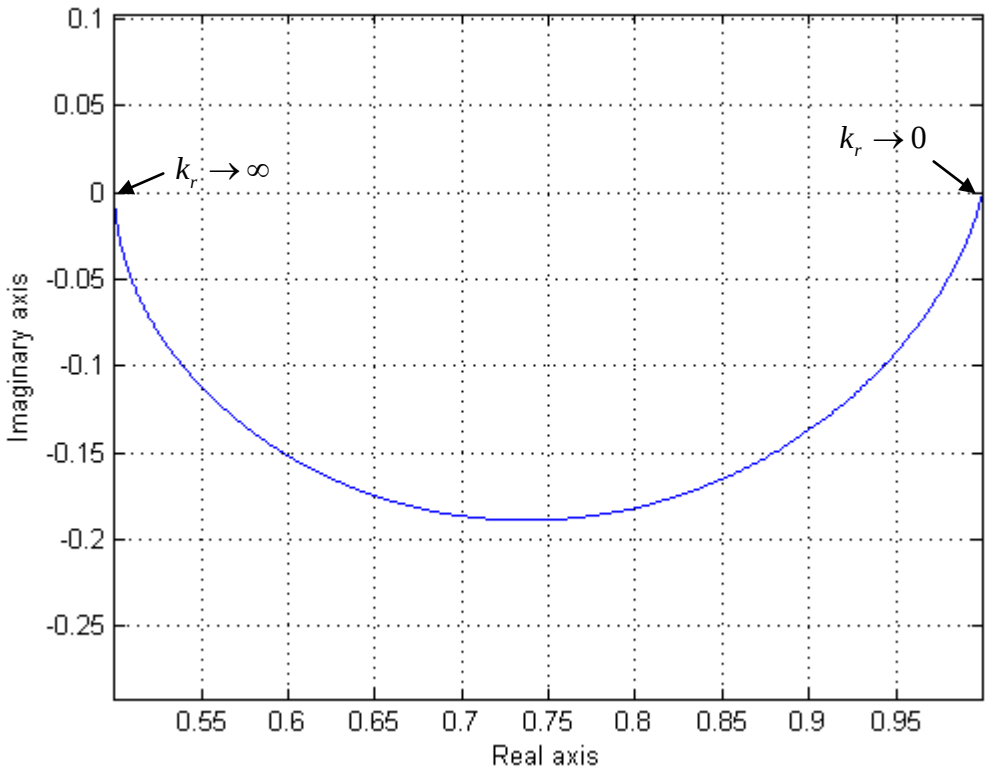


Figure 85: Argand diagram of Theodorsen function, reduced frequency raises from zero to infinite along the complex curve with clockwise direction.

The limiting value of (C.149) for $k_r \to 0$ is

$$\lim_{k_r\to 0} L(t)=-2\rho U\left\{\lim_{k_r\to 0}\mathrm{Re}\left\{\left[ik_r\int_{-1}^{1}\left(1-\xi^2\right)^{1/2}\dot{b}_0(\xi)d\xi+C(k_r)\int_{-1}^{1}\left[\left(\frac{1-\xi}{1+\xi}\right)^{1/2}\dot{b}_0(\xi)\right]d\xi\right]e^{i\omega t}\right\}\right\} \tag{C.151}$$

$$\Rightarrow \lim_{k_r\to 0} L(t)=-2\rho U\int_{-1}^{1}\left[\left(\frac{1-\xi}{1+\xi}\right)^{1/2}\underbrace{\mathrm{Re}\left\{\dot{b}_0(\xi)e^{i\omega t}\right\}}_{b(\xi;t)}\right]d\xi, \tag{C.152}$$

and using (C.63), it follows

$$\lim_{k_r \to 0} L(t) = \rho U \Gamma, \tag{C.153}$$

which conforms with the steady state result.

### C.7 Studying flapping motion with unsteady thin hydrofoil theory

Let's focus now to the interesting case of flapping motion that consists of a linear (heaving) motion

$$h(t) = \mathrm{Re}\left\{\dot{h}_0 e^{i\omega t}\right\}, \tag{C.154}$$

and a rotational (pitching) motion about a pivot axis, e.g. at the midchord

$$\theta_0(t) = \mathrm{Re}\left\{\dot{\theta}_0 e^{i\omega t}\right\}, \tag{C.155}$$

where $\dot{h}_0$ and $\dot{\theta}_0$ are the complex amplitude's of heaving and pitching motion respectively. These motions are considered to be small and thus the mean-camber line is $\eta(x;t) = h(t) + x\theta_0(t)$, and the normal velocity is evaluated using (C.4)

$$b(x;t) = \frac{\partial \Phi}{\partial y} = \frac{\partial y_c}{\partial t} - U_I \frac{\partial y_c}{\partial x} \tag{C.156}$$

$$\Rightarrow b(x;t) = \frac{dh(t)}{dt} + x\frac{d\theta_0(t)}{dt} - U_I \theta_0(t), \tag{C.157}$$

and using (C.117), (C.154), (C.155), it follows

$$\mathrm{Re}\left\{\dot{b}_0(x) e^{i\omega t}\right\} = \mathrm{Re}\left\{\left[i\omega\dot{h}_0 - U_I\dot{\theta}_0 + i\omega x\dot{\theta}_0\right] e^{i\omega t}\right\} \tag{C.158}$$

$$\Rightarrow \dot{b}_0(x) = \left[i\omega\dot{h}_0 - U_I\dot{\theta}_0 + i\omega x\dot{\theta}_0\right]. \tag{C.159}$$

Substituting now (C.159) in (C.149) we obtain

$$L(t) = -2\rho U \left\{ \mathrm{Re}\left\{ \left[ ik_r \underbrace{\int_{-1}^{1} \left(1-\xi^2\right)^{1/2} \left[ i\omega\dot{h}_0 - U_I\dot{\theta}_0 + i\omega\xi\dot{\theta}_0 \right] d\xi}_{I_A} \right. \right. \right.$$
$$\left. \left. \left. + C\left(k_r\right) \underbrace{\int_{-1}^{1} \left\{ \left( \frac{1-\xi}{1+\xi} \right)^{1/2} \left[ i\omega\dot{h}_0 - U_I\dot{\theta}_0 + i\omega\xi\dot{\theta}_0 \right] \right\} d\xi}_{I_B} \right] e^{i\omega t} \right\}. \tag{C.160}$$

Working with $I_A$ we have

$$I_A = \int_{-1}^{1} \left(1-\xi^2\right)^{1/2} \left[ i\omega\dot{h}_0 - U_I\dot{\theta}_0 + i\omega\xi\dot{\theta}_0 \right] d\xi \tag{C.161}$$

$$\Rightarrow I_A = \left( i\omega\dot{h}_0 - U_I\dot{\theta}_0 \right) \int_{-1}^{1} \left(1-\xi^2\right)^{1/2} d\xi + \left( i\omega\dot{\theta}_0 \right) \int_{-1}^{1} \left(1-\xi^2\right)^{1/2} \xi d\xi. \tag{C.162}$$

Notice that the first integral is the surface of a unit half circular disk, i.e. $\int_{-1}^{1} \left(1-\xi^2\right)^{1/2} d\xi = \pi/2$ and the second one is its moment about the center, i.e. $\int_{-1}^{1} \left(1-\xi^2\right)^{1/2} \xi d\xi = 0$, therefore

$$\Rightarrow I_A = \left( i\omega\dot{h}_0 - U_I\dot{\theta}_0 \right) \frac{\pi}{2}. \tag{C.163}$$

Working now with $I_B$ we have

$$I_B = \int_{-1}^{1} \left\{ \left( \frac{1-\xi}{1+\xi} \right)^{1/2} \left[ i\omega\dot{h}_0 - U_I\dot{\theta}_0 + i\omega\xi\dot{\theta}_0 \right] \right\} d\xi \tag{C.164}$$

$$\Rightarrow I_B = \left( i\omega\dot{h}_0 - U_I\dot{\theta}_0 \right) \int_{-1}^{1} \frac{1-\xi}{\left(1-\xi^2\right)^{1/2}} d\xi + i\omega\dot{\theta}_0 \int_{-1}^{1} \frac{\xi-\xi^2}{\left(1-\xi^2\right)^{1/2}} d\xi. \tag{C.165}$$

The above integrals are elementary, see Eq.(C.64), thus

$$I_B = \left( i\omega\dot{h}_0 - U_I\dot{\theta}_0 \right)\left( I_0 - I_1 \right) + i\omega\dot{\theta}_0 \left( I_1 - I_2 \right) \tag{C.166}$$

$$\Rightarrow I_B = \left( i\omega\dot{h}_0 - U_I\dot{\theta}_0 \right)\pi - i\omega\dot{\theta}_0 \frac{\pi}{2}. \tag{C.167}$$

Replacing (C.163) and (C.167) in (C.160) we obtain

$$L(t) = -2\rho U\left\{\mathrm{Re}\left\{ik_r\left(i\omega\dot{h}_0 - U_I\dot{\theta}_0\right)\frac{\pi}{2}\right\}e^{i\omega t} + \mathrm{Re}\left\{C\left(k_r\right)\left[\left(i\omega\dot{h}_0 - U_I\dot{\theta}_0\right)\pi - i\omega\dot{\theta}_0\frac{\pi}{2}\right]e^{i\omega t}\right\}\right\} \quad \text{(C.168)}$$

$$\Rightarrow L(t) = -2\pi\rho U^2\left\{\mathrm{Re}\left\{ik_r\left(ik_r\dot{h}_0 - \dot{\theta}_0\right)\frac{1}{2}\right\}e^{i\omega t} + \mathrm{Re}\left\{C\left(k_r\right)\left[\left(ik_r\dot{h}_0 - \dot{\theta}_0\right) - ik_r\dot{\theta}_0\frac{1}{2}\right]e^{i\omega t}\right\}\right\} \quad \text{(C.169)}$$

$$\Rightarrow L(t) = -2\pi\rho U^2\,\mathrm{Re}\left\{C\left(k_r\right)\left[ik_r\dot{h}_0 - \left(1+\frac{1}{2}ik_r\right)\dot{\theta}_0\right]e^{i\omega t}\right\} - \pi\rho\,\mathrm{Re}\left\{\left[\left(i\omega\right)^2\dot{h}_0 - Ui\omega\dot{\theta}_0\right]e^{i\omega t}\right\} \quad \text{(C.170)}$$

$$\Rightarrow L(t) = -2\pi\rho U^2\,\mathrm{Re}\left\{C\left(k_r\right)\left[ik_r\dot{h}_0 - \left(1+\frac{1}{2}ik_r\right)\dot{\theta}_0\right]e^{i\omega t}\right\} - \pi\rho\left[\frac{d^2h(t)}{dt^2} - U\frac{d\theta(t)}{dt}\right]. \quad \text{(C.171)}$$

In the above equations (C.170) and (C.171) the second term is the added mass component of lift force. Finally, we obtain the non-dimensional lift coefficient $C_L(t) = L(t)/\rho U^2$

$$C_L(t) = -2\pi\,\mathrm{Re}\left\{C\left(k_r\right)\left[ik_r\dot{h}_0 - \left(1+\frac{1}{2}ik_r\right)\dot{\theta}_0\right]e^{i\omega t}\right\} - \pi\,\mathrm{Re}\left\{\left[\left(ik_r\right)^2\dot{h}_0 - ik_r\dot{\theta}_0\right]e^{i\omega t}\right\}, \quad \text{(C.172)}$$

or

$$C_L(t) = -2\pi\,\mathrm{Re}\left\{C\left(k_r\right)\left[ik_r\dot{h}_0 - \left(1+\frac{1}{2}ik_r\right)\dot{\theta}_0\right]e^{i\omega t}\right\} - \pi\left[\frac{1}{U^2}\frac{d^2h(t)}{dt^2} - \frac{1}{U}\frac{d\theta(t)}{dt}\right]. \quad \text{(C.173)}$$

### C.8 Thin hydrofoils performing on perturbation sinusoidal-gust background field

We have already studied one type of unsteadiness that appears in lifting flow problems, i.e. the time dependent oscillating motions of the hydrofoil. Another example of unsteady motion is when the hydrofoil is moving with constant forward speed in a fluid which is non uniform i.e. a disturbed background field exists, for example a sinusoidal gust. The last problem has been studied by many scientist like Sears and Kerwin using theoretical or numerical methods, see e.g. Belibassakis (1993). Practical examples of this are the motion of a hydrofoil ship in waves, an airplane in turbulence or the motion of the propeller blades in a spatially non uniform ship's wake. Also, energy extraction from non-uniform internal wavy flows using biomimetc flapping-foil systems, could be another very interesting application that requires knowledge from both unsteady lifting body and unsteady background theories.

The background field is considered to be a stationary (with respect to the earth-fixed reference frame) sinusoidal transverse wave, i.e.

$$V_G\left(x\right) = V_G\cos k_G x = \mathrm{Re}\left\{\dot{V}_G e^{ik_{r,G}x}\right\}, \quad \text{(C.174)}$$

where $V_g$ is the amplitude of the sinusoidal gust and $k_{r,G} = \omega_{k,G} / U$ the non-dimensional gust reduced frequency.

With respect to the hydrofoil-fixed reference frame, the gust is an incident wave disturbance that travels with the forward speed of the foil $U$ and the radial frequency of the wave is $\omega_G = U \cdot k_{r,G}$. With respect to body-fixed reference frame (C.174) is written

$$V_G(x;t) = V_G \cos\left(k_{r,G} x + \omega_g t\right) = \mathrm{Re}\left\{\dot{V}_G e^{i\left(k_{r,G} x + \omega_g t\right)}\right\}. \tag{C.175}$$

In the present case, boundary condition (C.4) becomes

$$b(x;t) = \frac{\partial \Phi}{\partial y} = \frac{\partial y_c}{\partial t} - U_I \frac{\partial y_c}{\partial x} - V_G. \tag{C.176}$$

In the present paragraph we will obtain result for lift coefficient for a steady hydrofoil in the presence of gust. After that, using the principle of linear superposition, a solution for the more complex problem of flapping hydrofoil in sinusoidal background field can be obtained. Thus, from (C.175) and (C.176), it follows

$$b(x;t) = \mathrm{Re}\left\{\dot{V}_G e^{i\left(k_{r,G} x + \omega_g t\right)}\right\}, \tag{C.177}$$

and using (C.117), we obtain

$$\mathrm{Re}\left\{\dot{b}_0(x) e^{i\omega_g t}\right\} = \mathrm{Re}\left\{\dot{V}_G e^{i\left(k_{r,G} x + \omega_g t\right)}\right\} \tag{C.178}$$

$$\Rightarrow \dot{b}_0(x) = \dot{V}_G e^{i k_{r,G} x}. \tag{C.179}$$

We replace now (C.179) in (C.149)

$$L(t) = -2\rho U \,\mathrm{Re}\left\{\left[ i k_r \int_{-1}^{1} \left(1-\xi^2\right)^{1/2} \dot{V}_G e^{i k_{r,G} \xi} d\xi + C\left(k_r\right) \int_{-1}^{1} \left\{\left(\frac{1-\xi}{1+\xi}\right)^{1/2} \dot{V}_G e^{i k_{r,G} \xi}\right\} d\xi \right] e^{i\omega t} \right\}. \tag{C.180}$$

Evaluating the integrals in terms of Bessel functions we obtain

$$L(t) = -2\pi\rho U \,\mathrm{Re}\left\{\dot{V}_G e^{i\omega t} \left[ \underbrace{\frac{2i / \pi k_{r,G}}{H_1^{(2)}(k_{r,G}) + i H_0^{(2)}(k_{r,G})}}_{S\left(k_{r,G}\right)} \right]\right\}, \tag{C.181}$$

$S(k_{r,G})$ is the Sears function defined in terms Hankel functions of second kind, zero and first order:

$$S\left(k_{r,G}\right)=\frac{2i/\pi k_{r,G}}{H_1^{(2)}(k_{r,G})+iH_0^{(2)}(k_{r,G})}. \tag{C.182}$$

Function $S(k_{r,G})$ encompasses the memory effects due to the unsteady wake, and for low frequencies its limiting value is 1. The Argand diagram of Sears function is presented in Figure 86

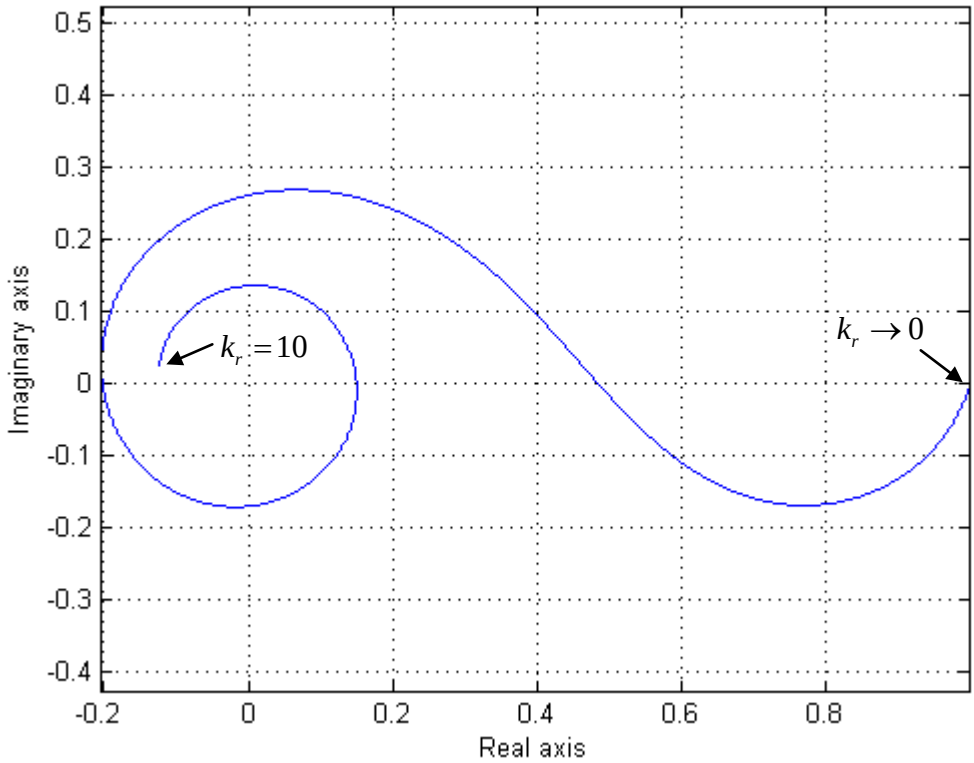


Figure 86: Argand diagram of Sears function, reduced frequency raises from zero to infinite along the complex curve.

Finally, we obtain the non-dimensional lift coefficient $C_L(t)=L(t)/\rho U^2$

$$C_L(t)=-2\pi\,\mathrm{Re}\left\{\left[\dot{V}_G/US\left(k_{r,G}\right)\right]e^{i\omega t}\right\}. \tag{C.183}$$

## References

Abbott, I.H., Von Doenhoff, A.E., 1959, "Theory of wing sections", *Dover Publications*.

Abramowitz, M., Stegun, I.A., 1964, "Handbook of mathematical functions", *U.S. Government Printing Office*.

Alexander, R.McN., 1983, "The history of fish mechanics", In: P.W. Webb and D. Weihs (eds.), Fish Biomechanics, New York: *Praeger Press*, 1–35.

Anderson, J.M., 1996, "Vorticity control for efficient propulsion", Ph.D. Dissertation, *Department of Ocean Engineering, Massachusetts Institute of Technology*, Cambridge, MA, USA.

Anderson, J.M., Streitlien, K., Barrett, D. S. & Triantafyllou, M.S., 1998, "Oscillating foils of high propulsive efficiency", *J. Fluid Mech,* 360, 41-72.

Anon., 1983, "Wave power for ship propulsion", *The Motor Ship*, 64(757), 67-69

Ausman, J.S., 1954, "Pressure limitation on the upper surface of a hydrofoil", Ph.D. Thesis in Mechanics Engineering at the *Univ. of California*, Berkeley, California.

Bal, S., 1999, "A potential based panel method for 2-D hydrofoils", *Ocean Engineering*, 26, 343-361.

Bandyopadhyay, P., Castano, J., Rice, J., Phillips, R., Nedderman, W., Macy, W., 1997, "Low-speed maneuvering hydrodynamics of fish and small underwater vehicles", *Journal of Fluids Engineering*, 119, 136–144.

Barrett D. S., Triantafyllou M.S., Yue K.P., Grosenbaugh, M.A., Wolfgang, M.J., 1999, "Drag reduction in fish-like locomotion", *Journ. Fluid Mech*, 392, 183-212.

Batchelor, G.K., 1967, "An introduction to fluid dynamics", *Cambridge University Press*.

Beer, G., Smith, I., Duenser, C., 2008, "The boundary element method with programming", *Springer-Verlag*.

Belibassakis, K., 1993, "Introduction to computational hydrodynamics. Numerical applications of thin hydrofoil theory", *NTUA*.

Belibassakis, K., 2009, "Effects of wave-induced ship motion on propeller operation with application to fouling estimation and propulsion optimization", *13th Congress Int. Maritime Assoc. Mediterranean* (IMAM2009).

Belibassakis, K., 2010, "Roll response of ship hull sections in variable bathymetry regions by a hybrid BEM - vortex particle pethod", *Journal of Hydrodynamics*, Ser B, Vol. 22, Issue 5, Supplement 1, 413-418.

Belibassakis, K., 2011, "A panel method based on vorticity distribution for the calculation of free surface flows around ship hull configurations with lifting bodies", *Proc. IMAM 2011*, Genoa, Italy.

Belibassakis, K.A., Athanassoulis, G.A., 2011, "A coupled-mode system with application to nonlinear water waves propagating in finite water depth and in variable bathymetry regions", *Coastal Engineering*, 58, 337-350.

Belibassakis, K.A., Athanassoulis, G.A., Gerostathis, Th., 2001, "A coupled-mode model for the refraction-diffraction of linear waves over steep three-dimensional bathymetry", *Applied Ocean Res.*, 23(6), 319-336.

Belibassakis, K.A., Gerostathis, Th. P., Kostas, K.V., Politis, C.G., Kaklis, P.D., Ginnis, A.I., Feuer, C., 2013, "A BEM-isogeometric method for the ship wave-resistance problem", *Ocean Engineering*, 60, 53-67.

Belibassakis, K.A., Politis, G.K., 2012a, "Hydrodynamic analysis of biomimetic wing systems for augmenting ship propulsion", *Proc. 22 Intern. Ocean and Polar Engineering Conference (ISOPE 2012)*, Rhodes-Greece.

Belibassakis, K.A., Politis, G.K., 2012b, "Roll stabilization by vertical thrust-producing flapping wings using active pitch control", *Proceedings of the 11th International Conference on the Stability of Ships and Ocean Vehicles*, Athens, Greece.

Belibassakis, K.A., Politis, G.K., Triantafyllou, M.S., 1997, "Application of the Vortex Lattice Method to the propulsive performance of a pair of oscillating wing-tails", *Proc. 8th CMEM97*, Rhodes, Greece.

Berenger, J.P., 1994, "A perfectly matched layer for the absorption of electromagnetic waves", *J. Comput. Phys.*, 114, 185-200.

Berg, A., 1985, "Trials with passive foil propulsion on M/S Kystfangst Project no. 672.138", *Technical report. Fiskeriteknologisk Forskningsinstitutt, Fartoyseksjon, Marinteknisk snter, Hakon Hakonsensgt.*, Trondheim, 34, 7000.

Blake, R.W., 1983, "Fish Locomotion", *Cambridge Univ. Press*, Cambridge, UK.

Blevins, R.D., 1984, "Applied fluid dynamics handbook", *Van Nostrand Reinhold Company*.

Borazjani, I., Sotiropoulos, F., 2008, "Numerical investigation of the hydrodynamics of carangiform swimming in the transitional and inertial flow regimes", *J. of Experimental Biology* 211, 1541-1558.

Bose N., 1992, "A time-domain panel method for analysis of foils in unsteady motion as oscillating propulsors", *11th Australasian Fluid Mechanics Conference*.

Bose, N., Lien, J., 1989, "Propulsion of a fin whale (Balaenoptera physalus): why the fin whale is a fast swimmer", *Proceedings of the Royal Society of London B,* 237, 175-200.

Bose, N., Lien, J., 1990, "Energy absorption from ocean waves: a free ride for cetaceans", *Proceedings of the Royal Society of London B,* 240, 591-605.

Breder, C.M., 1926, "The locomotion of fishes", *Zoologica*, 4, 159-256.

Brockett, T., 1965, "Steady two dimensional pressure distribution on arbitrary wing sections", *NACA TR* 452.

Burnett, R.F., 1979, "Wave energy for propelling craft - Nothing new", *The Naval Architect,* p. 239.

Chen, Z.M., 2012, "A vortex based panel method for potential flow simulation around a hydrofoil", *Journal of Fluids and Structures*, 28, 378-391.

Cheng, H. K. & Murillo, L. E., 1984, "Lunate-tail swimming propulsion as a problem of curved lifting line in unsteady flow. Part 1. Asymptotic Theory.", *J. Fluid Mech.*, 143, 327-350.

Chopra, M.G., 1974, "Hydromechanics of lunate-tail swimming propulsion", *Journal of Fluid Mechanics*, 64, 375-391.

Chopra, M.G., 1976, "Large amplitude lunate-tail theory of fish locomotion", *Journal of Fluid Mechanics*, 74, 161-182.

Collino, F., Monk, P., 1998, "Optimizing the perfectly matched layer", *Comp. Meth. Appl. Mech. Eng.*, 164, 157-171.

Colvile, R.N. et al, (2001), "The transport sector as a source of air pollution", *Atmospheric Environment*, 35, 1537-1565.

Cortelezzi, L., Chen, Y.C., Chang, H.L., 1997, "Nonlinear feedback control of the wake past a plate: from a low-order model to a higher-order model", *Physics of Fluids*, 9, 2009-2022.

Cottrell, J.A., Hughes, T.J.R., Bazilevs, Y., "Isogeometric analysis", *John Wiley and Sons*.

Dabnichki, P., La Mantia, M., 2007, "Dynamic loads and strength requirements for flapping wing", *Key Eng. Meter.*, 348-349:945-948.

De Silva, L.W.A., Yamaguchi, H., 2012, "Numerical study on active wave devouring propulsion", *Journal Marine Science & Technology*, DOI 101007.

De Laurier, J. D. & Harris, J. M., 1982, "Experimental study of oscillating wing propulsion", *J. Aircraft*, 19 (5), 368-373.

Dickinson, M.H., Lehmann, F.O., Sane, S., 1999, "Wing rotation and the aerodynamic basis of insect flight", *Science*, 284, 1954-1960.

Dragos, L., 2003, "Mathematical methods in aerodynamics", *Kluwer*.

Drucker, E.G., Lauder, G.V., 1999, "Locomotor forces on a swimming fish: three-dimensional wake dynamics quantified using digital particle image velocimetry", *Journal of Experimental Biology*, 202, 2393–2412.

Dybdahl, K., 1988, "Foilpropellen kan revolusjonere skipsfarten", Teknisk Ukeblad/Teknikk, 39, 10-11.

Von Ellenrieder, K.D., Parker, K., Soria, J., 2008, "Fluid mechanics of flapping wings", *Exp. Thermal Fluid Sci.*, 32, 1578–1589.

Ellington, C. P., 1984, "The aerodynamics of hovering insect flight IV", *Aerodynamic mechanisms. Phil. Trans. R. Soc. Lond. B*, 305, 79-113.

Filippas, E.S., 2011, "Boundary Element Methods and applications to simple problems of hydrodynamics and wave propagation in marine environment", *NTUA*,
available at: "http://arion.naval.ntua.gr/~banthy/panelm.pdf".

Filippas, E.S., Belibassakis, K.A., 2013, "Free surface effects on hydrodynamic analysis of flapping foil thrusters in waves", *32nd International Conference on Ocean, Offshore Mechanics and Arctic Engineering (OMAE 2013)*, Nantes, France.

Flannery, T., 2005, "The weather makers", *Penguin*.

Freymuth, P., 1988, "Propulsive vortical signature of plunging and pitching hydrofoils", *AIAA J.*, 26, 881-883.

Freymuth, P., 1990, "Thrust generation by an hydrofoil in hover modes", *Experiments in Fluids*, 9, 17-24.

Frydenland, O., Kerwin, J., 1977, "The development of numerical methods for computation of propeller unsteady forces", *Norwegian Maritime Research*, 5(2).

Gause, R., 1969, "US Patent Number: US003453981".

Geoghegan, J.J., 2008, "Boat moved only by waves, Sails to a seafaring first", *The New York Times*, July 8, 2008.

Giesing, J.P., Smith, A.M.O., 1967, "Potential flow about two-dimensional hydrofoil", J. Fluid Mechanics, 28, 113-129.

Glauert, H., 1926, "The elements of aerofoil and airscrew theory", *Cambridge University Press*, London.

Gopalkrishnan, R., Triantafyllou, M.S., Triantafyllou, G.S., Barrett, D.S., 1994, "Active vorticity control in a shear flow using a flapping foil", Journal of Fluid Mechanics, 274, 1–21.

Gray, J., 1936, "Studies in animal locomotion VI: The propulsive powers of the dolphin.", *J. Exp. Biol.*, 13, 192–199.

Gray, J., 1968, "Animal Locomotion", *Weidenfeld & Nicholson*, London.

Grue J., Mo A., Palm E., 1988, "Propulsion of a foil moving in water waves", *J. Fluid Mech.*, 186, 393-417.

Gunter, N.M., 1967, "Potential theory and its application to basic problems of mathematical physics", *Frederick Ungar publishing Co.*, New York.

Gursul, I., Ho, C.M., 1992, "High aerodynamic loads on an hydrofoil submerged in an unsteady stream", *AIAA Journal*, 30, 1117-1119.

Hart, D., Acosta, A., Leonard, A., 1992, "Observations of cavitation and wake structure of unsteady tip vortex flows", *In Proceedings of the International STG Symposium on Propulsors Cavitation*, Hamburg, Germany, 121-127.

Hess, J.L. & Smith, A.M.O., 1962, "Calculation of non-lifting potential flow about arbitrary 3-D bodies", *Douglas Aircraft*, Report E.S. 40622.

Hess, J.L., Smith, A.M.O., 1966, "Calculation of potential flow about arbitrary bodies", *Prog. Aeronaut. Sci.*, 8, 1-138.

Hess, J.L., 1972, "Calculation of potential flow around arbitrary three dimensional lifting bodies", *McDonnell Douglas Corporation*, Report no. MDC J5679-01.

He, M., Veitcha, B., Bose N., Colbourne, B., Liu P., 2006, "A three-dimensional wake impingement model and applications on tandem oscillating foils", *Ocean Engineering*, 34, 1197-1210.

Ho, C.M., Chen, S.H., 1981, "Unsteady Kutta condition of a plunging hydrofoil", *In: Michel, R., Cousteix, J., Houdeville, R., editors, Unsteady turbulent shear flows, Springer*, Berlin, 197-206.

Hoppe, K.G., 1989, "The dynamo-elastic oscillating foil propeller", *Schiff Hafen*, 5, 54–61.

Hover, F.S., Haugsdal, O., Triantafyllou, M.S., 2004, "Effect of angle of attack profiles in flapping-foil propulsion", *Journal of Fluids and Structures*, 19, 37-47.

Isshiki, H., 1982, "A theory of wave devouring propulsion", *J Soc Nav Archit Japan*, 151, 54–64.

Isshiki, H., Murakami, M., 1984, "A theory of wave devouring propulsion", *J Soc Nav Arch Japan*, 156, 102–114.

Jakobsen, E., 1981, "The foilpropeller, wave power for propulsion", In. Papers presented at the Second International Symposium on Wave & Tidal Energy, 363-369.

Johannessen, T.B., Swan, C., 1997, "Nonlinear transient water waves - part I. A numerical method of computation with comparisons to 2-D laboratory data", *Appl. Ocean Res.*, 19, 293-308.

Karpouzian, G., Spedding, G. & Cheng, H.K., 1990, "Lunate-tail swimming propulsion Part 2. Performance analysis", *J. Fluid Mech.*, 210, 329-351.

Kato, N., 1998. "Locomotion by mechanical pectoral fins", *Journal of Marine Science and Technology*, 3, 113–121.

Von Karman, T., Sears, W.R., 1938, "Hydrofoil theory for non-uniform motion", Journal of the Aeronautical Sciences, 5, 379–390.

Katz, J., Plotkin, A., 1991, "Low speed aerodynamics", McGraw Hill, New York.

Katz, J., Weihs, D., 1981, "Wake rollup and the Kutta condition for hydrofoils oscillating at high frequency", *AIAA J.*, 19(12), 1604-1606

Kerwin, J., Lee, C.S., 1978, "Prediction of steady and unsteady performance of marine propellers by numerical lifting surface theory", *SNAME Transactions*, 86.

Koochesfahani, M., 1989, "Vortical patterns in the wake of an oscillating foil", *AIAA J.*, 27, 1200-1205.

Koochesfahani, M.M., Dimotakis, P., 1988, "A cancellation experiment in a forced turbulent shear layer", *AIAA* Technical Paper 88-3713-CP.

Kress, R., 1989, "Linear integral equations", Springer.

Kress R., 1991, "Graduate texts in mathematics, numerical analysis", *Springer*.

Kundu, P.K., Cohen, I.M., 2004, "Fluid mechanics", *Elsevier Academic Press*.

La Mantia, M., Dabnichki, P., 2006, "Unsteady panel method for oscillating foils", *In: Gatmiri, B., Sellier, A., Aliabadi, M.H., editors, Advances in boundary element techniques*, 6, 91-96

La Mantia, M., Dabnichki, P., 2009, "Unsteady panel method for flapping foil", Engineering analysis with Boundary Elements, 33, 572-580.

Lai, J.C.S., Platzer, M.F., 1999, "Jet characteristics of a plunging hydrofoil", *AIAA Journal*, 37, 1529-1537.

Lai, P.S.K., Bose, N. & McGregor, R.C., 1993 "Wave propulsion from a flexible-armed, rigid-foil propulsor", *Marine Technol.*, 30 (1), 28-36.

Lauder, G., Tytel, E., 2006, "Hydrodynamics of undulatory propulsion", *Fish Physiology*, 23, 425-468.

Lee, C.S., Kerwin, J.E., 2003, "A B-spline higher-order panel method applied to two-dimensional lifting problem", *Journal of Ship Research*, 4, 290-298.

Lewis, R.I, 1991, "Vortex element methods for fluid dynamic analysis of engineering systems", *Cambridge University Press*.

Liebe, R., 2007, "Unsteady flow mechanisms on hydrofoils: the extended finite vortex model with applications", *In: Liebe, R., editor, A challenge to engineering design, Flow phenomena in nature, WIT Press*, 1, 283-339.

Lighthill, M.J., 1960, "Note on the swimming of slender fish", *J. Fluid Mech.*, 9, 305-317.

Lighthill, M.J., 1969, "Hydromechanics of aquatic propulsion: A survey. ", *Annual Review Fluid Mechanics*, 1, 413-446.

Lighthill, M.J., 1970, "Aquatic animal propulsion of high hydromechanical efficiency", *Journal of Fluid Mechanics*, 44, 265-301.

Lighthill, M.J., 1971, "Large amplitude elongated body theory of fish locomotion", *Proc. R. Soc. London*, B179, 125–138.

Lighthill, M. J., 1975, "Mathematical Biofluiddynamics", *SIAM*.

Lindsey, C.C., 1978, "Form, function, and locomotory habits in fish." *'Fish Physiology., 6. Locomotion' (Hoar, W. S., and Randall, D. J., Eds.),* Academic Press, New York., 1-100.

Liu, P., Bose N., 1997, "Propulsive Performance from oscillating propulsors" *Proc. R. Soc. Lond.*, A 453, 1763-1770.

Liu, P., Bose, N., 1999, "Hydrodynamic characteristics of a lunate shape oscillating propulsor", *Ocean Engin.*, 26, p.519.

Longuet-Higgins, M.S., Cokelet, E.D., 1976, "The deformation of steep surface waves on water. A numerical method of computation", *Proc. Roy. Soc. Lond.*, Ser. A, 350, 1-26.

Longvinovich, G.V., 1971, "Hydrodynamics of a thin, flexible body", *In Hydrodynamic Problems in Bionics, Joint Publications Research Service* - 52605, Washington, DC, 4-11.

MacCroskey, W. J., 1982, "Unsteady hydrofoils", *Ann. Rev. Fluid Mech.*, 14, 285-311.

Maresca, C., Favier, D. & Rebont, J., 1979, "Experiments on an hydrofoil at high angle of incidence in longitudinal oscillations", *J. Fluid Mech.*, 92, 671-690.

MARINTEK, ECON, CM, DNV, 2000, "Study of greenhouse gas emission from ships", *Final Report IMO.*

McCroskey, W.J., 1982, "Unsteady hydrofoils", *Annu. Rev. Fluid Mech.*, 14, 285-311.

McCune, J.E. & Tavares, T.S., 1993, "Perspective: Unsteady wing theory - The Karman/Sears legacy.", *Trans. ASME Fluids Engng.*, 115, 548-560.

Mikhlin, S.G., 1965, "Multidimensional singular integrals and integral equations", *Pergamon Press.*

Mohammadi-Amin, M., Ghadiri, B., Abdalla, M.M., Haddadpour, H., Breuker, R., 2012, "Continuous-time state-space unsteady aerodynamic modeling based on boundary element method", *Engineering Analysis with Boundary Elements*, 36, 789-798.

Moran, J., 1984, "An introduction to theoretical and computational aerodynamics", *J. Wiley & Sons*.

Morino, L., Gennaretti, M., 1992, "Boundary integral equation method for aerodynamics", *In: Atluri SN, editor. Computational nonlinear mechanics in aerospace engineering, progress in aeronautics and astronautics, vol. 146, American Institute of Aeronautics and Astronautics*, 279-321.

Morino, L., Kuo, C.C., 1974, "Subsonic potential aerodynamics for complex configurations: A general theory", *AIAA J.*, 12, 191-197.

Munk, M.M., 1923, "The determination of the angles of attack of zero lift and zero moment, Based on Munk's Integrals", *NACA TN*, 122.

Muskhelishvili, N.I., 1953, "Singular integral equations", *Nordhoff*, Groningen, Netherlands.

Newmann, J.N., 1977, "Marine hydrodynamics", *MIT press*.

Ohashi, H. & Ishikawa, N., 1972, "Visualization study of flow near the trailing edge of an oscillating hydrofoil", *Bull. JSME*, 15 (85), 840-847.

Ohmi, K., Coutanceau, M., Daube, O. & Loc, T. P., 1991, "Further experiments on vortex formation around an oscillating and translating hydrofoil at large incidences", *J. Fluid Mech.*, 225, 607-630.

Ohmi, K., Coutanceau, M., Loc, T. P. & Dulieu, A., 1990, "Vortex formation around an oscillating and translating hydrofoil at large incidences", *J. Fluid Mech.*, 211, 37-60.
Oshima, Y. & Natsume, A., 1980, "Flow field around an oscillating foil. In Flow Visualization II", *Proc. Second Intl Symp. on Flow Visualization*, Bochum, Germany, 295-299.

Oshima, Y. & Oshima, K., 1980 "Vortical flow behind an oscillating foil.", *Proc. 15th IUTAM Intl Congress*, North Holland, 357-368..

Paris F., Canas J. ,1997, "Boundary Element Methods", Oxford University Press.

Poling, D.R., Telionis, D.P., 1986, "The response of hydrofoils to periodic disturbances-the unsteady Kutta condition", *AIAA J.*, 24(2), 193-199.

Politis, G.K., 2009, "A BEM code for the calculation of flow around systems of independently moving bodies including free shear layer dynamics", *Advances in boundary element techniques X, WIT conference*, Athens, Greece.

Politis, G.K., 2011, "Application of a BEM time stepping algorithm in understanding complex unsteady propulsion hydrodynamic phenomena", *Ocean Engin.*, 38, 699-711.

Politis, G.K., 2011, "The boundary element method for 3-D fluid flow problems", *Notes for the course "Mathematical formulation of lifting flows", School of Naval Architecture and Marine Engineering, National Technical University of Athens*.

Politis G.K., Belibasakis K.A., 1999, "High propulsive efficiency by a system of oscillating wing tails", *Proc. 9th Inter. Conf on Computational Methods and Experimental Measurements, CMEM99, WIT*.

Politis, G.K., Politis, K., 2012, "Biomimetic propulsion under random heaving conditions, using active pitch control", *Journal of Fluids & Structures* (in press).

Politis, G.K. & Tsarsitalidis, V.T, 2009, "Simulating Biomimetic (Flapping Foil) Flows for Comprehension, Reverse Engineering and Design.", *First International Symposium on Marine Propulsors, SMP'09*, Trondheim, Norway

Politis, G.K. & Tsarsitalidis, V.T, 2010, "Understanding bird's flight using a 3-D BEM method and time stepping algorithm", *Proc. 4th IC-SCCE 2010*, Athens, Greece.

Politis, G.K. & Tsarsitalidis, V.T , 2011, "Exploring the Potential of an Oscillating Duct as a Marine Propulsor", *Proc. Second International Symposium on Marine Propulsors, SMP'11*, Hamburg, Germany.

Polyanin, A.D., Manzhirov A.V., 2008, "Handbook of integral equations", *Chapman & Hall/CRC*.

Popular Science, 1950, "Wave serve as boat's engine", February 1950, p.224.

Popular Science, 2008, "Wave runner", March 2008, p.35.
Rayner, J.M.V., 1979, "A vortex theory of animal flight mechanics", *Journal of Fluid Mechanics*, 91, 731-763.

Read, D.A., Hover, F.S., Triantafyllou, M.S., 2003, "Forces on oscillating foils for propulsion and maneuvering", *J. Fluids and Structures*, 17, 163-183.

Reynolds, W.C. & Carr, L.W., 1985, "Review of unsteady, driven, separated flows", *AIAA*, 85-0527.

Ritz, W., 1909, "Uber eine methode zur losung gewisser variations-probleme der mathematischen", *Physik. Journal fur reine und angewandte Mathematik*, 135, 1-61.

Riziotis, V.A., Voutsinas, S.G., 2007, "Dynamic stall modeling on hydrofoils based on strong viscous-inviscid interaction coupling"

Rozhdestvensky, K.V., Ryzhov, V.A, 2003, "Aero-hydrodynamics of flapping wing propulsors", *Progress in Aerospace Sciences*, 39, 585-633.

Satyanarayana, B., Davis, S., 1987, "Experimental studies of unsteady trailing-edge conditions", *AIAA J.*, 16(2), 125-129

Scherer, J.O., 1968, "Experimental and theoretical investigation of large amplitude oscillating foil propulsion systems", *US Army Engineering Research and Development Laboratories*.

Schouveiler, L., Hover, F.S., Triantafyllou, M.S., 2005, "Performance of flapping-foil propulsion", *J. Fluids Struct*, 20, 949-959.

Sfakiotakis, M., Lane, D.M., Davies, J.B.C., 1999, "Review of fishswimmin g modes for aquatic locomotion", *IEEE Journal of OceanicEngineering*, 24, 237–252.

Sparenberg J. A., 2002, "Survey of the mathematical theory of fish locomotion", *J. Engin Mathematics*, 44, 395-448.

Streitlien, K., Triantafyllou, G.S., Triantafyllou, M.S., 1996. Efficient foil propulsion through vortex control. AIAA Journal 34, 2315–2319.

Suzuki, S., Washizu, K., 1980, "Calculation of wing-body pressures in incompressible flow using Green's function method", *J. Aircraft*, 17 (5), 326-331

Taylor, G.I., 1952, "Analysis of the swimming of long and narrow animals", *Proc. R. Soc. London* A214, 158-183.

Taylor, G.K, Triantafyllou, M.S & Tropea, C., 2010, "Animal locomotion", *Springer Verlag*.

Terao, Y., 1982, "A floating structure which moves towards the waves (Possibility of wave devouring propulsion)", *Journal of the Kansai Society of Naval Architects*, Japan, 184. 51-54.

Terao, Y., Isshiki, H., 1991. "Wave Devouring Propulsion Sea Trial", *In. Eighteenth Symposium on Naval Hydrodynamics*, 287–296.

Theodorsen, T., Garrick, I.E., 1933, "General potential theory of arbitrary wing sections", *NACA TR*, 452.

Trefftz, E., 1926, "Ein gegenstuck zum Ritz'schen verfahren", *Proc. 2 int. Congress in Applied Mechanics*, Zurich, 131.

Triantafyllou, M.S., Techet, A.H., and Hover, F.S., 2004, "Review of experimental work in biomimetic foils". *IEEE J. Oceanic Eng.*, 29, 585–594.

Triantafyllou, M.S., Triantafyllou, G.S. & Gopalkrishnan R., 1991, "Wake mechanics for thrust generation in oscillating foils", *Phys. Fluids*, A 3(12).

Triantafyllou, M.S., Triantafyllou, G.S. & Grosenbaugh M.A., 1993, "Optimal thrust development in oscillating foils with application to fish propulsion", *Journal of Fluids and Structures*, 7, 205-224.

Triantafyllou, M.S, Triantafyllou, G.S., Yue, D.K.P., 2000, "Hydrodynamics of fishlike swimming", *An. Review Fluid Mech.*, 32**.**

Turkel, E., Yefet, A., 1998, "Absorbing PML boundary layers for wave-like equations", *Appl Numer. Math.*, 27(4), 533-557.

Van Dyke, M., 1975, "Perturbation methods in fluid mechanics", Stanford Parabolic Press.

Videler, J. J., 1993, "Fish Swimming", *Chapman and Hall*, New York.

Vladimirov, V.S., 1979, "Generalized functions in mathematical physics", *Mir Publishers*, Moscow.

Webb, P.W., Weihs, D., 1983, "Fish Biomechanics", *Praeger Publishers*, New York.

Webb, P.W., 1975, "Hydrodynamics and energetics of fish propulsion", *Bull. Fish. Res. Bd. Can.* 190, 1-159.

Woods, L.C., 1961, "The theory of subsonic plane flow", *Cambridge University Press.*

Wu, T.Y., 1961, "Swimming of a waving plate", *J. Fluid Mech.*, 10, 321-344.

Wu, T.Y., 1971, "Hydromechanics of swimming propulsion. Part 1. Swimming of a two-dimensional flexible plate at variable forward speeds in an inviscid fluid", *J. Fluid Mechanics* 46, 337-355.

Wu, T.Y., 1972, "Extraction of flow energy by a wing oscillating in waves", *J. Ship Res*, 14(1), 66–78.

Yeung, R.W., Bouger, Y.C., 1979, "A hybrid-integral equation method for steady two-dimensional ship waves", *Int. J. Num. Enging.*, 14, 317-336.

Young, J., Lai, J.C.S., 2004, "Oscillation frequency and amplitude effects on the wake of a plunging hydrofoil", *AIAA J.*, 42(10), 2042-2052.

Zhu Q., Wolfgang, M.J., Yue, D.K.P., Trianatafyllou, M.S., 2002, "Three dimensional flow structures and vorticity control in fish-like swimming", *J. Fluid Mech.*, 468, 1-28.